Investigation of the shell evolution in neutron-rich titanium nuclei using reduced transition strengths

Inaugural-Dissertation

zur

Erlangung des Doktorgrades

der Mathematisch-Naturwissenschaftlichen Fakultät

der Universität zu Köln

vorgelegt von

Alina Goldkuhle

aus Bielefeld

Hundt Druck GmbH, Köln
2020

Berichterstatter:	Prof. Dr. Alfred Dewald
(Gutachter)	Prof. Dr. Andreas Zilges
Tag der mündlichen Prüfung:	07. Dezember 2020

Meinen Eltern

Abstract

This work describes experimental studies that contribute to the understanding of the shell structure in the Ti-Cr-Fe region beyond $N = 28$. For exotic nuclei, as examined in this thesis, significant changes in the shell structure may occur. Therefore, such nuclei offer the possibility to investigate the properties and validity of nuclear models under extreme conditions. From the experimental data available so far on the 2_1^+ states in $N = 32$ isotones, the occurrence of a phase transition from predominant collective structures in ^{58}Fe to a neutron subshell closure is predicted, which evolves as the number of protons in the $\pi f_{7/2}$ orbital reduces, i.e. of ^{56}Cr$\rightarrow^{54}$Ti$\rightarrow^{52}$Ca, due to the weakening of the monopole interaction between the $\pi f_{7/2}$ orbital of protons and the $\nu f_{5/2}$ orbital of neutrons. However, modern shell-model calculations with different interactions, e.g. the GXPF1A, KB3G and FPD6 interactions, were not able to satisfactorily describe the observed staggering of the $B(E2; 2_1^+ \rightarrow 0_{\text{gs}}^+)$ values in ^{50,52,54}Ti, which probably results from neutron subshell closures.

Therefore, in this work reduced transition probabilities of the lowest transitions of the respective ground-state bands in ^{46,50,52,53,54}Ti were investigated experimentally by lifetime measurements, partly for the first time. The multinucleon-transfer reaction mechanism, which is a promising approach to the production of difficult to access and exotic atomic nuclei, was applied to study the evolution from nuclei in the valley of stability towards neutron-rich exotic Ti isotopes at the Grand Accélérateur National d'Ions Lourds (GANIL) in Caen, France: In the Cologne plunger for deep-inelastic reactions, a radioactive ^{238}U beam with an energy of 6.76 MeV/u impinged on a stretched ^{50}Ti target with $^{\text{nat}}$Cu layer in front of the target, while a $^{\text{nat}}$Mg degrader foil was used to decelerate the reaction products for measuring lifetimes using the Recoil Distance Doppler-shift (RDDS) technique. The reaction products of interest were identified with the magnetic spectrometer VAMOS++, while the gamma radiation was measured with the gamma tracking array AGATA. During this experiment beam-induced changes of the target occurred. These resulted in the fact that the distances between the target and degrader foil could not be extracted exactly, which are essential for an RDDS lifetime analysis. Therefore, another RDDS experiment was performed at the Cologne FN tandem accelerator using a fusion-evaporation reaction. The aim of this experiment was to determine the lifetimes of the 2_1^+ and 4_1^+ states of the ground-state band in the stable nucleus ^{46}Ti with high precision, in order to subsequently determine the unknown distances between the target and degrader foil of the experiment performed at GANIL. This nucleus was chosen because it was populated with sufficient statistics in the multinucleon-transfer reaction at GANIL and the lifetimes of its low-lying states are in the sensitive range for the distances chosen in this experiment. The data from the experiment on ^{46}Ti in Cologne were analyzed using the Differential Decay Curve method in $\gamma\gamma$ coincidences. The unknown distances from the GANIL experiment were then determined by comparing the experimental γ-ray spectra with those generated by Monte-Carlo simulations using the χ^2 method.
The lifetimes of the 2_1^+, 4_1^+, 6_1^+ and 8_1^+ in ^{52,54}Ti and the $(5/2^-)$, $7/2^-$, $9/2^-$, $11/2^-$ and $13/2^-$ states in ^{53}Ti were determined using both the DDCM and the minimum χ^2 method with the distances obtained in this way.

Furthermore, a third RDDS measurement was carried out within this work, also at the Cologne FN tandem accelerator, with the aim of determining the lifetime values of the lowest-lying states of the ground-state band in ^{50}Ti. Although this nucleus was also

populated during the measurement at GANIL, the additional measurement provided a more precise determination of the lifetimes based on the knowledge of the exact relative distances between the target and degrader foil. The lifetimes were analyzed in a particle-gamma evaluation.

The transition probabilities determined from the level lifetimes are interpreted based on shell-model predictions of different interactions in the $f_{7/2}, p_{3/2}, f_{5/2}, p_{1/2}$ valence space for protons and neutrons.

Contents

Introduction

In recent years, experimental nuclear structure physics has come to the fore by conducting experiments with radioactive beams, as they make it possible to access areas of the nuclear chart that cannot be reached by conventional methods. In this way, information about exotic nuclei - far from the valley of stability - can be obtained. However, the number of research institutions worldwide that have radioactive beams at their disposal is small, which is due to the high-technical effort and the associated high costs involved. The requirements for physicists who want to perform research at such accelerator facilities are therefore very high. Due to the limited beam time available, approved experiments have to be carried out successfully without major problems right from the start. In order to ensure such a friction-free procedure, test experiments are carried out in advance at smaller accelerator facilities, whose setup can be modified or optimized on site if any uncertainties arise. In the framework of this thesis, experiments have been carried out at various research facilities, with the main focus on the analysis of data obtained with stable radioactive beam at the large-scale facility GANIL in Caen, France. These investigations are supported and complemented by two further measurements, which were made at the FN tandem accelerator in Cologne, Germany.

The following chapter gives a short overview of the shell model with the interactions used in this thesis to interpret the experimental results, the experimental method with the analysis procedure, and the experimental setup at GANIL. This is followed by four publications in which the lifetime results and their interpretation on ^{46,52,53,54}Ti are presented. A short summary concludes the studies presented in this thesis, including the results of an additional measurement on ^{50}Ti.

1.1. Shell-model framework

In nuclear structure physics, the atomic nucleus is treated as a quantum-mechanical many-particle system of protons and neutrons, whose structure is determined by the properties of the strong nuclear force. At a certain number of protons and/or neutrons, the so-called *magic numbers* (2, 8, 20, 28, 50, 82 and 126), the nuclei show particular stability, i.e. at certain numbers the nucleons form closed configurations in the nucleus [1, 2]. This leads to the model idea that the protons and neutrons in the nucleus are arranged in shells, i.e. there exist discrete energy levels, similar to the electrons in the atom. This arrangement in the nucleus leads to the fact that one speaks of a shell structure of the atomic nuclei. Each shell can only hold a certain maximum number of nucleons of a specific type under consideration of the Pauli principle. If the last occupied orbital/shell is completely filled, special effects on the nuclear structure can occur. This effect is especially noticeable at the

magic numbers where the next free shell has a large energy gap to the fully occupied orbital. The achievement of such an occupation number is generally referred to as *shell closure*. The robustness of these magic numbers, and the location of shell closures for nuclei away from the valley of stability is a central issue in nuclear structure physics. It has been observed that for exotic nuclei, i.e. isotopes far from stability with extreme N/Z ratios, the magic numbers that apply to stable nuclei can change locally. One of the first unexpected shell closures was discovered in ^{24}O [3, 4] at $N = 16$, a surprisingly doubly-magic nucleus. Such effects, which are different from the magic numbers, are called *subshell closures*. Today this phenomenon can be explained by the contribution of three-body forces [5]. The sequence of individual single-particle orbitals can also change, as was found, for example, in the so-called *island of inversion* for neutron-rich magnesium isotopes [6]. Here, the shell gap of $N = 20$ for exotic nuclei disappears. The reason for this can be explained by the tensor force [7, 8].

The basic assumption of the shell model is that the nucleons are in a mean/spherical potential (mean field) by which they are held in the atomic nucleus. However, the assumption of the independence and spherical shape are strong simplifications, since interactions exist between the nucleons that cannot be described by the mean potential. Taking into account some residual interactions and considering the orbits in a deformed potential, the shell model can be improved. Thus, different effective interactions are used, which are each limited to defined areas of the chart of nuclides (see Sec. 1.1.1) [2].

1.1.1. The spherical shell model

The basic ideas for the description of the shell model are based on the single-particle model and assuming a spherical nucleus. The atomic nucleus with A nucleons is described by the Hamilton operator

$$H = \sum_{i=1}^{A} T_i + \sum_{i<j}^{A} V_{ij} \tag{1.1}$$

where T_i is the kinetic energy for each particle i and V_{ij} accounts for the strong two-body nucleon-nucleon interaction between the nucleons i and j with $\sum_{ij} V_{ij} = \frac{1}{2}\sum_{i\neq j} V(r_{ij})$[1] [2]. Since the Schrödinger equation using this Hamiltonian is unsolvable for many nucleons (V_{ij} is a function of the three relative position coordinates), Eq. (1.1) is rewritten using a distance-dependent central potential $V(r_i)$ as

$$H = \sum_{i=1}^{A}[T_i + V(r_i)] + \left[\sum_{i,j=1}^{A} V(r_{ij}) - \sum_{i}^{A} V(r_i)\right] \equiv H_0 + H_{\text{res}}. \tag{1.2}$$

[1] Every two-particle interaction is counted only once.

Here

$$H_0 = \sum_{i=1}^{A} \left(\frac{p_i^2}{2m_i} + V(r_i) \right)$$

describes the motion of a single particle, independent of the others, in a mean potential $V(r_i)$, where p_i and m_i are the momentum and mass of the nucleon and

$$H_{\text{res}} = \sum_{i,j=1}^{A} V(r_{ij}) - \sum_{i=1}^{A} V(r_i)$$

is the residual interaction, which thus includes the remaining nucleon-nucleon interactions [2]. By splitting the potential in Eq. (1.2), it is assumed that the residual interaction H_{res} can be treated as a small perturbation so that the nucleons are in a distance-dependent mean potential. Among the distance-dependent potential, only the harmonic-oscillator potential and the box potential can be treated analytically, where both potentials are infinitely high[2] [1]. In contrast, the Woods-Saxon potential[3]

$$V_{\text{WS}}(r) = -\frac{V_0}{1 + e^{(r-R)/a}} \tag{1.3}$$

is much more realistic, but it is only accessible to a numerical treatment. This potential reflects well the measured density distribution for the nucleons. As a result, the harmonic-oscillator levels are split after the orbital-angular momentum. By solving the Schrödinger equation, energy levels are obtained which, however, provide different shell closures than the magic numbers, especially for larger number of nucleons in the core, as Fig. 1.1 shows (left and middle column) [2].

Only in 1949, the shell closures that reproduce the magic numbers were found by O. Haxel, J. H. D. Jensen, H. E. Suess [9–12] and M. Goeppert-Mayer [13, 14]. Their ideas are based on the basic principle of the atomic shell, in which the spin-orbit coupling of the electron based on the electromagnetic interaction plays a significant role. This causes the experimentally observed splitting of spectral lines, which is called *fine structure*. A similar spin-orbit coupling has also been introduced for the strong interaction of nucleons [1]. The following approach then applies:

$$V(r_i) = V_0(r) + V_{\ell s}(r_i)(\vec{\ell} \cdot \vec{s}),$$

where $\vec{\ell}$ and $\vec{s}$ are the orbital-angular momentum and the spin. Applied to Eq. (1.3), the result is

$$V_{\text{WS}}(r) = -\frac{V_0}{1 + e^{(r-R)/a}} + V_{\ell s}(r_i)(\vec{\ell} \cdot \vec{s}). \tag{1.4}$$

[2] It is not a significant restriction for the consideration of bound states.

[3] with V_0 represents the potential well depth, a is a parameter representing the surface thickness of the nucleus, $R = r_0 A^{1/3}$ is the nuclear radius with $r_0 = 1.25\,\text{fm}$, and A is the mass number.

This modification, which gives good results for the energy eigenvalues of the shells, reproduces the experimentally found energy gaps of these shells, see the last column in Fig. 1.1.

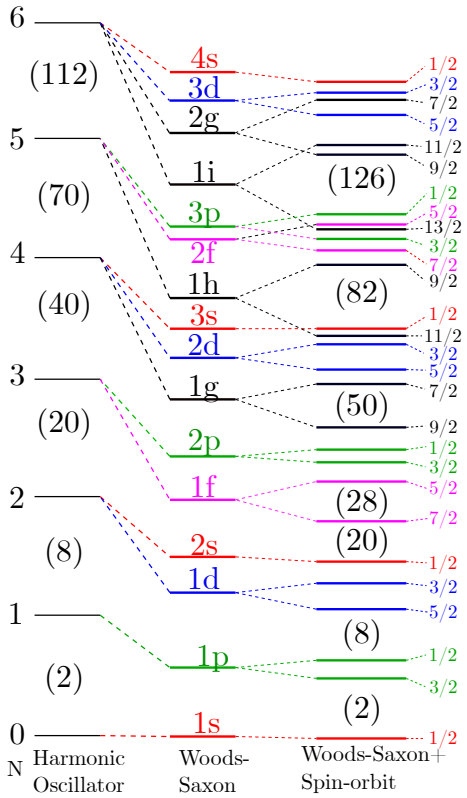

Figure 1.1.: Schematic representation of nucleon-energy levels of the harmonic-oscillator model (*left*), the Woods-Saxon potential (*middle*), and the Woods-Saxon potential including the spin-orbit coupling (*right*). Based on Fig. 3.2 in Ref. [2].

With Eq. (1.4) an exact description for the excitation spectrum of an atomic nucleus has been found, when only one nucleon outside the main shell closure is considered. In contrast, the shell model of multi-particle systems takes into account the residual interaction H_{res} between these valence nucleons, which essentially determines the internal excitation structure of an atomic nucleus, although it was introduced only as a perturbation of the mean potential. For this it is assumed that interactions of more than two nucleons are negligible. For heavier nuclei ($A \geq 50$), there is the problem that the sizes of the matrices (in which the residual interactions are diagonalized) increase, making the residual interaction difficult to handle. For such a number of nucleons, the shell model solved this problem by not treating all nucleons as active particles. Instead, the model space is split into an "inert" core and the valence space. Furthermore, the two-body interaction is replaced by an effective interaction that is adapted for a defined range of nuclei on the chart of nuclides.

The simplest approach for H_{res} is to take the δ interaction

$$V_{12} = -V_0\delta(r_1 - r_2)$$

from the class of the schematic effective interactions, which is only valid if two nucleons are at the same location. It provides satisfactory results to describe nuclei in the immediate vicinity of a core, but its results deteriorate as more valence nucleons are added to the core.

Another class of residual interactions are microscopic effective interactions based on Brueckner's G-Matrix theory [15] and a realistic nucleon-nucleon interaction. The two-body matrix elements of the residual interaction are fitted to experimental data of the respective model space. In general, they give better results than the schematic interactions.

Such effective interactions, based on realistic nucleon-nucleon potentials, were used in this work to describe the $^{50-54}$Ti ($Z = 22$ and $N = 28-32$) nuclei. For the region of Ti isotopes, the double-magic core ^{40}Ca ($N = Z = 20$) is a possible choice for the "inert" core. This leaves 2 valence protons and 8 to 12 valence neutrons to describe $^{50-54}$Ti. This model space comprises the $f_{7/2}$, $p_{3/2}$, $p_{1/2}$, and $f_{5/2}$ orbitals.

Shell-model interactions for the description of $Z = 22, N \leq 32$ nuclei

In this thesis, several effective interactions were used, such as GXPF1A [16], GXPF1B [17], KB3G [18], and FPD6 [19], as well as those modified from them. Numerous studies have already shown that by adjusting their parameters the shell-model calculations based on them can reproduce experimentally measured excitation energies of selected pf shell nuclei. In the following, a few basic features of these interactions are given.

The GXPF1A interaction is provided by Honma *et al.* and described in detail in Ref. [16]. It represents an improvement of the GXPF1 [20, 21] interaction, especially for the range of neutron-rich Sc-, Ti- and Ca isotopes. This two-body effective interaction describes the spectroscopic properties of the nuclei in the mass region $A = 47 - 66$. Both Hamiltonians, GXPF1 and GXPF1A, are based on microscopic calculations by Hjorth-Jensen, which were developed from the G-Matrix theory with the Bonn-C interaction [15]. The GXPF1A interaction is refined by systematically fitting the important linear combinations of two-body matrix elements to lowest states in nuclei with $A = 47 - 66$ [22]. A small modification to GXPF1A is the GXPF1B [17] interaction. This interaction was created by changing five $T = 1$ matrix elements and the single-particle energies that involved the $1p_{1/2}$ orbital [23].

The KB3G interaction is provided by Poves *et al.* [18] and is based on the KB3 interaction [24]. The KB3G Hamiltonian, well adopted for the pf shell-model space, is also based on the Kuo Brown's G-matrix [25] in the same way as KB3, but it is modified in some matrix elements with slight empirical improvement, see Ref. [18], to handle the $N = Z = 28$ shell closure and its surroundings correctly. The single-particle energies are obtained from experimental

levels of nuclei around ^{40}Ca. The KB3G interaction is quite a good choice for *pf* shell nuclei with Z, N up to ~ 26 and $A \leq 52$.

The FPD6 interaction is provided by Richter *et al.* [19] and is an empirical two-body interaction adjusted for $A = 41 - 49$ nuclei. This Hamiltonian has also been designed for full *pf* shell calculations. The FPD6 interaction has certain advantages for heavier nuclei, including ^{56}Ni, owing to a better effective gap between the $f_{7/2}$ orbital and the other *pf* shell orbitals [26].

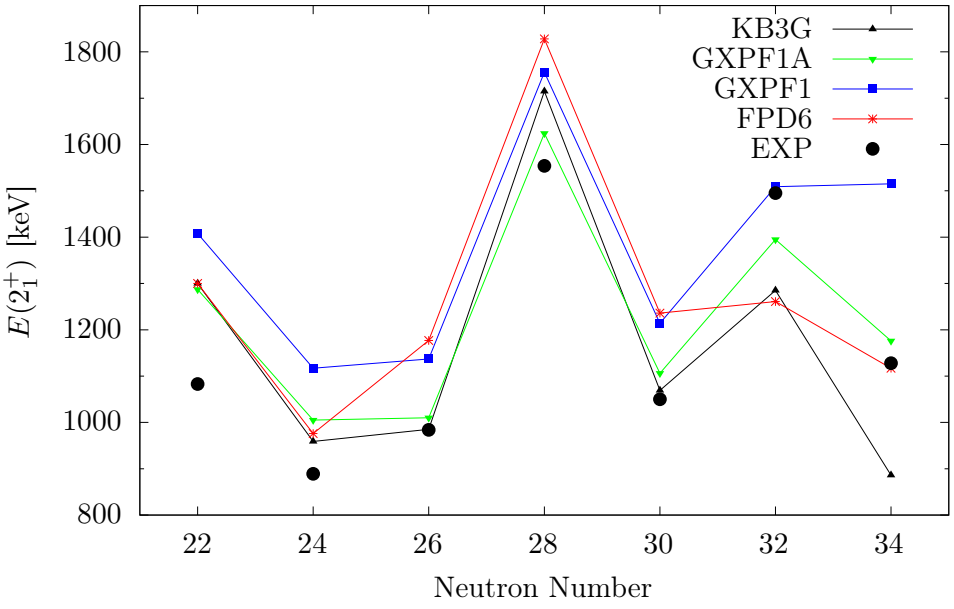

Figure 1.2.: Experimental and theoretical calculated excitation energies of the first excited 2_1^+ state in $^{44-56}$Ti. Shown are the results of shell-model calculations using the effective interactions of KB3G, GXPF1, GXPF1A and FPD6. See text for details.

Fig. 1.2 shows a comparison of the excitation energies of the first excited states calculated with the introduced interactions for the even-even titanium isotopes $^{44-56}$Ti. It can be clearly seen that the GXPF1 interaction overestimates the excitation energy of all depicted titanium isotopes, whereas the advanced interaction GXPF1A provides a better overall agreement with reduced deviations from the experimental values. In addition, calculations with the KB3G interaction also show a good agreement for $N = 24 - 30$. However, the excitation energies for Ti isotopes with $N = 22$ and $N > 30$ cannot be described sufficiently by this interaction. The FPD6 interaction also shows large deviations for the presented region. Only for $N = 34$ it provides a satisfactory agreement with the experimental value. Nearly all interactions overestimate the experimental values for $N = 22 - 30$, whereas most interactions predict lower values for $N = 32$. For $N = 34$ there is a mixed picture with over- and underestimations from the shell model calculations. Nevertheless, almost

all interactions reproduce the trend of the excitation energies, but in contrast, there were significant differences in the description of the transition strengths of $^{50-54}$Ti prior this work. Thus, for example, the theoretical calculations strongly overestimate the $B(E2; 2_1^+ \rightarrow 0_{gs}^+)$ value of ^{50}Ti [27] and the trend of the $B(E2)$ values for the $2_1^+ \rightarrow 0_{gs}^+$, $4_1^+ \rightarrow 2_1^+$, and $6_1^+ \rightarrow 4_1^+$ transitions in ^{52}Ti [28, 29] could not be reproduced. If one goes further into detail, additional anomalies are observed for individual interactions, such as the occupation numbers for the first excited states in the odd-mass ^{53}Ti. Especially calculations with the FPD6 interaction reveal deviations from the other interactions. The challenge for the interactions is to consistently describe the rapid shell evolution known in the neutron-rich $N = 30 - 40$ region.

Calculations with all interactions were performed by the author of the present thesis in communication with Dr. Andrey Blazhev of the University of Cologne using the shell-model NuShellX@MSU [30] and KShell [31] codes. All used large-scale shell-model calculations were performed by effective charges $e_\pi = 1.31\,e$ for protons and $e_\nu = 0.46\,e$ for neutrons as suggested in Ref. [32].
Another approach to describe the nuclear structure is the so-called *beyond-mean-field method*, in which the mean field is calculated self consistently from an empirical nucleon-nucleon interaction. By projecting the wave function into the eigenstates of the respective operator, the physical variables (such as angular momentum or particle number) are extracted. This approach provides promising results for the transition probabilities $B(E2; 2_1^+ \rightarrow 0_{gs}^+)$ in ^{52,54}Ti [33, 34].

1.2. Lifetime measurement

A reliable and at the same time efficient method for the lifetime measurement of excited nuclear states in the picosecond range is the so-called *Recoil Distance Doppler-Shift* (RDDS) method [35]. In order to achieve a high precision with very small relative errors ($\sim 5\,\%$) of the measured lifetimes, this method makes high demands on the surface quality of the target and stopper/degrader foils. The precision of the lifetime determination depends strongly on the accuracy of the distance determination of the two foils, which can deteriorate due to target changes caused by thermal expansion in the beam. The high accuracy of the lifetime values respectively the transition strengths derived from them allows a meaningful comparison with theoretical models even in cases where different predictions show only small deviations.

In this subchapter, the RDDS method with the plunger mechanism is presented. The Cologne compact plunger [35] for deep-inelastic reactions was used for lifetime measurements in the experiment performed at GANIL, where the Cologne coincidence plunger was used for the experiments at the Cologne FN tandem accelerator. For the data analysis, the

Differential Decay Curve method (DDCM) [36] (see Sec. 1.2.2) and the minimum χ^2 method were used.

1.2.1. The Recoil Distance Doppler-Shift Method

The RDDS method is based on the Doppler effect. In a reaction chamber under vacuum, two tautly stretched foils, the target and stopper foils, are mounted parallel to each other at a distance d. In the main experiment (at GANIL), a degrader foil was used instead of a stopper foil, which allows the identification of the reaction products with the magnetic spectrometer VAMOS++ [37]. The measuring technique when using a degrader is described below. The target is fixed in the center of the chamber, while the degrader can be moved in discrete steps, so that a precise adjustment of the distance between them is feasible. The used compact plunger for deep-inelastic reactions is depicted in Fig. 1.3 left.

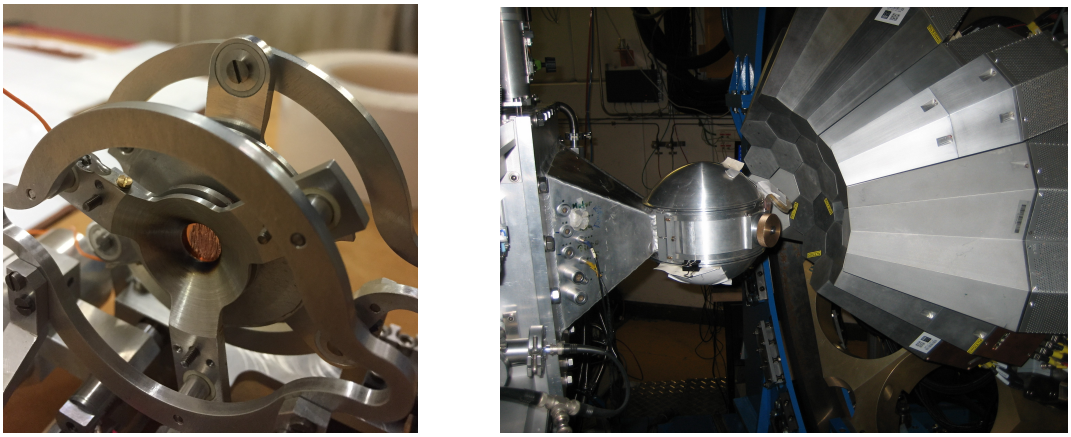

Figure 1.3.: *Left:* The Cologne compact plunger for deep-inelastic reactions. *Right:* The experimental setup at GANIL with AGATA in the right of the picture, the plunger chamber in the middle, and the flange to the spectrometer VAMOS++ in the left.

As the ion beam impinges on the target, a nuclear reaction happens between the projectile and target nuclei. The resulting recoil nuclei leave the target foil and fly with a velocity v_T in the direction of the degrader foil. After the distance d, the recoils are slowed down in the degrader to a reduced velocity v_D, and are identified in the magnetic spectrometer (VAMOS++). The excited nuclei de-excite to the ground state in a cascade of γ-ray transitions, either before or after passing the degrader. These γ rays are measured with the γ-ray spectrometer AGATA [38], depicted in Fig. 1.3 right. If the produced nucleus emits γ rays during the flight time to the degrader, this Doppler-shifted nucleus is detected in a detector (of AGATA) with the energy of

$$E(\beta_\mathrm{T}, \theta) = E_0 \frac{\sqrt{1-\beta_\mathrm{T}^2}}{1-\beta_\mathrm{T}\cos\theta} \approx E_0(1+\beta_\mathrm{T}\cos\theta), \tag{1.5}$$

where E_0 is the absolute energy of the γ-ray transition, θ is the angle between the velocity vector of the recoil and the emitted γ ray and $\beta_T = v_T/c$ is the recoil velocity after target with c the speed of light.

According to Eq. (1.5), the energy of the γ ray emitted is observed at two different energies (E_T, E_D) for each velocity ($\vec{v}_T$, $\vec{v}_D$), since the velocity of the recoils changes in the slowing-down process in the degrader. For simplicity, we assume that the slowing-down time in the degrader is short as compared to the level lifetime.

The principle and the setup of an RDDS experiment are illustrated schematically in Fig. 1.4.

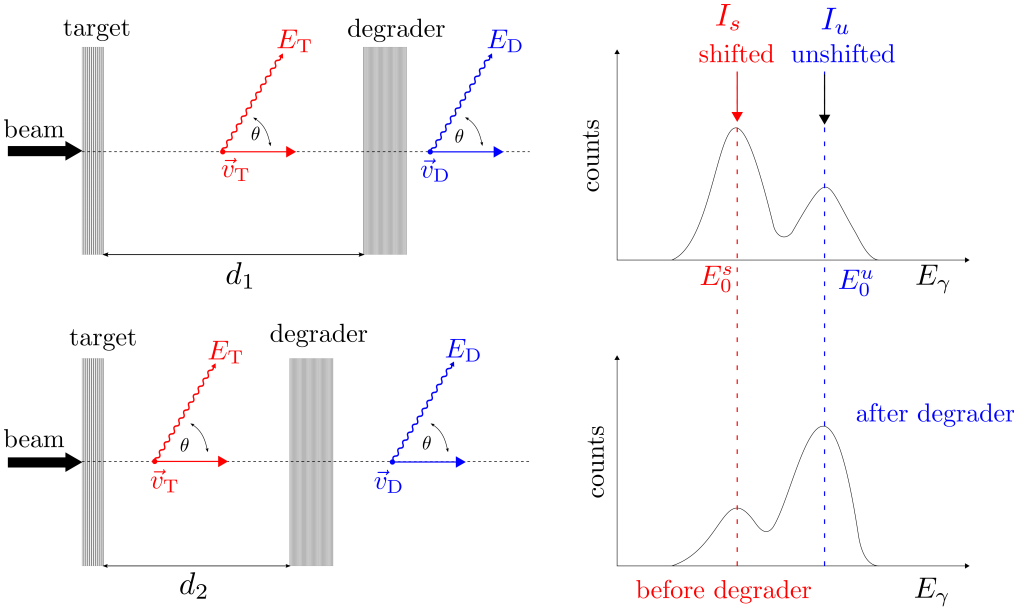

Figure 1.4.: Schematic representation of the RDDS method using the differential plunger with a degrader foil which slows down the nucleus. This velocity $\vec{v}_D$ is measured with the magnetic spectrometer and allows a Doppler correction for the γ rays. In the resulting γ-ray spectrum, the peak appears at the correct energy (E_0^u) in the laboratory frame. The variation of the intensities of the shifted (s) and unshifted (u) components at different distances is shown schematically in the corresponding γ-ray spectra. Note: For simplicity, the setup and the direction of the recoils have been drawn in the same direction as the beam. The arrangement present in the experiment is shown in Fig. 1.12, in which the structure is inclined in relation to the beam axis in the grazing-angle direction. See text for details. Graphic modified from Ref. [39].

The momentum information about the excited nucleus for the Doppler correction is measured in the detectors of the mass spectrometer (VAMOS++). The Doppler effect is corrected event-by-event using the velocity v_D. The energy emitted by the nucleus after passing the degrader then appears at the correct energy position E_0^u (unshifted) in the laboratory

frame, according to

$$E_0^u = E_0 = \frac{E_\mathrm{D}}{1 + \beta_\mathrm{D} \cos\theta}.$$

In case the nucleus decays before reaching the degrader, the γ rays appear at lower energy E_0^s (shifted) due to the energy loss in the degrader from the original value and AGATA in backward angles, according to

$$E_0^s = \frac{E_\mathrm{T}}{1 + \beta_\mathrm{T} \cos\theta}.$$

Therefore, the Doppler-corrected γ-ray spectrum shows two components for each γ-ray transition, one shifted (emitted before the degrader, red in Fig. 1.4), and one unshifted (emitted after the degrader, blue in Fig. 1.4), whose intensities correspond to the decay probability during the flight time before and after the degrader. This decay probability is directly related to the lifetime of the corresponding excited nuclear state and can therefore be obtained by measuring the intensities of the γ rays as a function of the distance between target and degrader. Due to the velocity distribution of the recoils, the shifted component is widened compared to the energy resolution of the detector.

To measure lifetimes, several distances between target and degrader are set and each kept constant for a certain time. This changes the flight time $t = d/v_\mathrm{T}$ of the excited nuclei to the degrader and also the intensities of the shifted and unshifted components. By measuring their intensity ratios, the lifetime of the excited nuclear states can be derived with the method described below.

1.2.2. The Differential Decay Curve method

The traditional analysis method for determining the lifetimes of excited nuclear states in the ps range from Doppler-shifted γ-ray transitions, is the so-called *Decay Curve Method* (DCM) [36]. It is based on the application of the Bateman equations to the curve resulting from the ratio of the intensities of the two components as a function of the distance between target and degrader. For this method, the knowledge about absolute distances are required, so that the "zero point" of the plunger is one of the quantities to be determined, in addition to the usual parameters such as lifetime, initial population or branching ratios [35].

A method further developed from this method is the Differential Decay Curve Method (DDCM), which was introduced by A. Dewald *et al.* [36] and has since become the standard method for evaluating lifetime measurements with the RDDS technique. The main advantage of this method is that only relative target-to-degrader distances are required and systematic errors can be detected very well, especially in combination with a $\gamma\gamma$-coincidence experiment.

Fig. 1.5 shows an extract of a level scheme. The lifetime τ_i from level l_i is to be determined, which is populated over a series of higher-lying levels l_h and in turn decays to lower-lying levels l_j. Directly populating transitions are designated **B**, indirectly populating transitions

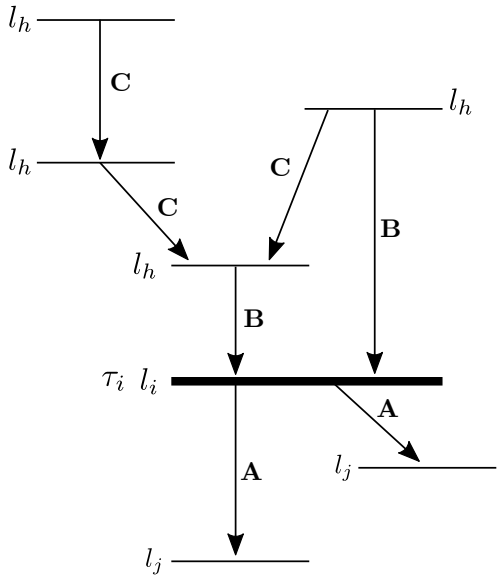

Figure 1.5.: Extract of a level scheme. The level l_i is of interest, which is populated by the levels l_h via direct (indirect) γ-ray transitions B (C) and decays to lower-lying levels l_j via A. See text for details.

C, and directly depopulating transitions **A**. Level l_i is populated by a cascade of transitions, so that the observable decay curve of this level includes the population history of all higher-lying levels l_h involved in the cascade. The differential equation is derived from the decay law by superposition of all decays involved

$$\frac{dn_i(t)}{dt} = -\lambda_i n_i(t) + \sum_h b_{hi}\lambda_h n_h(t), \tag{1.6}$$

with $n_i(t)$ and $n_h(t)$ are the number of nuclei in levels l_i and l_h at time t, $\lambda_i = 1/\tau_i$ and $\lambda_h = 1/\tau_h$ the decay probabilities and b_{hi} the branching ratio of the decay from level l_h to level l_i. The solution of Eq. (1.6) is (see Ref. [35])

$$R_i(t) = P_i(t)e^{-t\lambda_i} + \sum_{h=i+1}^{N} M_{hi}\left[(\lambda_i/\lambda_h)e^{-t\lambda_h} - e^{-t\lambda_i}\right]$$

with

$$M_{hi}(t)(\lambda_i/\lambda_h - 1) = b_{hi}P_h - b_{hi}\sum_{m=h+1}^{N} M_{mh} + \sum_{m=i+1}^{h-1} M_{hm}b_{mi}(\lambda_m/\lambda_h)$$

and P_i and P_h are the direct feeding intensities of each level.

Since the intensities described are observed in the experiment as an integral over a period

of time, the integral form of the above equation is used:

$$\int_t^\infty \frac{dn_i(t')}{dt'}dt' = -\underbrace{\lambda_i \int_t^\infty n_i(t')dt'}_{N_i(t)} + \sum_{h=i+1}^{N} b_{hi}\underbrace{\lambda_h \int_t^\infty n_h(t')dt'}_{N_h(t)},$$

where $N_i(t)$ and $N_h(t)$ are the decay functions of the levels l_i and l_h respectively. The integral on the left side of Eq. (1.6) gives

$$\int_t^\infty \frac{dn_i(t')}{dt'}dt' = n_i(\infty) - n_i(t) = -n_i(t),$$

because $n_i(\infty) = 0$. Therefore, Eq. (1.6) simplifies to

$$-n_i(t) = \frac{1}{\lambda_i}\frac{d}{dt}N_i(t) = -N_i(t) + \sum_{h=i+1}^{N} b_{hi}N_h(t).$$

With $\tau_i = \frac{1}{\lambda_i}$ finally the equation for the calculation of lifetimes according to the DDCM is obtained [35]:

$$\tau_i(t) = \frac{-N_i(t) + \sum_{h=i+1}^{N} b_{hi}N_h(t)}{\frac{d}{dt}N_i(t)}. \tag{1.7}$$

N_i and N_h are directly proportional to the intensities of the shifted and unshifted components in RDDS experiments.

For example, looking at a transition from level l_i to level l_j in Fig. 1.5, the intensity $P_i(t)$ of the unshifted component of this transition is proportional to $N_i(t)$ at the distance d and can be written as

$$P_i(t) = \epsilon(E_{\gamma i})\omega_A(\theta, t)p(t)N_i(t),$$

where $E_{\gamma i}$ is the energy of a transition from the level l_i, $\epsilon(E_{\gamma i})$ is the efficiency of the detector at the energy $E_{\gamma i}$, $\omega_A(\theta, t)$ is the angular-distribution coefficient, and $p(t)$ is a normalization coefficient that normalizes the individual measurements at different distances to the same number of produced nuclei. Since the experimentally determinable decay curves are proportional to the decay functions, Eq. (1.7) can be written as

$$\tau_i(t) = \frac{-R_i(t) + \sum_{h=i+1}^{N} b_{hi}\alpha_{hi}R_h(t)}{\frac{dR_i(t)}{dt}},$$

with

$$\alpha_{hi} = \frac{\omega_h(\theta)\epsilon(E_{\gamma h})}{\omega_i(\theta)\epsilon(E_{\gamma i})}.$$

The additional advantage of this lifetime calculation in $\gamma\gamma$-coincidence mode considering a gate on the shifted component from above the level of interest is that the lifetimes of the populating levels do not need to be known. Since a value $\tau_i(t)$ is determined for each point

in time t, the so-called *lifetime curve* or τ *curve*, this should have a constant curve within the measurement errors caused by the statistics. Deviations from the constant provide indications of systematic errors, which thus quickly become apparent and can be corrected.

1.2.3. Calculation of $B(\sigma\lambda)$ transition strengths

The *transition probability* T of γ-ray transitions with multipolarity $\sigma\lambda, \mu$ (with σ characterizes the type of radiation, electric or magnetic, λ denotes the angular momentum and $\mu = m_i - m_f$ is the difference between the initial (i) and final (f) magnetic sub state) can be described by (see Refs. [40, 41] and references therein)

$$T(\sigma\lambda,\mu) = \frac{8\pi(\lambda+1)}{\lambda[(2\lambda+1)!!]^2} \cdot \frac{1}{\hbar} \cdot \left(\frac{E_\gamma}{\hbar c}\right)^{2\lambda+1} \cdot |\langle f|\hat{\mathcal{M}}(\sigma\lambda,\mu)|i\rangle|^2$$

with $\hat{\mathcal{M}}(\sigma\lambda,\mu)$ the associated multipole-transition operator. The *total transition probability* is calculated by summing over all sub-processes μ with respect to the transition $I_i \to I_f$ according to:

$$\begin{aligned} T(\sigma\lambda,\mu) &= \sum_{\mu,m_f} T(\sigma\lambda,\mu|I_i m_i \to I_f m_f) \\ &= \frac{8\pi(\lambda+1)}{\lambda[(2\lambda+1)!!]^2} \cdot \frac{1}{\hbar} \cdot \left(\frac{E_\gamma}{\hbar c}\right)^{2\lambda+1} \cdot B(\sigma\lambda; I_i \to I_f), \end{aligned}$$

where the last factor $B(\sigma\lambda, I_i \to I_f)$ is called the *reduced transition probability* and can be expressed by the matrix elements describing the electromagnetic transition as follows

$$B(\sigma\lambda; I_i \to I_f) = \sum_{\mu,m_f} |\langle I_f m_f|\hat{\mathcal{M}}(\sigma\lambda,\mu)|I_i m_i\rangle|^2.$$

The reduced transition strength for $E\lambda$ and $M\lambda$ transitions determined for $I_i \to I_f$ are given in terms of the reduced matrix elements according to

$$\begin{aligned} B(E\lambda; I_i \to I_f) &= \frac{1}{2I_i+1}|\langle I_f|\hat{Q}_\lambda|I_i\rangle|^2 \\ B(M\lambda; I_i \to I_f) &= \frac{1}{2I_i+1}|\langle I_f|\hat{M}_\lambda|I_i\rangle|^2. \end{aligned}$$

The level lifetime related to a decay by a pure $E2$ transition can be numerically expressed in terms of the reduced quadrupole transition $B(E2)$ according to Refs. [40, 41]:

$$B(E2; I_i \to I_f) = \frac{2(5!!)^2}{24\pi} \cdot \frac{BR}{1+\alpha_{IC}} \cdot \left(\frac{\hbar c}{E_\gamma}\right)^5 \frac{\hbar}{\tau}, \tag{1.8}$$

where BR denotes the branching ratio of the considered decay branch and α_{IC} is the inner-conversion coefficient for de-excitations. It should be noted that in this experiment the inner-conversion coefficient is irrelevant since the recoils considered here have high-transition energies and low Z. If the branching ratio is neglected, Eq. (1.8) reduces to the following

$$B(E2; I_i \rightarrow I_f)\,[e^2\mathrm{fm}^4] = \frac{816}{(E_\gamma\,[\mathrm{MeV}])^5} \cdot \frac{1}{\tau\,[\mathrm{ps}]}$$

assuming these numerical values: $e^2 = 1.44\,\mathrm{MeV\,fm}$, $\hbar c = 197.33\,\mathrm{MeV\,fm}$ and $\hbar = 6.582 \cdot 10^{-22}\,\mathrm{MeV\,s}$. It is often the case that a transition can take place by more than one electromagnetic mode, e.g. transitions can have a mixed $E2/M1$ character. In this work, most important are transitions with $\Delta I = 1$. The multipole-mixing ratio $\delta = \delta(E2/M1)$ is defined according to:

$$\delta^2(E2/M1) = \frac{T(E2; I_i \rightarrow I_i - 1)}{T(M1; I_i \rightarrow I_i - 1)} = \frac{3}{100} \cdot \frac{B(E2)}{B(M1)} \cdot \left(\frac{E_\gamma}{\hbar c}\right)^2 \tag{1.9}$$

$$= 6.97 \cdot 10^{-5} \cdot (E_\gamma\,[\mathrm{MeV}])^2 \cdot \frac{B(E2)\,[e^2\mathrm{fm}^4]}{B(M1)\,[\mu_N^2]} \frac{\mu_N^2}{e^2\mathrm{fm}^4\mathrm{MeV}^2}, \tag{1.10}$$

with the nuclear magneton $\mu_N = 3.152 \cdot 10^{-14}\,\mathrm{MeV/T}$ and the identity $\hbar c = 6.582 \cdot 10^{14}\,e\mathrm{T\,fm}^2$ used for Eq. (1.10). In such a case, the level lifetime is related to the $B(E2)$ value according to:

$$\tau\,[\mathrm{ps}] = \frac{BR}{1+\alpha_{IC}} \cdot \frac{\delta^2}{1+\delta^2} \cdot \frac{1}{E_\gamma\,[\mathrm{MeV}]^5} \cdot \frac{816}{B(E2; I_f \rightarrow I_i - 1)\,[e^2\mathrm{fm}^4]}. \tag{1.11}$$

1.3. The Application at GANIL

The main experiment carried out as part of this work was performed at GANIL (Grand Accélérateur d'Ions Lourds) in Caen (France) in April 2016, to investigate exotic neutron-rich Ti isotopes. The GANIL facility plays an important role in experimental nuclear physics as well as many other fields of research (astrophysics, atomic physics, radiobiology or material irradiation). Due to continuous development of the accelerator facility, not only stable beams but also intense exotic beams can be made [42]. The latter are produced by the ISOL method [43] at the SPIRAL2 facility.

The setup used for this study comprised the high resolution magnetic spectrometer VAMOS++ [37] for an event-by-event particle identification, the AGATA detector array [38] for the γ-ray detection as well as the plunger device for the lifetime measurement using the RDDS method. The complete setup is shown schematically in Fig. 1.6.

In the following the mass spectrometer VAMOS++ and the detector array AGATA are described.

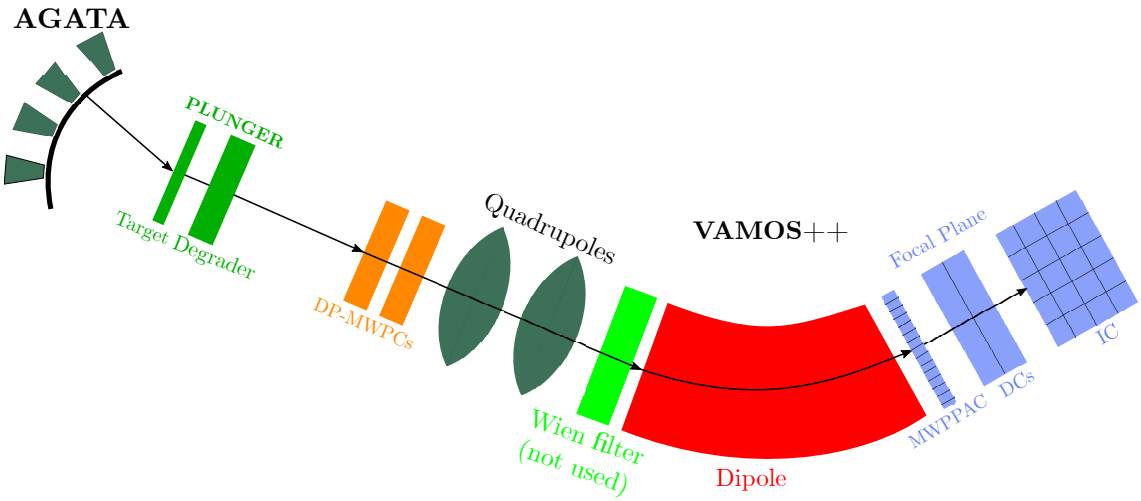

Figure 1.6.: Schematic representation of the experimental setup at GANIL including optical elements, the plunger, AGATA and VAMOS++ (not to scale).

VAMOS++

The *VAriable MOde Spectrometer* (VAMOS++) is a large acceptance magnetic spectrometer [37, 44–46] which allows to identify the transmitted nuclei on the basis of Z (proton number) and A (mass number) via an event-by-event reconstruction. During the experiment, it was positioned at the grazing angle of 45°[4] relative to the beam axis in order to have the highest acceptance for the reaction channel of interest with respect to the grazing angle of the multinucleon-transfer reaction. In combination with AGATA, it allows to perform spectroscopic studies using multinucleon-transfer reactions with heavy stable and radioactive ion beams. As shown in Fig. 1.6, VAMOS++ consists of several components, where each plays an individual role in trajectory reconstruction.

The **Dual Position sensitive Multi Wire Proportional Counter (DP-MWPC)**, at the entrance of the spectrometer, gives a start signal for the determination of the time of flight, measures the position of the incoming reaction products on the x and y axis and their emission angle with respect to the target.

Two large aperture quadrupoles follow as optical elements used to focus the ions, of which the first quadrupole focuses in the vertical plane (y direction) and the second quadrupole in the horizontal plane (x direction). The distance between the entrance detector and the first quadrupole is 1 m and the gap between the two quadrupoles is 30 cm.

The next optical element[5] is the **large magnetic dipole**. The task of this optical element is to bend the ion trajectories according to their magnetic rigidity ($B\rho$) in the horizontal plane, perpendicular to the magnetic-field vector.

[4] corresponds to the maximum rotation of VAMOS++
[5] For this experiment, the Wien filter, which usually follows the quadrupoles, was not used.

The focal plane detection system includes the **Multi Wire Parallel Plate Avalanche Counter (MWPPAC)**, two **Drift Chambers (DC)** and the **Ionization Chambers (ICs)**. The MWPPAC gives the stop signal of the ion and together with the DP-MWPC it is used to obtain the time of flight. The DCs measure the horizontal (x) and vertical (y) positions as well as the emission angles θ, φ of the recoiling reaction products to reconstruct their trajectories. The last detector (ICs) in the focal plane is made of four segments along the velocity vector of the particle, each of which is further segmented into five pads measuring the energy loss ΔE of the ions and the total energy E. These parameters are required for the Z identification, which is illustrated in Fig. 1.7. The parallel curves corresponds to a given Z.

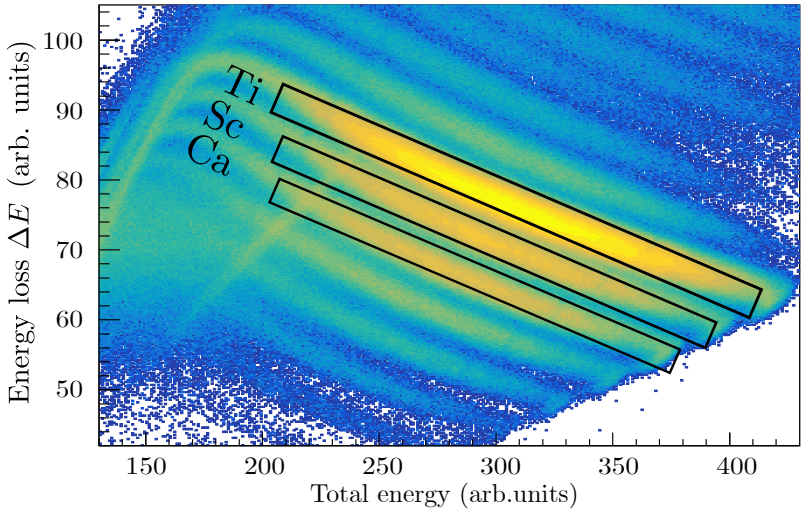

Figure 1.7.: Energy loss ΔE in the first five ICs as a function of the total energy E for the Z identification. The isotopes of titanium ($Z = 22$), scandium ($Z = 21$), and calcium ($Z = 20$) are marked schematically with black rectangles.

AGATA

The *Advanced Gamma Tracking Array* (AGATA) [38] is an array of position-sensitive high-purity Ge (HPGe) detectors where each crystal is 36-fold segmented. AGATA is characterized by the excellent energy resolution of its detectors. By using pulse-shape analysis (PSA) and γ-ray tracking, it is possible to determine the position of all γ-ray interactions inside the crystal and to reconstruct the Compton-scattered γ rays inside the array. The aim of further development of this powerful array is a 4π solid angle coverage with 180 Ge crystals in 60 AGATA triple clusters (ATC) to achieve a maximum detection efficiency. Each ATC consists of three different shaped HPGe crystals arranged in one cryostat [38, 47]: type A (red), type B (green), and type C (blue), displayed in Fig. 1.8. Each crystal is also assigned a serial number (A001, A002, etc.) and the segments are labeled as shown in Fig. 1.9.

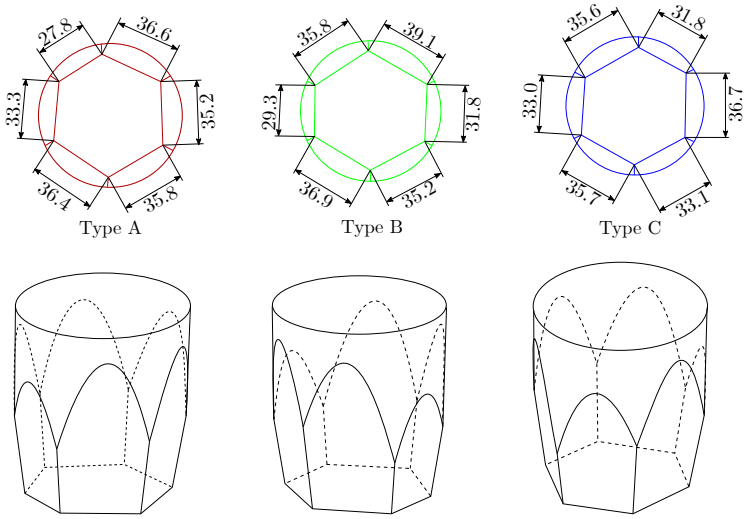

Figure 1.8.: Drawing of the three types A, B, and C of the AGATA crystal geometries. All dimensions are given in mm. Graphic adapted from Ref. [47].

Each HPGe crystal has a length of 9 cm and a diameter of 8 cm before shaping and is divided into six azimuthal and six longitudinal segments. The azimuthal segments are labeled in rings (1 to 6), with each ring divided into six equally sized sectors a to f, see Fig. 1.9. Together with the frond-end-electronics it is possible to collect the energy, time and spatial information for a γ ray by pulse-shape analysis of the detector signals. The positions of the interaction points and the energy release at each point are used for the trajectory reconstruction of the γ rays in the detector in three dimensions. The full energy deposited in the crystal is collected in the core using the electrons produced in the ionization process. At GANIL, the AGATA array covers a solid angle of nearly 1π, which can be equipped with a maximum of 41 Ge crystals composed of 13 ATC and 1 cryostat with 2 crystals. In combination with the spectrometer VAMOS++, a highly efficient and a very selective detection system is provided, in which the AGATA array is positioned at backward angles with respect to the VAMOS++ optical axis.

In the experiment of this work, the AGATA array was composed of 10 ATC, so that the setup was comprised 30 crystals (with 29 functioning detectors) and set at backwards angle (position from $\sim 135°$ to $175°$ with respect to the "entrance axis" of VAMOS++) in order to achieve a maximum sensitivity to the variation of the Doppler shift. Each detector was located 22.8 cm from the target.

1.3.1. Reaction mechanism

Depending on the impact parameter b, which indicates the distance between the trajectory of the projectile and the target and the energy of the projectile, nuclear reactions are classified as shown schematically in Fig. 1.10. The sum of the two nuclear radii involved in

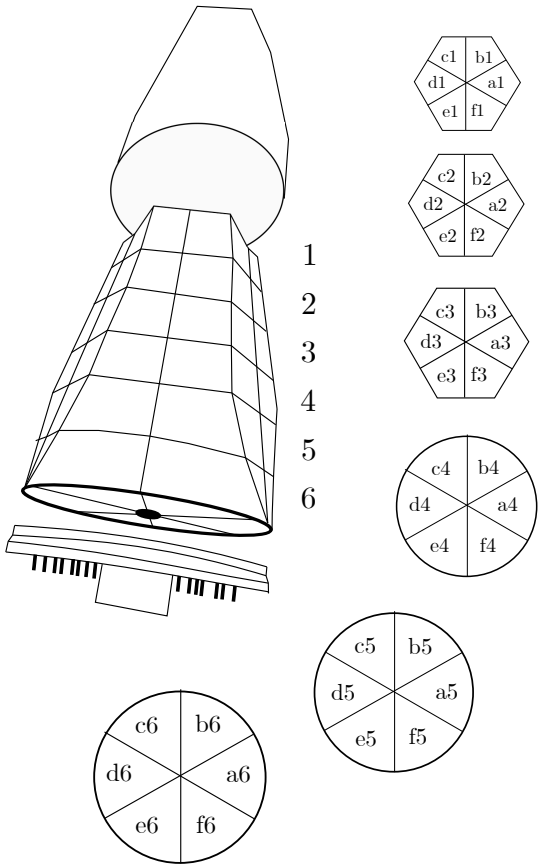

Figure 1.9.: Segmentation of the AGATA HPGe capsules as taken from Ref. [38]. Along the crystal axis the external contact is subdivided into six rings labeled 1 to 6. Each ring is subdivided into six sectors labeled a to f. Graphic adapted from Ref. [38].

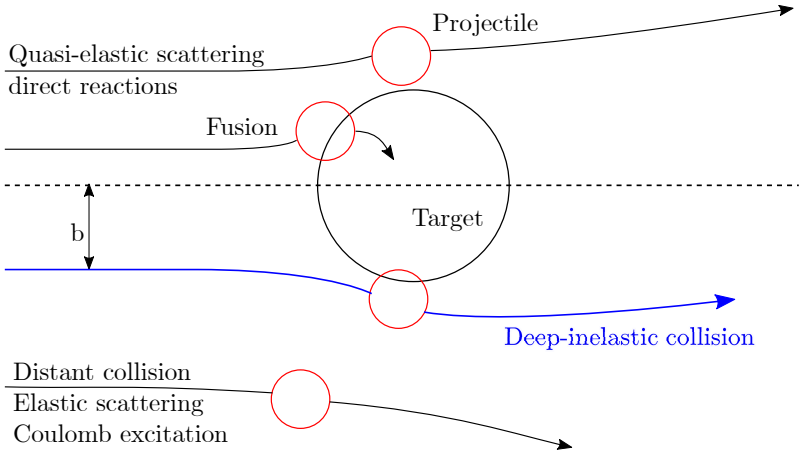

Figure 1.10.: Schematic classification of heavy-ion collisions showing the trajectories at different impact parameters b corresponding to different reactions. Figure modified from Ref. [1].

the reaction indicates the minimum distance d between the projectile and the target. By comparing the two distances, b and d, the most important reactions can be classified as follows:

- **Distant reactions** ($b >> d$) This group includes elastic scattering of the projectile or a Coulomb excitation on both impact partners where there is no contact between the nuclei so that no nucleons can be transferred.
- **Quasi Elastic (QE) or Deep-Inelastic Collision (DIC) Reactions** ($b \sim d$) In reactions of this type, the impact partners can transfer a certain number of nucleons without losing their target-like or beam-like character. The *Multi-Nucleon Transfer* (MNT) reaction used in the main experiment of this work belongs to this group, in which a small number of selected states are populated and decay by single γ-ray transitions or low multiplicity γ-ray cascades.
- **Fusion reactions** ($b < d$) In fusion reactions, nuclear states with particularly high angular momentum can be generated in which the projectile fuses with in the target nucleus as projectiles and temporarily form a common heavy compound nucleus. In this process, the entire orbital-angular momentum of the projectile is converted into the angular momentum of the new compound nucleus, which can emit few light particles (fusion-evaporation reactions) or even split (fusion-splitting reactions).

MNT reactions are a typical tool to produce neutron-rich nuclei, as conventionally used in this experiment to populate $^{46-54}$Ti. The advantage of MNT reactions is that medium to low angular-momentum states are populated, which decay by single γ-ray transitions or low multiplicity of γ-ray cascades. The scattering angle for the direction of the reaction

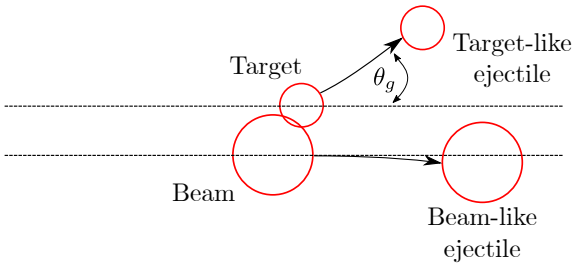

Figure 1.11.: Scheme of a nuclear reaction. Beam-like and target-like ejectiles and the grazing angle θ_g are shown. See text for details.

products (ejectiles), where the reaction cross section is maximum, is called *grazing angle*. In Fig. 1.11, the angle is referred to as θ_g, which corresponds to the closest distance d between the projectile and the target when the nuclei are in contact [48]:

$$d = \left(\frac{Z_b Z_t e^2}{4\pi\epsilon_0 E_{\text{kin}}}\right) \cdot \left(1 + \csc\frac{\theta_g}{2}\right) \approx 1.2\left(A_b^{1/3} + A_t^{1/3}\right) \text{ [fm]},$$

where $Z_b e$ and $Z_t e$ are the nuclear charges of the beam and the target respectively, and A_b and A_t their mass numbers. The knowledge about the grazing angle is important because the products are formed in the MNT reaction with relatively small cross sections. To obtain the highest possible statistics, the detectors for ion identification (in VAMOS++) should be placed at this angle.
A detailed description of MNT processes in heavy ions can be found in Ref. [48].

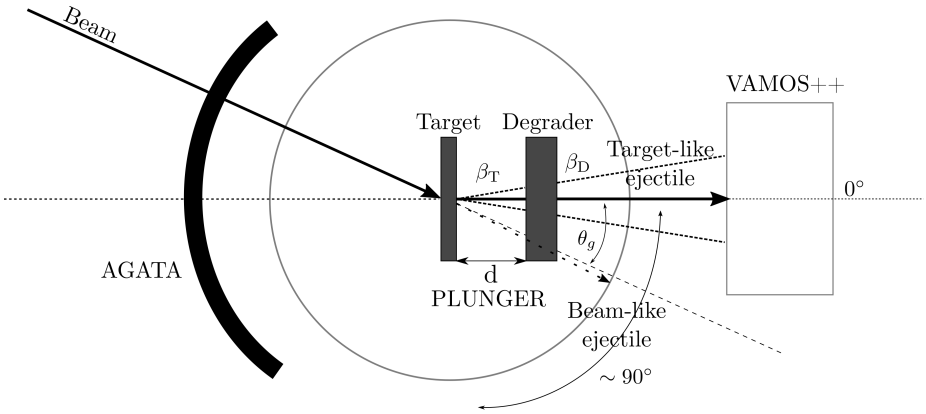

Figure 1.12.: Schematic representation of the experimental setup (not to scale). The grazing angle θ_g is around 45°. See text for details. Graphic modified from Ref. [39].

The reaction used in the main experiment was ^{238}U+^{50}Ti. The ^{238}U beam impinged on the ^{50}Ti target with an energy of 6.76 MeV/u. The grazing angle of the reaction in the laboratory frame was around 45°. For the experiment, the setup was arranged as shown in Fig. 1.12 to perform the experiment of the optimal detection configuration. AGATA is arranged at backward angles relative to the axis of the spectrometer VAMOS++ to maximize the Doppler effect, which is necessary for the RDDS measurement. The plunger is positioned in the center of the reaction chamber, but rotated by 45° so that the target and degrader foils are perpendicular to the entrance of the VAMOS++ spectrometer, which is also rotated by 45°. The grazing angle of the reactions of interest was estimated with the GRAZING code [49] before the experiment. It is based on the semi-classical model of few-nucleon transfers with low-energy dissipation developed by A. Winther [50, 51].

Target problems

During the experiment at GANIL, structural target changes occurred, see Fig. 1.13, which were not predicted despite previous estimates of the target temperature in the beam spot. After first using a 0.9 mg/cm^2 thick ^{54}Cr target with 0.6 mg/cm^2 natural Mg fronting as a stretchable support which got large wrinkles when exposed to the ^{238}U beam, two ^{50}Ti

targets (1.5 mg/cm^2 self-supporting and 1.2 mg/cm^2 on 0.4 mg/cm^2 ^{nat}Cu) were then used, but they got similar wrinkles with a depth of $\sim 100 - 200\mu$m. The idea of vapor deposition of a Cu fronting was born from the consideration that Cu has better thermal properties than Ti. The readout by the feedback system showed that the wrinkles appeared after a short time and then seemed to remain "stable". The changes in the targets, as seen in Fig. 1.13, initially strongly suggested that in addition to the folds, small cracks or holes must have formed. A 300x or 650x magnification, however, could convince of the opposite. Figures 1.14 – 1.17 show photographs[6] of such magnifications produced by a scanning electron microscope. After the first used target showed damages within the beam spot with a diameter of 2-3 mm, the idea came up to widen the beam in order to minimize the thermal load by defocusing. The beam was widened to the full cone diameter of about 10 mm, which worked well. However, this step did not result in any improvements regarding target damage. The damage over the entire enlarged beam spot is shown in Fig. 1.13.

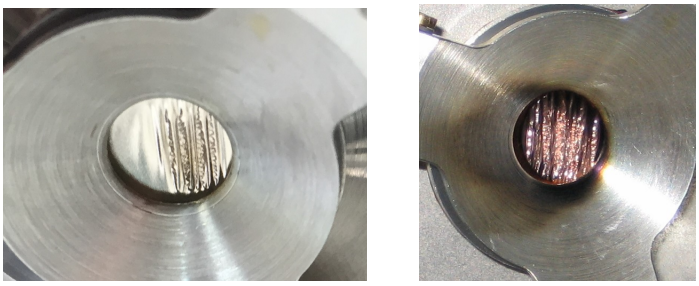

Figure 1.13.: Damaged ^{50}Ti targets display wrinkles with a depth of $\sim 100 - 200\,\mu$m. *Left:* 1.5 mg/cm^2 self-supporting ^{50}Ti target, *right:* 1.2 mg/cm^2 ^{50}Ti with Cu fronting facing the beam.

In initial thoughts, the colleagues and experts from the Institute of Physics II of the University of Cologne saw the hammering of the swift heavy ions as a possible cause of the target damage, which results in an expansion of the sample vertical to the beam direction and a shrinkage parallel to it. The rapid thermal expansion about the ion path causes shear stresses which relax by viscous flow. The rapid cooling of the hot cylindrical ion-track freezes in viscous strains and was discovered by Klaumünzer *et al.* [52] in metallic glass. The energy loss of a ^{238}U beam with an energy of 6.76 MeV/u in a 1.2 mg/cm^2 thick ^{50}Ti target, rotated by 45° with respect to the beam direction, is 148 MeV. With an assumed diameter of a ^{50}Ti atom of $10^{-4}\,\mu$m, the target thickness yields $3.76 \cdot 10^4$ Ti atoms. This leads to an energy loss of 3.94 keV/atom and is much more than the melting energy. The effect is supported by sticking together of the target and degrader after running at contact. Nevertheless, the question remains open why this phenomenon occurs in titanium and chromium (on magnesium) but not in other targets like nickel. When a fast projectile penetrates a solid, the projectile is continuously decelerated as it loses kinetic energy along its trajectory through atomic processes such as excitation, ionization or electron capture.

[6] taken by L. Hadman from the Institute of Physics II, University of Cologne.

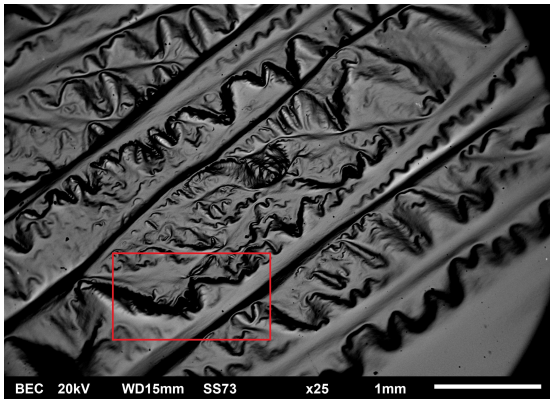

Figure 1.14.: Backscattered electrons, magnification x 25. The red framed section is shown in Fig. 1.15 in a 90x magnification.

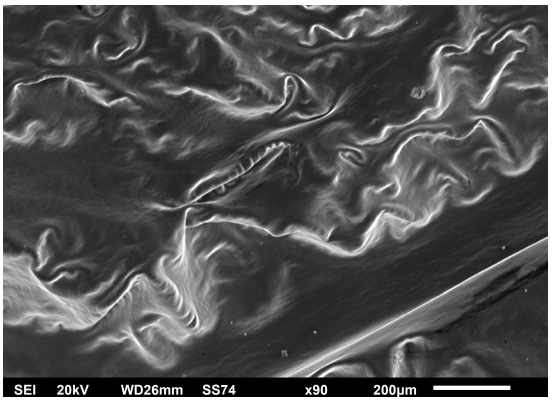

Figure 1.15.: Secondary electrons, magnification x 90.

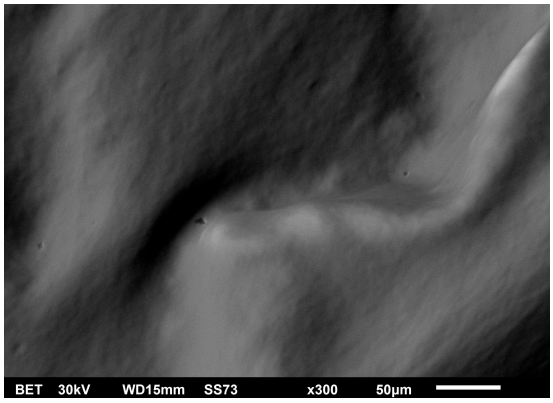

Figure 1.16.: Backscattered electrons, magnification x 300.

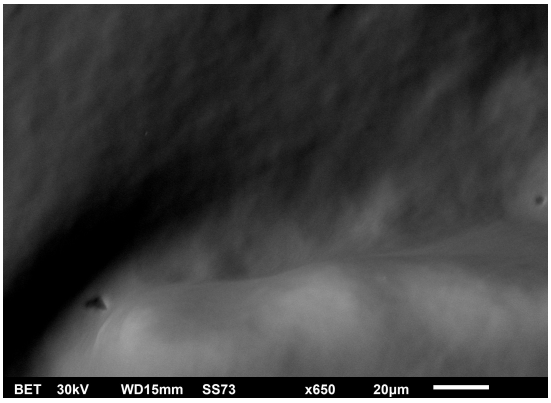

Figure 1.17.: Backscattered electrons, magnification x 650.

The total stopping power of a projectile ion in a solid target is composed of two different energy loss mechanisms: nuclear stopping (with stopping power S_n) and electronic stopping (with stopping power S_e). The first represents the transfer of energy and momentum during elastic collisions between atomic nuclei, the latter the transfer of energy during inelastic collisions, by which the electrons of the solid state material are excited and ionized. The nuclear stopping occurs mainly at energies up to several hundred keV, whereas the influence of the electronic stopping power increases with increasing particle energy, so that it is several orders of magnitude higher than the nuclear stopping for projectiles with energies in the MeV range.

When the projectiles pass through a solid state target, the degree of damage to the solid state material along the trajectory depends on the amount of energy deposited by the

projectile in the target. The lattice vibrations of the atomic nuclei in the solid state are excited by the projectile at a very long distance from the projectile trajectory or at very low-energy deposition. If the energy deposited by the projectile is larger than the binding energy, individual target atoms can leave their lattice sites, causing defects, interstitial atoms or Frenkel defects. These point defects can migrate in the target and form an accumulation of defects. At a high-energy deposition of the projectile, a large number of defects are generated, which is the consequence of atomic-collision cascades. All atoms are removed from their lattice sites in a highly-ionized state in the region of the trajectory and start moving. The result is a plasma-like state, which is characteristic of a particle track. These particle tracks are created by the interaction of fast projectile ions with matter. In the field of electronic-stopping power, two models have been proposed to explain the origin of the ion's passage through matter: (i) ionic-spike model [53], which describes the high-electronic ionization resulting from the energy transfer of the incident ions to the electrons, (ii) thermal-spike model [54], which is based on the high-temperature rise of the electronic subsystem, which is the main effect of the damage occurring in our experiment. Wang *et al.* [55] have shown that the behavior of the S_e of metals under irradiation by fast heavy ions is well correlated with the predictions of the thermal-spike model. The sensitivity to S_e of a metal is linked to:
(i) the melting point T_m: the lower T_m the higher the sensitivity to S_e causing damage
(ii) the electron-phonon coupling g: the larger g the higher the sensitivity to S_e.

To predict the S_e sensitivity, Wang *et al.* [55] defined a "test parameter" $\eta = \frac{Q}{\Delta H_f}$, where Q is the mean-energy density deposited in the lattice of a cylinder of radius λ [56] and $Q = 0.63\, S_e/\pi\lambda^2$. ΔH_f represents the energy to melt a metal. For $\eta > 1.3$ materials are classified as S_e sensitive, whereas materials are classified as S_e insensitive if $\eta < 0.7$. For $0.7 < \eta < 1.3$ no conclusion can be drawn about the sensitivity. Nevertheless, it does not help to apply a more insensitive material to a sensitive material, as was done with Cu or Mg in this experiment. An alloy is formed, if at all, only at a thin boundary layer, so that no compensation of the effect is possible by the more insensitive layer. The experimental result can be seen on the right photo in Fig. 1.13.
The magnitude of this test parameter η ultimately provide the answer to the incoming question as to why titanium and chromium in particular are susceptible to damage in contrast to nickel. For Ti (Cr) the result is $\eta = 5.4\,(5.3)$, whereas Ni has a much lower value of 2.2, but experimentally it is not always damaged. S_e insensitive materials are for example Mg with $\eta = 0.61$ or Cu with $\eta = 0.42$.

A thorough investigation of the target damage occurring in the GANIL experiment was explicitly included in Ref. [57]. It has been shown that the thermal-spike model can solve the puzzle, which is why some metallic-target materials deform due to a rapid local temperature rise, while others remain unchanged. For future experiments with similar parameters,

estimates should be made in advance with this model to avoid target damage, for example by adjusting the beam energy or the target material.

1.4. Nuclear structure of the neutron-rich mass region around titanium

The shell structure that gives a basic understanding of the atomic nucleus has been found to often change drastically as a result of the rearrangement of single-particle levels in exotic nuclear regions. The $A = 60$ region represents a rich testing ground for such effects. For example, an increasing collectivity was identified from transition strengths in neutron-rich ^{62,64,66}Fe [58–60] close to ^{68}Ni with doubly-magic character [61]. The data from Refs. [58, 59] resulted in a conclusive description of these nuclei with respect to the observed high collectivity [62] with the LNPS interaction developed for the *fpgd* valence space [63]. Recent work on ^{58,60,62}Cr at NSCL [64] allowed to test these new calculations very successfully on a broader framework [65].

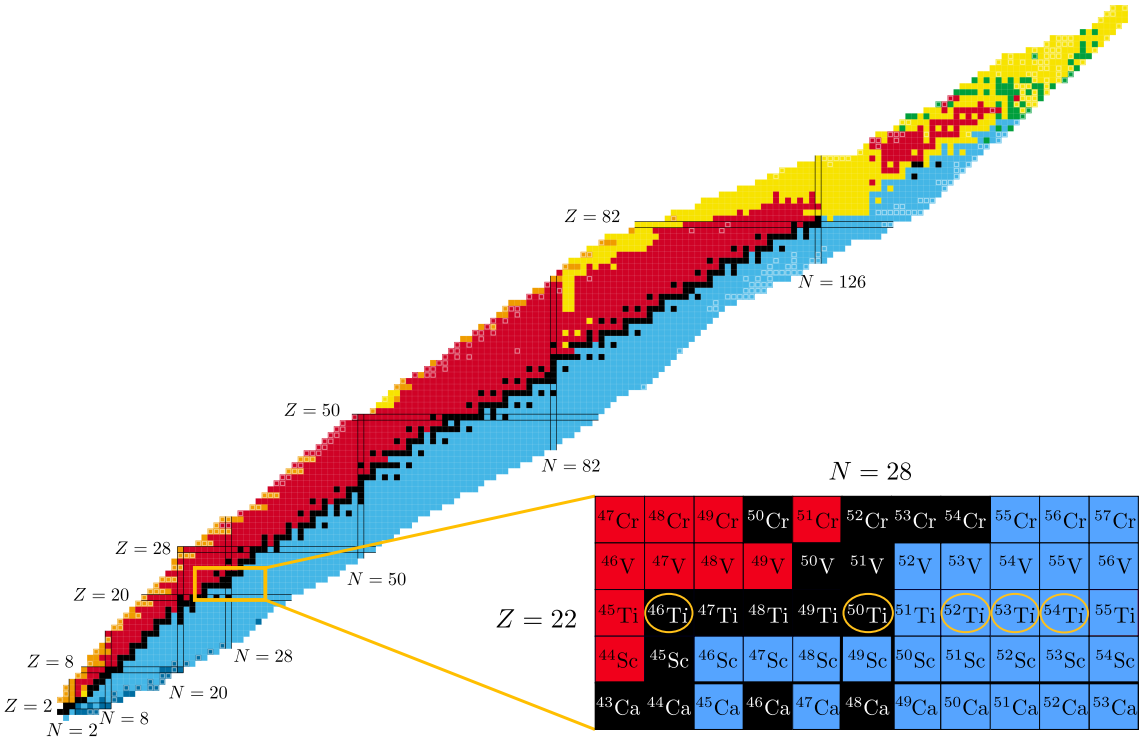

Figure 1.18.: Nuclear landscape with a cutout of the mass region of interest. The nuclei studied within this thesis are marked yellow. Graphic taken from Ref. [66].

Neutron-rich Ti isotopes are of particular interest for an understanding of the shell structure in the Ti-Cr-Fe region beyond $N = 28$. Figure 1.18 displays the nuclear landscape and the mass region of interest with the nuclei studied in this thesis. A number of experiments with

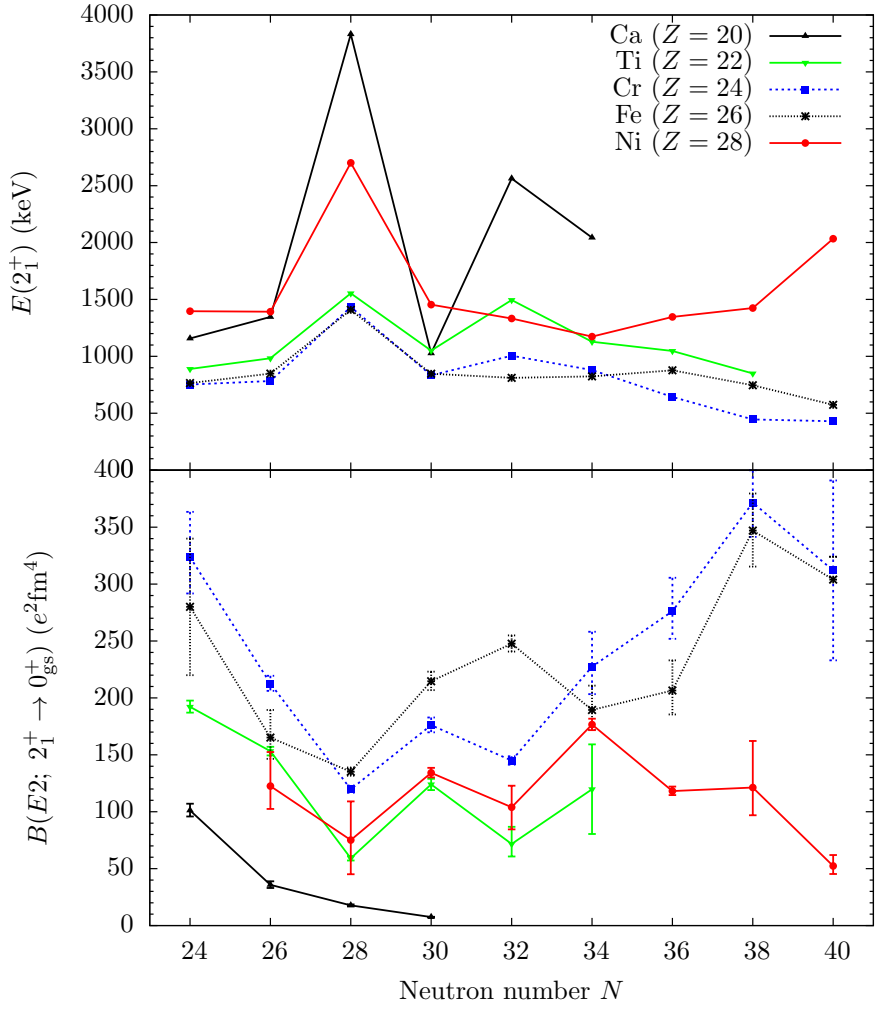

Figure 1.19.: Systematics of the excitation energies for the first 2_1^+ state (*top*) and $B(E2; 2_1^+ \rightarrow 0_{gs}^+)$ values (*bottom*) for even-even nuclei with $20 \leq Z \leq 28$. There is a significant increase in the excitation energies for all applied nuclei at $N = 28$, of which $^{48}_{20}$Ca$_{28}$ and $^{56}_{28}$Ni$_{28}$ are doubly magic. For the $N = 32$ isotones, however, this increase is not as pronounced. The $B(E2; 2_1^+ \rightarrow 0_{gs}^+)$ values show local minima at $N = 28$ and $N = 32$ (only Ti, Ni, Cr). For references of the values, see Table C.1 in the Appendix.

different techniques such as beta decay (^{54,55,56}Ti [67]), Coulomb excitation (^{52,54,56}Ti [68]), knockout reactions (^{55}V, ^{55}Ti [69]) and fusion-evaporation reactions (^{56,57}Cr [70]) have already been used to investigate the shell structure in these neutron-rich isotopes. A special attention is paid to the formation of strong shell effects in nuclides with $N = 32$, since they occupy a full valence $\nu 2p_{3/2}$ orbital in the shell-model space. For the known nuclides, this orbital is energetically close to the $\nu 1f_{5/2}$ orbital, which prevents the occurrence of shell effects. However, the excitation energies of the 2_1^+ states of nuclei below $Z = 24$ show a systematic increase at $N = 32$, see Fig. 1.19, which provides an indication of shell effects.

In the case of Ti isotopes, a similar peaking of the 2_1^+ energy at $N = 32$ is observed as for Ca isotopes, although with a reduced amplitude. For Cr, this effect is much weaker and for Fe and Ni it disappears completely. This suggest the appearance of a phase transition from predominant collective structures in ^{58}Fe towards the existence of a reduced $N = 32$ neutron subshell closure in Ti isotopes [71], the quenching of which has also been confirmed in vanadium [72]. This subshell closure develops for decreasing number of protons in the $\pi 1f_{7/2}$ orbital, i.e. from ^{56}Cr→ ^{54}Ti → ^{52}Ca, whereby the neutrons in the $\nu 1f_{5/2}$ orbital are less bound. This phenomenon, which is typical for shell effects, is attributed to the weakening of the monopole interaction between the $\pi 1f_{7/2}$–$\nu 1f_{5/2}$ orbitals. The $N = 32$ shell gap in Ti isotopes is discussed in Refs. [21, 68] to result from spin-orbit splitting of the neutron $\nu 2p_{1/2}$ and $\nu 2p_{3/2}$ orbitals and a weakening of the $\pi 1f_{7/2} - \nu 1f_{5/2}$ monopole interaction (see Ref. [73]). In addition, a decreasing number of protons in the $\pi 1f_{7/2}$ orbitals, i.e. from Ni to Ca, is assumed to cause an inversion of the $\nu 1f_{5/2}$ and $\nu 2p_{1/2}$ orbitals that finally causes the opening of a gap between the $\nu 1f_{5/2}$ orbital and the $\nu 2p_{1/2}$, $\nu 2p_{3/2}$ orbitals and thus should lead to the $N = 32$ subshell closure [74]. The corresponding $B(E2; 2_1^+ \rightarrow 0_{\mathrm{gs}}^+)$ values in Ti and Cr support this presumed subshell closure by a local minimum, see Fig. 1.19.

In a work by D.-C. Dinca *et al.* [68], the $B(E2; 2_1^+ \rightarrow 0_{\mathrm{gs}}^+)$ values in ^{54,56}Ti were determined in intermediate Coulomb excitation for the first time and support a subshell closure in $^{54}\mathrm{Ti}_{32}$. Shell-model calculations were performed in Ref. [68] both with the GXPF1 interaction and the modified version GXPF1A by M. Honma *et al.* [21], in which the matrix elements of the interaction involving mostly the $\nu 2p_{1/2}$ orbital were readjusted. However, the calculations in Ref. [68] only provide a description of the excitation energies of known levels in the even-even Ti nuclei, including those above the 6_1^+ state in ^{54}Ti, which involve neutron excitations across the $N = 32$ shell gap [16]. The measured $B(E2; 2_1^+ \rightarrow 0_{\mathrm{gs}}^+)$ values highlight the limitations of the calculations as they are unable to reproduce the magnitude of the transition rates in the semi-magic ^{50}Ti and their staggering across even-even ^{50,52,54,56}Ti. Further, the data from Ref. [68] do not provide any indication of an additional $N = 34$ subshell gap predicted with the GXPF1 interaction. In contrast, the lack of the latter subshell closure is accounted for by the GXPF1A [21] interaction. Results from a beyond mean-field approach support a $N = 32$ shell closure and predict the non-existence of a shell closure at $N = 34$ [33], but nevertheless, are also unable to reproduce the ominous staggering of $B(E2; 2_1^+ \rightarrow 0_{\mathrm{gs}}^+)$ values in the neutron-rich Ti and Cr isotopes reasonably. Also J. L. Egido [75] has developed two approaches (TRSB and TRSC [75]) based on the generator-coordinate method (GCM) and the conserving of symmetry. Especially, the results from the TRSB approach provide a promising description of the present experimental $E(2_1^+)$ and $B(E2; 2_1^+ \rightarrow 0_{\mathrm{gs}}^+)$ values, whereas the results from TRSC fully overestimate the excitation energies for the Ti isotopes shown in Fig. 1.20 and they cannot reproduce the amplitude in the $B(E2; 2_1^+ \rightarrow 0_{\mathrm{gs}}^+)$ staggering.

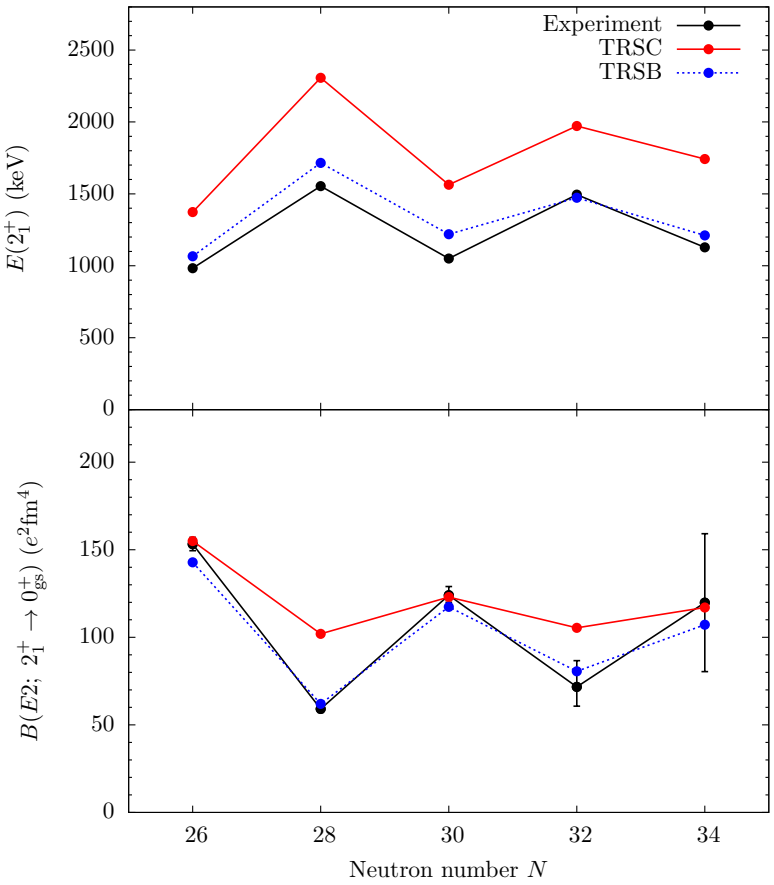

Figure 1.20.: Systematics of excitation energies for the first 2_1^+ state (*top*) and $B(E2; 2_1^+ \rightarrow 0_{gs}^+)$ values (*bottom*) in the titanium isotopes with $26 \leq N \leq 34$ in two approaches: time reversal symmetry conserving (red) and time reversal symmetry breaking (blue). The data points for TRSB and TRSC are taken from Ref. [76]. See text for details.

The level scheme of the odd ^{53}Ti is satisfactorily described by calculations both with the GXPF1 and GXPF1A interactions [77]. However, no experimental transition strengths of this nucleus were known until before this work, so that no comparison with theoretical predictions was possible. For the neighboring ^{55}V, only the level scheme was investigated [78], but also here no transition strengths are known. The excitation energies of the lower negative parity levels are well described in Ref. [78] with the KB3G, GXPF1A and GXPF1B interactions, but large inconsistencies were found for higher excitations. Positive parity states that are likely to have contributions from the $\nu g_{9/2}$ orbital were not included in the calculation. It was found that $^{55}\mathrm{V}_{32}$ can be viewed as a single proton coupled to $^{54}\mathrm{Ti}_{32}$ with aspects of the shell stability. This is illustrated by noting the similarity in the excitation energy between the lowest-lying $11/2^-$ and $15/2^-$ states at 1433 keV and 2508 keV in ^{55}V dominated by recoupling of the $\pi f_{7/2}$ proton with the 2_1^+ and 4_1^+ states in

^{54}Ti at 1495 keV and 2508 keV, generated by the proton $\pi f_{7/2}^2$ configuration. Excited states at low energy are generated by the promotion of at least one neutron to a $\nu p_{1/2}$ or $\nu f_{5/2}$ orbital. Those exhibit a high degree of mixing due to the close proximity of these orbitals. The determination of transition strengths will allow to clearly identify the structure of the lowest states especially with respect to the robustness of the $N = 32$ subshell closure. The very recent theoretical work by L. Coraggio *et al.* [79] on neutron-rich isotopes north-east of ^{48}Ca discusses in detail influences from the $\pi 1f_{7/2}$, $\pi 2p_{3/2}$ and $\nu 2p_{3/2}$, $\nu 2p_{1/2}$, $\nu 1f_{5/2}$, $\nu 1g_{9/2}$ orbitals in realistic shell-model calculations including an additional role of the $\nu 2d_{5/2}$ orbital. The evolution of the 2_1^+ energies resulting from the $N = 32$ subshell closure was described. A slight staggering of the $B(E2; 2_1^+ \rightarrow 0_{\mathrm{gs}}^+)$ values was also reproduced, but the results are still insufficient as they cannot reproduce the magnitude of the $B(E2; 2_1^+ \rightarrow 0_{\mathrm{gs}}^+)$ staggering at all [79].

Since according to the state-of-the-art shell-model calculations with different interactions, e.g. GXPF1A, KB3G or FPD6, are not able to describe satisfactorily this observed staggering of the $B(E2; 2_1^+ \rightarrow 0_{\mathrm{gs}}^+)$ values in ^{50,52,54,56}Ti presumably resulting from neutron subshell closures, the experiments presented in this thesis were performed to accurately determine the transition strengths between the lowest excited states from level lifetimes measured with the RDDS method in ^{50,52,54}Ti. Available data in these nuclei suggest systematic errors that could lead to the discrepancy between theory and experiment. The insufficient theoretical picture highly supports the need for precise measurements of transition strengths between yrast states in ^{54}Ti. Besides a precise knowledge of the $B(E2; 2_1^+ \rightarrow 0_{\mathrm{gs}}^+)$ value, the $4_1^+ \rightarrow 2_1^+$ and $6_1^+ \rightarrow 4_1^+$ transition strengths are essential to achieve a conclusive picture of the evolving shell structure from the contributions of different orbitals to the corresponding excited states. In addition, the results of this work should close the lack of knowledge about the transition strengths of the odd-mass nucleus ^{53}Ti, which is important as a direct neighbor of ^{54}Ti to have a better understanding of the single-particle orbitals at $N = 32$. The ratios of these transition strengths will further allow to deduce β and γ deformation parameters unknown for this exotic region so far.

1.5. Overview of the publications

The central topic of this cumulative thesis is the determination of reduced transition probabilities by lifetime measurements of neutron-rich ^{52,53,54}Ti isotopes using multinucleon-transfer-reactions and a fusion-evaporation reaction for an additional investigation of ^{46}Ti. The results as well as the significance of the publications in the context of the dissertation will be presented below.

The first publication "Lifetime measurement of excited states in ^{46}Ti" [80] presents a study, in which the lifetimes of the low-lying states, 2_1^+, 4_1^+, 6_1^+ and 8_1^+, of the yrast band in ^{46}Ti were precisely determined. The results of this RDDS experiment were important for the data analysis of the main experiment of this work in order to determine its plunger distances by means of high-precision data on lifetimes in ^{46}Ti. Although numerous experiments on the stable ^{46}Ti isotope have been performed in the past and many data on level lifetimes have been published, some results were significantly different and the uncertainty was partly relatively high. In addition to the author of this thesis, the plunger working group from Cologne took part in the measurement. The experiment was also supervised by this group as well as by additional people from the Institute of Nuclear Physics of the University of Cologne, who helped out during the shift operation. The RDDS experiment was carried out by Dr. C. Fransen and Dr. C. Müller-Gatermann. The data of the experiment were sorted by the author, who also performed the lifetime analysis. The author interpreted the results and wrote the paper. During proofreading, the second author, Dr. C. Fransen, improved the text linguistically, and several other co-authors made minimal suggestions for changes.

The second paper "Lifetime measurements in ^{52,54}Ti to study shell evolution toward $N = 32$" [81] focuses on the nuclear structure of the neutron-rich ^{52}Ti and ^{54}Ti isotopes. For the analysis of the data of this experiment performed at GANIL, the unknown distances between target and degrader had to be reproduced first. This problem was solved by a χ^2 minimization by comparing experimental spectra of ^{46}Ti from the multinucleon-transfer experiment with spectra generated by Monte-Carlo simulations. For this purpose, the lifetimes in ^{46}Ti determined from the first publication were used. This paper pays special attention to the lifetimes of the low-lying states of the yrast bands (2_1^+, 4_1^+, 6_1^+) in ^{52,54}Ti analyzed by the DDCM in γ-ray singles and the deduced transition strengths. The experimental results are interpreted using state-of-the-art shell-model calculations using different interactions. The RDDS experiment was conceived by Dr. T. Braunroth, Dr. C. Fransen, and Dr. C. Müller-Gatermann. The author of this thesis as well as Dr. B. Birkenbach, Dr. T. Braunroth, Dr. C. Fransen, Dr. L. Lewandowski, Dr. C. Müller-Gatermann, and Dr. A. Vogt from the Institute for Nuclear Physic of the University of Cologne, participated in the experiment E696 at GANIL. The group was supported by the locals of GANIL as well as other members of the collaboration both for the setup of the experiment and for the shift operation. The data obtained from this experiment were

prepared and presorted with the support of PhD E. Clément and PhD A. Lemasson and the necessary channel selection of Ti was made by the author as well as the final sorting of the data. The subsequent lifetime analysis was carried out by the author herself, who interpreted the results in cooperation with Dr. A. Blazhev using the shell-model calculations she performed herself, except for the GXPF1B-nf7 interaction, which was developed by Dr. A. Blazhev. The paper was written by the author of this thesis. The second author, Dr. C. Fransen, has improved the linguistic style in some parts of the proofreading as well as added suggestions for the content. Some text passages of the discussion were prepared in cooperation with Dr. A. Blazhev, the third author. Some co-authors proposed minor content and language modifications or additions before submission to the journal.

The third publication "Preliminary results of lifetime measurements in neutron-rich ^{53}Ti" [82] contains results of the analysis of the data set also taken from the main experiment. In the foreground of this paper is the lifetime analysis of the odd-mass nucleus ^{53}Ti, which, like ^{52,54}Ti, plays an important role in the shell evolution around $N = 32$. Preliminary lifetimes of the $(5/2^-)$ to $13/2^-$ states were evaluated using the DDCM γ-ray in singles but the lifetime analysis revealed additional slowing-down effects that were caused by the deceleration of the recoils in the degrader, but no correction was done to take the effect into account. Despite the preliminary results, the publication of this study is important because it shows suggestions or proposals for improvement that have emerged from the data analysis. The study shows that the DDCM reaches its limits at this nucleus and that it cannot be used to achieve final results without further corrections. The first-time publication of these data signals that another analysis method must be consulted or corrections must be taken into account for the finalization of the lifetimes, so that the research results can be examined within the framework of theoretical calculations.

The tasks of the conception, preparation and execution of the experiment as well as the sorting and analysis of the data according to those of the second publication. The author of the thesis is once again the first author of the paper. In the end of the completion of the manuscript, the co-authors proposed minimal linguistic changes.

Final data on lifetimes of the $(5/2^-)$ to $13/2^-$ states in ^{53}Ti determined by a χ^2 minimization are presented in the fourth publication "Lifetime measurements of excited states in neutron-rich ^{53}Ti: benchmarking effective shell-model interactions" [83], with results extracted using Monte-Carlo simulations in order to take the slowing-down effects into account. Electrical and magnetic transition strengths were determined and compared with theoretical calculations, that give new information on the nuclear structure of ^{53}Ti, and are used to benchmark different shell-model calculations using established interactions in the fp shell. Before these two publications, no information on lifetimes in ^{53}Ti was known. The results were interpreted in cooperation with Dr. A. Blazhev. A. Goldkuhle wrote the paper of which some passages of the discussion were formulated by Dr. A. Blazhev, whose content

was developed in cooperation with the first author. The first author has included linguistic changes as well as additions to the content by the co-authors before submitting it to the journal.

Finally, the results of the four publications including those of another third RDDS experiment on ^{50}Ti are briefly summarized. An overview of the ongoing work and an outlook on possible future activities will then be given.

Publication I:
Lifetime measurement of excited states in ^{46}Ti

Eur. Phys. J. A (2019) **55**: 53
DOI 10.1140/epja/i2019-12722-6

THE EUROPEAN PHYSICAL JOURNAL A

Regular Article – Experimental Physics

Lifetime measurement of excited states in ^{46}Ti

A. Goldkuhle[a], C. Fransen, A. Dewald, K. Arnswald, M. Bast, M. Beckers, A. Blazhev, T. Braunroth, G. Hackenberg, G. Häfner, J. Litzinger, J. Jolie, C. Müller-Gatermann, F. von Spee, N. Warr, D. Werner, and K.O. Zell

Institut für Kernphysik, Universität zu Köln, D-50937 Köln, Germany

Received: 19 December 2018 / Revised: 11 February 2019
Published online: 18 April 2019

Communicated by A. Gade

Abstract. The level lifetimes of the yrast 2_1^+, 4_1^+ and 6_1^+ states and an upper limit of the lifetime of the 8_1^+ state in ^{46}Ti have been measured with high accuracy exploiting the recoil distance Doppler-shift method (RDDS) and using $\gamma\gamma$ coincidences. The nuclei were populated by the fusion evaporation reaction ^{40}Ca(^{9}Be, 2p1n)^{46}Ti at a beam energy of $E = 33$ MeV at the FN tandem accelerator of the University of Cologne, Germany. Lifetimes were extracted using the established differential decay curve method (DDCM).

1 Introduction

In the past years a large number of experiments have been performed to study the nuclear structure of the low-lying states in ^{46}Ti which is situated midshell between $N = 20$ and $N = 28$. For this purpose, several fusion evaporation reactions [1–3], neutron/proton scattering reactions [4,5] and alpha induced reactions [6,7] have been used.

The motivation for the experiment of this work was to measure level lifetimes of the lowest yrast states in ^{46}Ti precisely, with a special focus on the 2_1^+ and 4_1^+ states, because the published values partly differ by more than a factor of 7 for the 2_1^+ state and 2 for the 4_1^+ state (see table 1). Thus the results for the level lifetime of the 2_1^+ state given in refs. [4,8,9] deviate strongly from the other measurements and in ref. [2] no absolute value could be determined, but only a lower limit. The other lifetime values [1, 10,11] do not all agree within the small error bars of 5–10%. In addition, the level lifetime determined in ref. [12] shows a large uncertainty of 26.6%. The lifetime value of the 4_1^+ state from ref. [13] does not correspond to the results of other experiments as listed in table 1. However, it has to be noted that it is not clear how this value was determined in ref. [13]. The other lifetimes of the 4_1^+ state given in refs. [1,2,4,7,11] agree within their errors, but in some cases also show large uncertainties ($\sim 42\%$ [7]).

Of all previous lifetime measurements, only in ref. [1] the recoil distance Doppler-shift (RDDS) method was used, but it was not measured in $\gamma\gamma$-coincidence mode. All other experiments presented in refs. [2–4,6,7,11,14] used the Doppler-shift attenuation method (DSAM), of which in refs. [2,14,3,7] $\gamma\gamma$-coincidences were measured. Of these works, the authors only of ref. [2] state that they determined the lifetime using an energy gate on the Doppler-shifted component of a feeding transition of the respective level. In refs. [10,8] lifetime data were calculated using the centroid-shift and self-absorption method. It should be noted that the latter method is ineffective for the determination of the lifetime of the 2_1^+ because of the small level width ($\sim 10^{-5}$ eV) and the small ^{46}Ti content in a natural isotope mixture. In general, DSAM is used for measurements when lifetimes in the range of 10^{-12} s to 10^{-14} s are expected. Since in ^{46}Ti lifetimes are predicted in a range of 10^{-12} s, DSAM is a critical method for a lifetime analysis. Furthermore, measurements without coincidence conditions cannot rule out unobserved side-feeding, which can lead to falsified results.

However, a maximum of two detectors were used in all measurements, with the majority of the experiments listed here using only one detector. Consequently, $\gamma\gamma$-coincidence measurements were not possible for these measurements using only one detector. The advantage of coincidence measurements is the possibility of setting energy gates eliminating unobserved transitions. Furthermore, considerations suggest that the RDDS method, especially in combination with coincidence measurements, has great advantages in the consideration and avoidance of systematic errors.

In this work we determined level lifetimes of the lowest yrast states in ^{46}Ti with high precision in a $\gamma\gamma$-coincidence experiment at the Cologne FN Tandem accelerator with the RDDS method using the Cologne coincidence plunger [15]. Unlike previous experiments, lifetimes were determined using the differential decay curve method

[a] e-mail: agoldkuhle@ikp.uni-koeln.de

Table 1. Comparison of experimental values of the lifetimes in ^{46}Ti using different methods from previous works.

I^π	E_{level} (keV)	τ (ps)
2_1^+	889.3	$2.0^{+5.0}_{-1.0}$ [4][1]
		> 3 [2][3]
		6.5(7) [1][5]
		6.7(5) [10][6]
		7.9(21) [12][8]
		8.1(4) [11][1]
		9.7(24) [9][8]
		14.1(21) [8][7]
4_1^+	2009.8	1.9(8) [7][2]
		2.1(4) [2][3]
		2.3(2) [11][1]
		2.6(3) [1][5]
		$2.8^{+0.7}_{-0.4}$ [4][1]
		$4.6^{+1.7}_{-0.9}$ [13][8]
6_1^+	3298.9	$1.45^{+0.25}_{-0.15}$ [4][1]
		1.5(3) [2][3]
		1.5(7) [1][5]
		1.5(5) [7][2]
		1.6(2) [6][1]
8_1^+	4896.9	0.6(3) [7][2]
		0.65(13) [2][3]
		0.86(29) [3][2]
		1.33(33) [14][4]

[1] Using DSAM [4,6,11].
[2] Using DSAM in $\gamma\gamma$-coincidence mode [3,7].
[3] Using DSAM in $\gamma\gamma$-coincidence mode with a gate from above [2].
[4] Using DSAM, gated by charged particle detection [14].
[5] Using the RDDS method [1].
[6] Using the centroid-shift self comparison method [10].
[7] Using the self-absorption method [8].
[8] Not accessible [9,12,13].

(DDCM) [16]. To exclude contributions from an unknown delayed side-feeding to the measured lifetime values, we employed γ-ray energy gates on the flight component of the feeding transition of the respective level for the lifetime analysis (so-called gating from above).

High-precision and reliable lifetime data are also important for the normalization or scaling in challenging experiments reaching very exotic nuclei, *e.g.* Coulomb excitation measurements with radioactive beams. For these types of experiments, knowledge of lifetimes provides a constraint for the analysis of Coulomb excitation data, making it possible to disentangle the contribution from diagonal and transitional matrix elements [17].

Due to the large differences in the individual measurements, it is necessary to determine precise lifetimes in ^{46}Ti to check the reliability of the adopted values.

2 Experimental setup

The RDDS experiment on ^{46}Ti was performed at the FN tandem accelerator of the University of Cologne, Germany, using the Cologne coincidence plunger device [15]. Excited states in ^{46}Ti were populated with the ^{40}Ca(^{9}Be, 2p1n)^{46}Ti fusion-evaporation reaction at a beam energy of 33 MeV. The plunger target was made of ^{40}Ca with a thickness of 0.6 mg/cm^2 and was evaporated onto a 2 mg/cm^2 ^{197}Au fronting facing the beam. It was additionally protected against oxidation by a 0.2 mg/cm^2 ^{197}Au backing. The recoiling nuclei were stopped in a 3.5 mg/cm^2 gold foil. Their maximum velocity after the target was 0.83% of the speed of light. Both the target and the stopper foils were mounted parallel to each other and perpendicular to the beam axis. Deexciting γ-rays emitted before and in the stopper were detected by eleven high-purity Germanium (HPGe) detectors. These were mounted in two rings: six HPGe detectors were positioned at 45° and five at 142.3° with respect to the beam axis. Data were collected for 14 target-to-stopper distances from electrical contact to 100 μm, each measured for approximately 4 h. The target-stopper distances were monitored by a capacitance measurement [16]. The fluctuations induced by the beam were compensated with a piezoelectric device using an automatic feedback system [16].

3 Data analysis and results

For the data analysis $\gamma\gamma$-coincidence matrices were built using the sorting code SOCO2 [18]. The data from different HPGe detectors were grouped into rings with the same polar angles. The intensities of the γ-ray lines observed for each target to stopper distance had to be normalized to the corresponding number of ^{46}Ti to correct both for different measuring times and beam current fluctuation. This was performed in the following way: first, energy gates were set on the total intensities, *i.e.* intensities of Doppler-shifted and unshifted components for the decays from the 2_1^+, 4_1^+, 6_1^+ and 8_1^+ states individually. In a second step, the summed intensities of both components of all respective higher lying yrast states up to the 10_1^+ state were determined. For each set of matrices, these intensities are proportional to the number of ^{46}Ti nuclei produced at the corresponding distance and can be used as normalization factors. Random coincidences were subtracted from prompt γ-ray events with a condition for the accepted time differences of coincident events.

The lifetimes of the states were determined from the intensities of the shifted and unshifted components of the different transitions using the DDCM, for which only relative distances are needed. The data was analyzed by gating on the Doppler-shifted component of each direct feeding transition of the respective level of interest and intensities were determined by fitting Gaussian functions to both shifted and unshifted peaks. During the fitting procedure the peak positions as well as the peak widths of the unshifted components were fixed. This coincidence technique

allows for the elimination of systematic errors usually induced in RDDS-singles measurements by the unknown feeding history (from states that lie higher in energy). With this procedure all uncertainties from side-feeding are eliminated. For a gate on the shifted component of direct feeding transition of the state of interest, the lifetime is extracted from the intensities of the depopulating transition for each distance x according to

$$\tau(x) = \frac{I_{\mathrm{us}}(x)}{\frac{\mathrm{d}}{\mathrm{d}x} I_{\mathrm{sh}}(x)} \frac{1}{v}\,, \tag{1}$$

where I_{us} and I_{sh} are the areas of the unshifted and shifted peaks, respectively and v the mean velocity of the recoils. Accordingly, it is possible to derive a lifetime value for the level of interest at each target-to-stopper distance, which should be independent of the distance. As a result, eq. (1) leads to a constant line of lifetime values as a function of distances. Lifetimes determined from different $\gamma\gamma$ matrices are statistically independent.

The lifetimes are obtained by taking the weighted average of the lifetimes for different ring combinations. Here, it was possible to obtain the mean velocity $\overline{\beta}$ independently for each ring, utilizing the measured Doppler shift of the peaks according to

$$E_{\mathrm{sh}} = E_{\mathrm{us}} \cdot \frac{\sqrt{1-\overline{\beta}^2}}{1-\overline{\beta}\cdot\cos(\theta)}\,, \tag{2}$$

where E_{us} (E_{sh}) is the energy of the unshifted (shifted) component, θ the detector angle and $\overline{\beta} = v/c$. Therefore, individual gates were set on both components of the $4_1^+ \rightarrow 2_1^+$, $6_1^+ \rightarrow 4_1^+$ and $8_1^+ \rightarrow 6_1^+$ decay transitions and the corresponding $2_1^+ \rightarrow 0_{\mathrm{gs}}^+$, $4_1^+ \rightarrow 2_1^+$ and $6_1^+ \rightarrow 4_1^+$ decay transitions were analyzed to obtain a velocity for each distance i. However, "distance-dependent" velocities were observed, caused by a relative width of the velocity distribution of approximately 36%, because γ-ray intensities on the shifted peaks have more contributions from slower recoils at smaller distances. This effect implies a systematic variation of the centroid of the shifted peaks as a function of distance x (see fig. 1). It was taken into account by scaling the distances by a factor of $\beta_i/\beta_{\mathrm{max}}$ with respect to the maximum velocity of $\beta_{\mathrm{max}} = 0.83\%$ of the speed of light measured at the longest distance of 100 μm. By determining these effective distances, the effect of "distance-dependent velocities" could be canceled out.

This low recoil velocity after the target leads to small Doppler shifts. As a result, the shifted and unshifted components of the respective γ-ray line overlap and are not separated completely from each other (see spectra in fig. 1). Nevertheless, the development of intensity ratios of the shifted and unshifted components with increasing distances is clearly visible (see fig. 1).

Figure 2 shows the γ-ray statistics of the experiment in the forward ring at 45°. It is summed up over all distances with a gate on the shifted component of the $10_1^+ \rightarrow 8_1^+$ transition. The spectrum only shows γ-rays of ^{46}Ti without any contamination.

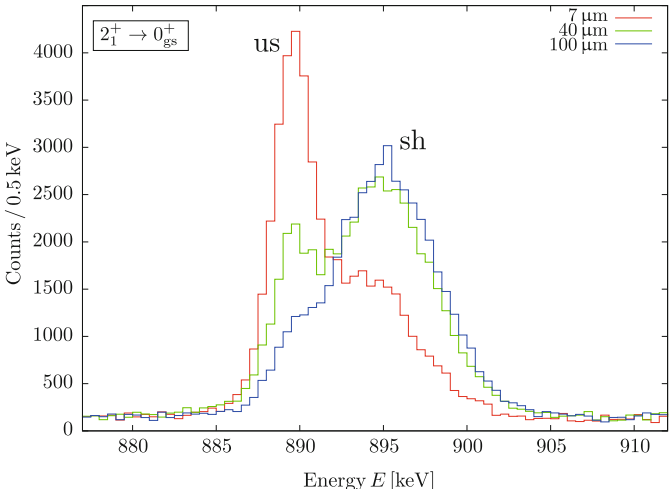

Fig. 1. (Color online) Exemplary γ-ray spectra from the $2_1^+ \rightarrow 0_{\mathrm{gs}}^+$ transition at three different distances (7 μm, 40 μm, 100 μm) in the ring at 45°. Spectra are produced from gates on the shifted component of the $4_1^+ \rightarrow 2_1^+$ transition. It can be clearly seen that the shifted component moves towards the unshifted component with decreasing distance due to the changing velocity distribution with respect to the distance. The shifted (sh) and unshifted (us) components are additionally labeled. See text for details.

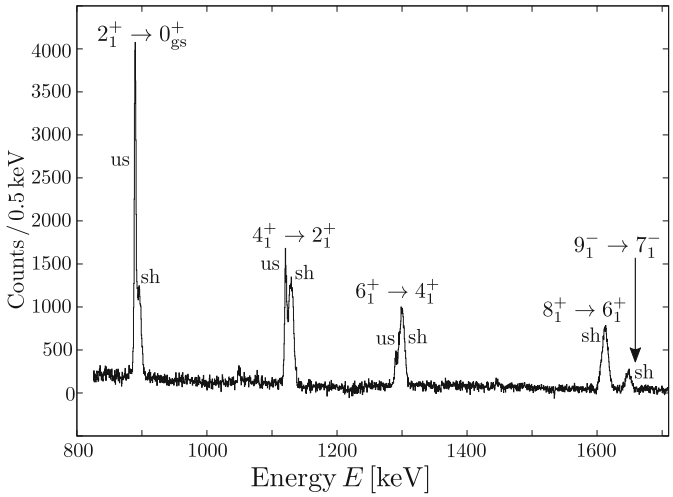

Fig. 2. γ-ray spectrum summed over all distances with a gate on the shifted component of the $10_1^+ \rightarrow 8_1^+$ transition and measured with the detectors in the ring at 45°. The shifted (sh) and unshifted (us) components of the underlying transitions of the yrast-band and the shifted component of the $9_1^- \rightarrow 7_1^-$ transition were observed.

Lifetime fits of continuously connected second-order polynomials to shifted and unshifted decay transitions, performed with NAPATAU [19] are illustrated in fig. 3. The lifetime, indicated by a constant line, is determined at each distance. Deviations from this behavior indicate systematic effects, which can be identified with this method. The weighted average value for the lifetime τ is taken of the points inside of the sensitive region, *i.e.*, where the derivative of the decay curve is largest. The final mean

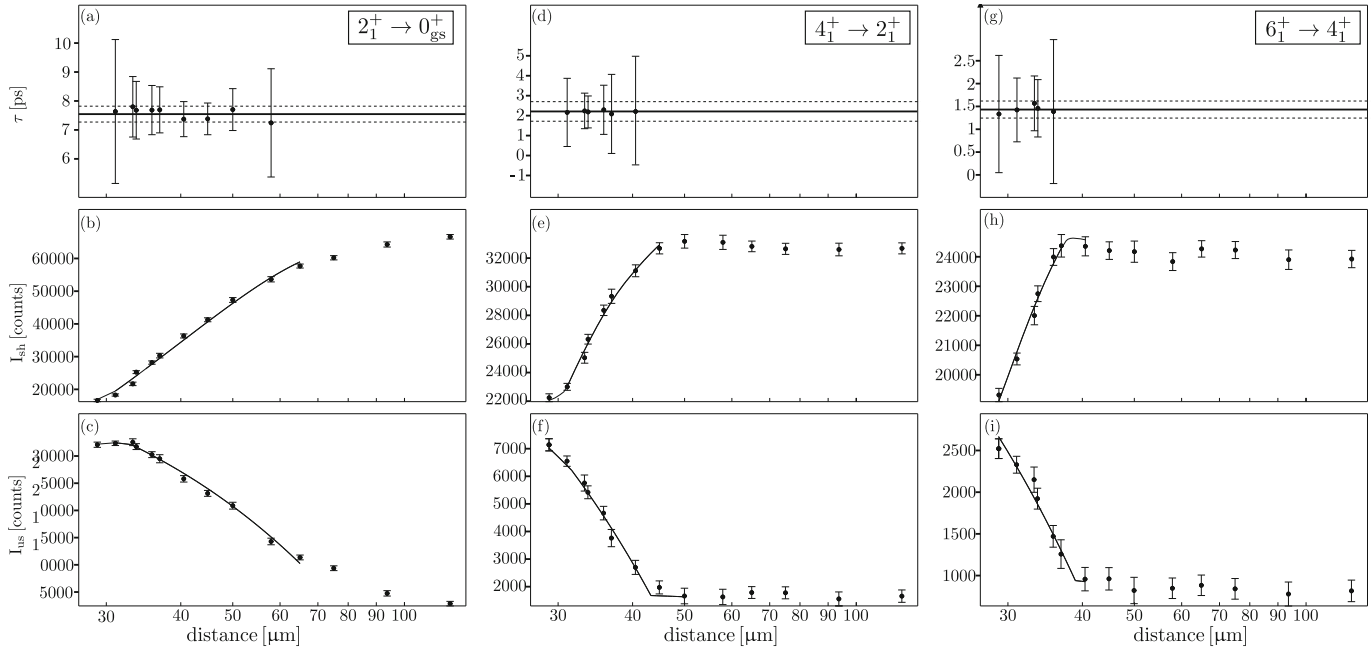

Fig. 3. τ-curves of the 2_1^+, 4_1^+ and 6_1^+ states (a), (d), (g) in ^{46}Ti using the forward ring at 45° with gates on the feeding transition from the 4_1^+, 6_1^+ and 8_1^+ states, respectively. The black solid lines in (a), (d), (g) represent the weighted mean value of the lifetimes; dashed lines mark the statistical uncertainty. In addition, the intensities of the shifted (b), (e), (h) and unshifted (c), (f), (i) components are shown. The polynomial fit function to the measured intensities is presented in solid black in (b), (c), (e), (f), (h), (i). Note the logarithmic distance scale.

Table 2. Results of the lifetimes and reduced transition probabilities of the first four yrast states in ^{46}Ti from this work.

I^π	E_{Level} (keV)	E_γ (keV)	τ (ps) (ring 1)	τ (ps) (ring 2)	$\overline{\tau}$ (ps)	$B(E2; I_1^+ \rightarrow (I-2)_1^+)$ (e^2 fm^4)
2_1^+	889.3	889.3	7.55(27)	7.92(24)	7.76(18)	$189.9^{+4.4}_{-4.3}$
4_1^+	2009.8	1120.5	2.21(50)	2.19(31)	2.20(26)	211^{+28}_{-22}
6_1^+	3298.9	1289.1	1.34(47)	1.43(50)	1.38(34)	167^{+55}_{-33}
8_1^+	4896.9	1597.9	≤ 1.2	≤ 1.2	≤ 1.2	≥ 66

lifetimes, weighted averaged from the forward and backward ring yield $\tau(2_1^+) = 7.76(18)$ ps, $\tau(4_1^+) = 2.20(26)$ ps, $\tau(6_1^+) = 1.38(34)$ ps and $\tau(8_1^+) \leq 1.2$ ps. The spectra from the different rings yield consistent values and the results are summarized along with the $B(E2)$ transition strengths in table 2. Furthermore, the results were verified by determining lifetimes using additional indirect gates, *i.e.* gates were set on the flight components of the $6_1^+ \rightarrow 4_1^+$ and $8_1^+ \rightarrow 6_1^+$ decay transitions and the $2_1^+ \rightarrow 0_{gs}$ and $6_1^+ \rightarrow 4_1^+$ transitions were analyzed. The statistical uncertainty of the lifetime value is dominated by the distribution of the individual τ-values. The uncertainty of the recoil velocity resulting from the uncertainty of the mean polar angle $\Delta\theta = 3°$ and the relative target-to-stopper distances measured with a high precision of $\Delta x \leq 0.1\,\mu$m in the sensitive range, define the systematic errors (approx. 3% of the respective lifetimes) of the lifetime. The final experimental error of the lifetime includes the root sum squared of the statistical and the systematic uncertainties. For the lifetime of the 8_1^+ state, our data yielded only an upper limit because, for all distances, only the shifted component of this decay is visible after gating on the shifted component of the $10_1^+ \rightarrow 8_1^+$ transition. Higher lying decay transitions are not visible in the spectrum.

4 Conclusion

In summary, reliable lifetimes and lifetime limits of excited states in the yrast band of ^{46}Ti up to the 8_1^+ state were measured and the resulting $E2$ transition probabilities were determined. The present lifetime of the 2_1^+ state $\tau(2_1^+) = 7.76(18)$ ps in ^{46}Ti agrees with the adopted average lifetime of all available lifetime data [4] within the uncertainty, but the uncertainty of the present lifetime value is smaller than the mean error of the average lifetime. The present lifetimes of the 4_1^+ and 6_1^+ states also agree with previous results [2,6,7,11,1,4]. The upper limit for the lifetime of the 8_1^+ state from this work also agrees with the lifetime value known for this state from earlier works [2, 3,7,14]. It must be stressed that, unlike most of the previous measurements, the present lifetimes are not prone

to side-feeding due to the analysis of gated coincidence data. Furthermore, excellent statistics were achieved due to a quite efficient setup and by choosing a reaction with a relatively large cross section to ^{46}Ti.

With regard to the discussion of the last lifetime measurement [11], the longer lifetime for the 2_1^+ state determined in this work leads to a smaller g-factor value and approaches the values of the shell model calculations used there.

Therefore, the current results can be used for normalization and scaling in other experiments, *e.g.* Coulomb excitation experiments.

We thank all the operators in Cologne for the professional support during the experiment. The research leading to these results has been supported partly by Deutsches Bundesministerium für Bildung, Wissenschaft, Forschung und Technologie (BMBF) under Contract No. 05P18PKFN9.

Data Availability Statement This manuscript has no associated data or the data will not be deposited. [Authors' comment: All data generated during this study are contained in this published article.]

References

1. W. Dehnhardt *et al.*, Phys. Rev. C **7**, 1471 (1973).
2. N. Rammo *et al.*, J. Phys. G: Nucl. Phys. **8**, 101 (1982).
3. A.R. Poletti *et al.*, Phys. Rev. C **23**, 1550 (1981).
4. M. Rahman *et al.*, Nucl. Phys. A **401**, 253 (1983).
5. P. Assimakopoulos *et al.*, Nucl. Phys. A **180**, 131 (1972).
6. J. Durell *et al.*, J. Phys. A: Math. Nucl. Gen. **7**, 1448 (1974).
7. G. Dracoulis *et al.*, J. Phys. G: Nucl. Phys. **4**, 1323 (1978).
8. D.K. Kaipov *et al.*, Zh. Eksperim. Teor. Fiz. **44**, 1811 (1963).
9. G. Tandon, Bull. Am. Phys. Soc. **12**, 683 (1967).
10. A. Kluge, W. Thomas, Nucl. Instrum. Methods **134**, 525 (1976).
11. R. Ernst *et al.*, Phys. Rev. Lett. **84**, 416 (2000).
12. A.F. Akkerman *et al.*, Izv. Akad. Nauk SSSR Ser. Fiz. **27**, 862 (1963).
13. C.M. Rozsa *et al.*, Bull. Am. Phys. Soc. **17**, 536 (1972).
14. J.A. Cameron *et al.*, Phys. Rev. C **58**, 808 (1998).
15. A. Dewald *et al.*, Prog. Part. Nucl. Phys. **67**, 786 (2012).
16. A. Dewald *et al.*, Z. Phys. A **334**, 163 (1989).
17. M. Zielińska *et al.*, Eur. Phys. J. A **52**, 99 (2016).
18. N. Saed-Samii, *Lifetime measurements using the FATIMA array in combination with EXOGAM@ILL* (2013), unpublished.
19. B. Saha, *Computer code NAPATAU*, Institute for Nuclear Physics, Cologne, unpublished.

Publication II:
Lifetime measurements in ^{52,54}Ti to study shell evolution toward N = 32

Lifetime measurements in ^{52,54}Ti to study shell evolution toward $N = 32$

A. Goldkuhle,[1,*] C. Fransen,[1] A. Blazhev,[1] M. Beckers,[1] B. Birkenbach,[1] T. Braunroth,[1] E. Clément,[2] A. Dewald,[1] J. Dudouet,[3] J. Eberth,[1] H. Hess,[1] B. Jacquot,[2] J. Jolie,[1] Y.-H. Kim,[4] A. Lemasson,[2] S. M. Lenzi,[5,6] H. J. Li,[2] J. Litzinger,[1] C. Michelagnoli,[5,6,2] C. Müller-Gatermann,[1] B. S. Nara Singh,[7,8] R. M. Pérez-Vidal,[9] D. Ralet,[10,11,12] P. Reiter,[1] A. Vogt,[1] N. Warr,[1] K. O. Zell,[1] A. Ataç,[13] D. Barrientos,[14] C. Barthe-Dejean,[2] G. Benzoni,[15] A. J. Boston,[16] H. C. Boston,[16] P. Bourgault,[2] I. Burrows,[17] J. Cacitti,[2] B. Cederwall,[13] M. Ciemala,[18] D. M. Cullen,[7] G. De France,[2] C. Domingo-Pardo,[9] J.-L. Foucher,[2] G. Fremont,[2] A. Gadea,[9] P. Gangnant,[2] V. González,[19] J. Goupil,[2] C. Henrich,[12] C. Houarner,[2] M. Jean,[2] D. S. Judson,[16] A. Korichi,[10] W. Korten,[20] M. Labiche,[17] A. Lefevre,[2] L. Legeard,[2] F. Legruel,[2] S. Leoni,[15,21] J. Ljungvall,[10] A. Maj,[18] C. Maugeais,[2] L. Ménager,[2] N. Ménard,[2] R. Menegazzo,[5] D. Mengoni,[5,6] B. Million,[15] H. Munoz,[2] D. R. Napoli,[22] A. Navin,[2] J. Nyberg,[23] M. Ozille,[2] Zs. Podolyak,[24] A. Pullia,[15,25] B. Raine,[2] F. Recchia,[5,6] J. Ropert,[2] F. Saillant,[2] M. D. Salsac,[20] E. Sanchis,[19] C. Schmitt,[2] J. Simpson,[17] C. Spitaels,[2] O. Stezowski,[3] Ch. Theisen,[20] M. Toulemonde,[26] M. Tripon,[2] J.-J. Valiente Dobón,[22] G. Voltolini,[2] and M. Zielińska[20]

(AGATA Collaboration)

[1]*Institut für Kernphysik, Universität zu Köln, 50937 Köln, Germany*
[2]*GANIL, CEA/DRF-CNRS/IN2P3, BP 55027, 14076 Caen Cedex 05, France*
[3]*Université de Lyon, CNRS/IN2P3, IPN-Lyon, F-69622 Villeurbanne, France*
[4]*Institut Laue-Langevin, BP 156, 38042 Grenoble Cedex 9, France*
[5]*INFN Sezione di Padova, I-35131 Padova, Italy*
[6]*Dipartimento di Fisica e Astronomia dell'Università di Padova, I-35131 Padova, Italy*
[7]*Nuclear Physics Group, Schuster Laboratory, University of Manchester, Manchester, M13 9PL, United Kingdom*
[8]*School of Computing Engineering and Physical Sciences, University of the West of Scotland, Paisley, PA1 2BE, United Kingdom*
[9]*Instituto de Físcia Corpuscular, CSIC-Universidad de Valencia, E-46071 Valencia, Spain*
[10]*Centre de Spectrométrie Nucléaire et de Spectrométrie de Masse - CSNSM,CNRS/IN2P3 and Université Paris-Sud, F-91405 Orsay Campus, France*
[11]*GSI, Helmholtzzentrum für Schwerionenforschung GmbH, 64291 Darmstadt, Germany*
[12]*Institut für Kernphysik, Technische Universität Darmstadt, 64289 Darmstadt, Germany*
[13]*Department of Physics, Royal Institute of Technology, SE-10691 Stockholm, Sweden*
[14]*CERN, CH-1211 Geneva 23, Switzerland*
[15]*INFN Sezione di Milano, I-20133 Milano, Italy*
[16]*Oliver Lodge Laboratory, The University of Liverpool, Liverpool, L69 7ZE, United Kingdom*
[17]*STFC Daresbury Laboratory, Daresbury, Warrington WA4 4AD, United Kingdom*
[18]*The Henryk Niewodniczański Institute of Nuclear Physics, Polish Academy of Sciences, ul. Radzikowskiego 152, 31-342 Kraków, Poland*
[19]*Departamento de Ingeniería Electrónica, Universitat de Valencia, Burjassot, Valencia, Spain*
[20]*Irfu, CEA, Université Paris-Saclay, F-91191 Gif-sur-Yvette, France*
[21]*Dipartimento di Fisica, Università di Milano, I-20133 Milano, Italy*
[22]*Laboratori Nazionali di Legnaro, INFN, I-35020 Legnaro, Italy*
[23]*Department of Physics and Astronomy, Uppsala University, SE-75120 Uppsala, Sweden*
[24]*Department of Physics, University of Surrey, Guildford, GU2 7XH, United Kingdom*
[25]*University of Milano, Department of Physics, I-20133 Milano, Italy*
[26]*CIMAP-GANIL (CEA-CNRS-ENSICAEN-Université de Caen), BP 5133, 14070 Caen, France*

(Received 22 August 2019; published 18 November 2019)

Lifetimes of the excited states in the neutron-rich ^{52,54}Ti nuclei, produced in a multinucleon-transfer reaction, were measured by employing the Cologne plunger device and the recoil-distance Doppler-shift method. The experiment was performed at the Grand Accélérateur National d'Ions Lourds facility by using the Advanced Gamma Tracking Array for the γ-ray detection, coupled to the large-acceptance variable mode spectrometer for an event-by-event particle identification. A comparison between the transition probabilities obtained from the measured lifetimes of the 2_1^+ to 8_1^+ yrast states in ^{52,54}Ti and that from the shell-model calculations based on the

*Corresponding author: agoldkuhle@ikp.uni-koeln.de

well-established GXPF1A, GXPF1B, and KB3G fp shell interactions support the $N = 32$ subshell closure. The $B(E2)$ values for ^{52}Ti determined in this work are in disagreement with the known data, but are consistent with the predictions of the shell-model calculations and reduce the previously observed pronounced staggering across the even-even titanium isotopes.

DOI: 10.1103/PhysRevC.100.054317

I. INTRODUCTION

Understanding the evolution of shell structure toward the drip lines is one of the driving forces for many theoretical and experimental efforts, as investigations have shown that the shell structure often changes significantly as a result of the rearrangement of single-particle levels in exotic nuclear regions [1]. In this context, the $N = 40$ island of inversion represents a rich testing ground. For example, while ^{68}Ni shows doubly shell-closure character, an increase in collectivity is apparent both from excitation energies and transition strengths in the neutron-rich $^{58-66}$Cr [2–5] and $^{62-70}$Fe [5–8] nuclei close to the $Z = 28$ shell closure. The experimental data assisted a comprehensive description of these nuclei with respect to the high collectivity predicted using the modern shell-model calculations [2,6].

Studies of neutron-rich Ti isotopes are also essential for an understanding of the shell structure in the Ti-Cr-Fe region beyond $N = 28$ and toward $Z = 20$. Known $B(E2, 2_1^+ \rightarrow 0_{gs}^+)$ transition probabilities in ^{54}Ti [9], ^{56}Cr [10,11], ^{58}Fe [12], and ^{60}Ni [13] isotones, which in a shell-model framework can be viewed as having a completely filled valence $\nu 2p_{3/2}$ orbital, suggest a phase transition. In particular, the collective structure in ^{58}Fe evolves to a neutron-subshell closure along the isotonic chain with decreasing proton number, i.e., from ^{56}Cr over ^{54}Ti to ^{52}Ca. This observation is supported by an increased staggering of the 2_1^+ level energies for decreasing proton number as shown in Fig. 1. At the neutron shell closure $N = 28$, the isotones show a local rise in the 2_1^+ state energy but at $N = 32$ a different behavior is observed: only ^{52}Ca, ^{54}Ti, and ^{56}Cr exhibit a local increase in the 2_1^+ energy. The corresponding $B(E2; 2_1^+ \rightarrow 0_{gs}^+)$ values suggest a weak and very localized subshell closure at $N = 32$ [14–16] for the Ca, Ti, and Cr isotones, which collapses for Fe and Ni. This behavior was investigated in several recent experiments on ^{52,54,56}Ti and ^{58}Cr using deep-inelastic reactions [17,18], β decay [16,19], as well as Coulomb excitation at intermediate energies [9]. Essentially, all the experimental and theoretical works indicate the subshell closure at $N = 32$ is weaker compared to that at $N = 28$.

A possible explanation could be an effect similar to that for $N = 40$ isotones described in works of Otsuka *et al.* [20–22], where the proton-neutron tensor force contribution to the monopole component of the residual interaction was proposed as one of the driving factors behind the shell evolution at $N = 40$. This ensures that the $N = 40$ gap is reduced by removing protons from the $\pi 1f_{7/2}$ subshell. For nuclei close to $N = 32$, a similar effect could result in a reverse order of the $\nu 1f_{5/2}$ and $\nu 2p_{1/2}$ orbitals and is assumed to open up the shell gap at $N = 32$, i.e., the energy difference between the $\nu 2p_{3/2}$ and $(\nu 2p_{1/2}, \nu 1f_{5/2})$ orbitals with decreasing proton number from $Z = 28$ to $Z = 20$ [14].

For a better understanding of the shell evolution, data on $E2$ transition strengths between higher-spin states in ^{54}Ti ($N = 32$) are essential, which are not available to date. Furthermore, the shell-model predictions so far do not agree with the $B(E2)$ data of the neighboring ^{52}Ti that is only two neutron away but exhibits different $B(E2)$ behavior as a function of spin to that of ^{50}Ti and ^{54}Ti, e.g., ^{52}Ti has relatively high $B(E2; 2_1^+ \rightarrow 0_{gs}^+)$ and $B(E2; 6_1^+ \rightarrow 4_1^+)$ values but a low $B(E2; 4_1^+ \rightarrow 2_1^+)$ value. In contrast, experimental (theoretical) results for ^{50}Ti (^{54}Ti) show relatively high $B(E2)$ values for the $2_1^+ \rightarrow 0_{gs}^+$ and $4_1^+ \rightarrow 2_1^+$ transitions and a low $B(E2)$ value for the $6_1^+ \rightarrow 4_1^+$ transition. So far, no successful shell-model description could be reached for ^{52}Ti, motivating a new detailed investigation of ^{52,54}Ti in order to obtain a comprehensive picture of the evolving shell structure with regard to the emergence of a $N = 32$ subshell closure for $Z < 26$.

In this work, the evolution of the shell structure in ^{52,54}Ti is studied by measuring the lifetimes of the first 2_1^+, 4_1^+, 6_1^+, and 8_1^+ states in the yrast band by employing the recoil-distance Doppler-shift (RDDS) method [23]. The deduced $E2$ transition strengths are discussed together with the state-of-the-art shell-model calculations.

II. EXPERIMENTAL SETUP

The experiment was performed at the Grand Accélérateur National d'Ions Lourds (GANIL) in Caen, France using the Cologne plunger for deep-inelastic reactions [23]. The ^{52,54}Ti nuclei were produced via two-neutron and four-neutron multinucleon-transfer reactions induced by a ^{238}U beam at an energy of $E(^{238}\text{U}) = 1608.9$ MeV (6.76 MeV/u) impinging on a ^{50}Ti target. The target was $\approx$1.5 mg/cm^2 thick and had a $^{\text{nat}}$Cu layer of $\approx$0.4 mg/cm^2 in front of the target. The plunger device including target and degrader foils was

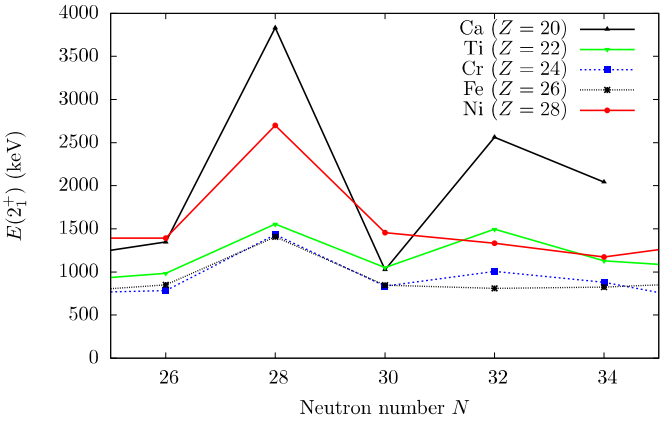

FIG. 1. Evolution of experimental excitation energies $E(2_1^+)$ in neutron-rich even-even Ca-Ni nuclei with $20 \leqslant Z \leqslant 28$ and $26 \leqslant N \leqslant 34$.

placed close to the grazing angle of the multinucleon-transfer reactions of interest at an angle of 45° with respect to the beam axis. Target and degrader foils were mounted orthogonal to the entrance axis of the magnetic spectrometer VAMOS++ [24–26]. The ^{50}Ti target layer had an effective thickness of ≈2.1 mg/cm^2 resulting in an effective ^{238}U beam energy of 6.16 MeV/u in the middle of the ^{50}Ti layer, taking into account the energy loss in the Cu layer with an effective thickness of ≈0.57 mg/cm^2. A ^{nat}Mg degrader foil with a thickness of ≈3.2 mg/cm^2 was placed downstream the target. The targetlike recoils were thus slowed down before entering the VAMOS++ magnetic spectrometer, consisting of two quadrupoles, a dipole magnet, and an array of focal plane detectors, for an event-by-event particle identification. A schematic drawing of the experimental setup is shown in Fig. 1 of Ref. [27] (without the EXOGAM detectors). The focal plane detection system was used to identify the mass (A), charge (Q) and atomic number (Z) of the reaction products. It consisted of a multiwire proportional counter (MWPC), four drift chambers and a segmented ionization chamber. The dual position-sensitive multiwire proportional counter (DPS-MWPC) [26] placed at the entrance of the spectrometer provided the start signal for the time-of-flight (TOF) and the position (x, y) of the recoiling reaction products. Together with the MWPC at the focal plane, they provide the TOF and the direction of the velocity of the ions for Doppler correction. The drift chambers, which also detected the position (x, y) as well as the emission angles (θ, ϕ) of the recoiling reaction products, were used together with the DPS-MWPC to determine the trajectory of the ions after the dipole magnet. Finally, the ionization chamber was employed for measuring the total energy E and energy loss ΔE of the ions at the focal plane. In the present experiment, the magnetic field of the VAMOS++ dipole was set such that a magnetic rigidity of $B\rho = 0.975$ Tm was selected for the central trajectory in the spectrometer.

Prompt γ rays were detected by the Advanced Gamma Tracking Array (AGATA) [28,29]. At the time of this experiment, it consisted of 29 36-fold encapsulated germanium detectors in ten cryostats placed at a radial distance of ≈23.5 cm to the target center and covered angles from 120°–175° with respect to the optical axis of the spectrometer. Using the velocity vector reconstructed by VAMOS++ and the position of the first γ-ray interaction in AGATA, the observed γ rays were Doppler corrected on an event-by-event basis using the angle between the scattered particle and the direction of γ rays detected in AGATA. The γ-ray interaction points, determined by the pulse shape analysis (PSA) using GRID search algorithm techniques [30], were tracked by using the Orsay forward tracking (OFT) algorithm [31]. The particle velocity after passing through the degrader foil is used for the Doppler correction. Therefore, the slow component, corresponding to photon emissions after the degrader, occurs at the nominal γ-ray energy whereas the fast component is shifted toward lower energies, as AGATA was located at backward angles.

Data were taken at six different nominal target-to-degrader distances between 70 μm and 1000 μm for about 24 h per distance, which results in sensitivity to lifetimes ranging from a few ps to about 400 ps.

FIG. 2. Beam-induced changes observed for the ^{50}Ti plunger target. The originally stretched target foil was severely damaged. Here, the side of the target with the copper layer that was facing the beam.

A. Target degradation and effective plunger distances

During the experiment, despite the low beam current of 0.1 pnA, beam-induced changes of the ^{50}Ti target occurred, even though estimates of the beam spot temperature from the momentum transfer of the beam did not indicate any significant thermal load. A self-supporting ^{50}Ti target with a thickness of ≈1.5 mg/cm^2 was used at first. This target developed wrinklelike structures with amplitudes of about 100 μm soon after being exposed to the 6.76 MeV/u ^{238}U beam with a beam current of 0.1 pnA. To improve heat conductivity, this target was replaced by the aforementioned ≈1.5 mg/cm^2 ^{50}Ti target with an additional ≈0.4 mg/cm^2 copper that was evaporated onto the ^{50}Ti foil. The copper layer was facing the beam. This target experienced similar damages after being exposed to the beam (see Fig. 2). Nevertheless, as no other alternative was available, the ^{50}Ti target with the additional copper layer was used. After a careful analysis, the observed degradation of the target can be explained as resulting from the sensitivity of the Ti material to the electronic stopping of heavy ions (see Ref. [32]). This effect leads to a drastic increment of the lattice temperature of Ti induced by the irradiation by the highly energetic ^{238}U ions (so-called thermal spikes) and thus to structural damages of the Ti target foil. Titanium is very sensitive to this effect due to its large Debye temperature on the one hand and its low thermal conductivity on the other hand. This observation can be reproduced within the thermal-spike model (see, e.g., Ref. [33]). The degrader, on the other hand, showed no such effects since magnesium has a much lower Debye temperature and a higher thermal conductivity.

For this reason, a direct and precise determination of the distances between the plunger target and the degrader was not possible. Instead, average absolute distances for each distance setting need to be specified as the structural changes to target continue to take place during the ^{238}U beam exposure. These distances are referred to as the effective distances and can be extracted from γ-ray spectra related to nuclear states whose lifetimes are known with high precision. A strongly populated reaction channel produced ^{46}Ti (see Fig. 3 for the corresponding spectrum), for which a high-precision RDDS

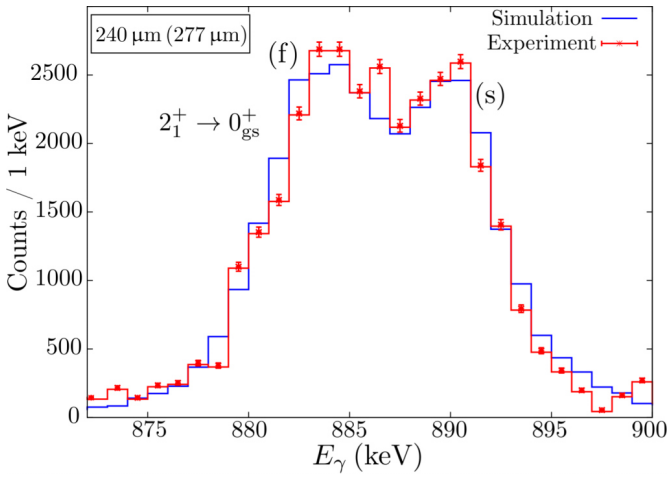

FIG. 3. Experimental (red) and simulated (blue) γ-ray energy spectra of ^{46}Ti at an effective target-to-degrader distance of 277 μm, Doppler corrected for the degraded component. The fast (f) and slow (s) components are also labeled. See text for details.

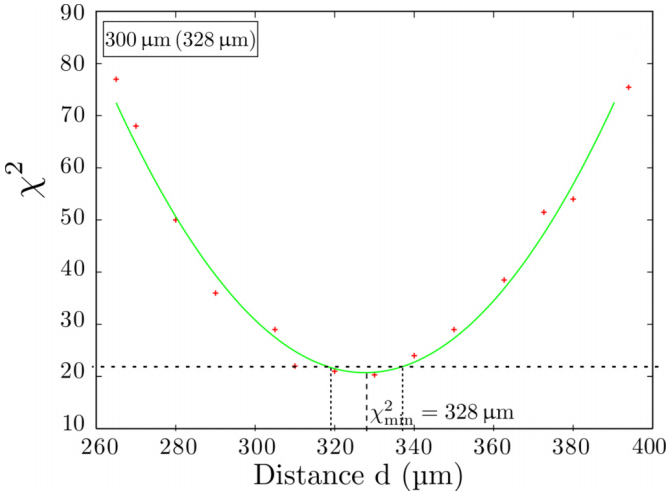

FIG. 4. Determination of the mean distance using the standard χ^2 method for a nominal distance of 300 μm. As indicated, the errors of the χ^2 method are deduced from lifetimes with $\chi^2_{min} + 1$. See text for details.

measurement was performed only recently with results published in Ref. [34]. Since ^{46}Ti isotopes were produced via multinucleon-transfer reactions, only the low-lying states 2_1^+, 4_1^+, and 6_1^+ were populated, so that other feeding can be excluded. Feeding corrections for the observed transitions from the 4^+ and 6^+ states were taken into account in the analysis.

For the determination of effective distances, γ-ray spectra for ^{46}Ti were created through a versatile GEANT4-based Monte Carlo simulation tool [35] using a precise experimental geometry including that for the target chamber and the AGATA detectors. For the distance determination, distance assumptions were provided to the simulation toolkit and their values were varied in discrete steps. For illustration, Fig. 3 shows a representative comparison of the experimental spectra showing the $2_1^+ \rightarrow 0_{gs}^+$ transition in ^{46}Ti at a nominal distance of 240 μm with the best-fitting simulation, assuming a separation following the described approach. For each comparison between the simulated and the experimental spectrum, a χ^2 value was calculated according to the following modified version of the least-squares method:

$$\chi^2 = \sum_i \left(\frac{i_{exp} - i_{sim}}{\Delta i_{exp}} \right)^2,$$

where i_{exp} (i_{sim}) is the number of counts in bin i in the experimental (simulated) spectrum. The chosen range was restricted to both the fast and slow components of the considered transition. An example of this approach with the χ^2 method is depicted in Fig. 4 for the nominal distance of 300 μm. A similarly good description using the χ^2 method can be observed for the other distances. The statistical uncertainty is extracted from distance values at $\chi^2_{min} + 1$ (cf. Fig. 4). Table I shows the effective distances d resulting from the individual ^{46}Ti simulations.

The velocities of the recoil ions were determined as follows: the velocity after the degrader was measured directly by VAMOS++, whereas the velocity between target and degrader was deduced from the experimentally observed Doppler shift between the two components of the transitions. The mean recoil velocity behind the target (degrader) is $\beta_T = 12.70(21)$ % [$\beta_D = 11.68(23)$%] of the speed of light.

III. DATA ANALYSIS AND RESULTS

Figure 5(a) shows the energy loss ΔE versus the total energy E spectra, using which the recoils with specific atomic number Z can be identified. The mass-over-charge A/Q ratio and the mass A are determined from the TOF, the path through the spectrometer, and the magnetic rigidity. The mass resolution for the isotopic chains, shown in Fig. 5(b), was $\frac{\Delta M}{M} \approx 1.4$ %, so that an unambiguous identification of the reaction residues in the mass region around $A = 50$ was possible.

Figure 6 shows the γ-ray spectra after Doppler correction with $\beta_D = 11.68\%$ for the slow component detected with AGATA in coincidence with ^{54}Ti and ^{52}Ti ions identified in VAMOS++, summed over all six distances. Therefore, the slow component appears at nominal γ-ray energy while the fast component has lower energy. It can be clearly seen that the statistics for ^{52}Ti is $\approx$ 13 times higher than that for ^{54}Ti.

TABLE I. Effective distances d resulting from a comparison with the simulations and corresponding nominal distances d_{exp} used for the measurement (i.e., relative to electrical contact at the start of the experiment).

d_{exp} (μm)	d (μm)
70	102(8)
150	198(9)
180	200(6)
240	277(10)
300	328(9)

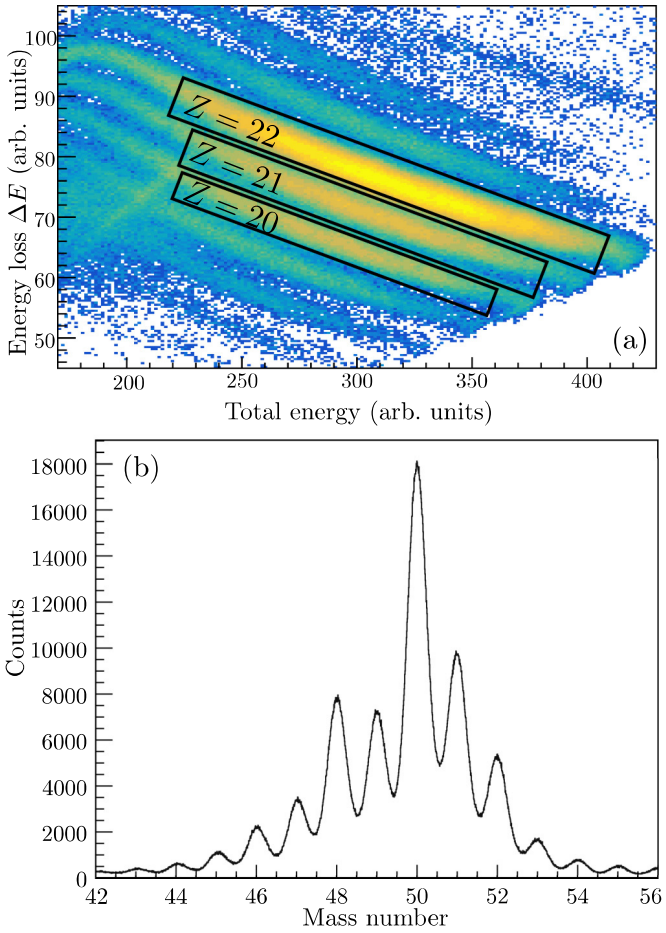

FIG. 5. (a) Energy loss of the targetlike reaction products in VAMOS++ as a function of total detected energy. The isotopes of titanium ($Z = 22$), scandium ($Z = 21$), and calcium ($Z = 20$) are marked schematically with black rectangles. (b) Mass spectrum showing resolution for the titanium isotopic chain.

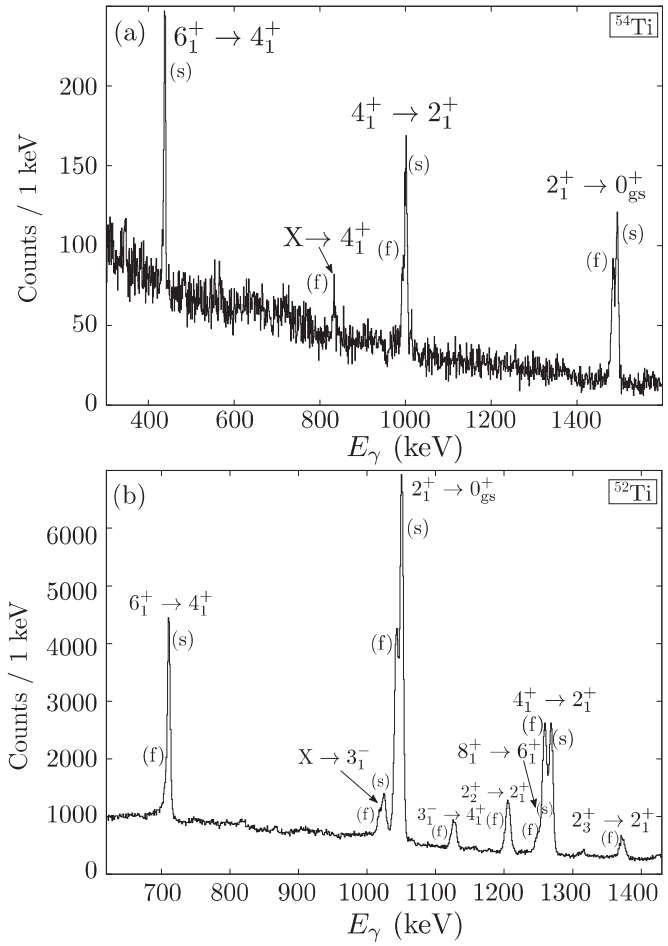

FIG. 6. γ-ray spectra in coincidence with ions identified as ^{54}Ti (a) and ^{52}Ti (b), summed over all six distances. In this energy range four (eight) γ-ray decays are visible in ^{54}Ti (^{52}Ti). The fast (f) and slow (s) components are labeled.

The clearly visible variations of the intensities of the fast and slow components with the distance d in the Doppler-corrected energy spectra for the $2_1^+ \rightarrow 0_{gs}^+$ transition in ^{54}Ti at three different distances are shown in Fig. 7. During the fitting procedure, the peak positions and widths were fixed. The latter were determined by calibrating the line width using the γ-ray spectra of ^{50,52,53}Ti, which have a significantly higher level of statistics than that of ^{54}Ti. Due to the relatively small difference in the velocity of $\Delta v = 0.0102\,c$, the fast and slow components of the γ-ray lines are not well separated from each other.

Lifetimes of the excited states in ^{52,54}Ti were extracted from the γ-ray intensities for each distance in the sensitive range (see Eq. (20) in Ref. [23]) using the differential decay curve method (DDCM) [36]. The lifetime of an excited state should not depend on the target-to-degrader distances at which it has been determined, therefore, τ values are expected to remain unchanged with plunger distance. In ^{54}Ti it is possible to identify five transitions: $2_1^+ \rightarrow 0_{gs}^+$ (1495 keV), $4_1^+ \rightarrow 2_1^+$ (1002 keV), $6_1^+ \rightarrow 4_1^+$ (439 keV), $8_1^+ \rightarrow 6_1^+$ (2523 keV), and a transition at 840 keV from a state with unknown spin and parity J^π deexciting to the 4_1^+ state. Only for the $2_1^+ \rightarrow 0_{gs}^+$ and $4_1^+ \rightarrow 2_1^+$ transitions both components are visible for all distances. For the 439 keV $6_1^+ \rightarrow 4_1^+$ transition, only the slow component is visible at all distances. Therefore, only a lower limit of the 6_1^+ lifetime could be determined. In contrast, for the $8_1^+ \rightarrow 6_1^+$ transition at 2523 keV only the fast component is visible at all distances, and as a consequence only an upper limit of the 8_1^+ lifetime was deduced. In ^{52}Ti it is possible to identify ten transitions: $2_1^+ \rightarrow 0_{gs}^+$ (1050 keV), $4_1^+ \rightarrow 2_1^+$ (1268 keV), $6_1^+ \rightarrow 4_1^+$ (711 keV), $8_1^+ \rightarrow 6_1^+$ (1258 keV), $2_2^+ \rightarrow 2_1^+$ (1214 keV), $2_3^+ \rightarrow 2_1^+$ (1382 keV), $3_1^- \rightarrow 4_1^+$ (1135 keV), $(10_1^+) \rightarrow 8_1^+$ (2406 keV), $10_2^+ \rightarrow 8_1^+$ (3232 keV), and $J^\pi \rightarrow 3_1^-$ (1025 keV). It should be noted that the γ-ray spectra are particle-gated singles spectra. For the lifetime determination of the 2_1^+, 4_1^+, 6_1^+, and 8_1^+ states, a feeding correction was carried out by subtracting the intensities of the slow component of a direct feeder from the intensity of the slow component of γ decay of the state to be analyzed. All contributions from states outside the yrast band have been neglected due to nonobserved slow components, which means that these states are characterized by a rather small lifetime. It should be

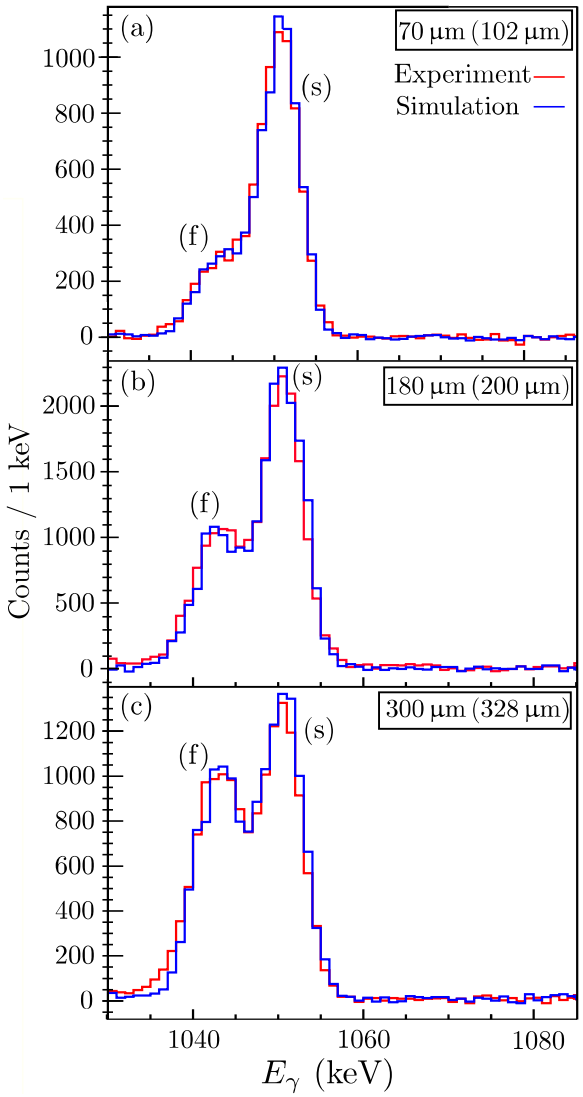

FIG. 7. Simulated (blue) and experimental (red) particle-gated singles γ-ray energy spectra showing the $2_1^+ \rightarrow 0_{gs}^+$ transition at 1050 keV in ^{52}Ti at three target-to-degrader distances at backward angles. The development of intensity ratios of the fast (f) and slow (s) components with increasing distances is clearly visible.

mentioned that the fast component of the $4_1^+ \rightarrow 2_1^+$ transition is equal in energy to the slow component of the $8_1^+ \rightarrow 6_1^+$ transition. In order to account for this, an intensity function depending on the spin was first established by determining the intensities of the fast and slow components of the $2_1^+ \rightarrow 0_{gs}^+$, $6_1^+ \rightarrow 4_1^+$, and $10_2^+ \rightarrow 8_1^+$ transitions in ^{52}Ti in the spectrum summed up over all distances. This intensity function was compared to the corresponding one in ^{48}Ti, this is possible due to similarity of the level schemes. Using the intensity function, in the sum spectrum the added intensities ($I_{f+s,sum}(J_1^+ \rightarrow (J-2)_1^+)$) of the fast and slow components of the $4_1^+ \rightarrow 2_1^+$ and $8_1^+ \rightarrow 6_1^+$ transitions in ^{52}Ti were calculated. Then the intensities of the $2_1^+ \rightarrow 0_{gs}^+$ transitions were determined for each distance ($I_{f+s,dist}(2_1^+ \rightarrow 0_{gs}^+)$) and the unknown intensities of the $4_1^+ \rightarrow 2_1^+$ and $8_1^+ \rightarrow 6_1^+$ were calculated according to $I_{f+s,dist}(J_1^+ \rightarrow (J-2)_1^+) = \alpha_i \cdot I_{f+s,dist}(2_1^+ \rightarrow 0_{gs}^+)$ with $\alpha_i = \frac{I_{f+s,sum}(J_1^+ \rightarrow (J-2)_1^+)}{I_{f+s,sum}(2_1^+ \rightarrow 0_{gs}^+)}$, with $I_{f+s,sum}(2_1^+ \rightarrow 0_{gs}^+)$ is the added intensity of the fast and slow components of the $2_1^+ \rightarrow 0_{gs}^+$ transition in the sum spectrum. The relevant plots for the lifetime analysis for the decay of the 2_1^+ and 4_1^+ states in ^{54}Ti (^{52}Ti) are shown in Fig. 8 (Fig. 9). Fits of the intensities of the two components were performed with the NAPATAU code [39]. Here a feeding correction was carried out so that the summed intensity of I_s and I_f does not have to be constant. The different plot curves of the intensity of the slow components of Figs. 8 and 9 result from the different slopes in the intensities of the fast components. The weighted average lifetime is calculated using the points inside the region of sensitivity, i.e., from the maximum of the slope of the decay curve to its half value. The weighted averages of the mean lifetimes in ^{52,54}Ti are summarized along with the corresponding $E2$ transition strengths in Table II. The statistical uncertainty of each lifetime value is dominated by the distribution of the individual τ values. The uncertainty of the recoil velocity and the uncertainty of the relative target-to-degrader distances have dominant contributions to the systematic errors of the lifetime. The final experimental error of the lifetime results from the root sum squared of the statistical and the systematic uncertainties.

In addition, the lifetimes determined according to DDCM were verified with the GEANT4-based Monte Carlo tool. Figure 7 shows a comparison between the experimental and simulated γ-ray spectra for ^{52}Ti at three different distances.

The lifetime $\tau(2_1^+) = 1.3(5)$ ps of the 2_1^+ state in ^{54}Ti determined in this work corresponds to a reduced transition probability of $B(E2; 2_1^+ \rightarrow 0_{gs}^+) = 84^{+53}_{-23}\, e^2\text{fm}^4$ and agrees with the adopted lifetime $\tau(2_1^+) = 1.53(27)$ ps with corresponding $B(E2; 2_1^+ \rightarrow 0_{gs}^+) = 72^{+15}_{-11}\, e^2\text{fm}^4$ [9] within their error limits.

In ^{52}Ti there is a considerable discrepancy between the new $B(E2; J_1^+ \rightarrow (J-2)_1^+)$ values in this work for 2_1^+, 4_1^+, 6_1^+ yrast states and the previously measured $B(E2)$ values [37,38] (see Fig. 13). The lifetime values of the 2_1^+ and 4_1^+ states from Ref. [37] and this measurement differ by a factor of approximately 2.

IV. DISCUSSION

A. Systematics

The results of this work yield new insights into the shell evolution for neutron-rich Ti, Cr, and Fe isotopes. Figure 10 illustrates the systematics of excitation energies and the evolution of $B(E2; 2_1^+ \rightarrow 0_{gs}^+)$ values for even-even nuclei with $20 \leqslant Z \leqslant 28$ and $26 \leqslant N \leqslant 34$. The $B(E2; 2_1^+ \rightarrow 0_{gs}^+)$ value in ^{52}Ti has been obtained in the present work, that for ^{54}Ti is taken from Ref. [9] (being consistent with the present result but subject to a smaller uncertainty), and the remaining values are adopted ones [40]. At the neutron shell closure $N = 28$, all depicted isotopes are characterized by high excitation energies of the first 2_1^+ state and relatively small $B(E2; 2_1^+ \rightarrow 0_{gs}^+)$ values (see Fig. 10). At $N = 30$ all isotones show a reduction of the 2_1^+ energies, but the $B(E2; 2_1^+ \rightarrow 0_{gs}^+)$ values exhibit a

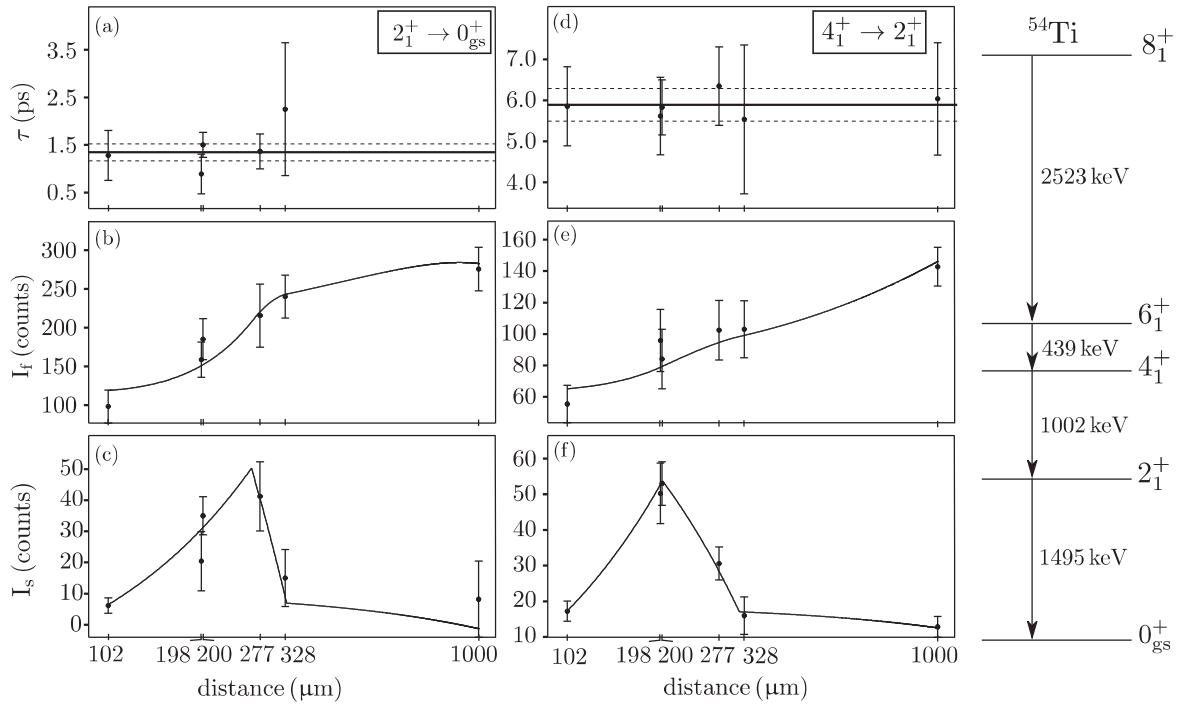

FIG. 8. Lifetime curves (a), (d) for the 2_1^+ (left) and 4_1^+ (middle) states in ^{54}Ti. Black solid lines in (a), (d) represent the weighted mean value of the lifetime; dashed lines mark the statistical uncertainty. In addition, the intensities of the fast (b), (e) and slow (c), (f) components are shown, where the latter are corrected for delayed observed feeding. The polynomial fit function to the intensities is presented in solid black in (b), (e) and (c), (f). Note the logarithmic distance scale. Right: Partial level scheme with the relevant γ-ray transitions in the yrast band in ^{54}Ti.

clear increase with the only exception case of ^{50}Ca. The newly measured value for ^{52}Ti indicates only a shallow increase compared to the neighboring values and fits nicely into the isotonic evolution.

Increasing the neutron number by two and four, the behavior of the 2_1^+ energies of Ca isotopes at $N = 32, 34$ is attributed to the local $\nu 2p_{3/2}$ and $\nu 2p_{1/2}$ subshell closures as discussed in Refs. [14,20]. Figure 11 shows the relevant

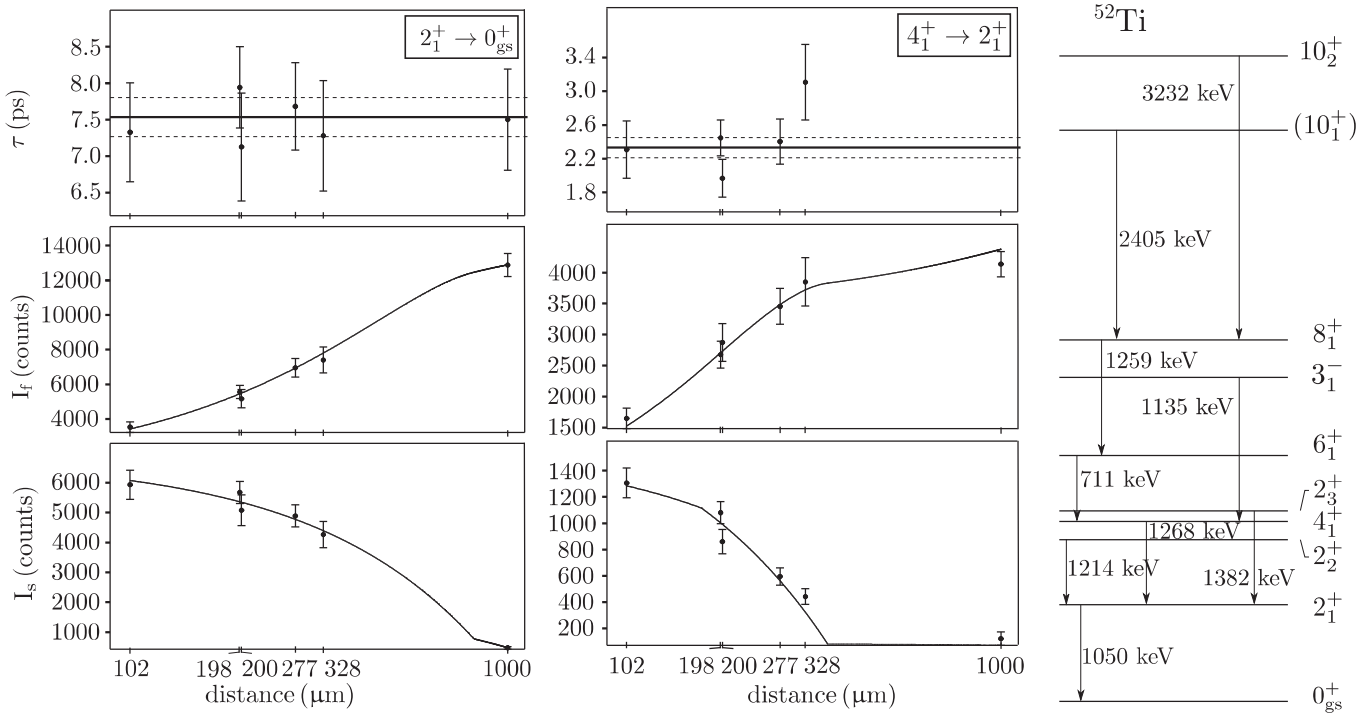

FIG. 9. Same as Fig. 8 for ^{52}Ti.

TABLE II. Lifetime values for the first four yrast states in ^{52,54}Ti obtained in the present experiment compared to previous experimental values taken from Refs. [9,37,38]. The corresponding experimental $B(E2; J_1^+ \rightarrow (J-2)_1^+)$ values are presented as well.

Nucleus	^{52}Ti				^{54}Ti			
	Lifetime (ps)		$B(E2)$ (e^2fm^4)		Lifetime (ps)		$B(E2)$ (e^2fm^4)	
I_1^+	This work	Previous	This work	Previous	This work	Previous	This work	Previous
2_1^+	7.5(4)	5.19(20) [37]	86^{+5}_{-4}	124^{+5}_{-5} [37]	1.3(5)	1.53(27) [9]	84^{+53}_{-23}	72^{+15}_{-11} [9]
4_1^+	2.3(3)	4.76(58) [37]	109^{+16}_{-13}	53^{+7}_{-6} [37]	5.9(9)	–	139^{+25}_{-18}	–
6_1^+	45.0(31)	36.7(63) [38]	100^{+7}_{-6}	123^{+25}_{-18} [38]	$\geqslant$380	–	$\leqslant$132	–
8_1^+	29.4(21)	–	8.8^{+1}_{-1}	–	$\leqslant$1.4	–	$\geqslant$5.7	–

neutron orbitals above $N = 28$ are $\nu 2p_{3/2}$, $\nu 1f_{5/2}$, and $\nu 2p_{1/2}$. In most of the known nuclei close to stability, the $\nu 1f_{5/2}$ orbital is energetically close to $\nu 2p_{3/2}$. Therefore, no $N = 32$ shell closure is observed as shown on the left of Fig. 11 [9,42]. As the number of protons in the $\pi 1f_{7/2}$ orbital are decreased, i.e., from nickel to calcium, the $\nu 1f_{5/2}$ orbital becomes less bound, and at $^{52}_{20}$Ca$_{32}$ the order of the $\nu 1f_{5/2}$ and $\nu 2p_{1/2}$ orbitals becomes inverted [14,20]. The raising of the $\nu 1f_{5/2}$ orbital produces a gap between the lower-lying $\nu 2p_{3/2}$ and the higher-lying $\nu 1f_{5/2}$ and $\nu 2p_{1/2}$ orbitals. This leads to the local $N = 32$ subshell closure (see right side of Fig. 11) and the higher 2_1^+ energy in ^{52}Ca [14,16]. Thus, the phase transition from predominantly collective structures in ^{60}Ni to a neutron subshell closure at ^{52}Ca can be attributed to the weakening of the attractive proton-neutron interaction between the $\pi 1f_{7/2}$ and $\nu 1f_{5/2}$ orbitals with decreasing number of protons in the $\pi 1f_{7/2}$ orbital [14,20].

Figure 10 shows that in the case of the Ti isotopes, a similar peaking of 2_1^+ energy is observed at $N = 32$ as for the Ca isotopes, although with a reduced amplitude, while for Cr this effect is much weaker and for Fe and Ni completely disappears. This speaks for the existence of a reduced $N = 32$ subshell closure in the Ti isotopes, which has recently been confirmed in mass measurements [42]. The systematics of $B(E2; 2_1^+ \rightarrow 0_{gs}^+)$ values in Ti isotopes obtained in earlier experiments showed a staggering anticorrelated with the subshell closures at $N = 28$ and $N = 32$. The revised $B(E2; 2_1^+ \rightarrow 0_{gs}^+)$ value in ^{52}Ti reduces the amplitude of this staggering. The underlying nuclear structure of the lowest yrast states and $E2$ strengths can be addressed in the framework of the nuclear shell model.

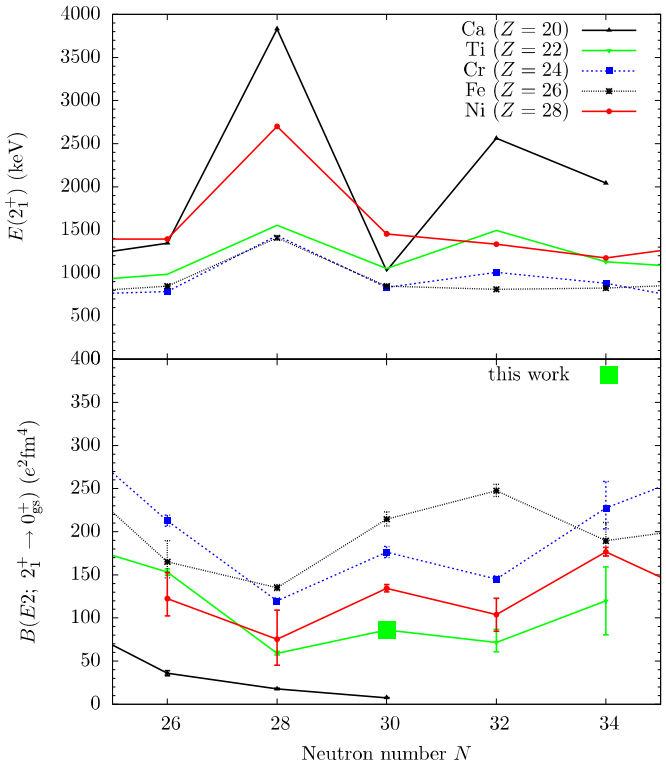

FIG. 10. Systematics of excitation energies for the 2_1^+ state (top) and the evolution of the $B(E2; 2_1^+ \rightarrow 0_{gs}^+)$ (bottom) values in even-even nuclei with $20 \leqslant Z \leqslant 28$ and $26 \leqslant N \leqslant 34$ including the result for ^{52}Ti obtained in the present work. For ^{54}Ti the result from Ref. [9] is shown due to its smaller uncertainty.

B. Comparison with shell-model calculations

In the present work, shell-model calculations were performed with the code NUSHELLX@MSU [43] using three interactions, namely, KB3G [44], GXPF1A [45], and GXPF1B [46]. The model space comprises the full pf main shell, coupled to a $^{40}_{20}$Ca core. Effective charges $e_\pi = 1.31\,e$ and $e_\nu = 0.46\,e$ were used for protons and neutrons, respectively, for all interactions [47]. The choice of the neutron effective

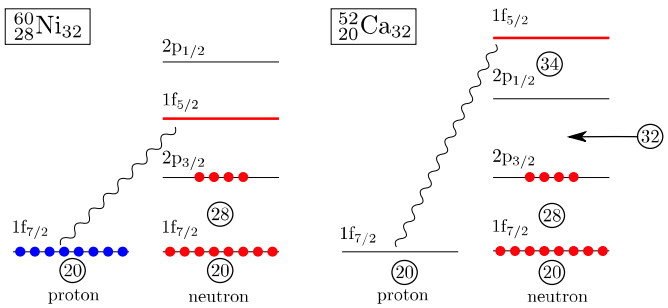

FIG. 11. Schematic illustration of shell evolution from Ni to Ca for neutron orbits. The wavy line represents the interaction between the proton in the $1f_{7/2}$ orbit and the neutron in the $1f_{5/2}$ orbit. See text for more details. Adopted from Ref. [41].

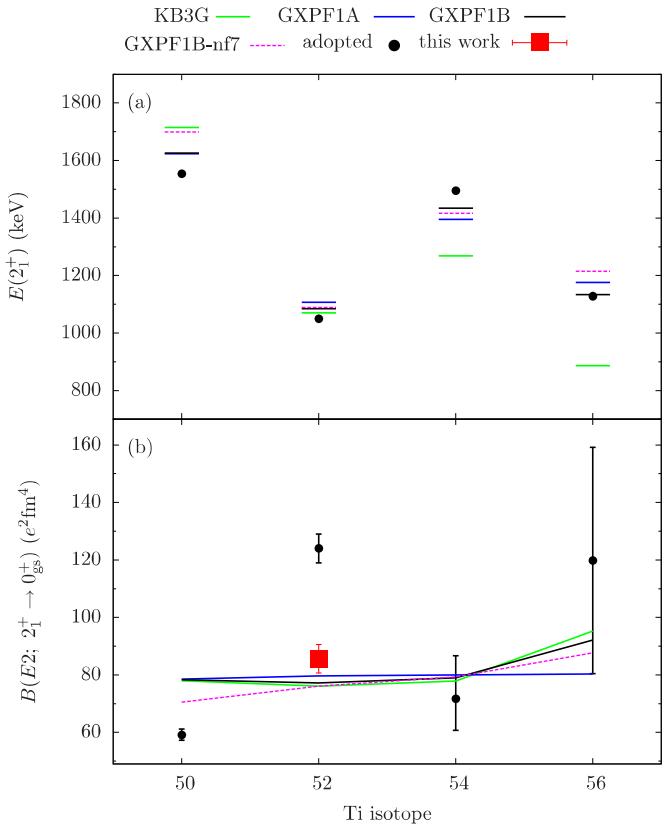

FIG. 12. Comparison of experimental 2_1^+ excitation energies (a) and $B(E2; 2_1^+ \rightarrow 0_{gs}^+)$ transition strengths (b) with the results of shell-model calculations using the KB3G, GXPF1A, GXPF1B, and GXPF1B-nf7 interactions for $^{50-56}$Ti.

charge is justified for the neighboring isotopes with $N > 28$ [48], while the microscopically justified proton effective charge [47] has an intermediate value between the standard isoscalar $e_\pi = 1.5\,e$ value and the value of $e_\pi = 1.15\,e$, which is suggested to be more adequate for the $\pi 1f_{7/2}$ orbital and especially for the $N = Z$ region [49].

Figure 12 shows a comparison of experimental and shell-model systematics of the 2_1^+ energies and the $B(E2; 2_1^+ \rightarrow 0_{gs}^+)$ values for $^{50-56}$Ti. The excitation energies are listed in Table III. All used interactions describe the experimental excitation energies reasonably well.

As seen in Fig. 12 the previously adopted values displayed a staggering in the $B(E2; 2_1^+ \rightarrow 0_{gs}^+)$ values, which has been a topic of several works. Although the established interactions were able to describe the excitations energies in these Ti isotopes and the structure of the neighboring nuclei, they were generally unable to exactly reproduce the staggering in the experimental $B(E2; 2_1^+ \rightarrow 0_{gs}^+)$ values in neutron-rich Ti isotopes using isoscalar proton and neutron effective charges [9,48,50]. As can be seen from Fig. 12, the new $B(E2; 2_1^+ \rightarrow 0_{gs}^+)$ systematics for $^{50-54}$Ti exhibits a clearly weaker staggering with a rather flat behavior around $N = 30$ and similar values. A splitting in the $B(E2; 2_1^+ \rightarrow 0_{gs}^+)$ trends becomes apparent for ^{56}Ti, where the values obtained using GXPF1A and GXPF1B interactions differ clearly from each other, with the latter one showing an increased value closer to the experimental result. Since the GXPF1B interaction was optimized to describe the local subshell closure at $N = 34$ in ^{54}Ca [46], it is not surprising that it also reproduces the isotone ^{56}Ti better than GXPF1A. The KB3G interaction yields a similar good description for $^{52-56}$Ti. Regarding ^{50}Ti ($N = 28$), there is clear overprediction of the $B(E2; 2_1^+ \rightarrow 0_{gs}^+)$ values by all shell-model interactions. One possible explanation is that proton particle-hole excitations across the $Z = 20$ ^{40}Ca core are present in the 0_{gs}^+ state and, to a lesser extent, in the 2_1^+ state, which are not accounted for in this model space, leading to an overprediction of the $E2$ strength. Another explanation is given by the inspection of the wave function of the 0_{gs}^+ and 2_1^+ states in ^{50}Ti in the GXPF1A (GXPF1B) calculations, which each predict about 30% (for the 0_{gs}) and 38% (for the 2_1^+) configurations with neutron particle-hole excitations across the $N = 28$ shell, which increase the specific $B(E2; 2_1^+ \rightarrow 0_{gs}^+)$ strength. Therefore, to reduce the $E2$ strength from neutron $N = 28$ cross-shell excitations, an ad hoc modification of the GXPF1B interaction was introduced, called GXPF1B-nf7, where the single-particle energy of the $\nu 1f_{7/2}$ orbital was lowered by 1 MeV. The results for GXPF1B-nf7 are presented in Figs. 12, 13, and Table III) and compared to the experimental values and those calculated using other interactions. This interaction has only a qualitative value, but may be relevant for $^{50-52}$Ti and generally provides the best results for the $^{50-56}$Ti $B(E2; 2_1^+ \rightarrow 0_{gs}^+)$ systematics. The transition

TABLE III. Experimental excitation energies for the 2_1^+, 4_1^+, and 6_1^+ states in ^{50,52,54,56}Ti compared to those resulting from shell-model calculations using GXPF1A, GXPF1B, GXPF1B-nf7, and KB3G interactions. For a better comparison the root-mean-square deviation (*RMSD*) for each interaction is provided.

	Excitation energy E (keV)												
	^{50}Ti			^{52}Ti			^{54}Ti			^{56}Ti			
	2_1^+	4_1^+	6_1^+	2_1^+	4_1^+	6_1^+	2_1^+	4_1^+	6_1^+	2_1^+	4_1^+	6_1^+	*RMSD*
Experiment	1553	2675	3199	1050	2318	3029	1495	2496	2936	1128	2288	2978	–
GXPF1A	1624	2562	3237	1106	2251	2932	1395	2465	2975	1176	2278	2868	72.6
GXPF1B	1626	2568	3234	1084	2239	2922	1434	2476	2974	1134	2296	2873	66.8
GXPF1B-nf7	1699	2572	3153	1089	2229	2899	1416	2468	2965	1215	2312	2900	82.9
KB3G	1715	2841	3383	1069	2356	3048	1285	2452	3048	886	1995	2873	159.1

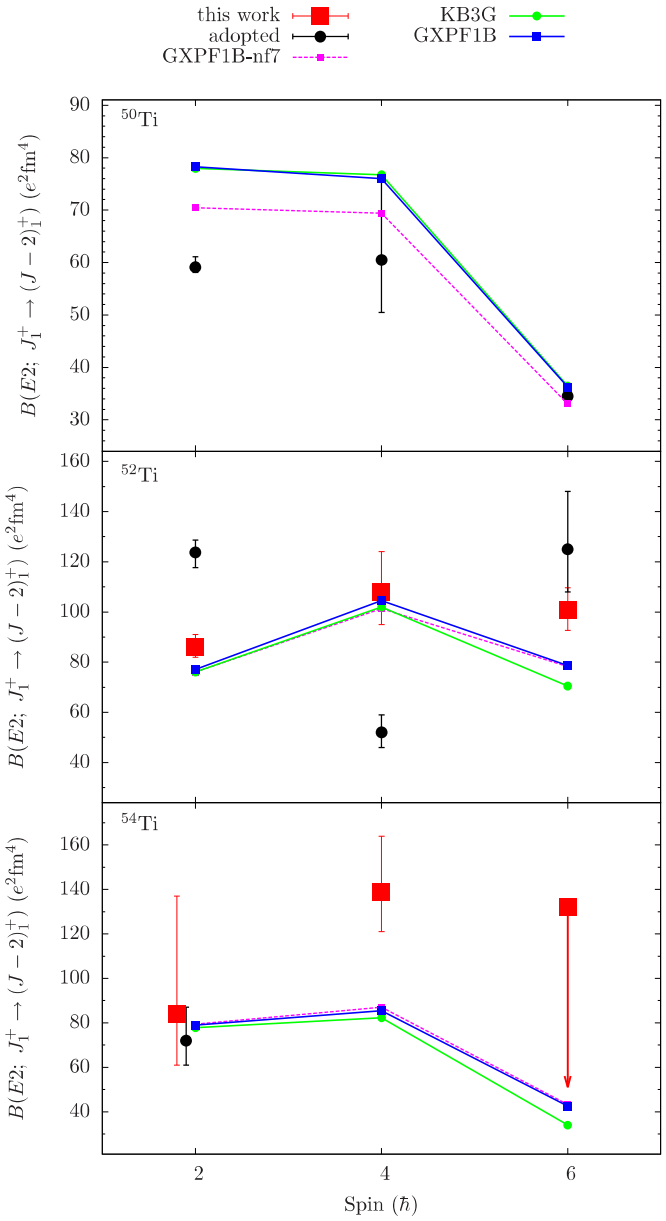

FIG. 13. Comparison of experimental $B(E2; J_1^+ \to (J-2)_1^+)$ values in ^{50,52,54}Ti with the results of the shell-model calculations with different effective interactions. See text for details.

strengths in the calculations are computed as $B(E2; J_1^+ \to (J-2)_1^+) = (A_p e_\pi + A_n e_\nu)^2/(2J_1+1)$ [51]. Here, A_p and A_n (in units of fm^2) are the proton and neutron amplitudes and are summarized in Table IV for the $2_1^+ \to 0_{gs}$ transitions in $^{50-56}$Ti for four different interactions. Small A_n are characteristic of shell gaps at $N = 28$ and $N = 32$, as discussed in Ref. [9].

In conclusion, the general flat trends in the $B(E2; 2_1^+ \to 0_{gs}^+)$ values of the shell model can be understood as resulting from a fine balance of proton and neutron amplitudes. Specifically, the variation in the $B(E2; 2_1^+ \to 0_{gs}^+)$ values due to A_n is nearly canceled by that due to A_p, leading to constant $B(E2; 2_1^+ \to 0_{gs}^+)$ values calculated using these effective charges. Thus, regarding the systematics of the lowest transition strengths, a consistent picture between experimental and theoretical results emerges.

TABLE IV. Proton and neutron amplitudes for the $2_1^+ \to 0_{gs}^+$ of four different interactions for even-even $^{50-56}$Ti. See text for more details.

	^{50}Ti		^{52}Ti		^{54}Ti		^{56}Ti	
$2_1^+ \to 0_{gs}^+$	A_p	A_n	A_p	A_n	A_p	A_n	A_p	A_n
GXPF1A	11.59	10.06	9.96	15.17	11.54	10.62	11.02	12.21
GXPF1B	11.58	10.01	9.66	15.19	11.72	9.81	11.31	14.43
GXPF1B-nf7	11.83	7.12	9.84	14.36	11.76	9.82	11.72	12.16
KB3G	11.87	9.21	9.37	15.70	10.76	12.24	10.30	18.09

In the following, the properties of the higher-spin states in the even $^{50-54}$Ti are discussed. As the trends between GXPF1A and GXPF1B for these isotopes are similar, only the results using the GXPF1B interaction are discussed below. Figure 13 shows a comparison between the experimental results and the shell-model calculations for the $B(E2; J_1^+ \to (J-2)_1^+)$ values.

For ^{50}Ti, the experimental $B(E2; 2_1^+ \to 0_{gs}^+)$ value from Ref. [52] is slightly lower than that estimated by the present calculations, independent of the interaction. As already mentioned above, this could be attributed to either the proton particle-hole excitations across the $Z = 20$ ^{40}Ca core present in the 0_{gs}^+ state, which are not accounted for in this model space, or, as discussed above, the $B(E2)$ value could be overestimated due to the degree of neutron particle-hole excitation across $N = 28$ as qualitatively demonstrated by the calculation using the GXPF1B-nf7 interaction. The adopted $B(E2; 4_1^+ \to 2_1^+)$ and $B(E2; 6_1^+ \to 4_1^+)$ values agree well (within 2σ) with the theoretical predictions for all interactions. The shell-model calculations predict that the 2_1^+, 4_1^+, 6_1^+ states in ^{50}Ti have a proton character dominated in $\geqslant$70% by configurations of the type $\pi_{J^+} \otimes \nu_{0^+}$.

For the neighboring nucleus ^{52}Ti, the predictions generally agree well with the new $B(E2)$ values (see Fig. 13). Only the $B(E2; 2_1^+ \to 0_{gs}^+)$ and $B(E2; 6_1^+ \to 4_1^+)$ values are slightly overestimated or underestimated. In contrast to ^{50}Ti, the wave function of the 2_1^+ state has a dominant neutron character with $\approx$50% $\pi_{0^+} \otimes \nu_{2^+}$ and $\approx$30% $\pi_{2^+} \otimes \nu_{0^+}$ configuration. The two neutrons above $N = 28$ occupy predominantly the $2p_{3/2}$ orbital in which they can couple to a maximum angular momentum of $2\hbar$. Therefore, the higher-spin 4_1^+, 6_1^+ yrast states cannot be of pure neutron character. For the 4_1^+ state, mixed proton-neutron configurations $\approx$30% $\pi_{2^+} \otimes \nu_{2^+}$ and $\approx$40 % $\pi_{4^+} \otimes \nu_{0^+}$ prevail for KB3G and GXPF1B. The wave functions of the three interactions are similar for the case of the 6_1^+ state. The configuration $\pi_{6^+} \otimes \nu_{0^+}$ has the largest contribution to the wave function ($\leqslant$50%), followed by the mixed configurations of type $\pi_{4^+} \otimes \nu_{2^+}$ and $\pi_{6^+} \otimes \nu_{2^+}$ ($\leqslant$12%). We note the very good agreement between the new experimental $B(E2)$ values from the present work and the theory both having the opposite trend as a function of spin to the adopted data from Refs. [37,38]. The new results are free of the longstanding contradiction between the shell model and

adopted $B(E2; 2_1^+ \rightarrow 0_{gs}^+)$ in ^{52}Ti, thus putting in doubt the previous experimental results.

For ^{54}Ti, i.e., four neutrons above $N = 28$, all interactions reproduce fairly accurately the $B(E2; 2_1^+ \rightarrow 0_{gs}^+)$ value from Ref. [9] and yield very similar $B(E2; 4_1^+ \rightarrow 2_1^+)$ values. However, the predicted values are clearly lower than $B(E2; 4_1^+ \rightarrow 2_1^+) = 139^{+25}_{-18}\, e^2\text{fm}^4$ determined in the present work. For the $6_1^+ \rightarrow 4_1^+$ transition, the calculations yield $B(E2)$ values half the size of those for the $4_1^+ \rightarrow 2_1^+$ and $2_1^+ \rightarrow 0_{gs}^+$ transitions. From our data, we have an upper limit of $B(E2; 6_1^+ \rightarrow 4_1^+) \leqslant 132\, e^2\text{fm}^4$, which agrees with the calculations. In addition, the experimental lower limit of $B(E2; 8_1^+ \rightarrow 6_1^+) \geqslant 5.7\, e^2\text{fm}^4$ agrees with $7.0\, e^2\text{fm}^4$ calculated using the GXPF1B interaction. The wave functions calculated using the KB3G and GXPF1B interactions show a distinct proton occupation as found in the case of ^{50}Ti. For the 2_1^+ state, the proton occupation yields $\approx$50% $\pi_{2^+} \otimes \nu_{0^+}$ corresponding to a subshell closure of $\nu 2p_{3/2}$. This confirms that the $p_{3/2}$ and $f_{5/2}$ orbitals are not close to each other. Also the other higher-lying states $J = 4_1^+$, 6_1^+ show a clear proton character ($\approx$60% $\pi_{4^+} \otimes \nu_{0^+}$ and $\geqslant$70% $\pi_{6^+} \otimes \nu_{0^+}$ for both KB3G and GXPF1B interactions). The trend in the predicted $B(E2; J_1^+ \rightarrow (J-2)_1^+)$ values resembles with that for ^{50}Ti, which is another signature of the $N = 32$ subshell closure.

V. SUMMARY

The structure of the neutron-rich nuclei ^{52,54}Ti produced via multinucleon-transfer reactions in inverse kinematics was investigated. The lifetime of the 2_1^+ state in ^{54}Ti was remeasured. The transition probability obtained from the measured lifetime of the 2_1^+ state is in agreement with that from an earlier Coulomb-excitation work [9]. The lifetime of the 4_1^+ state in ^{54}Ti, a lower limit for the 6_1^+ state, and an upper limit for the 8_1^+ state were determined for the first time.

The comparison with shell-model calculations shows the following outcome: In ^{54}Ti the trend of the $B(E2; J_1^+ \rightarrow (J-2)^+)$ values agrees well with the results of shell-model calculations using various interactions, only the experimental result of the $B(E2; 4_1^+ \rightarrow 2_1^+)$ value is underestimated.

In ^{52}Ti, the lifetimes of the 2_1^+, 4_1^+, and 6_1^+ states were remeasured with a surprising result. The transition probabilities obtained from the lifetimes determined in this work show an opposite trend with spin to the literature $B(E2; J_1^+ \rightarrow (J-2)_1^+)$ values [37,38]. The $B(E2; 2_1^+ \rightarrow 0_{gs}^+)$ value obtained in the present work is smaller than the adopted value. A similar behavior was noted for the $6_1^+ \rightarrow 4_1^+$ transition strength. While, the new $B(E2; 4_1^+ \rightarrow 2_1^+)$ value is larger than the adopted value. In contrast to the previously adopted results for ^{52}Ti, the new results on $B(E2; J_1^+ \rightarrow (J-2)_1^+)$ values are well reproduced within the shell model. Compared to those for the neighboring isotopes, the new $B(E2; 2_1^+ \rightarrow 0_{gs}^+)$ results reduce the amplitude of the staggering along the titanium isotopic chain $^{50-54}$Ti. The experimental and theoretical results confirm a subshell closure at $N = 32$ in ^{54}Ti that is somewhat weaker compared to that at $N = 28$.

ACKNOWLEDGMENTS

We thank the GANIL team for the professional support during the experiment. The research leading to these results has received funding from the German BMBF under Contract No. 05P18PKFN9 and partially supported by Generalitat Valenciana, Conselleria d'Educació, Investigació, Cultura i Esport under the grant PROMETEU/2019/005 and Ministerio de Ciencia, Innovación y Universidades Spain, under grants SEV-2014-0398 and FPA2017-84756-C4 and by the European Commission FEDER funds.

[1] B. A. Brown, Prog. Part. Nucl. Phys. **47**, 517 (2001).
[2] T. Braunroth, A. Dewald, H. Iwasaki, S. M. Lenzi, M. Albers, V. M. Bader, T. Baugher, T. Baumann, D. Bazin, J. S. Berryman *et al.*, Phys. Rev. C **92**, 034306 (2015).
[3] A. Gade, R. V. F. Janssens, T. Baugher, D. Bazin, B. A. Brown, M. P. Carpenter, C. J. Chiara, A. N. Deacon, S. J. Freeman, G. F. Grinyer *et al.*, Phys. Rev. C **81**, 051304(R) (2010).
[4] S. M. Lenzi, F. Nowacki, A. Poves, and K. Sieja, Phys. Rev. C **82**, 054301 (2010).
[5] C. Santamaria, C. Louchart, A. Obertelli, V. Werner, P. Doornenbal, F. Nowacki, G. Authelet, H. Baba, D. Calvet, F. Château *et al.*, Phys. Rev. Lett. **115**, 192501 (2015).
[6] W. Rother, A. Dewald, H. Iwasaki, S. M. Lenzi, K. Starosta, D. Bazin, T. Baugher, B. A. Brown, H. L. Crawford, C. Fransen *et al.*, Phys. Rev. Lett. **106**, 022502 (2011).
[7] J. Ljungvall, A. Gorgen, A. Obertelli, W. Korten, E. Clement, G. deFrance, A. Burger, J. P. Delaroche, A. Dewald, A. Gadea, L. Gaudefroy, M. Girod, M. Hackstein, J. Libert, D. Mengoni, F. Nowacki, T. Pissulla, A. Poves, F. Recchia, M. Rejmund, W. Rother, E. Sahin, C. Schmitt, A. Shrivastava, K. Sieja, J. J. Valiente-Dobon, K. O. Zell, and M. Zielinska, Phys. Rev. C **81**, 061301(R) (2010).
[8] H. L. Crawford, R. M. Clark, P. Fallon, A. O. Macchiavelli, T. Baugher, D. Bazin, C. W. Beausang, J. S. Berryman, D. L. Bleuel, C. M. Campbell *et al.*, Phys. Rev. Lett. **110**, 242701 (2013).
[9] D. C. Dinca, R. V. F. Janssens, A. Gade, D. Bazin, R. Broda, B. A. Brown, C. M. Campbell, M. P. Carpenter, P. Chowdhury, J. M. Cook, A. N. Deacon, B. Fornal, S. J. Freeman, T. Glasmacher, M. Honma, F. G. Kondev, J. L. Lecouey, S. N. Liddick, P. F. Mantica, W. F. Mueller, H. Olliver, T. Otsuka, J. R. Terry, B. A. Tomlin, and K. Yoneda, Phys. Rev. C **71**, 041302(R) (2005).
[10] H. Hübel, A. Bürger, T. R. Saito, H. Grawe, P. Reiter, J. Gerl, M. Górska, H. J. Wollersheim, A. Al-Khatib, A. Banu *et al.*, Acta Physica Hungarica A) Heavy Ion Physics **25**, 197 (2006).
[11] M. Seidlitz, P. Reiter, A. Dewald, O. Möller, B. Bruyneel, S. Christen, F. Finke, C. Fransen, M. Górska, H. Grawe *et al.*, Phys. Rev. C **84**, 034318 (2011).

[12] M. J. LeVine, E. K. Warburton, and D. Schwalm, Phys. Rev. C **23**, 244 (1981).
[13] O. Kenn, K.-H. Speidel, R. Ernst, J. Gerber, P. Maier-Komor, and F. Nowacki, Phys. Rev. C **63**, 064306 (2001).
[14] D. Steppenbeck, S. Takeuchi, N. Aoi, P. Doornenbal, M. Matsushita, H. Wang, H. Baba, N. Fukuda, S. Go, M. Honma *et al.*, Nature (London) **502**, 207 (2013).
[15] J. I. Prisciandaro, P. F. Mantica, B. A. Brown, D. W. Anthony, M. W. Cooper, A. Garcia, D. E. Groh, A. Komives, W. Kumarasiri, P. A. Lofy *et al.*, Phys. Lett. B **510**, 17 (2001).
[16] A. Huck, G. Klotz, A. Knipper, C. Miehé, C. Richard-Serre, G. Walter, A. Poves, H. L. Ravn, and G. Marguier, Phys. Rev. C **31**, 2226 (1985).
[17] R. V. F. Janssens, B. Fornal, P. F. Mantica, B. A. Brown, R. Broda, P. Bhattacharyya, M. P. Carpenter, M. Cinausero, P. J. Daly, A. D. Davies *et al.*, Phys. Lett. B **546**, 55 (2002).
[18] B. Fornal, S. Zhu, R. V. F. Janssens, M. Honma, R. Broda, P. F. Mantica, B. A. Brown, M. P. Carpenter, P. J. Daly, S. J. Freeman *et al.*, Phys. Rev. C **70**, 064304 (2004).
[19] S. N. Liddick, P. F. Mantica, R. Broda, B. A. Brown, M. P. Carpenter, A. D. Davies, B. Fornal, T. Glasmacher, D. E. Groh, M. Honma *et al.*, Phys. Rev. C **70**, 064303 (2004).
[20] T. Otsuka, T. Suzuki, R. Fujimoto, H. Grawe, and Y. Akaishi, Phys. Rev. Lett. **95**, 232502 (2005).
[21] T. Otsuka, R. Fujimoto, Y. Utsuno, B. A. Brown, M. Honma, and T. Mizusaki, Phys. Rev. Lett. **87**, 082502 (2001).
[22] T. Otsuka, T. Suzuki, M. Honma, Y. Utsuno, N. Tsunoda, K. Tsukiyama, and M. Hjorth-Jensen, Phys. Rev. Lett. **104**, 012501 (2010).
[23] A. Dewald, O. Möller, and P. Petkov, Prog. Part. Nucl. Phys. **67**, 786 (2012).
[24] S. Pullanhiotan, M. Rejmund, A. Navin, W. Mittig, and S. Bhattacharyya, Nucl. Instrum. Methods Phys. Res., Sect. A **593**, 343 (2008).
[25] M. Rejmund, B. Lecornu, A. Navin, C. Schmitt, S. Damoy, O. Delaune, J. M. Enguerrand, G. Fremont, P. Gangnant, L. Gaudefroy *et al.*, Nucl. Instrum. Methods Phys. Res., Sect. A **646**, 184 (2011).
[26] M. Vandebrouck, A. Lemasson, M. Rejmund, G. Fremont, J. Pancin, A. Navin, C. Michelagnoli, J. Goupil, C. Spitaels, and B. Jacquot, Nucl. Instrum. Methods Phys. Res. A **812**, 112 (2016).
[27] Y. H. Kim, A. Lemasson, M. Rejmund, A. Navin, S. Biswas, C. Michelagnoli, I. Stefan, R. Banik, P. Bednarczyk, S. Bhattacharya *et al.*, Eur. Phys. J. A **53**, 162 (2017).
[28] S. Akkoyun, A. Algora, B. Alikhani, F. Ameil, G. de Angelis, L. Arnold, A. Astier, A. Ataç, Y. Aubert, C. Aufranc *et al.*, Nucl. Instrum. Methods Phys. Res. A **668**, 26 (2012).
[29] E. Clément, C. Michelagnoli, G. de France, H. Li, A. Lemasson, C. B. Dejean, M. Beuzard, P. Bougault, J. Cacitti, J.-L. Foucher *et al.*, Nucl. Instrum. Methods Phys. Res. A **855**, 1 (2017).
[30] R. Venturelli and D. Bazzacco, LNL Annual Report 2004 (2005), p. 220.
[31] A. Lopez-Martens, K. Hauschild, A. Korichi, J. Roccaz, and J.-P. Thibaud, Nucl. Instrum. Methods Phys. Res. A **533**, 454 (2004).
[32] Z. G. Wang, C. Dufour, E. Paumier, and M. Toulemonde, J. Phys.: Condens. Matter **6**, 6733 (1994).
[33] M. Toulemonde, E. Paumier, and C. Dufour, Radiat. Eff. Defects Solids **126**, 201 (1993).
[34] A. Goldkuhle, C. Fransen, A. Dewald, K. Arnswald, M. Bast, M. Beckers, A. Blazhev, T. Braunroth, G. Hackenberg, G. Häfner *et al.*, Eur. Phys. J. A **55**, 53 (2019).
[35] T. Braunroth (private communication).
[36] A. Dewald, S. Harissopulos, and P. von Brentano, Z. Phys. A Atomic Nuclei **334**, 163 (1989).
[37] K.-H. Speidel, J. Leske, S. Schielke, S. C. Bedi, O. Zell, P. Maier-Komor, S. J. Q. Robinson, Y. Y. Sharon, and L. Zamick, Phys. Lett. B **633**, 219 (2006).
[38] B. A. Brown, D. B. Fossan, A. R. Poletti, and E. K. Warburton, Phys. Rev. C **14**, 1016 (1976).
[39] B. Saha, Computer code NAPATAU, 2002.
[40] ENSDF database, 2019.
[41] T. Otsuka and Y. Tsunoda, J. Phys. G: Nucl. Part. Phys. **43**, 024009 (2016).
[42] E. Leistenschneider, M. P. Reiter, S. Ayet San Andrés, B. Kootte, J. D. Holt, P. Navrátil, C. Babcock, C. Barbieri, B. R. Barquest, J. Bergmann *et al.*, Phys. Rev. Lett. **120**, 062503 (2018).
[43] B. Brown and W. Rae, Nucl. Data Sheets **120**, 115 (2014).
[44] A. Poves, J. Sánchez-Solano, E. Caurier, and F. Nowacki, Nucl. Phys. A **694**, 157 (2001).
[45] M. Honma, T. Otsuka, B. A. Brown, and T. Mizusaki, Eur. Phys. J. A - Hadrons and Nuclei **25**, 499 (2005).
[46] M. Honma, T. Otsuka, and T. Mizusaki, RIKEN Accel. Prog. Rep. **41**, 32 (2008).
[47] M. Dufour and A. P. Zuker, Phys. Rev. C **54**, 1641 (1996).
[48] J. J. Valiente-Dobón, D. Mengoni, A. Gadea, E. Farnea, S. M. Lenzi, S. Lunardi, A. Dewald, T. Pissulla, S. Szilner, R. Broda *et al.*, Phys. Rev. Lett. **102**, 242502 (2009).
[49] R. du Rietz, J. Ekman, D. Rudolph, C. Fahlander, A. Dewald, O. Möller, B. Saha, M. Axiotis, M. A. Bentley, C. Chandler *et al.*, Phys. Rev. Lett. **93**, 222501 (2004).
[50] A. Poves, F. Nowacki, and E. Caurier, Phys. Rev. C **72**, 047302 (2005).
[51] B. Brown, A. Arima, and J. McGrory, Nucl. Phys. A **277**, 77 (1977).
[52] S. Raman, C. Nestor, and P. Tikkanen, At. Data Nucl. Data Tables **78**, 1 (2001).

Publication III:
Preliminary results of lifetime measurements in neutron-rich ^{53}Ti

Preliminary results of lifetime measurements in neutron-rich ^{53}Ti

Alina Goldkuhle[1*], *Christoph* Fransen[1], *Alfred* Dewald[1], *Navin* Alahari[2], *Marcel* Beckers[1], *Benedikt* Birkenbach[1], *Andrey* Blazhev[1], *Thomas* Braunroth[1], *Emmanuel* Clément[2], *Gilles* De France[2], *Jérémie* Dudouet[3,4], *Jürgen* Eberth[1], *Herbert* Hess[1], *Bertrand* Jacquot[2], *Yung-Hee* Kim[5], *Antoine* Lemasson[2], *Silvia Monica* Lenzi[6,7], *Hongjie* Li[2], *Joa* Ljungvall[3], *Julia* Litzinger[1], *Caterine* Michelagnoli[2,6,7], *Claus* Müller-Gatermann[1], *Daniel Ricardo* Napoli[8], *Bondili Sreenivasa* Nara Singh[9], *Rosa Maria* Perez-Vidal[10], *Damian* Ralet[3,11,12], *Peter* Reiter[1], *Maurycy* Rejmund[2], *Andreas* Vogt[1], *Nigel* Warr[1], *Karl Oskar* Zell[1], *Magda* Zielińska[13], and the AGATA-Collaboration

[1]Institut für Kernphysik, Universität zu Köln, 50937 Köln, Germany
[2]GANIL, CEA/DRF-CNRS/IN2P3, BP 55027, 14076 Caen Cedex 5, France
[3]CSNSM, Université Paris-Sud, CNRS/IN2P3, Université Paris-Saclay, F-91405 Orsay, France
[4]Université de Lyon, Université de Lyon 1, CNRS/IN2P3, IPN-Lyon, F-69622 Villeurbanne, France
[5]Institut Laue-Langevin, BP 156, 38042 Grenoble Cedex 9, France
[6]INFN Sezione di Padova, I-35141 Padova, Italy
[7]Dipartimento di Fisica e Astronomia dell'Università di Padova, I-35131 Padova, Italy
[8]Laboratori Nazionali di Legnaro, INFN, I-35020 Legnaro, Italy
[9]Nuclear Physics Group, Schuster Laboratory, University of Manchester, Manchester, UK
[10]GSI, Helmholtzzentrum für Schwerionenforschung GmbH, 64291 Darmstadt, Germany
[11]Institut für Kernphysik, Technische Universität Darmstadt, 64289 Darmstadt, Germany
[12]Instituto de Física Corpuscular, CSIC-Universidad de Valencia, E-46071 Valencia, Spain
[13]Irfu, CEA, Université Paris-Saclay, F-91191 Gif-sur-Yvette, France

Abstract. To study the nuclear structure of neutron-rich titanium isotopes, a lifetime measurement was performed at the Grand Accélérateur National d'Ions Lourds (GANIL) facility in Caen, France. The nuclei were produced in a multinucleon-transfer reaction by using a 6.76 MeV/u ^{238}U beam. The Advanced Gamma Tracking Array (AGATA) was employed for the γ-ray detection and target-like recoils were identified event-by-event by the large-acceptance variable mode spectrometer (VAMOS++). Preliminary level lifetimes of the $(5/2^-)$ to $13/2^-$ states of the yrast band in the neutron-rich nucleus ^{53}Ti were measured for the first time employing the recoil distance Doppler-shift (RDDS) method and the compact plunger for deep inelastic reactions. The differential decay curve method (DDCM) was used to obtain the lifetimes from the RDDS data.

1 Introduction

The nuclear structure in the region of neutron-rich Ti isotopes is of enhanced interest due to the observed features hinting at subshell closures at $N = 32, 34$ [1]. For example, in neutron-rich $^{50-56}$Ti isotopes the staggering of the excitation energies for the 2_1^+ state points to emergence of subshells. In case of ^{53}Ti, the excited states were reported by prompt γ-ray spectroscopy following β decay [2]. The knowledge was extended by studies performed at the Gammasphere spectrometer [3] to identify the ^{53}Ti yrast cascade for the first time and to determine the excitation energy of states with spins up to $I^\pi = 21/2^-$. In addition, the experimental yrast structure was compared with shell-model calculations where the experimental data are particularly well described by calculations using the GXPF1 and GXPF1A interactions [3]. For the level energies this is directly related to the fact that the $\nu 1f_{5/2}$ and $\nu 1p_{1/2}$ orbitals are well separated from the $\nu 1p_{3/2}$ orbital, a fact that also gives rise to the subshell closure at $N = 32$. In contrast, calculations with the FPD6 Hamiltonian do not predict gaps at $N = 32, 34$. In order to verify the previous findings on shell closures, lifetimes of excited states are of great importance. From these, transition probabilities can be determined which represent important quantities to test the shell structure. In this work preliminary data of lifetimes for the $(5/2^-)$ to $13/2^-$ states of the yrast band of ^{53}Ti are presented for the first time.

2 Experimental Details

Excited states in neutron-rich titanium isotopes were populated as products of a multinucleon-transfer reaction induced by a ^{238}U beam at an energy of $E(^{238}\text{U}) = 1608.9\,\text{MeV}$ (= 6.76 MeV/u) at the Grand Accélérateur National of d'Ions Lourds (GANIL) in Caen, France. The experimental setup consisted of the compact plunger for lifetime measurements of excited states produced in deep inelastic reactions [4] in combination with the Advanced Gamma Tracking Array (AGATA) [5] γ-ray spectrometer consisting of 29 36-fold segmented capsules in 10

*e-mail: agoldkuhle@ikp.uni-koeln.de

cryostats. A 1.5 mg/cm^2 enriched ^{50}Ti plunger target was used, on which a natural copper fronting with a thickness of 0.4 mg/cm^2 for heat conduction was evaporated. A ^{nat}Mg degrader foil with a thickness of 3.2 mg/cm^2 was placed downstream from the target. Both the target and degrader foils were placed at an angle of 45° with respect to the incoming beam which is close to the grazing angle of the multinucleon transfer reaction. Since the expected lifetimes in the neutron-rich titanium isotopes are a few picoseconds, the recoil distance Doppler-shift (RDDS) method [6] was employed. The target-like reaction products were detected and identified in the large-acceptance variable mode spectrometer VAMOS++ [7–9]. These products exit the target foil with an average velocity v_T resulting $\beta_T = v_T/c = 12.7(2)\,\%$. The Mg foil degrades the energy of the ions to 3.68 MeV/u resulting in an average velocity of $\beta_D = 11.7(2)\,\%$ that was measured directly by VAMOS++. β_T was deduced from the experimental Doppler-shift between the two components of the transitions:

$$E_{\mathrm{sh}}(\Delta\beta,\theta) = E_{\mathrm{us}} \cdot \frac{\sqrt{1-\Delta\beta^2}}{1-\Delta\beta\cdot\cos(\theta)}, \qquad (1)$$

where E_{sh} is the energy of the fast component, i.e. the emission before the degrader, and E_{us} is the intrinsic γ-ray energy of the degraded component, i.e. the emission after the degrader, which depends on the velocity difference $\Delta\beta = \beta_T - \beta_D$ as well as the polar angle θ. During the experiment beam induced structural changes of the target prevented a determination of the distances between target and degrader, which are essential for a lifetime analysis. This problem could be solved by determining effective distances using precisely known lifetimes of ^{46}Ti [10]. Detailed information about the distance determination will be given in Ref. [11]. A total of six target-to-degrader distances, ranging from 130 µm and 1000 µm, were set during the experiment, each with a measurement time of about 24 hours.

3 Data analysis and results

The reaction products were completely identified on an event-by-event basis using VAMOS++. The matrix of the energy loss obtained in the sum of the first three rows of the ionization chamber versus the total energy measured in the sum of all rows was used for the Z identification. The mass A and mass over charge (A/Q) were obtained from the time-of-flight, the total energy and the magnetic rigidity ($B\rho$). Further details will be given in Ref. [11]. After the particle identification Doppler-corrected γ-ray singles spectra could be generated for each nucleus by means of corresponding Z and A gates. The differential decay curve method (DDCM) [12] was employed for the lifetime analysis using the γ-ray singles spectra. Figure 1 shows the γ-ray statistics for ^{53}Ti in a sum spectrum in which the spectra of all six distances were added up. It was possible to identify nine transitions of ^{53}Ti (cf. Fig. 1) that are clearly visible after Doppler correction for the degraded component. These correspond to the decays of the first six

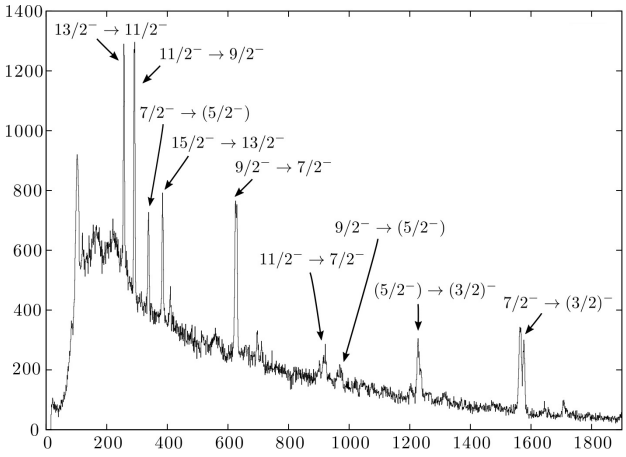

Figure 1. Doppler-corrected γ-ray spectrum in coincidence with ions identified as ^{53}Ti, summed over all six distances. Nine γ-ray decays are observed.

excited states up to the $15/2^-$ state of the yrast band in ^{53}Ti. The level scheme in Fig. 2 contains only the transitions and levels observed in this work.

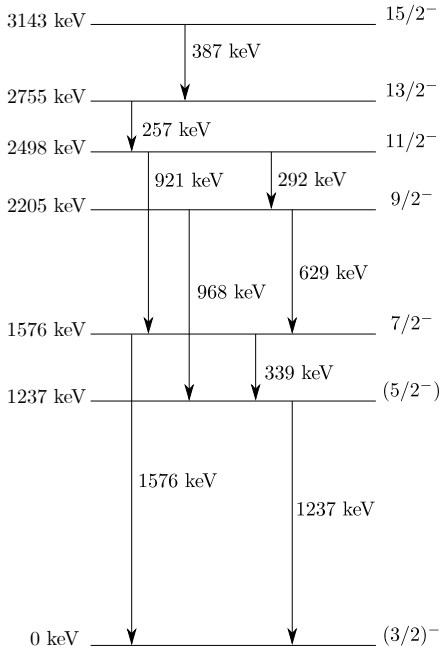

Figure 2. Partial level scheme of ^{53}Ti relevant for the present experiment.

For the evaluation of the $7/2^-$ state the decay into the $(3/2)^-$ state was used (1576 keV), on the one hand due to the clear separation of the fast and degraded components, respectively, and on the other hand because it is by far the strongest decay branch. Furthermore, the γ-ray energy of the transition $7/2^- \rightarrow (5/2^-)$ is significantly lower with 339 keV and the Doppler shift is therefore smaller, which leads to a worse separation of the two components. In addition, the latter decay has a relative intensity of only 33 [13] normalized to the strongest decay with a relative intensity of 100. Only the decay into the $7/2^-$ state

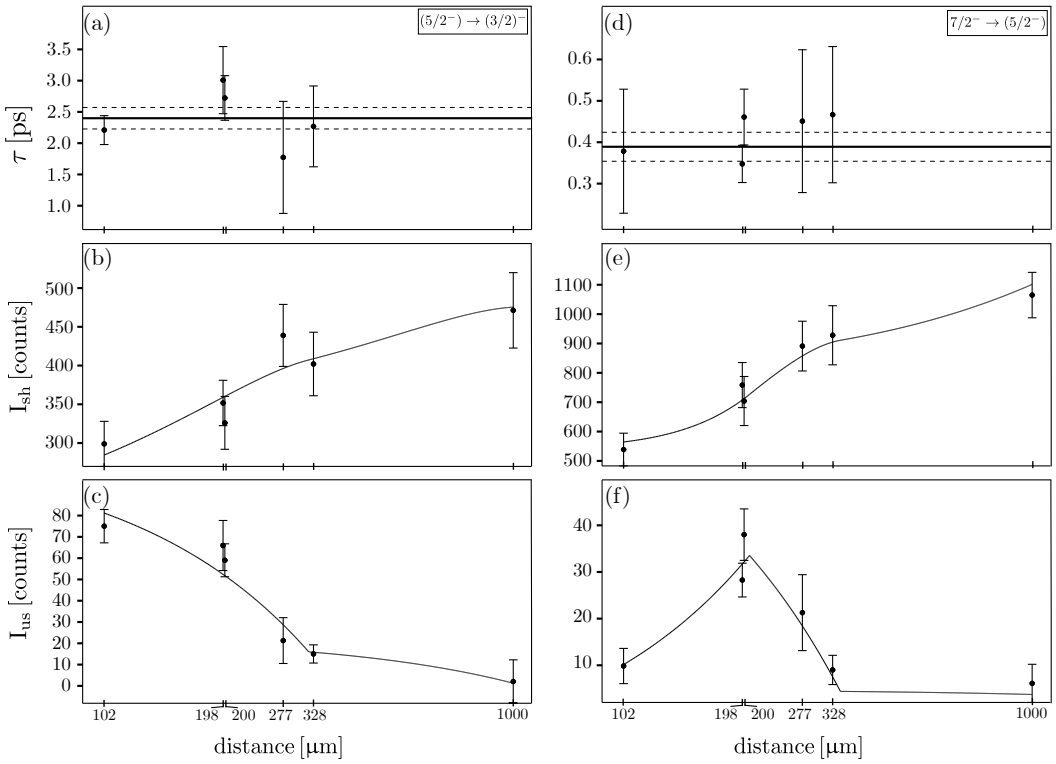

Figure 3. Plot of lifetime analysis for the $(5/2^-)$ and $7/2^-$ states in ^{53}Ti. In the upper panels (a), (d) the black solid lines represent the weighted mean value of the lifetimes; dashed lines mark the statistical uncertainty. The intensities of the fast and degraded components are shown in (b),(e) and (c),(f), respectively. For the intensity determination of the degraded component (c),(f) a feeding correction was considered. Note the logarithmic distance scale.

(629 keV) could be used to determine the lifetime of the $9/2^-$ state, since this decay was much stronger with a relative intensity of 100 than the decay into the $(5/2^-)$ state (968 keV, 10.5). However, a smaller Doppler-shift is present due to the smaller transition energy. Although two transitions depopulate the $11/2^-$ state, the transition to the $9/2^-$ state with only 292 keV is not suitable for the analysis, so the transition to the $7/2^-$ state (921 keV) was used even tough it only has a relative intensity of 17 as compared to the strongest decay branch with a relative intensity of 100. Due to the insufficient separation of the $15/2^- \rightarrow 13/2^-$ transition, it was not possible to evaluate the lifetime of the $15/2^-$ state.

The peak positions and widths of the degraded components were fixed with calibrations of the strongest decay of ^{50,52,53}Ti. The lifetime is extracted from intensities of the depopulating transition after subtraction of the observed feeding for each distance x according to:

$$\tau(x) = \frac{I^d_{\mathrm{us}}(x) - \alpha \cdot I^p_{\mathrm{us}}(x)}{\frac{d}{dx} I^d_{\mathrm{sh}}(x)} \frac{1}{v_T} \qquad (2)$$

s where I^d_{us} and I^d_{sh} are the efficiency-corrected and normalized intensities of the degraded and fast components of the depopulating (d) and populating (p) state, α includes the branching ratios and $v_T = \beta_T \cdot c$ is the mean velocity of the recoils before the degrader. According to DDCM, lifetime values are derived at each target-to-degrader distance and a constant line of lifetime values as a function of the distance is expected. Deviations from this constant line are indicators of systematic effects that can be detected using this method. Preliminary lifetime fits for the $(5/2^-) \rightarrow (3/2)^-$ and $7/2^- \rightarrow (3/2)^-$ transitions performed with the program NAPATAU [14] are shown in Fig. 3. Similar fits could also be generated for the higher lying states $9/2^-$, $11/2^-$ and $13/2^-$.

The middle panels (b),(e) show the intensities of the fast components of the depopulating transition and the lower panels (c),(f) those of the degraded components taking into account a feeding correction for observed feeders of the respective level of interest. As a result of these two, the deduced lifetime is shown in the upper panels (a),(d). The data are still under analysis, thus experimental preliminary results of measured lifetime values for the $(5/2^-)$ to $13/2^-$ states in ^{53}Ti are summarized in Table 1.

Table 1. Results of the preliminary lifetime values of the first five yrast states in ^{53}Ti from this work.

I^π	E_{Level} (keV)	E_γ (keV)	τ (ps)
$(5/2^-)$	1237.1	1237.1	2.4 ± 0.5
$7/2^+$	1576.3	1576.3	0.4 ± 0.4
$9/2^-$	2205.8	629.6	1.1 ± 0.5
$11/2^-$	2498.1	921.8	3.5 ± 0.7
$13/2^-$	2755.9	257.8	2.4 ± 0.6

Since the slowing down of the recoils in the degrader does not happen instantaneously, but takes a finite time, slowing down effects occur here (Doppler Shift-Attenuation (DSA)). These lead to the fact that the degraded peak has no longer a Gaussian shape, but a tail in the direction of the flight component, which should be assigned to the slow component, because the degrader is already reached. This can be problematic for the analysis of RDDS measurements with insufficient separation of the components, since these decays in the spectrum cannot be distinguished from those in which a recoil decays in flight between target and degrader. This effect depends on the lifetime and increases strongly with decreasing lifetime. In general, a correction for lifetimes smaller than 2 ps is considered. This applies especially to the lifetimes of the $7/2^-$ and $9/2^-$ states for which such a correction must be made in a next step and is planned by means Monte-Carlo-Simulations using the G4LifeTimeG toolkit [15].

4 Summary

Preliminary lifetime values of five excited states of the yrast band in ^{53}Ti were determined for the first time. The next step is to finalize the results by considering DSA effects for very short lifetimes. The results can be used to test shell-model predictions for different interactions. In addition to the existing calculations in Ref. [3], further interactions should be used to evaluate their predictability. With the new experimental transition strengths the description of the nuclear structure in ^{53}Ti may be improved. Further, the predicted evolution of shell closures at $N = 32, 34$ can be tested.

Acknowledgements

The authors would like to thank the staff at GANIL involved in this work for their support. Special thanks go to the operators for the excellent focusing of the beam. This work was supported by the German Research Foundation “Bundesministerium für Bildung und Forschung” (BMBF) under contract number 05P18PKFN9.

References

[1] D.C. Dinca, R.V.F. Janssens, A. Gade, D. Bazin, R. Broda, B.A. Brown, C.M. Campbell, M.P. Carpenter, P. Chowdhury, J.M. Cook et al., Phys. Rev. C **71**, 041302 (2005)

[2] L.A. Parks, C.N. Davids, R.C. Pardo, Phys. Rev. C **15**, 730 (1977)

[3] B. Fornal, S. Zhu, R.V.F. Janssens, M. Honma, R. Broda, B.A. Brown, M.P. Carpenter, S.J. Freeman, N. Hammond, F.G. Kondev et al., Phys. Rev. C **72**, 044315 (2005)

[4] A. Dewald, O. Möller, P. Petkov, Progress in Particle and Nuclear Physics **67**, 786 (2012)

[5] S. Akkoyun, A. Algora, B. Alikhani, F. Ameil, G. de Angelis, L. Arnold, A. Astier, A. Ataç, Y. Aubert, C. Aufranc et al., Nuclear Instruments and Methods in Physics Research Section A: Accelerators, Spectrometers, Detectors and Associated Equipment **668**, 26 (2012)

[6] A. Dewald, O. Möller, P. Petkov, Progress in Particle and Nuclear Physics **67**, 786 (2012)

[7] S. Pullanhiotan, M. Rejmund, A. Navin, W. Mittig, S. Bhattacharyya, Nuclear Instruments and Methods in Physics Research Section A: Accelerators, Spectrometers, Detectors and Associated Equipment **593**, 343 (2008)

[8] M. Rejmund, B. Lecornu, A. Navin, C. Schmitt, S. Damoy, O. Delaune, J. Enguerrand, G. Fremont, P. Gangnant, L. Gaudefroy et al., Nuclear Instruments and Methods in Physics Research Section A: Accelerators, Spectrometers, Detectors and Associated Equipment **646**, 184 (2011)

[9] M. Vandebrouck, A. Lemasson, M. Rejmund, G. Frémont, J. Pancin, A. Navin, C. Michelagnoli, J. Goupil, C. Spitaels, B. Jacquot, Nuclear Instruments and Methods in Physics Research Section A: Accelerators, Spectrometers, Detectors and Associated Equipment **812**, 112 (2016)

[10] A. Goldkuhle, C. Fransen, A. Dewald, K. Arnswald, M. Bast, M. Beckers, A. Blazhev, T. Braunroth, G. Hackenberg, G. Häfner et al., The European Physical Journal A **55**, 53 (2019)

[11] A. Goldkuhle et al. (2019), submitted for Phys. Rev. C

[12] A. Dewald, S. Harissopulos, P. von Brentano, Zeitschrift für Physik A Atomic Nuclei **334**, 163 (1989)

[13] H. Junde, Nuclear Data Sheets **86**, 2689 (2000)

[14] B. Saha, *Computer code* NAPATAU, Institute for Nuclear Physics, University of Cologne, unpublished

[15] S. Agostinelli, J. Allison, K. Amako, J. Apostolakis, H. Araujo, P. Arce, M. Asai, D. Axen, S. Banerjee, G. Barrand et al., Nuclear Instruments and Methods in Physics Research Section A: Accelerators, Spectrometers, Detectors and Associated Equipment **506**, 250 (2003)

Publication IV:
Lifetime measurements of excited states in neutron-rich ^{53}Ti: benchmarking effective shell-model interactions

Lifetime measurements of excited states in neutron-rich ^{53}Ti: Benchmarking effective shell-model interactions

A. Goldkuhle,[1,*] A. Blazhev,[1] C. Fransen,[1] A. Dewald,[1] M. Beckers,[1] B. Birkenbach,[1] T. Braunroth,[1] E. Clément,[2] J. Dudouet,[3,4] J. Eberth,[1] H. Hess,[1] B. Jacquot,[2] J. Jolie,[1] Y.-H. Kim,[5] A. Lemasson,[2] S. M. Lenzi,[6,7] H. J. Li,[2] J. Litzinger,[1] C. Michelagnoli,[2,5] C. Müller-Gatermann,[1,8] B. S. Nara Singh,[9,10] R. M. Pérez-Vidal,[11] D. Ralet,[4] P. Reiter,[1] A. Vogt,[1] N. Warr,[1] and K. O. Zell[1]

[1]*Institut für Kernphysik, Universität zu Köln, 50937 Köln, Germany*
[2]*GANIL, CEA/DRF-CNRS/IN2P3, BP 55027, 14076 Caen Cedex 05, France*
[3]*Université Lyon, Université Claude Bernard Lyon 1, CNRS/IN2P3, IP2I Lyon, UMR 5822, F-69622, Villeurbanne, France*
[4]*Centre de Spectrométrie Nucléaire et de Spectrométrie de Masse - CSNSM, CNRS/IN2P3 and Université Paris-Sud, F-91405 Orsay Campus, France*
[5]*Institut Laue-Langevin, BP 156, 38042 Grenoble Cedex 9, France*
[6]*INFN, Sezione di Padova, I-35131 Padova, Italy*
[7]*Dipartimento di Fisica e Astronomia dell'Università di Padova, I-35131 Padova, Italy*
[8]*Physics Division, Argonne National Laboratory, 9700 South Cass Avenue, Lemont, Illinois 60439, USA*
[9]*Nuclear Physics Group, Schuster Laboratory, University of Manchester, Manchester M13 9PL, United Kingdom*
[10]*School of Computing Engineering and Physical Sciences, University of the West of Scotland, Paisley PA1 2BE, United Kingdom*
[11]*Instituto de Física Corpuscular, CSIC-Universidad de Valencia, E-46071 Valencia, Spain*

(Received 16 July 2020; accepted 10 November 2020; published 30 November 2020)

Level lifetimes of the yrast $(5/2^-)$ to $13/2^-$ states in the neutron-rich nucleus ^{53}Ti, produced in a multinucleon-transfer reaction, have been measured for the first time. The recoil distance Doppler-shift method was employed and lifetimes of the excited states were extracted by a lineshape analysis aided by GEANT4-based Monte-Carlo simulations. The experiment was performed at the Grand Accélérateur National d'Ions Lourds facility in Caen, France, by using the Advanced Gamma Tracking Array for the γ-ray detection coupled to the large-acceptance variable mode spectrometer for an event-by-event particle identification and the Cologne plunger for deep-inelastic reactions. Reduced transition probabilities, deduced from the lifetimes, give new information on the nuclear structure of ^{53}Ti, and are used to benchmark different shell-model calculations using established interactions in the fp shell.

DOI: 10.1103/PhysRevC.102.054334

I. INTRODUCTION

The evolution of the shell structure in exotic nuclei such as neutron-rich titanium isotopes ($Z = 22$) is one of the central topics of current experimental and theoretical research in nuclear physics. This attention can be attributed to the physics phenomena arising from a rearrangement of neutron single-particle levels as protons are removed from the $\pi 1f_{7/2}$ orbital. For example, changes in the energy spacings between the orbitals and/or their arrangement can have a significant impact on global nuclear properties such as nuclear shape. Probably the best known example of an unexpected structural change is the "island of inversion" in neutron-rich exotic nuclei at $N = 20$ (see for example Ref. [1] and the references therein). Due to the promotion of neutrons across the $N = 20$ shell closure, deformed rather than spherical ground-state configurations exist in this island. This phenomenon is due to three aspects, namely, the strong interaction between valence protons and the promoted neutrons, interactions between the promoted neutrons themselves and shifts in the energies of the individual particles [1].

Interactions between protons and neutrons also explain the recently observed existence of subshell closure at $N = 34$ [2] and at $N = 32$ [3–6], the latter developing in the isotonic chain ^{58}Fe $\rightarrow$ ^{56}Cr $\rightarrow$ ^{54}Ti $\rightarrow$ ^{52}Ca, as the number of protons in the $\pi 1f_{7/2}$ shell decrease and the doubly magic ^{48}Ca is approached. [3]. Theoretical studies interpret this subshell closure as a result of the spin-orbit splitting of the $\nu 2p_{1/2}$ and $\nu 2p_{3/2}$ orbitals and an attenuation of the $\pi 1f_{7/2}$-$\nu 1f_{5/2}$ monopole interaction. A decreasing number of protons in the $\pi 1f_{7/2}$ orbital, i.e., from Ni to Ca, leads to an uplift of the $\nu 1f_{5/2}$ orbital in energy. In fact, this effect can cause an inversion of the $\nu 1f_{5/2}$ and $\nu 2p_{1/2}$ orbitals [6], forming a gap between the $\nu 2p_{3/2}$ orbital on one side and $\nu 2p_{1/2}$ and $\nu 1f_{5/2}$ orbitals on the other side, and thus giving rise to the $N = 32$ subshell closure [3–5].

To verify these findings, lifetimes of excited states are of great importance, since transition probabilities determined from these lifetimes can be used for testing the nuclear

*Corresponding author: agoldkuhle@ikp.uni-koeln.de

structure theories in this region. A recent publication presented new experimental results on ^{52,54}Ti allowing for an investigation of their nuclear structure [7]. The newly determined transition strengths in ^{52}Ti [7] contradict the previous results of Ref. [8] and show an opposite trend to the literature values of $B(E2; J_1^+ \rightarrow (J-2)_1^+)$ as a function of the yrast spin. The new experimental data on ^{52}Ti are now consistent with those of the neighboring nuclei as well as with predictions of shell-model (SM) calculations [7].

Different experimental techniques were used to study nuclei in this region, such as deep-inelastic reactions (^{52,54}Ti [9]), β decay (^{54,55,56}Ti [4]), Coulomb excitation (^{52,54,56}Ti [10]), fusion-evaporation reactions (^{55}V and ^{55}Ti [11]), knockout reactions (^{56}Cr [12]; ^{52}Ca [5]; ^{54}Ca [6]), and fragmentation reactions (^{50}Ca, ^{56}Ti [13]) and the recently performed multinucleon-transfer reaction [7].

Odd-mass Ti isotopes with $A \leqslant 51$ have been investigated [14–17], too. The isotopes ^{45,47,49,51}Ti were studied [18] with the deformed configuration mixing shell model and the effective charges and $E2$ transitions were analyzed in fp shell nuclei, especially Ti isotopes with $A = 44$–50 [19]. Lifetimes and lifetime limits in ^{49,51}Ti isotopes were also determined using the Doppler-shift attenuation (DSA) method [15].

As a direct neighbor of ^{54}Ti$_{32}$, the odd-mass nucleus ^{53}Ti is important to have better understanding of the single-particle orbitals at $N = 32$. Information on excited states in the odd-mass nucleus ^{53}Ti was first reported by a prompt γ-ray spectroscopy study, following the β decay [20]. The knowledge of the yrast cascade in ^{53}Ti was extended via the studies performed with the Gammasphere spectrometer, for which ^{48}Ca beam-induced deep-inelastic reactions on thick ^{208}Pb and ^{238}U targets were used. Excitation energies of states with spins up to $I^\pi = 21/2^-$ were determined for the first time [21]. With special focus on the (sub)shell closure at $N = 32$, the experimental yrast structure was compared with SM calculations using the well-established interactions GXPF1 and GXPF1A and a good agreement between experimental and theoretical results was found [21]. Preliminary results of level lifetimes in ^{53}Ti from this experiment have been already published in Ref. [22]. Here, we report final lifetime results for ^{53}Ti by comparing experimental γ-ray spectra with GEANT4 Monte-Carlo simulated spectra. Reduced transition probabilities are determined from the lifetimes and are compared with the results of SM calculations using different interactions allowing to benchmark the latter.

II. EXPERIMENT

The recoil distance Doppler-shift (RDDS) experiment was performed at the Grand Accélérateur National d'Ions Lourds (GANIL) in Caen, France. The nuclei of interest, in particular $^{46–54}$Ti, were populated via a multinucleon-transfer reaction induced by a ^{238}U beam at an energy of $E(^{238}\text{U}) = 1608.9$ MeV ($= 6.76$ MeV/u) impinging on a $\approx$1.5 mg/cm^2 enriched ^{50}Ti target with a $\approx$0.4 mg/cm^2 thick $^{\text{nat}}$Cu layer backing facing the beam to improve the heat dissipation. Details on the experiment are given in Ref. [7]. The experimental setup was composed of three parts, namely, (i) the Advanced Gamma Tracking Array (AGATA) [23,24] γ-ray spectrometer consisting of 29 36-fold segmented, encapsulated high-purity germanium (HPGe) crystals in ten cryostats placed at backward angles with respect to the beam direction, (ii) the VAriable MOde high acceptance Spectrometer (VAMOS++) [25–27], and (iii) the compact plunger for deep inelastic reactions [28]. The reaction products were detected and identified with the large acceptance magnetic spectrometer VAMOS++ using a trajectory reconstruction technique. It consisted of Multi-Wire Parallel Plate Avalanche Counter (MWPPAC), four Drift Chambers (DC), and a segmented Ionization Chamber (IC). The horizontal and vertical positions (x, y) required for the trajectory reconstruction are measured by the DC. The IC is used for the measurement of the energy loss ΔE and the total energy E. The Time of Flight (TOF) is determined from the signals of the Dual Position-Sensitive Multi-Wire Proportional Counter (DPS-MWPC) and the MWPPAC, one of which is positioned at the entrance of the spectrometer and the other one at the entry of the focal plane. The VAMOS++ setup permits the measurement of all the parameters needed for the determination of the mass M, the charge state Q, the atomic number Z, and the angles θ_{lab} and φ_{lab} with respect to the target position. Both the target and degrader foils were placed at an angle of 45° with respect to the incoming beam which is close to the grazing angle of the multinucleon-transfer reaction. Data were collected at six nominal target-to-degrader distances between 70 μm and 1000 μm for about 1 day per distance, which results in sensitivity to the expected lifetimes. However, during the experiment, beam-induced changes in the target occurred [29], which had such great effects that the distances between the target and degrader could not be determined directly and precisely. Therefore, an in-depth distance determination was necessary first, which was carried out with Monte-Carlo simulations, see Ref. [7].

III. DATA ANALYSIS AND RESULTS

The reaction products were completely identified on an event-by-event basis using VAMOS++. The matrix of the energy loss obtained in the sum of the first three segments of the ionization chamber versus the total energy measured in the sum of all segments was used for the Z identification. The mass A and mass over charge (A/Q) were obtained from the TOF, the total energy and the magnetic rigidity $(B\rho)$. The procedure for the ion identification is described in Ref. [7]. A Doppler-reconstructed γ-ray spectrum is depicted in Fig. 1, which shows the γ-ray yield correlated to ^{53}Ti. A total of nine transitions in ^{53}Ti could be identified unambiguously after Doppler correction for the degraded component.

The dominant peak at 1237 keV corresponds to the $(5/2^-) \rightarrow 3/2^-_{\text{g.s.}}$ transition. The $(5/2^-)$ state is known to be fed by transition energies 339 keV [$7/2^- \rightarrow (5/2^-)$] as well as 968 keV [$9/2^- \rightarrow (5/2^-)$]. A further dominant peak can be seen at $E_\gamma = 1576$ keV ($7/2^- \rightarrow 3/2^-_{\text{g.s.}}$). The $7/2^-$ state is known to be fed by transitions at 921 keV ($11/2^- \rightarrow 7/2^-$) as well as at 629 keV ($9/2^- \rightarrow 7/2^-$). In addition, three more transitions are visible at $E_\gamma = 292$ keV ($11/2^- \rightarrow 9/2^-$), $E_\gamma = 257$ keV ($13/2^- \rightarrow 11/2^-$), and $E_\gamma = 387$ keV

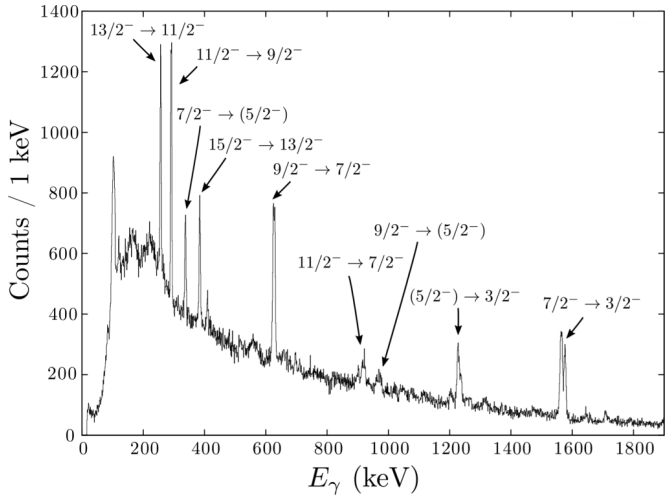

FIG. 1. Doppler-corrected γ-ray spectrum in coincidence with ions identified as ^{53}Ti, summed up over all six distances. Nine γ ray decays are observed. Spin-parity assignments taken from Ref. [21]. See text for details.

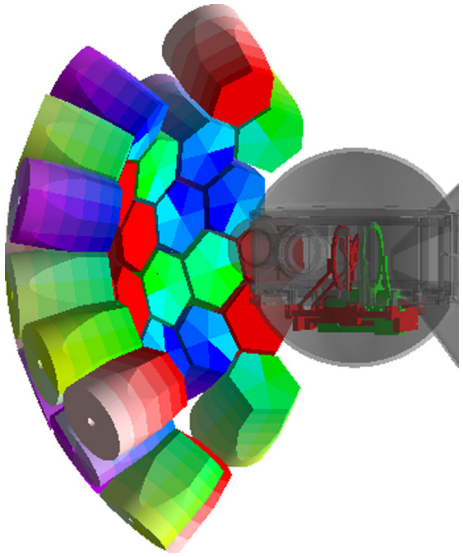

FIG. 3. Replication of the experimental geometry as provided by the improved GEANT4 toolkit [32]. Shown are the plunger chamber, the detector crystals and their housing. See text for details.

$(15/2^- \rightarrow 13/2^-)$. The corresponding level scheme is illustrated in Fig. 2.

Lifetimes of excited states from this data set were determined using the Differential Decay Curve method (DDCM)

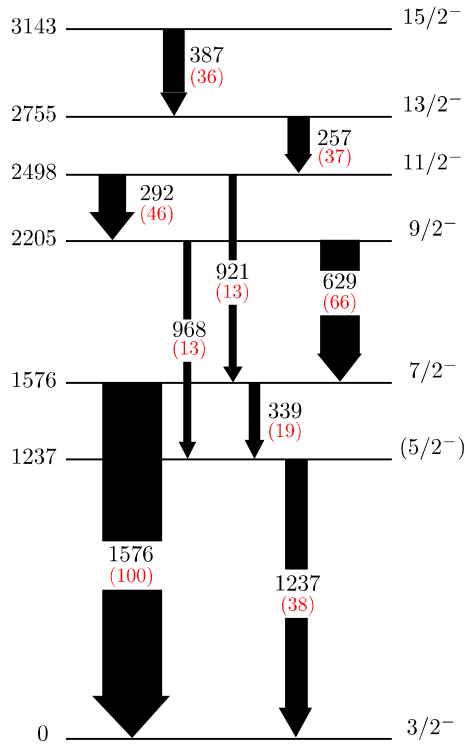

FIG. 2. Partial energy level scheme of ^{53}Ti as observed in the present work. All energies are given in keV. Levels with spin-parity assignments taken from Ref. [21]. The thickness of the arrows is proportional to the relative transition intensities (red marked) normalized to the $7/2^- \rightarrow 3/2^-$ transition. See text for details.

[30]. Preliminary results of the lifetime analysis revealed slowing-down effects (DSA) that was caused by the deceleration of the recoils in the degrader [22]. In Ref. [22], no correction was done to take the effect into account. In the present work, the lifetimes were extracted using Monte-Carlo simulations in order to take the slowing-down effects into account.

The lifetimes are determined by comparing the spectra measured in γ-ray singles and the simulated one obtained by the dedicated Monte-Carlo simulation GEANT4 Toolkit [31]. This tool was developed and has been improved [32] to include the AGATA configuration used in the experiment. An accurate description of the geometry with respect to the foils, beam tube and HPGe detectors provided by the tool, is illustrated in Fig. 3.

Initial values of lifetimes fed to the simulation toolkit are varied in a range of max. $\tau_{\chi^2_{\min}} \pm 3$ ps in steps of 0.2 ps. For each lifetime assumption, a χ^2 value was calculated following the least-squares method using

$$\chi^2 = \sum_i \left(\frac{i_{\text{exp}} - i_{\text{sim}}}{\Delta i_{\text{exp}}} \right)^2,$$

where i_{exp} (i_{sim}) is the number of counts in bin i in the experimental (simulated) spectrum. The simulated statistics are larger than the experimental ones by a factor of 10. The experimental and simulated γ-ray spectra were normalized to each other after a background correction was performed on the simulated spectrum by calculating the background using a ROOT function [33]. The range was chosen to restrict both the fast and slow components of the considered transition. The simulations with the lowest χ^2 value, the experimental spectra and the resulting reduced χ^2 values, which depends on the lifetime value used for the simulation, are presented for five distances in the sensitive range for the $7/2^- \rightarrow 3/2^-_{\text{g.s.}}$

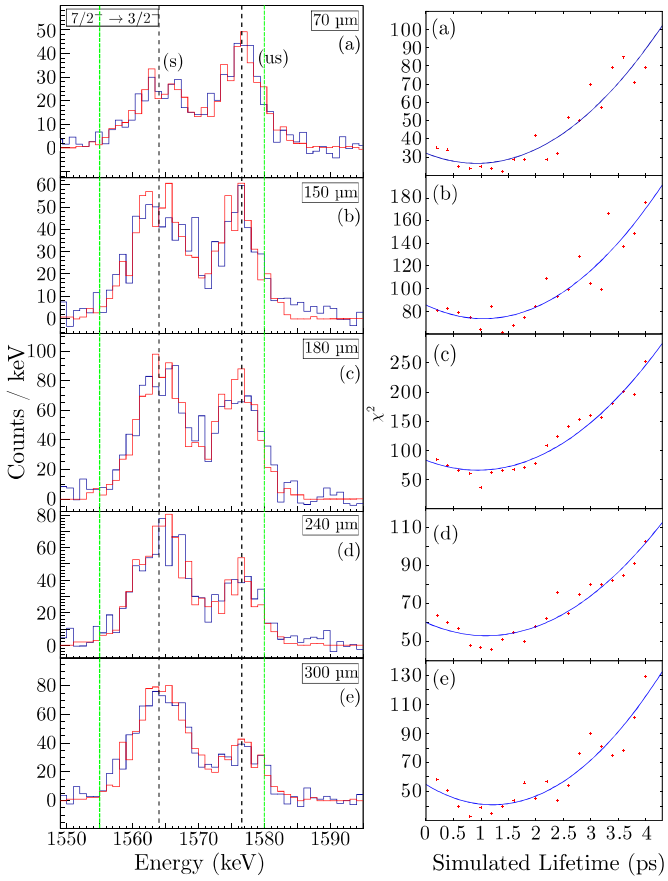

FIG. 4. Left: Comparison of fits of the simulated GEANT4 γ-ray $7/2^- \rightarrow 3/2^-_{\text{g.s.}}$ transition (red) and measured spectra (blue) at five distances (a)–(e) used for the lifetime determination. The vertical black dashed lines mark the shifted (s) and unshifted (us) components after Doppler correction for the degraded component, the green dashed lines mark the area used for calculation of the χ^2 values. Right: Reduced χ^2 values (red dots) versus simulated lifetime with a best fitting of the quadratic function (blue line) for each distance. See text for details.

transition in Fig. 4. The lifetime values of the excited states of interest were fixed from top to bottom in the level scheme with respect to the excitation energies. The population ratios of the individual states were determined from the γ-ray spectrum summed over all distances and were utilized to perform simulations. The final lifetime results from the average of the individual lifetime values of each target-to-degrader distance. The statistical error of the lifetime determined by the χ^2 method is derived from the lifetimes with $\chi^2 + 1$.

The final results for lifetimes of the $(5/2^-)$ to $13/2^-$ states in ^{53}Ti are summarized in Table I. For the $15/2^-$ state, an effective lifetime with $\tau = 2.2$ ps was assumed, because the separation of the shifted and degraded components was not possible. In addition, the low statistics of this transition (to the $13/2^-$ state) made the determination of the actual lifetime of the $15/2^-$ state impossible. This effective lifetime is the cumulative lifetime of the $15/2^-$ state including all feeding times of all of the higher-lying levels, including those that

TABLE I. Results of the lifetime analysis ^{53}Ti by means of simulations. See text for details.

$J_i \rightarrow J_f$	E_γ^{lit} [21] (keV)	$\tau_{\text{present}}(J_i)$ (ps)
$(5/2^-) \rightarrow 3/2^-_{\text{g.s.}}$	1237.1	1.5(9)
$7/2^- \rightarrow 3/2^-_{\text{g.s.}}$	1576.3	1.0(4)
$9/2^- \rightarrow (5/2^-)$	968.6	2.8(7)
$11/2^- \rightarrow 7/2^-$	921.8	3.2(5)
$13/2^- \rightarrow 11/2^-$	257.8	2.9(5)

were not observed. With the exception of the $9/2^-$ state, the lifetimes determined in this work are consistent with the lifetime values within the error limits determined using DDCM in Ref. [22]. It should be highlighted that the lifetime value of the $9/2^-$ state differs from the previous value [22] because the determination in the present work has been done by taking the slowing-down effects in to account.

IV. DISCUSSION

The nuclear shell model has proved to be rather successful in describing experimental excitation energies of even-even neutron-rich titanium and neighboring nuclei [4,6,9,10]. On the other hand, although the order of magnitude of $E2$ strengths for the even-even Ti isotopes above $N = 28$ could be reproduced, the experimental values showed some pronounced staggering for the lowest transition, which could not be accounted for by the theory [8,10]. Our recent experimental results on ^{52,54}Ti [7] and especially the considerable revision of the $E2$ strength from the 2_1^+ and 4_1^+ states in ^{52}Ti, greatly reduced the above-mentioned $B(E2; 2_1^+ \rightarrow 0^+_{\text{g.s.}})$ staggering and with respect to the $E2$ strengths of the yrast band in ^{52}Ti solved previous contradiction with theory.

In the neighboring ^{53}Ti, the yrast nuclear structure was discussed by Fornal *et al.* [21] in the light of SM calculations using the FPD6 [34] and GXPF1(A) [35] interactions, although without having information on experimental transition strengths. In this section, based on our new experimental results, we address again the nuclear structure of ^{53}Ti comparing with SM calculations in the fp model space. These calculations were performed with the NuShellX@MSU code [36] using four established effective interactions, namely, FPD6 [34], KB3G [37], GXPF1A [35] and GXPF1B [38]. For all interactions, effective charges of $e_\pi = 1.31\,e$ and $e_\nu = 0.46\,e$ [39] were used to calculate $B(E2)$ values, which proved to be a good choice in our previous publication [7]. All $M1$ strengths were calculated using free-nucleon g factors $g_p^s = 5.586$, $g_n^s = -3.826$, $g_p^l = 1.0$, and $g_n^l = 0.0$ as the spin-orbit partner orbitals are all present in the model space as well as to ease the comparison between the theories.

In Fig. 5, a partial level scheme of ^{53}Ti is compared to SM calculations using the above-mentioned interactions. With the exception of the FPD6 interaction, the calculated energies agree well with the experimental ones. An almost perfect match is provided by the KB3G interaction, which, in contrast

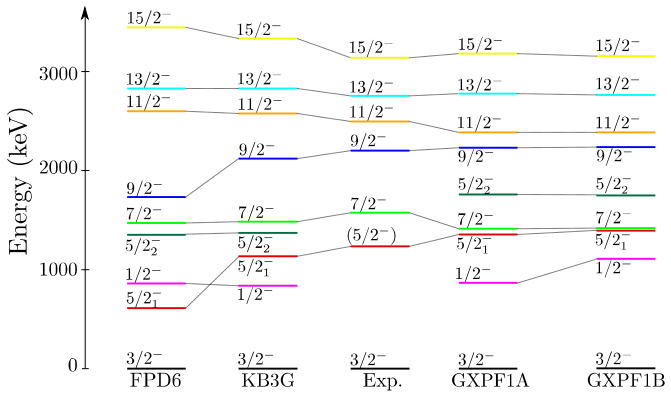

FIG. 5. Comparison of experimental level energies for ^{53}Ti and the results of the full fp shell-model calculations using the FPD6, GXPF1A, GXPF1B, and KB3G interactions. See text for details.

to the GXPF1A and GXPF1B interactions, has a clear separation of the $5/2^-_1$ and $7/2^-$ levels, similar in magnitude to the experiment. The FPD6 interaction predicts lower energies for the $5/2^-_1$ and $9/2^-$ states leading to an inversion of the $1/2^-$ and $5/2^-_1$ states and a considerable splitting between $5/2^-_1$ and $7/2^-$, as well as $9/2^-$ and $11/2^-$, which contradicts the experiment. This is due to known "monopole defects" of the FPD6, which, above $N = 28$, result in a lower position of the $\nu f_{5/2}$ orbital and a higher position of $\nu p_{1/2}$, and has been discussed already in Ref. [37]. The shift of the $1/2^-$ state from GXPF1A to GXPF1B observed in Fig. 5 results from an increase in the single-particle energy of the $\nu p_{1/2}$ orbital and a modification of the matrix elements involving this orbital [38]. Since the $1/2^-$ state is still experimentally unknown it will not be discussed here. Figure 6 contains the leading wave function configurations of the valence neutrons of selected states in ^{53}Ti resulting from SM calculations with FPD6, KB3G, and GXPF1A. For all cases shown, the corresponding proton configuration is $\pi f^2_{7/2}$, which is by far the most dominant one. As the numbers for GXPF1A and GXPF1B for the discussed states are very similar, both for the

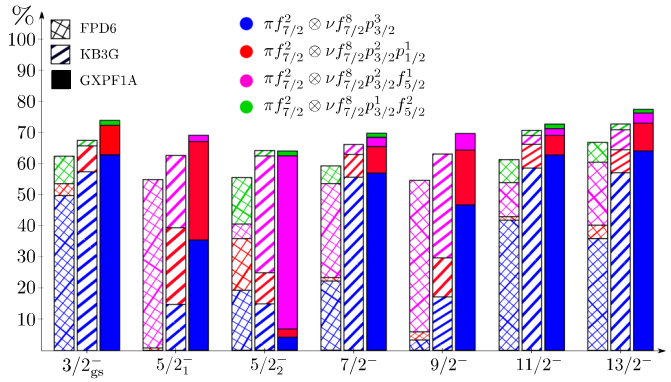

FIG. 6. Leading neutron configurations of selected states up to $13/2^-$ with corresponding proton configuration $\pi f^2_{7/2}$. Configurations with contributions >5% for at least one interaction are shown. See text for details.

wave functions and consequently for the transition strengths, in the following, only the GXPF1A results are shown and discussed.

As shown in Fig. 6 and already discussed by Fornal *et al.* [21], the GXPF1A interaction predicts that the structure of the yrast states with spins from $I = 3/2$ to $13/2$ is dominated at the level of 35–65% by a single SM configuration $\pi f^2_{7/2} \otimes \nu f^8_{7/2} p^3_{3/2}$ (depicted in blue), which corresponds to one neutron hole in the $p_{3/2}$ orbital, i.e., in the $N = 32$ subshell closure. The second most dominant neutron configuration according to GXPF1A is the $\nu f^8_{7/2} p^2_{3/2} p^1_{1/2}$ (depicted in red) and is particularly strong for the $5/2^-_1$ and $9/2^-$ states. The predictions using the KB3G interaction for the structures of the $3/2^-, 7/2^-, 11/2^-, 13/2^-$ states is similar to that of GXPF1A. In the case of the $5/2^-$ and $9/2^-$ states apart from blue and red configurations, KB3G predicts significant mixing also from $\nu f^8_{7/2} p^2_{3/2} f^1_{5/2}$ configuration (depicted in pink). In particular the pink configuration dominates for the $9/2^-$ state. The leading configurations of the FPD6 clearly distinguish themselves from the other two interactions. As mentioned, due to the low-lying $\nu f_{5/2}$ orbital, the discussed yrast states have strong or dominant configurations in which one or more neutrons occupy that orbital (see Fig. 6). This is especially obvious for the $5/2^-_1$ state and will be discussed later in the text.

Although the energies of the excited states can differentiate between the SM interactions, a better benchmarking of the latter can be done by experimental reduced transition probabilities. This work presents the first experimental results on state lifetimes in ^{53}Ti, from which data reduced strengths have been obtained and compared with the calculated values.

The results of the theoretical and experimental electric and magnetic transition strengths are given in Fig. 7, whose numerical values are listed in Table II in the Appendix. The transitions $13/2^- \rightarrow 11/2^-$, $11/2^- \rightarrow 9/2^-$, $9/2^- \rightarrow 7/2^-$, $7/2^- \rightarrow (5/2^-)$, and $(5/2^-) \rightarrow 3/2^-$ are of mixed $E2/M1$ multipolarity and therefore one needs to know the multipole mixing ratio $\delta(E2/M1)$, defined as the ratio of the corresponding transition probabilities [40]. A pure $M1$ transition would have a value of $\delta(E2/M1)$ equal to zero, while an infinite value corresponds to a pure $E2$ transition. The knowledge of $\delta(E2/M1)$ for the above transitions is limited. In Ref. [21] values of $\arctan(\delta)$ are given for $9/2^- \rightarrow 7/2^-$ and $11/2^- \rightarrow 9/2^-$, from which we calculate $(9/2^- \rightarrow 7/2^-)\ |\delta(E2/M1)| = 0.0133 \pm 0.0003$ and $(11/2^- \rightarrow 9/2^-)\ |\delta(E2/M1)| = 0.052 \pm 0.018$, testifying a dominant $M1$ character and allowing to extract the $B(E2)_{\rm exp}$ and $B(M1)_{\rm exp}$ (marked with an asterisk in the figure). Due to the scaling of Fig. 7(a), the $B(E2; 11/2^- \rightarrow 9/2^-)_{\rm exp} = 280^{+230}_{-160}\ e^2{\rm fm}^4$ is not shown. For the other transitions of mixed $E2/M1$ character, upper limits of $B(E2)_{\rm exp}$ and $B(M1)_{\rm exp}$ were calculated assuming the extreme cases of a pure $E2$ or a pure $M1$ character. The error bars (upper limits) of the $B(\sigma L)_{\rm exp}$ and $B(\sigma L)^{\delta_{\rm SM}}_{\tau_{\rm exp}}$ (solid lines) are determined largely by the error bars of the state lifetimes and branching ratios, as well as, to a minor degree, by the error bars of the above $\delta_{\rm exp}$, where applicable.

With respect to the $\Delta J = 2$ $E2$ transitions, all theoretical results have a good agreement with the experimental values

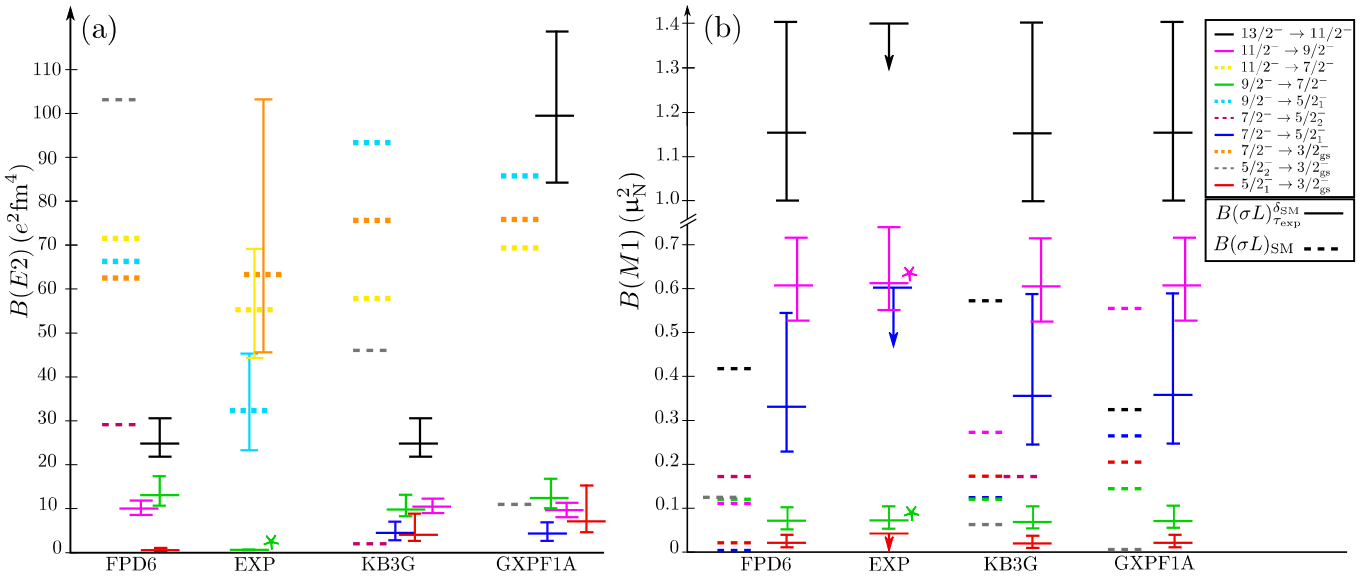

FIG. 7. Comparison of experimental $B(M1)_{\mathrm{exp}}$, $B(E2)_{\mathrm{exp}}$ values and results $B(\sigma L)_{\mathrm{SM}}$ (dashed lines) of the full *fp* shell-model calculations using the FPD6, GXPF1A, and KB3G interactions for transitions of mixed $E2/M1$ and pure $E2$ character in ^{53}Ti. For transitions where experimental $E2/M1$ multipole mixing ratios are available [21], the transition strengths are marked with an $*$, while for the other mixed transitions upper limits of the transition strengths were calculated by assuming the extreme cases of pure $E2$ transitions. $B(\sigma L)^{\delta_{\mathrm{SM}}}_{\tau_{\mathrm{exp}}}$ (solid lines) contains transition strengths, calculated from the experimental lifetimes using mixing ratios deduced from the respective shell-model $E2$ and $M1$ strength and the corresponding E_γ^{exp}. See text for details and Table II in the Appendix for the numerical values.

for the $7/2^- \to 3/2^-_{\mathrm{g.s.}}$ and $11/2^- \to 7/2^-$ transitions within the error bars, while the $9/2^- \to (5/2^-)$ transition strength is overestimated by all presented calculations [see Fig. 7(a)]. For the mixed $E2/M1$ transitions, obviously the upper limits of $B(E2)_{\mathrm{exp}}$ (not shown in Fig. 7) are much larger than the SM $E2$ strengths, and their magnitude shows that these transitions must have a dominant $M1$ character. This is nicely reproduced by the theory, which also predicts dominant $M1$ components. Using the SM $E2$ and $M1$ matrix elements of the corresponding interaction and the E_γ^{exp}, we calculate SM-based multipole mixing ratios (see Table II in the Appendix). Then, using these δ_{SM} and the experimental lifetimes, we calculate $B(M1)^{\delta_{\mathrm{SM}}}_{\tau_{\mathrm{exp}}}$ and $B(E2)^{\delta_{\mathrm{SM}}}_{\tau_{\mathrm{exp}}}$ (solid lines), which should present a more realistic estimate of "experimental" strengths than the upper limits of pure $E2$ or $M1$ strengths. Since the $E2$ strengths for mixed transitions ($\Delta J = 1$) are highly sensitive to the value of $\delta(E2/M1)$, only the more precise and extremely low $B(E2; 9/2^- \to 7/2^-)$ value could be meaningfully compared with the calculations, of which all fail to reproduce it. On the other hand, the $M1$ components are not so sensitive to the $\delta(E2/M1)$, and the resulting $B(M1)_{\mathrm{exp}}$ as well as $B(M1)^{\delta_{\mathrm{SM}}}_{\tau_{\mathrm{exp}}}$ values, could be used to test the SM interactions [see Fig. 7(b)].

When comparing the experimental and SM $B(M1)$ values presented in Fig. 7(b), one notices several points. The $B(M1)_{\mathrm{exp}}$ strength of the $9/2^- \to 7/2^-$ transition is well reproduced by all interactions. The $B(M1; 11/2^- \to 9/2^-)_{\mathrm{exp}}$ value is reproduced only by the GXPF1A interaction. Generally, the SM $M1$ strengths agree with the experimental upper limits for the $7/2^- \to (5/2^-)$ and $13/2^- \to 11/2^-$ transitions, but only GXPF1A matches the $B(M1)^{\delta_{\mathrm{SM}}}_{\tau_{\mathrm{exp}}}$ value for the $7/2^- \to 5/2^-_1$, while all of the other interactions underestimate the large $B(M1; 13/2^- \to 11/2^-)^{\delta_{\mathrm{SM}}}_{\tau_{\mathrm{exp}}}$ value by factor of 2 to 3.

The most interesting case for us presents the $M1$ strength of the $(5/2^-) \to 3/2^-$ transition. While both improved interactions, KB3G and GXPF1A, overestimate the $B(M1; (5/2^-) \to 3/2^-)_{\mathrm{exp}}$ limit by about a factor of 4 to 5, only the deficient FPD6 reproduces the experimental limit and the $B(M1)^{\delta_{\mathrm{SM}}}_{\tau_{\mathrm{exp}}}$ estimate correctly. An inspection of the leading neutron configurations for the relevant states (see Fig. 6) shows that the difference is found in the predicted nuclear structure of the $5/2^-_1$ state. While the FPD6 predicts a dominant neutron configuration $\nu f^8_{7/2} p^2_{3/2} f^1_{5/2}$ (∼55%) with the protons coupled to spin zero, in GXPF1A the dominant configuration is $\nu f^8_{7/2} p^3_{3/2}$ (∼36%) with the protons coupled to spin 2, as well as about 32% of $\nu f^8_{7/2} p^2_{3/2} p^1_{1/2}$. Although the calculations using the KB3G interaction predict a more mixed wave function made out of three leading neutron configurations, the main similarity to the calculations performed with the GXPF1A interaction and main difference to those using the FPD6 interaction is the considerable amount of (∼25%) $\nu f^8_{7/2} p^2_{3/2} p^1_{1/2}$ configuration. Thus, the relatively strong $B(M1; 5/2^-_1 \to 3/2^-)$ in KB3G and GXPF1A can be explained by spin-flip transitions $\nu p_{1/2} \leftrightarrow \nu p_{3/2}$. In contrast, the small $B(M1)$ value predicted by the FPD6 interaction corresponds to the strong decrease of spin-flip components $\nu p_{1/2} \leftrightarrow \nu p_{3/2}$.

As Fig. 5 shows, the FPD6 energy of the $5/2_1^-$ is significantly lower than the experiment value, while the $5/2_2^-$ state is close to the experimental $(5/2^-)$ state. In order to compare the properties of the $5/2_2^-$ states in the different interactions, we have shown their theoretical energies in Fig. 5, their configurations in Fig. 6 and results for two transitions in Fig. 7. Figure 6 reveals that the neutron configurations of the calculated $5/2_2^-$ states are more mixed, but the common feature for all interactions is that when compared to the corresponding $5/2_1^-$ state, there is an exchange of the dominant configurations with respect to the orbital where the odd neutron resides. To give an example, in FPD6 the $\nu f_{7/2}^8 p_{3/2}^2 f_{5/2}^1$ configuration is dominant in $5/2_1^-$, but one of the least in $5/2_2^-$. This yields a clearly changed amount of $\nu p_{1/2} \leftrightarrow \nu p_{3/2}$ strength for the $5/2_2^- \rightarrow 3/2^-$ $M1$ transition which is shown in Fig. 7(b). For each of the interactions, one can see the direct relation between the percentage of $\nu f_{7/2}^8 p_{3/2}^2 p_{1/2}^1$ in the wave functions of the $5/2_{1,2}^-$ states and their $M1$ strength to the ground state. Thus, apparently the "proper" amount of $\nu p_{1/2}^1$ component in the wave function of the $5/2_1^-$ state seems to be crucial in describing the $B(M1; 5/2_1^- \rightarrow 3/2^-)$ strength.

In addition to this main component, other $M1$ strengths could come from spin-flip transitions of the type $f_{7/2} \leftrightarrow f_{5/2}$. The amount of proton $f_{7/2} \leftrightarrow f_{5/2}$ components should be nearly independent of the neutron single-particle energies and proton-truncated calculations showed minimal effect on these SM $B(M1)$ strengths. Therefore, we have studied the effect of neutron excitations from the $f_{7/2}$ orbital across the $N = 28$ shell to the calculated $B(M1; 5/2_1^- \rightarrow 3/2^-)$ strength. In the case of FPD6, these effects work constructively and double the strength from $0.01\,\mu_N^2$, in the truncated calculation, to the $0.02\,\mu_N^2$ in the nontruncated one. On the other hand in KB3G and GXPF1A, the configurations with *np-nh* neutron excitations across the $N = 28$ shell work destructively, reducing the amount of $\nu p_{3/2}^3$ configuration in the $3/2_{\text{g.s.}}^-$ state and of the $\nu p_{3/2}^2 p_{1/2}^1$ configuration in the $5/2_1^-$ state, thus leading to a reduction of the $M1$ strengths down to the values shown in Fig. 7(b).

Altogether, we come to the conclusion, that the $B(M1; 5/2_1^- \rightarrow 3/2^-)$, as well as other $M1$ strengths in ^{53}Ti, play a special role in benchmarking and understanding the nuclear structure in this and neighboring nuclei. At the moment, none of the presented effective SM Hamiltonians could describe simultaneously all of the newly measured transition strengths. Therefore, it would be interesting to see how interactions including three-body forces [41] and, in particular, the microscopic $NN + 3N$ interaction [42] in the extended $pfg_{9/2}$ model space would perform for ^{53}Ti. Recently, this interaction was successfully used to describe the magnetic moment of the $3/2_{\text{g.s.}}^-$ in ^{51}Ca [43], which is the $N = 31$ isotone of ^{53}Ti. One should mention that this $NN + 3N$ interaction also predicts a "low-lying" $5/2_1^-$ state in ^{49}Ca, but nevertheless it describes the excited spectrum of ^{51}Ca similarly as well as KB3G, and better than GXPF1A (see Fig. 10 of Ref. [42]), which indicates that this interaction may well solve the issue of the $\nu p_{1/2}$ occupation and the $B(M1; 5/2_1^- \rightarrow 3/2^-)$ strength in ^{53}Ti.

V. SUMMARY

In this work, the $5/2^-$ to $15/2^-$ states of the yrast band in ^{53}Ti were populated in a multinucleon-transfer reaction and their lifetimes were measured with the recoil distance Doppler-shift technique for the first time. The analysis required a precise preparation of the data, followed by the extraction of lifetimes of the excited states by comparing the γ-ray line shapes from GEANT4 Monte-Carlo simulations with experimental Doppler-corrected transitions and a χ^2 minimization. Both the level scheme and the electric and magnetic transition probabilities were compared to predictions of shell-model calculations using the established fp interactions KB3G, GXPF1A, GXPF1B, and FPD6. The level scheme can be described best with KB3G, but also calculations with GXPF1A and GXPF1B perform fairly well. The transition probabilities are not reproduced simultaneously by any of the presented theoretical calculations. A special attention is drawn to the $B(M1; 5/2_1^- \rightarrow 3/2^-)$ value which is determined to be relatively low, in contradiction to the predictions of the established KB3G, GXPF1A, and GXPF1B interactions. An important aspect of that $M1$ strength is the amount of $\nu p_{1/2}^1$ components in the wave function of the yrast $(5/2^-)$ state. Further developments on the theory side are required in order to explain these transition strengths. Improved experimental information would be also beneficial. For example, due to missing $E2/M1$ mixing ratios, absolute transition probabilities for $\Delta J = 1$ transitions cannot be used for a further test of the performed SM calculations. Of similar importance is also the experimental identification of the $1/2_1^-$ state.

ACKNOWLEDGMENTS

The authors are grateful to the GANIL staff for the professional support during the experiment. The research leading to these results has received from the German BMBF under Contract Nos. 05P18PKFN9 and 05P19PKFNA, the European Union Seventh Framework through ENSAR under Contract No. 262010, and partially supported by Ministry of Science, Spain, under Grant Nos. FPA2017-84756-C4 and SEV-2014-0398, by the EU FEDER funds, and by the U.S. Department of Energy, Office of Science, Office of Nuclear Physics, under Contract No. DE-AC02-06CH11357.

APPENDIX: EXPERIMENTAL AND THEORETICAL RESULTS

The numerical values for results of the theoretical and experimental electric and magnetic transition strengths given in Fig. 7 are listed in Table II.

TABLE II. Experimental and theoretical transition energies E_γ and transition strengths $B(M1)$, $B(E2)$ using FPD6, KB3G, and GXPF1A interactions. For the two transitions where experimental $E2/M1$ multipole mixing ratios are available [21] the transitions strengths are marked with an $*$, while for the other mixed transitions upper limits of the transition strengths were calculated by assuming the extreme cases of pure $M1$ or $E2$ transition. The columns denoted by $B(\sigma L)^{\delta_{\rm SM}}_{\tau_{\rm exp}}$ contain transition strengths, calculated from the experimental lifetimes using mixing ratios deduced from the respective shell-model $E2$ and $M1$ strength and the corresponding $E_\gamma^{\rm exp}$.

Interaction	$J_i^\pi \to J_f^\pi$	$E_\gamma^{\rm exp}$ (keV)	$E_\gamma^{\rm SM}$ (keV)	$B(M1)_{\rm exp}$ (μ_N^2)	$B(E2)_{\rm exp}$ ($e^2{\rm fm}^4$)	$B(M1)^{\delta_{\rm SM}}_{\tau_{\rm exp}}$ (μ_N^2)	$B(E2)^{\delta_{\rm SM}}_{\tau_{\rm exp}}$ ($e^2{\rm fm}^4$)	$B(M1)_{\rm SM}$ (μ_N^2)	$B(E2)_{\rm SM}$ ($e^2{\rm fm}^4$)	$\delta(E2/M1)$ SM + $E_\gamma^{\rm exp}$
FPD6	$5/2_1^- \to 3/2^-_{\rm g.s.}$	1237	611	$\leqslant 0.04$	$\leqslant 370$	$0.02^{+0.02}_{-0.01}$	$0.44^{+0.48}_{-0.17}$	0.02	0.46	0.05
	$5/2_2^- \to 3/2^-_{\rm g.s.}$		1352					0.12	104.1	
	$7/2^- \to 3/2^-_{\rm g.s.}$	1576	1471	–	63^{+40}_{-18}	–	–	–	62.4	–
	$7/2^- \to 5/2_1^-$	339	860	$\leqslant 0.60$	$\leqslant 48000$	$0.33^{+0.22}_{-0.10}$	3900^{+2600}_{-1200}	0.002	28.4	0.31
	$7/2^- \to 5/2_2^-$		120					0.17	29.2	
	$9/2^- \to 5/2_1^-$	968	1124	–	32^{+13}_{-9}	–	–	–	66.2	–
	$9/2^- \to 5/2_2^-$		383					–	38.4	–
	$9/2^- \to 7/2^-$	629	264	$0.07^{+0.03}_{-0.02}*$	$0.47^{+0.16}_{-0.10}*$	$0.07^{+0.03}_{-0.02}$	$13.1^{+4.4}_{-2.6}$	0.12	23. 4	0.07
	$11/2^- \to 7/2^-$	921	1130	–	55^{+14}_{-11}	–	–	–	71.6	–
	$11/2^- \to 9/2^-$	292	866	$0.61^{+0.11}_{-0.08}*$	$280^{+230}_{-160}*$	$0.61^{+0.11}_{-0.08}$	$10.3^{+1.9}_{-1.4}$	0.11	0.95	0.01
	$13/2^- \to 11/2^-$	257	228	$\leqslant 1.40$	$\leqslant 30000$	$1.16^{+0.24}_{-0.17}$	$25.1^{+5.2}_{-3.7}$	0.42	20.4	0.01
KB3G	$5/2_1^- \to 3/2^-_{\rm g.s.}$	1237	1136	$\leqslant 0.04$	$\leqslant 370$	$0.02^{+0.02}_{-0.01}$	$4.4^{+4.8}_{-1.7}$	0.17	38.8	0.16
	$5/2_2^- \to 3/2^-_{\rm g.s.}$		1352					0.06	46.4	
	$7/2^- \to 3/2^-_{\rm g.s.}$	1576	1484	–	63^{+40}_{-18}	–	–	–	75.6	–
	$7/2^- \to 5/2_1^-$	339	348	$\leqslant 0.60$	$\leqslant 48000$	$0.36^{+0.24}_{-0.11}$	$4.5^{+2.9}_{-1.4}$	0.12	0.48	0.01
	$7/2^- \to 5/2_2^-$		132					0.17	2.35	
	$9/2^- \to 5/2_1^-$	968	987	–	32^{+13}_{-9}	–	–	–	93.3	–
	$9/2^- \to 5/2_2^-$		771					–	0.22	–
	$9/2^- \to 7/2^-$	629	639	$0.07^{+0.03}_{-0.02}*$	$0.47^{+0.16}_{-0.10}*$	$0.07^{+0.03}_{-0.02}$	$9.6^{+3.2}_{-1.9}$	0.12	14.9	0.06
	$11/2^- \to 7/2^-$	921	1095	–	55^{+14}_{-11}	–	–	–	57.8	–
	$11/2^- \to 9/2^-$	292	456	$0.61^{+0.11}_{-0.08}*$	$280^{+230}_{-160}*$	$0.61^{+0.11}_{-0.08}$	$10.3^{+1.9}_{-1.4}$	0.27	4.10	0.01
	$13/2^- \to 11/2^-$	257	251	$\leqslant 1.40$	$\leqslant 30000$	$1.16^{+0.24}_{-0.17}$	$25.1^{+5.2}_{-3.7}$	0.57	19.6	0.01
GXPF1A	$5/2_1^- \to 3/2^-_{\rm g.s.}$	1237	1356	$\leqslant 0.04$	$\leqslant 370$	$0.02^{+0.02}_{-0.01}$	$7.4^{+8.2}_{-2.8}$	0.20	81.4	0.21
	$5/2_2^- \to 3/2^-_{\rm g.s.}$		1742					0.002	11.0	
	$7/2^- \to 3/2^-_{\rm g.s.}$	1576	1413	–	63^{+40}_{-18}	–	–	–	75.8	–
	$7/2^- \to 5/2_1^-$	339	57	$\leqslant 0.60$	$\leqslant 48000$	$0.36^{+0.24}_{-0.11}$	$4.5^{+2.9}_{-1.4}$	0.26	0.94	0.01
	$9/2^- \to 5/2_1^-$	968	874	–	32^{+13}_{-9}	–	–	–	85.7	–
	$9/2^- \to 5/2_2^-$		488					–	0.02	–
	$9/2^- \to 7/2^-$	629	817	$0.07^{+0.03}_{-0.02}*$	$0.47^{+0.16}_{-0.10}*$	$0.07^{+0.03}_{-0.02}$	$13.1^{+4.4}_{-2.6}$	0.14	27.4	0.08
	$11/2^- \to 7/2^-$	921	975	–	55^{+14}_{-11}	–	–	–	69.3	–
	$11/2^- \to 9/2^-$	292	158	$0.61^{+0.11}_{-0.08}*$	$280^{+230}_{-160}*$	$0.61^{+0.11}_{-0.08}$	$10.3^{+1.9}_{-1.4}$	0.55	10.9	0.01
	$13/2^- \to 11/2^-$	257	389	$\leqslant 1.40$	$\leqslant 30000$	$1.16^{+0.24}_{-0.17}$	$100.4^{+20.9}_{-14.8}$	0.32	18.7	0.02

[1] E. K. Warburton, J. A. Becker, and B. A. Brown, Mass systematics for $A = 29$–44 nuclei: The deformed $A \sim 32$ region, Phys. Rev. C **41**, 1147 (1990).

[2] S. Chen, J. Lee, P. Doornenbal, A. Obertelli, C. Barbieri, Y. Chazono, P. Navrátil, K. Ogata, T. Otsuka, F. Raimondi *et al.*, Quasifree Neutron Knockout from ^{54}Ca Corroborates Arising $n = 34$ Neutron Magic Number, Phys. Rev. Lett. **123**, 142501 (2019).

[3] J. Prisciandaro, P. Mantica, B. Brown, D. Anthony, M. Cooper, A. Garcia, D. Groh, A. Komives, W. Kumarasiri, P. Lofy *et al.*, New evidence for a subshell gap at $N = 32$, Phys. Lett. B **510**, 17 (2001).

[4] S. N. Liddick, P. F. Mantica, R. Broda, B. A. Brown, M. P. Carpenter, A. D. Davies, B. Fornal, T. Glasmacher, D. E. Groh, M. Honma *et al.*, Development of shell closures at $N = 32, 34$. I. β decay of neutron-rich Sc isotopes, Phys. Rev. C **70**, 064303 (2004).

[5] A. Gade, R. V. F. Janssens, D. Bazin, R. Broda, B. A. Brown, C. M. Campbell, M. P. Carpenter, J. M. Cook, A. N. Deacon, D.C. Dinca, B. Fornal, S. J. Freeman, T. Glasmacher, P.G. Hansen, B. P. Kay, P. F. Mantica, W. F. Mueller, J. R. Terry, J. A. Tostevin, and S. Zhu, Cross-shell excitation in two-proton knockout: Structure of ^{52}Ca, Phys. Rev. C **74**, 021302(R) (2006).

[6] D. Steppenbeck, S. Takeuchi, N. Aoi, P. Doornenbal, M. Matsushita, H. Wang, H. Baba, N. Fukuda, S. Go, M. Honma *et al.*, Evidence for a new nuclear 'magic number' from the level structure of ^{54}Ca, Nature **502**, 207 (2013).

[7] A. Goldkuhle, C. Fransen, A. Blazhev, M. Beckers, B. Birkenbach, T. Braunroth, E. Clément, A. Dewald, J. Dudouet, J. Eberth *et al.* (AGATA Collaboration), Lifetime measurements in ^{52,54}Ti to study shell evolution toward $N = 32$, Phys. Rev. C **100**, 054317 (2019).

[8] K.-H. Speidel, J. Leske, S. Schielke, S. Bedi, O. Zell, P. Maier-Komor, S. Robinson, Y. Sharon, and L. Zamick, Low-level structure of ^{52}Ti based on g factor and lifetime measurements, Phys. Lett. B **633**, 219 (2006).

[9] R. V. F. Janssens, B. Fornal, P. F. Mantica, B. A. Brown, R. Broda, P. Bhattacharyya, M. P. Carpenter, M. Cinausero, P. J. Daly, A. D. Davies *et al.*, Structure of ^{52,54}Ti and shell closures in neutron-rich nuclei above ^{48}Ca, Phys. Lett. B **546**, 55 (2002).

[10] D. C. Dinca, R. V. F. Janssens, A. Gade, D. Bazin, R. Broda, B. A. Brown, C.M. Campbell, M. P. Carpenter, P. Chowdhury, J. M. Cook, A. N. Deacon, B. Fornal, S. J. Freeman, T. Glasmacher, M. Honma, F. G. Kondev, J. L. Lecouey, S. N. Liddick, P. F. Mantica, W. F. Mueller, H. Olliver, T. Otsuka, J.R. Terry, B. A. Tomlin, and K. Yoneda, Reduced transition probabilities to the first 2^+ state in ^{52,54,56}Ti and development of shell closures at $N = 32, 34$, Phys. Rev. C **71**, 041302(R) (2005).

[11] S. Zhu, R. Janssens, B. Fornal, S. Freeman, M. Honma, R. Broda, M. Carpenter, A. Deacon, B. Kay, F. Kondev *et al.*, One-particle excitations outside the ^{54}Ti semi-magic core: The ^{55}V and ^{55}Ti yrast structures, Phys. Lett. B **650**, 135 (2007).

[12] A. Gade, R. V. F. Janssens, D. Bazin, B. A. Brown, C. M. Campbell, M. P. Carpenter, J. M. Cook, A. N. Deacon, D.-C. Dinca, S. J. Freeman *et al.*, One-neutron knockout in the vicinity of the $N = 32$ sub-shell closure: ^{9}Be(^{57}Cr, ^{56}Cr $+\gamma$)X, Phys. Rev. C **74**, 047302 (2006).

[13] P. Maierbeck, Untersuchung von Ein-Teilchen-Zuständen in neutronenreichen Kalzium- und Titanisotopen, Dissertation, Technische Universität München (2009).

[14] M. Niikura, E. Ideguchi, N. Aoi, H. Baba, T. Fukuchi, Y. Ichikawa, H. Iwasaki, T. Kubo, M. Kurokawa, M. Liu *et al.*, Yrast spectroscopy in $^{49-51}$Ti via fusion-evaporation reaction induced by a radioactive beam, Euro. Phys. J. A **42**, 471 (2009).

[15] N. Taccetti, P. A. Mando, P. Sona, and K. P. Lieb, Lifetime measurements in ^{49}Ca and ^{51}Ti, J. Phys. G **13**, 393 (1987).

[16] P. A. Mandò, G. Poggi, P. Sona, and N. Taccetti, γ decay and lifetimes of excited levels in ^{49}Ti, Phys. Rev. C **23**, 2008 (1981).

[17] J. Weaver, M. Grace, D. Start, R. Zurmühle, D. Balamuth, and J. Noé, Lifetime and angular-correlation measurements in ^{47}Ti, Nucl. Phys. A **196**, 269 (1972).

[18] A. Dhar, D. Kulkarni, and K. Bhatt, The energy spectra and electromagnetic transitions of odd-a titanium isotopes, Nucl. Phys. A **285**, 93 (1977).

[19] A. K. Dhar and K. H. Bhatt, Effective charges and $E2$ transitions in $1f - 2p$ shell nuclei, Phys. Rev. C **16**, 792 (1977).

[20] L. A. Parks, C. N. Davids, and R. C. Pardo, β decay and mass of the new neutron-rich isotope ^{53}Ti, Phys. Rev. C **15**, 730 (1977).

[21] B. Fornal, S. Zhu, R. V. F. Janssens, M. Honma, R. Broda, B. A. Brown, M. P. Carpenter, S. J. Freeman, N. Hammond, F. G. Kondev *et al.*, Yrast structure of neutron-rich ^{53}Ti, Phys. Rev. C **72**, 044315 (2005).

[22] A. Goldkuhle, C. Fransen, A. Dewald, N. Alahari, M. Beckers, B. Birkenbach, A. Blazhev, T. Braunroth, E. Clément, G. De France *et al.*, Preliminary results of lifetime measurements in neutron-rich ^{53}Ti, EPJ Web Conf. **223**, 01022 (2019).

[23] S. Akkoyun, A. Algora, B. Alikhani, F. Ameil, G. de Angelis, L. Arnold, A. Astier, A. Ataç, Y. Aubert, C. Aufranc *et al.*, AGATA-Advanced GAmma Tracking Array, Nucl. Instrum. Methods Phys. Res. A **668**, 26 (2012).

[24] E. Clément, C. Michelagnoli, G. de France, H. Li, A. Lemasson, C. B. Dejean, M. Beuzard, P. Bougault, J. Cacitti, J.-L. Foucher *et al.*, Conceptual design of the AGATA 1π array at GANIL, Nucl. Instrum. Methods Phys. Res. A **855**, 1 (2017).

[25] S. Pullanhiotan, M. Rejmund, A. Navin, W. Mittig, and S. Bhattacharyya, Performance of VAMOS for reactions near the Coulomb barrier, Nucl. Instrum. Methods Phys. Res. A **593**, 343 (2008).

[26] M. Rejmund, B. Lecornu, A. Navin, C. Schmitt, S. Damoy, O. Delaune, J. Enguerrand, G. Fremont, P. Gangnant, L. Gaudefroy *et al.*, Performance of the improved larger acceptance spectrometer: VAMOS++, Nucl. Instrum. Methods Phys. Res. A **646**, 184 (2011).

[27] M. Vandebrouck, A. Lemasson, M. Rejmund, G. Frémont, J. Pancin, A. Navin, C. Michelagnoli, J. Goupil, C. Spitaels, and B. Jacquot, Dual Position Sensitive MWPC for tracking reaction products at VAMOS++, Nucl. Instrum. Methods Phys. Res. A **812**, 112 (2016).

[28] A. Dewald, O. Möller, and P. Petkov, Developing the recoil distance Doppler-Shift technique towards a versatile tool for lifetime measurements of excited nuclear states, Prog. Part. Nucl. Phys. **67**, 786 (2012).

[29] Ch. Stodel, M. Toulemonde, C. Fransen, B. Jacquot, E. Clément, G. Frémont, M. Michel, and C. Dufour, "Thermal Spike" model applied to thin targets irradiated with swift heavy ion beams at few MeV/u, EPJ Web Conf. **229**, 05001 (2020).

[30] A. Dewald, S. Harissopulos, and P. von Brentano, The differential plunger and the differential decay curve method for the analysis of recoil distance Doppler-shift data, Z. Phys. A **334**, 163 (1989).

[31] S. Agostinelli, J. A. K. Amako, J. Apostolakis, H. Araujo, P. Arce, M. Asai, D. Axen, S. Banerjee, G. Barrand, F. Behner *et al.*, Geant4-a simulation toolkit, Nucl. Instrum. Methods Phys. Res. A **506**, 250 (2003).

[32] T. Braunroth (private communication, 2019).

[33] R. Brun and F. Rademakers, ROOT – An object oriented data analysis framework, Nucl. Instrum. Methods Phys. Res. A **389**, 81 (1997), new computing techniques in Physics Research V .

[34] W. Richter, M. V. D. Merwe, R. Julies, and B. Brown, New effective interactions for the 0f1p shell, Nucl. Phys. A **523**, 325 (1991).

[35] M. Honma, T. Otsuka, B. A. Brown, and T. Mizusaki, Shell-model description of neutron-rich pf-shell nuclei with a new effective interaction GXPF1, Euro. Phys. J. A **25**, 499 (2005).

[36] B. Brown and W. Rae, The Shell-Model Code NuShellX@MSU, Nucl. Data Sheets **120**, 115 (2014).

[37] A. Poves, J. Sánchez-Solano, E. Caurier, and F. Nowacki, Shell model study of the isobaric chains $A = 50$, $A = 51$ and $A = 52$, Nucl. Phys. A **694**, 157 (2001).

[38] M. Honma, T. Otsuka, and T. Mizusaki, Shell-model description of neutron-rich Ca isotopes, RIKEN Accel. Prog. Rep. **41**, 32 (2008).

[39] M. Dufour and A. P. Zuker, Realistic collective nuclear Hamiltonian, Phys. Rev. C **54**, 1641 (1996).

[40] J. M. Blatt, V. F. Weisskopf, *Theoretical Nuclear Physics* (Springer-Verlag, New York, 1979).

[41] H.-W. Hammer, A. Nogga, and A. Schwenk, Colloquium: Three-body forces: From cold atoms to nuclei, Rev. Mod. Phys. **85**, 197 (2013).

[42] J. D. Holt, J. Menéndez, J. Simonis, and A. Schwenk, Three-nucleon forces and spectroscopy of neutron-rich calcium isotopes, Phys. Rev. C **90**, 024312 (2014).

[43] R. F. GarciaRuiz, M. L. Bissell, K. Blaum, N. Frommgen, M. Hammen, J. D. Holt, M. Kowalska, K. Kreim, J. Menendez, R. Neugart, G. Neyens, W. Nortershauser, F. Nowacki, J. Papuga, A. Poves, A. Schwenk, J. Simonis, and D. T. Yordanov, Ground-state electromagnetic moments of calcium isotopes, Phys. Rev. C **91**, 041304(R) (2015).

Discussion and conclusions

The aim of the presented studies was the investigation of effects in the shell structure of neutron-rich Ti isotopes around the neutron subshell closure at $N = 32$ far from stability by means of the electric and magnetic transition strengths. In the following, the content of the individual publications is briefly summarized.

In the first part of this work, the publication "Lifetime measurement of excited states in ^{46}Ti" [80] presents the results of an RDDS experiment on ^{46}Ti including the determination of lifetime values. Excited nuclear states in ^{46}Ti were populated in a fusion-evaporation reaction at a ^{9}Be beam energy of 33 MeV at the Cologne FN tandem accelerator. The advantage of this RDDS experiment over previous experiments is that the obtained data could be evaluated in $\gamma\gamma$ coincidences. For this purpose, the DDCM was used in the $\gamma\gamma$-coincidence mode to determine precise and reliable lifetime values of the first excited 2_1^+ to 6_1^+ states and an upper limit of the lifetime for the 8_1^+ state. The results of this chosen analysis method have a smaller uncertainty than the published average values.
Although in the past a large number of experiments were performed on this nucleus, the published data were sometimes contradictory or afflicted with considerable uncertainty. A possible reason could be the experimental techniques used. Out of a large number of experiments, the RDDS technique was used in only one experiment. However, in that experiment no $\gamma\gamma$-coincidences were analyzed, thus unobserved delayed feeding cannot be completely ruled out. The data of the remaining experiments were analyzed using the DSA method, which is generally not well suited for the expected lifetimes. A precise lifetime determination especially for the 2_1^+ and 4_1^+ state was necessary for the distance determination between the target and degrader foil in the main experiment performed at GANIL.

The second publication of this work "Lifetime measurements in ^{52,54}Ti to study shell evolution toward $N = 32$" [81] presents results of lifetimes and reduced transition strengths in ^{52,54}Ti of low-lying states of their yrast bands. Neutron-rich Ti isotopes were populated in a multinucleon-transfer reaction with a ^{238}U beam at 6.76 MeV/u impinging on a ^{50}Ti target in an RDDS experiment at GANIL. For the analysis, the distances between the target and degrader foil had to be reproduced first, which could not be determined in a conventional way due to unexpected beam-induced changes of the target. Using the precise lifetimes in ^{46}Ti [80], determined in the first part of this thesis, it was possible to determine the unknown distances with Monte-Carlo simulations by comparing simulated and experimental γ-ray spectra using the minimum χ^2 method. The resulting distances were used for the further lifetime analysis in which the lifetime values of the first excited states in ^{52,54}Ti were determined by evaluating the γ-ray singles spectra using the DDCM. The obtained results were additionally verified by a χ^2 minimization between experimental

and simulated γ-ray spectra.

In ^{54}Ti there was only a literature value for the lifetime of the 2_1^+ state from an earlier Coulomb-excitation experiment [68], which is consistent with the value remeasured in this work within the error limits. For the first time, the lifetime of the 4_1^+ state as well as an upper lifetime limit of the 6_1^+ state in ^{54}Ti was determined in this thesis. The neighboring ^{52}Ti had already been significantly further researched. Here literature values of the lifetimes of the 2_1^+, 4_1^+ and 6_1^+ states existed. However, the previous experimental values in ^{52}Ti behaved unusually compared to its neighbors ^{50}Ti and ^{54}Ti. The new $B(E2; 2_1^+ \rightarrow 0_{gs}^+)$ and $B(E2; 6_1^+ \rightarrow 4_1^+)$ values are smaller than the previous values, while the $B(E2; 4_1^+ \rightarrow 2_1^+)$ value is larger than the previous value and thus a similar picture of the transition strengths depending on the spin as that of the neighboring nuclei is obtained. The excitation energies and the obtained transition strengths of the two nuclei were compared with shell-model calculations using different interactions (GXPF1A/B, KB3G, FPD6). In both nuclei a consistent picture was obtained. In particular, the good agreement of the trend between theoretical and experimental transition strengths in ^{52}Ti should be emphasized. With its new $B(E2)$ values, a long time unsolved mystery could be solved. Existing values prior to this work showed large differences to the predictions of shell-model calculations using the mentioned interactions, as theoretical predictions could not even reproduce the trend of the experimental values. In addition to the established interactions used, the modified GXPF1B [17] interaction, called GXPF1B-nf7, was introduced by the authors of the publication, where the single-particle energy of the $\nu 1f_{7/2}$ orbital was lowered by 1 MeV. With the predictions of this interaction, significantly improved results were obtained for the transition strengths in ^{50}Ti compared to the other used interactions. For ^{52,54}Ti, the GXPF1B-nf7 interaction as well as the GXPF1B interaction describe the experimental data well.

The third publication "Preliminary results of lifetime measurements in neutron-rich ^{53}Ti" [82] includes preliminary results of a lifetime analysis of ^{53}Ti using the same data set as the second publication. In this work, a total of five lifetimes ($(5/2^-)$ to $13/2^-$) of the yrast band in ^{53}Ti could be evaluated for the first time, also using the DDCM. The results have to be considered as preliminary, because they do not include a correction for the DSAM effects observed after using of the analysis method.

This correction is described in the fourth publication "Lifetime measurements of excited states in neutron-rich ^{53}Ti: benchmarking effective shell-model interactions" [83], in which final lifetime values in ^{53}Ti are presented by correcting the mentioned DSAM effect from the third publication. For this purpose, the lifetimes of the $(5/2^-)$ to $13/2^-$ states were determined using the minimum χ^2 method instead of the DDCM, in a similar way as the lifetime determination described in the second publication. Furthermore, the experimental excitation energies were compared with the predictions of shell-model calculations of

established interactions in the fp shell (GXPF1A/B, KB3G and FPD6). The KB3G interaction best reproduces the experimental excitation energies, but calculations with the GXPF1A and GXPF1B interactions perform fairly well, too. The calculation with the FPD6 interaction shows significant deviations, with the gaps between the $5/2^-_1$ and $7/2^-$ levels and between the $9/2^-$ and $11/2^-$ levels being determined to be clearly too large. The low-lying $5/2^-_1$ state as well as the inversion of the $1/2^-_1$ and $5/2^-_1$ levels is still noticeable. Although the calculations with the different interactions satisfactorily describe the experimental level energies, none of the interactions used can fully reflect the corresponding transition strengths. The $B(M1; 5/2^-_1 \rightarrow 3/2^-)$ value is a peculiarity, as this value contradicts the relatively low value predicted by the theoretical calculations. The contribution of the $M1$ strength of the $\nu p^1_{1/2}$ component in the wave function of the $(5/2^-)$ state is important. However, further developments on the theoretical side are needed to explain these strengths and improved experimental information would be beneficial. A decisive quantity that would clearly specify the statements of the specific transition strengths would be the $E2/M1$ mixing ratio for $J = 1$ transitions, which is still missing. According to the systematics of the $3/2^-$, $1/2^-$, and $5/2^-$ states of the neighboring nuclei, i.e. ^{55}Cr and ^{51}Ca, the previously unobserved $1/2^-$ state in ^{53}Ti should also be energetically lower than the $(5/2^-)$ state. Since the experimental results of this paper suggest a revision of some matrix elements in the theoretical calculations, it is even more important to identify the $1/2^-$ state experimentally in order to know the position of this state.

The two presented measurements of this work were complemented by an additional RDDS experiment performed at the 10 MV FN tandem accelerator of the University of Cologne with the aim of measuring the lifetimes of the 2^+_1 and 4^+_1 states in ^{50}Ti. The discrepancy between the experimentally determined $B(E2; 2^+_1 \rightarrow 0^+_{\mathrm{gs}})$ value in the Coulomb-excitation experiment described in Ref. [27] and predictions of shell-model calculations using different interactions motivated a re-measurement of the lifetime values especially for the 2^+_1 state. To populate ^{50}Ti isotopes, the proton-transfer reaction ^{51}V(^{11}B,^{12}C)^{50}Ti at a beam energy of 21.5 MeV was used. The recoiling nuclei were produced in a 0.6 mg/cm^2 thick ^{51}V target and were stopped in a 2.8 mg/cm^2 thick Nb foil. The γ rays were detected using eleven single-crystal HPGe detectors placed in two angular rings - six detectors in the forward direction ($\theta_1 = 45°$) and five detectors in the backward direction ($\theta_2 = 142.3°$). Additionally, an array of six solar cell detectors at backward angles between 115° and 165° for detection of recoiling light reactions fragments was placed in the plunger chamber at a distance of about 15 mm between their centers and the target. The data were collected at 9 target-to-stopper distances in a range near the electrical contact up to 800 µm, each of which was measured about 24 hours. The level lifetimes of the 2^+_1 and 4^+_1 states were analyzed in a particle-gamma analysis using the DDCM, whose results are shown in Fig. A.1 in the Appendix A. For a $\gamma\gamma$- or even particle-$\gamma\gamma$-analysis, the statistics were unfortunately not sufficient. Although this nucleus was also populated in the main experiment at GANIL

and lifetimes could be obtained in γ-ray singles using the DDCM, the Cologne experiment provides more reliable results due to the larger number of plunger distances in the sensitive range as well as the knowledge of the relative distances.

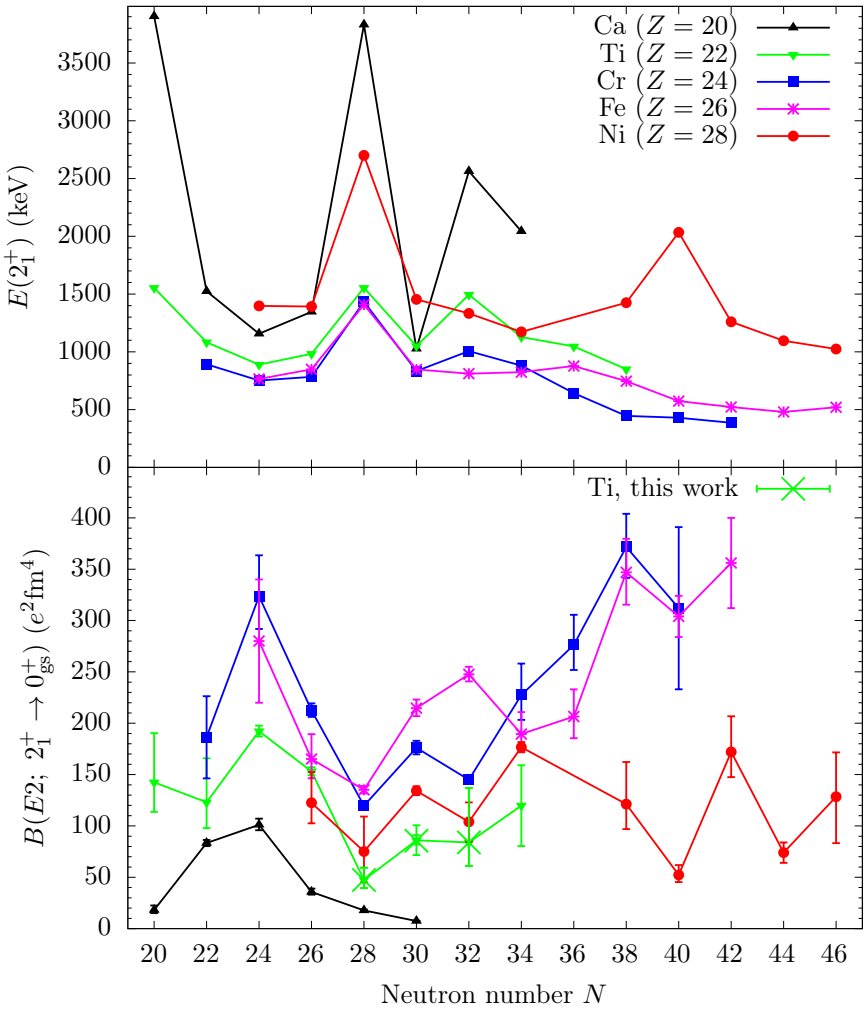

Figure 6.1.: Systematics of $E(2_1^+)$ and $B(E2; 2_1^+ \rightarrow 0_{gs}^+)$ values in even-even nuclei with $20 \leq Z \leq 28$ and $20 \leq N \leq 46$. For references of the experimental values, see Table C.1 in the Appendix.

Fig. 6.1 shows the systematics of the 2_1^+ excitation energies as well as the $B(E2; 2_1^+ \rightarrow 0_{gs}^+)$ values for the even-even nuclei with $20 \leq Z \leq 28$ and $20 \leq N \leq 46$, including the results obtained in this thesis (marked with green crosses).
The distinct local maximum of the $E(2_1^+)$ values reflecting the considerable energy gap and the corresponding local minimum of the $B(E2; 2_1^+ \rightarrow 0_{gs}^+)$ values comparable to single-particle estimates characterize the neutron shell closure at $N = 28$. The $B(E2; 2_1^+ \rightarrow 0_{gs}^+)$ value in ^{50}Ti of $46^{+8}_{-6}\, e^2\text{fm}^4$ remeasured in this work is smaller compared to the previous

literature value of $55(2)\,e^2\mathrm{fm}^4$ [1], but within the error limits, the values are compatible. On the one hand, the local minimum in the $B(E2; 2_1^+ \rightarrow 0_{\mathrm{gs}}^+)$ values is amplified by the newly determined value in ^{50}Ti, on the other hand the discrepancy to the predictions for this transition of the shell-model calculations is increased. A modification of the matrix elements or the increase of the valence space in the theoretical calculations could lead to a proper description of the experimental results. The measured lifetime value $\tau = 6.5(3)\,\mathrm{ps}$ for the 4_1^+ state corresponds to $B(E2; 4_1^+ \rightarrow 2_1^+) = 71(3)\,e^2\mathrm{fm}^4$ and it is consistent with the previous result of $B(E2; 4_1^+ \rightarrow 2_1^+) = 60(12)\,e^2\mathrm{fm}^4$ [85] within the errors. The uncertainty of the value was reduced from 20 % of the literature value to ∼5 %. At the same time, the discrepancy between experimental results and predictions of shell-model calculations could be reduced by the larger determined $B(E2; 4_1^+ \rightarrow 2_1^+)$ value. In particular, the GXPF1B-nf7 interaction introduced in the second publication yields $B(E2; 4_1^+ \rightarrow 2_1^+) = 69\,e^2\mathrm{fm}^4$ and thus it results in an excellent agreement with the newly determined experimental value.

At $N = 32$, a slightly different picture results: In case of Ti, a similar peaking of the 2_1^+ excitation energy is observed as for the Ca isotopes, although with a reduced amplitude (see Fig. 6.1). For Cr, this effect is much weaker and for Fe and Ni completely disappears. This behavior implies the existence of a reduced subshell closure at $N = 32$ in the Ti isotopes and has been confirmed in mass measurements [71]. Regarding the $B(E2)$ systematics, the new results in Ti show almost no minimum at $N = 32$ and a staggering of the $B(E2; 2_1^+ \rightarrow 0_{\mathrm{gs}}^+)$ values is no longer visible, which earlier experiments showed. However, due to the smaller uncertainty, the measured value for ^{54}Ti in Ref. [68] seems more reliable and the amplitude of the staggering is significantly weakened by the newly determined, smaller $B(E2; 2_1^+ \rightarrow 0_{\mathrm{gs}}^+)$ value in ^{52}Ti compared to the previous measurement in Ref. [28]. The anti-correlation between the two observables, i.e. the 2_1^+ excitation energy and the transition strengths, from both experimental and theoretical results confirm the subshell closure in ^{54}Ti, which, however, is weaker compared to its counterpart at $N = 28$. The magic feature in ^{54}Ti can be explained by the monopole component of the proton-neutron tensor force [86–88]. Figure 6.2 illustrates the formation of the subshell closure at $N = 32$. At ^{60}Ni, the $\nu 1f_{5/2}$ orbital is energetically close to the $\nu 2p_{3/2}$ orbital and no $N = 32$ shell closure is observed. This absence of a subshell closure is manifested in the decrease of the 2_1^+ excitation energies from ^{58}Ni to ^{60}Ni. By decreasing the number of protons in the $\pi 1f_{7/2}$ orbital, i.e. from nickel to calcium via titanium, the $\nu 1f_{5/2}$ orbital becomes less bound, and at ^{54}Ti the order of the $\nu 1f_{5/2}$ and $\nu 2p_{1/2}$ orbitals is inverted. The raising of the $\nu 1f_{5/2}$ orbital produces a gap between the lower-lying $\nu 2p_{3/2}$ orbital and the higher-lying $\nu 1f_{5/2}$ and $\nu 2p_{1/2}$ orbitals, so that a $N = 32$ subshell closure appears at ^{54}Ti [74]. With further reduction of the proton number by two, i.e. calcium, an additional subshell closure appears at $N = 34$ by increasing the magnitude of the $\nu p_{1/2} - \nu f_{5/2}$ energy gap and has been experimentally confirmed by γ-ray spectroscopy of ^{54}Ca [74]. This effect can be explained by the strong attractive

[1] weighted mean of $56^{+3}_{-2}\,e^2\mathrm{fm}^4$ Ref. [27] and $52^{+6}_{-5}\,e^2\mathrm{fm}^4$ Ref. [84].

force between the $\pi 1f_{7/2}$ and $\nu 1f_{5/2}$ orbitals where the tensor and central forces provide an additional contribution, since the addition of protons in the $\pi 1f_{7/2}$ orbital lowers the single-particle energy of the neutron $\nu 1f_{5/2}$ orbital.

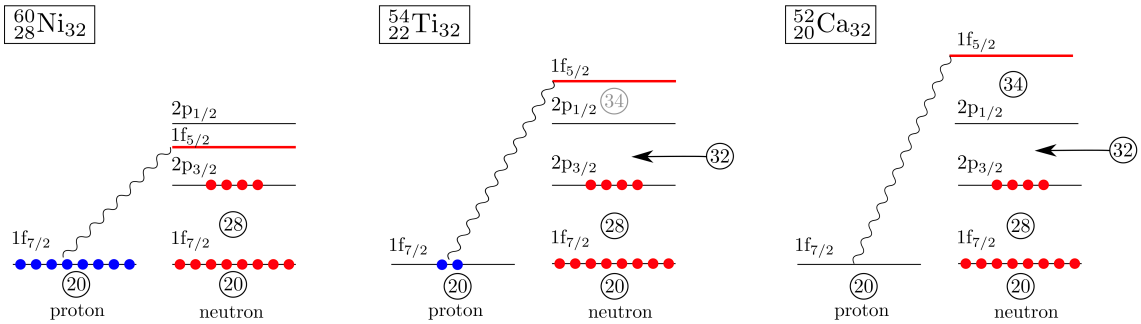

Figure 6.2.: Schematic illustration of the shell evolution by the influence of the monopole interaction produced by the tensor force on the single-particle energy of the $\nu 1f_{5/2}$ orbital from nickel to calcium via titanium for $N = 32$ [20]. See text for details.

Also, the theoretical results presented in the fourth publication on the investigations of ^{53}Ti, the direct one-hole neighbor of ^{54}Ti, support the shell closure at $N = 32$. As shown, the $(5/2^-)$ state in this nucleus plays an important role in benchmarking and understanding the nuclear structure in this and neighboring nuclides. Although the FPD6 interaction does not adequately represent the excitation energies, it is the only one that predicts the low $M1$ strength of the $5/2^-_1 \rightarrow 3/2^-_1$ transition, in contrast to the KB3G and GXPF1A/B interactions. This effect is supported by the dominant neutron configuration $\nu f^8_{7/2} p^2_{3/2} f^1_{5/2}$ (55%), which forecasts the $\nu f_{5/2} \leftrightarrow \nu p_{3/2}$ transition mainly from single-particle nature. The wave functions of the other interactions are of a stronger mixed character, predicting considerable (25-32 %) configurations with a single neutron in the $\nu p_{1/2}$ orbital including other particles coupled to 2^+. Although the occupation of the $\nu p_{1/2}$ orbital is in agreement with the $N = 32$ shell closure, the suggested presence of configurations with the occupation of this orbital implies a strong coupling to the $\nu p_{3/2}$ orbital and spin-flip transitions of the type $\nu p_{1/2} \leftrightarrow \nu p_{3/2}$, which leads to an increased $M1$ strength for the $5/2^-_1 \rightarrow 3/2^-_1$ transition. However, the interactions which do not fully reflect the experimental transitions strengths may require a revision of some matrix elements, which calls for a larger experimental data set including the new results.

Summarized, in this work 17 lifetime values as well as 2 lifetime limits in ^{46,50,52,53,54}Ti were determined, partly for the first time. The newly determined $B(E2; 2^+_1 \rightarrow 0^+_{gs})$ values in the even-even nuclei ^{50,52,54}Ti weaken the fluctuation of these $B(E2)$ values from preceding investigations and mostly provide a better agreement with the predictions of established shell-model calculations. The subshell closure at $N = 32$ was confirmed with the results of the present thesis.

Future work and experiments in the titanium region

The shell evolution around the neutron subshell closure at $N = 32$ in neutron-rich Ti isotopes was further investigated in the available studies. In addition to the nuclei evaluated in the present work, the same data set can be used to determine the lifetime of the 6_1^+ state in the stable nucleus ^{48}Ti that has been populated in the multinucleon-transfer reaction, too. Figure 6.3 shows the Doppler-corrected γ-ray spectrum for ^{48}Ti (*left*) and the evolution of the shifted and unshifted components at three different distances for the $6_1^+ \rightarrow 4_1^+$ transition (*right*). The authors of Refs. [89, 90] could previously only determine lower limits with $> 1.8\,\text{ps}$ and $> 10\,\text{ps}$ for the 6_1^+ state in ^{48}Ti using the DSA method, so an exact analysis is still missing.

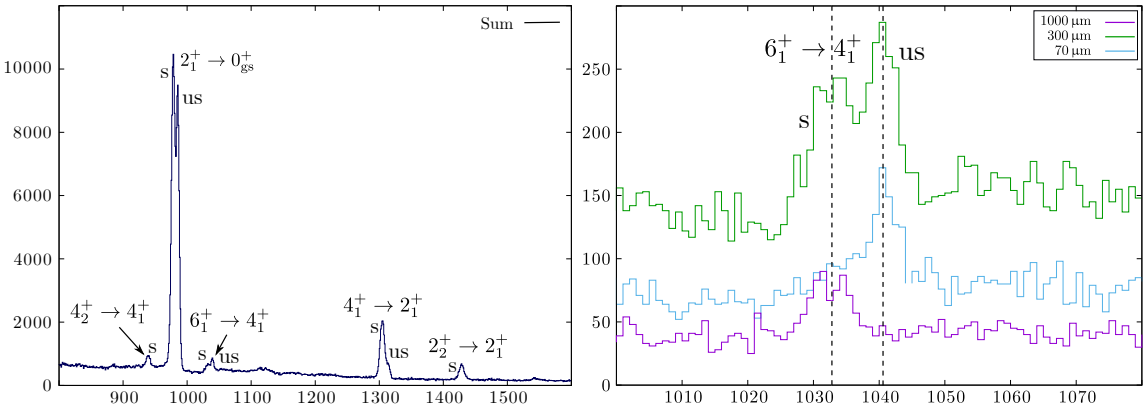

Figure 6.3.: *Left:* Doppler-corrected γ-ray spectrum in coincidence with ions identified as ^{48}Ti, summed up over all six distances. In this energy range, five transitions are observed. Spin-parity assignments taken from Ref. [91]. *Right:* Doppler-corrected γ-ray spectra from the $6_1^+ \rightarrow 4_1^+$ transition at three different distances (label: 70 µm, 300 µm, and 1000 µm.)

With respect to the results obtained in this thesis, it is of interest to close the gaps on experimental mixing ratios in the odd-mass ^{53}Ti in order to be able to interpret the experimental results in more detail. Angular distribution measurements are suitable for this purpose. In addition, it is important to identify the $1/2^-$ state predicted by the shell-model calculations in order to determine both the sequence of the single-particle energies, since various interactions make different predictions, and to explain the resulting position of the $\nu p_{1/2}$ orbital.

The experiment at GANIL was motivated to determine lifetimes not only in ^{54}Ti but also in ^{55}V and ^{56}Ti. However, the statistics of the γ-ray spectra are far too small in the individual distances for a reliable lifetime determination of these two nuclei. Detailed studies on these nuclei as well as even much more exotic titanium isotopes like ^{58,60,62}Ti are of great interest due to the low number of studies so far [68, 92, 93].

This brings us closer to the island of inversion around $N = 40$ in north-east direction

of the nuclear map. Since the nuclides $^{58-60}$Cr, $^{59-63}$Mn, and ^{64}Fe in this region have been only recently thoroughly investigated [58, 62, 64], the neighboring island of inversion around $N = 50$, especially for chromium and iron, could be studied in a next step. On theoretical side, a fusion of the two latter islands [94] is expected, and on the experimental side, first steps in the investigation of chromium isotopes beyond $N = 40$ were already made in Ref. [95]. Further experiments are needed to study the structure in more detail. Such experiments on very exotic atomic nuclei in this region could take place at the GSI Darmstadt. Within the FAIR project (**F**acility **f**or **A**ntiproton and **I**on **R**esearch) [96], an increase in the intensity of the available radioactive secondary beams by up to a factor of 10000 compared to the current facility is expected. This will be achieved by the use of superconducting synchrotrons as well as by a higher acceptance of all components for beam guidance and a six-stage Super FRS [97]. This allows the investigation of radioactive nuclei far from stability with extreme neutron-proton asymmetry. Alternatively, the new **F**acility for **R**are **I**sotope **B**eams (FRIB) at the Michigan State University could be used for similar studies, for which the first experiments have only recently been proposed, including the two islands of inversion around $N = 40$ and $N = 50$.

A. Lifetime curves for ^{50}Ti

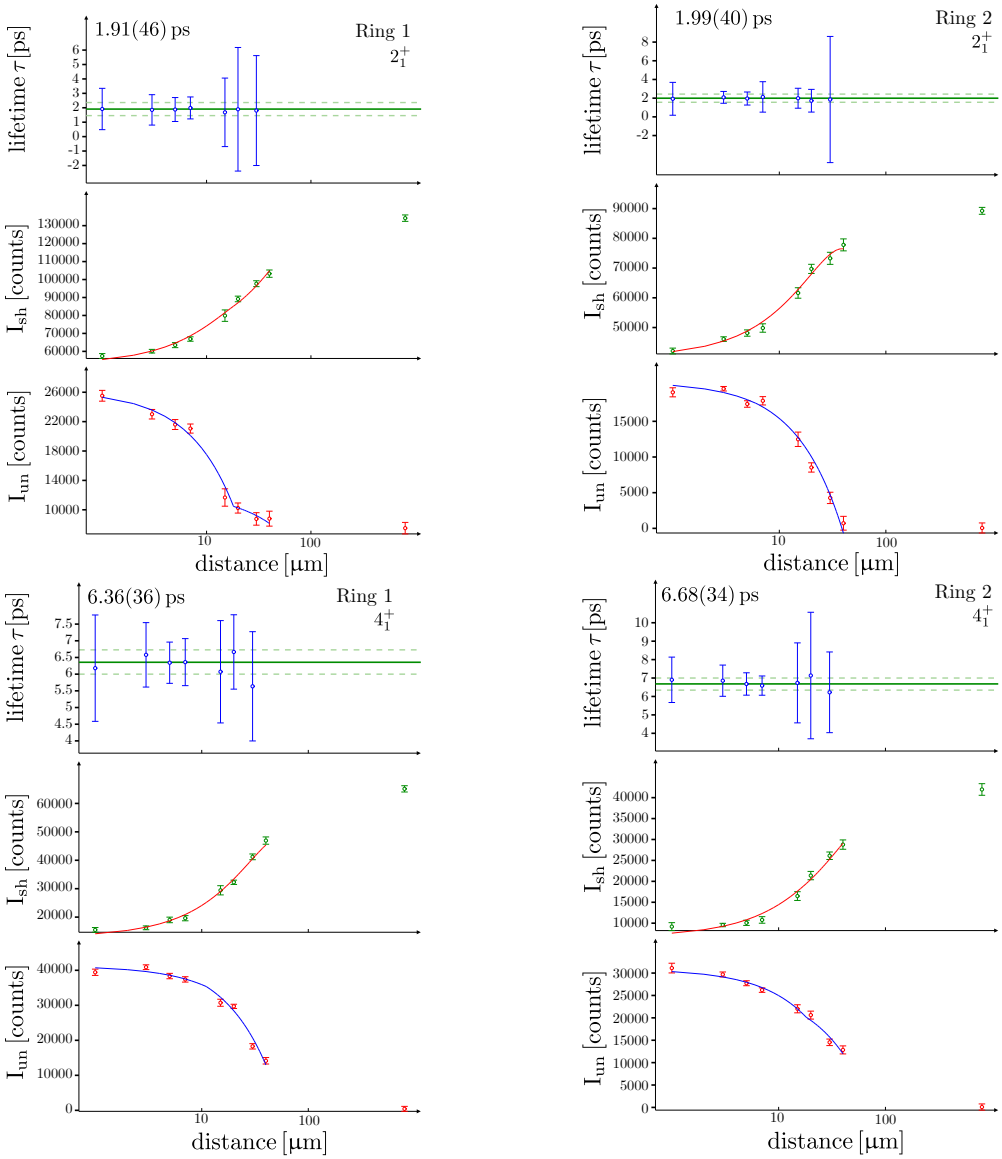

Figure A.1.: Lifetime curves for the 2_1^+ and 4_1^+ states in ^{50}Ti. The upper panels show the weighted mean value (solid lines) of the lifetimes with the statistical uncertainties (dashed lines). The middle panels represent the intensities of the shifted component and the lower panel those of the unshifted component. The polynomial fit functions to the measured intensities are displayed in red respectively blue.

B. Experimental and theoretical results

B.1. Experimental results and shell-model calculations for ^{50,52,54}Ti

^{50}Ti						
Signature	**Exp.**	**FPD6**	**KB3G**	**GXPF1A**	**GXPF1B**	**GXPF1B-nf7**
$E(2_1^+)$ (keV)	1554*	1828	1715	1624	1626	1698
$E(4_1^+)$ (keV)	2675*	2929	2841	2562	2568	2572
$E(6_1^+)$ (keV)	3199*	3523	3384	3237	3234	3152
$E_\gamma(2_1^+ \to 0_{gs}^+)$ (keV)	1554*	1828	1715	1624	1626	1698
$E_\gamma(4_1^+ \to 2_1^+)$ (keV)	1121*	1101	1126	938	942	874
$E_\gamma(6_1^+ \to 4_1^+)$ (keV)	523*	594	543	675	666	580
$B(E2; 2_1^+ \to 0_{gs}^+)$ (e^2fm^4)	46^{+8}_{-6}	89	78	78	78	70
$B(E2; 4_1^+ \to 2_1^+)$ (e^2fm^4)	71(3)	92	77	77	76	69
$B(E2; 6_1^+ \to 4_1^+)$ (e^2fm^4)	-	48	36	37	36	33

Table B.1.: Experimental results and results of shell-model calculations using different interactions with modified effective charges $e_\pi = 1.31e$ for protons and $e_\nu = 0.46e$ for neutrons for ^{50}Ti. Values marked with an $*$ are taken from Ref. [98].

^{52}Ti						
Signature	**Exp.**	**FPD6**	**KB3G**	**GXPF1A**	**GXPF1B**	**GXPF1B-nf7**
$E(2_1^+)$ (keV)	1050*	1237	1070	1107	1084	1090
$E(4_1^+)$ (keV)	2318*	2294	2356	2252	2240	2229
$E(6_1^+)$ (keV)	3029*	3178	3048	2933	2922	2899
$E(8_1^+)$ (keV)	4287*	4832	4416	4297	4240	4231
$E_\gamma(2_1^+ \to 0_{gs}^+)$ (keV)	1050*	1237	1070	1107	1084	1090
$E_\gamma(4_1^+ \to 2_1^+)$ (keV)	1268*	1057	1286	1145	1156	1139
$E_\gamma(6_1^+ \to 4_1^+)$ (keV)	711*	884	692	693	682	670
$E_\gamma(8_1^+ \to 6_1^+)$ (keV)	1259*	1654	1368	1364	1318	1332
$B(E2; 2_1^+ \to 0_{gs}^+)$ (e^2fm^4)	85^{+5}_{-4}	92	76	80	77	76
$B(E2; 4_1^+ \to 2_1^+)$ (e^2fm^4)	109^{+16}_{-13}	106	102	106	105	101
$B(E2; 6_1^+ \to 4_1^+)$ (e^2fm^4)	100^{+7}_{-6}	80	70	80	79	78
$B(E2; 8_1^+ \to 6_1^+)$ (e^2fm^4)	8(1)	56	40	45	45	42

Table B.2.: Experimental results and results of shell-model calculations using different interactions with modified effective charges $e_\pi = 1.31e$ for protons and $e_\nu = 0.46e$ for neutrons for ^{52}Ti. Values marked with an $*$ are taken from Ref. [99].

	^{54}Ti					
Signature	**Exp.**	**FPD6**	**KB3G**	**GXPF1A**	**GXPF1B**	**GXPF1B-nf7**
$E(2_1^+)$ (keV)	1495*	1261	1268	1395	1435	1416
$E(4_1^+)$ (keV)	2496*	2246	2452	2465	2475	2468
$E(6_1^+)$ (keV)	2936*	3157	3049	2975	2975	2965
$E(8_1^+)$ (keV)	5459*	5005	5192	5465	5548	5549
$E_\gamma(2_1^+ \to 0_{gs}^+)$ (keV)	1495*	1261	1268	1395	1435	1416
$E_\gamma(4_1^+ \to 2_1^+)$ (keV)	1002*	985	1184	1070	1040	1052
$E_\gamma(6_1^+ \to 4_1^+)$ (keV)	439*	911	597	510	500	497
$E_\gamma(8_1^+ \to 6_1^+)$ (keV)	2523*	1848	2143	2490	2573	2584
$B(E2; 2_1^+ \to 0_{gs}^+)$ (e^2fm^4)	84^{+53}_{-23}	101	78	80	79	79
$B(E2; 4_1^+ \to 2_1^+)$ (e^2fm^4)	139^{+25}_{-18}	107	82	88	86	87
$B(E2; 6_1^+ \to 4_1^+)$ (e^2fm^4)	≤ 132	68	34	43	43	43
$B(E2; 8_1^+ \to 6_1^+)$ (e^2fm^4)	≥ 5.7	43	2	9	7	5

Table B.3.: Experimental results and results of shell-model calculations using different interactions with modified effective charges $e_\pi = 1.31e$ for protons and $e_\nu = 0.46e$ for neutrons for ^{54}Ti. Values marked with an $*$ are taken from Ref. [100].

B.2. Experimental results and shell-model calculations for ^{53}Ti

	^{53}Ti				
Signature	**Exp.**	**FPD6**	**KB3G**	**GXPF1A**	**GXPF1B**
$E(5/2_1^-)$ (keV)	1237*	611	1136	1356	1392
$E(5/2_2^-)$ (keV)	-	1352	1352	1742	1734
$E(7/2^-)$ (keV)	1576*	1471	1484	1413	1415
$E(9/2^-)$ (keV)	2205*	1735	2123	2230	2234
$E(11/2^-)$ (keV)	2498*	2601	2579	2388	2382
$E(13/2^-)$ (keV)	2756*	2829	2830	2777	2382
$E(15/2^-)$ (keV)	3143*	3447	3333	3184	3154
$\tau(5/2_1^-)$ (ps)	1.5(9)	12.28	0.22	0.11	0.07
$\tau(5/2_2^-)$ (ps)	-	0.17	0.36	1.84	1.01
$\tau(7/2^-)$ (ps)	1.0(4)	1.74	1.31	1.91	1.34

continued on next page...

...continued from previous page

Signature	**Exp.**	**FPD6**	**KB3G**	**GXPF1A**	**GXPF1B**
$\tau(9/2^-)$ (ps)	2.8(7)	5.40	1.51	0.69	0.49
$\tau(11/2^-)$ (ps)	3.2(5)	0.70	1.77	8.84	6.38
$\tau(13/2^-)$ (ps)	2.9(5)	4.70	5.92	3.01	2.36
$\tau(15/2^-)$ (ps)	2.2	0.32	0.38	0.81	0.61
$B(E2; 7/2_1^- \to 3/2_1^-)$ (e^2fm^4)	63^{+40}_{-18}	62.4	75.6	75.8	74.5
$B(E2; 9/2_1^- \to 5/2_1^-)$ (e^2fm^4)	32^{+13}_{-9}	66.2	93.3	86.7	82.9
$B(E2; 9/2_1^- \to 7/2_1^-)$ (e^2fm^4)	$0.47^{+0.16}_{-0.10}\star$	23.4	14.9	27.4	27.2
$B(E2; 11/2_1^- \to 7/2_1^-)$ (e^2fm^4)	55^{+14}_{-11}	71.6	57.8	69.3	70.5
$B(E2; 11/2_1^- \to 9/2_1^-)$ (e^2fm^4)	$280^{+230}_{-160}\star$	0.95	4.10	10.9	10.7
$B(M1; 9/2_1^- \to 7/2_1^-)$ (μ_N^2)	$0.07^{+0.03}_{-0.02}\star$	0.12	0.12	0.14	0.14
$B(M1; 11/2_1^- \to 9/2_1^-)$ (μ_N^2)	$0.61^{+0.11}_{-0.08}\star$	0.11	0.27	0.55	0.62

Table B.4.: Experimental results and results of shell-model calculations using different interactions with modified effective charges $e_\pi = 1.31e$ for protons, $e_\nu = 0.46e$ for neutrons, and the standard g-factors $g_p^s = 5.586$, $g_n^s = -3.826$, $g_p^l = 1.0$, $g_n^l = 0.0$ for ^{53}Ti. Values marked with an $*$ are taken from Ref. [101]. For transitions where experimental $E2/M1$ multipole mixing ratios are available [77], the values are marked with a $\star$.

C. Experimental Data - Systematics

Nucleus	$E(2_1^+)$ (keV)	$B(E2; 2_1^+ \rightarrow 0_{gs}^+)$ (e^2fm^4)
$^{40}_{20}Ca_{20}$	3904.38(3) [102]	$183^{+1.1}_{-1.0}$ [102]
$^{42}_{20}Ca_{22}$	1524.71(3) [103]	$83.1^{+3.1}_{-2.9}$ [103]
$^{44}_{20}Ca_{24}$	1157.019(4) [104]	$100.7^{+5.9}_{-5.3}$ [104]
$^{46}_{20}Ca_{26}$	1346.0(3) [105]	$33.7^{+2.3}_{-2.1}$ [1]
$^{48}_{20}Ca_{28}$	3831.72(6) [91]	$17.7^{+0.9}_{-0.8}$ [91]
$^{50}_{20}Ca_{30}$	1026.72(10) [98]	7.5(2) [98]
$^{52}_{20}Ca_{32}$	2563(1) [99]	-
$^{54}_{20}Ca_{34}$	2043(19) [74]	-
$^{42}_{22}Ti_{20}$	1554.6(3) [103]	$141.6^{+47.3}_{-28.4}$ [103]
$^{44}_{22}Ti_{22}$	1083.06(9) [104]	$122.4^{+42.6}_{-25.1}$ [104]
$^{46}_{22}Ti_{24}$	889.286(3) [105]	192.0(53) [105]
$^{48}_{22}Ti_{26}$	983.5390(24) [91]	$152.2^{+3.9}_{-3.7}$ [91]
$^{50}_{22}Ti_{28}$	1553.794(8) [98]	$59.1^{+2.0}_{-1.9}$ [98]
$^{52}_{22}Ti_{30}$	1050.06(9) [99]	$123.6^{+5.0}_{-4.6}$ [99]
$^{54}_{22}Ti_{32}$	1494.8(8) [100]	71.4(126) [68]
$^{56}_{22}Ti_{34}$	1128.2(4) [108]	119.8(394) [68]
$^{58}_{22}Ti_{36}$	1047(4) [92]	-
$^{60}_{22}Ti_{38}$	850(5) [92]	-
$^{46}_{24}Cr_{22}$	892.5(5) [109]	186(40) [110]
$^{48}_{24}Cr_{24}$	752.19(11) [91]	$321.9^{+39.6}_{-31.8}$ [91]
$^{50}_{24}Cr_{26}$	783.31(3) [98]	$211.3^{+6.7}_{-6.3}$ [98]
$^{52}_{24}Cr_{28}$	1434.091(14) [99]	$119.1^{+3.3}_{-3.1}$ [99]
$^{54}_{24}Cr_{30}$	834.855(3) [100]	$174.4^{+6.8}_{-6.3}$ [100]
$^{56}_{24}Cr_{32}$	1006.61(20) [108]	143.5(38) [2]
$^{58}_{24}Cr_{34}$	880.7(2) [113]	$192^{+17.7}_{-16.1}$ [3]
$^{60}_{24}Cr_{36}$	643.90(20) [116]	242^{+23}_{-21} [4]
$^{62}_{24}Cr_{38}$	446(1) [117]	$342.8^{+27.4}_{-23.9}$ [5]
$^{64}_{24}Cr_{40}$	429.3(19)[6]	312(79) [120]
$^{66}_{24}Cr_{40}$	386(10) [95]	-
$^{48}_{26}Fe_{22}$	969.5(5) [121]	-
$^{50}_{26}Fe_{24}$	764.9(3) [98]	280(60) [110]

continued on next page...

[1] Weighted mean of 35.6(26) e^2fm^4 [105], $39.8^{+22.1}_{-9.6}$ e^2fm^4 [106] and $25.4^{+5.5}_{-3.8}$ e^2fm^4 [107].
[2] Weighted mean of 110(38) e^2fm^4 [111] and 143.8(38) e^2fm^4 [112].
[3] Weighted mean of 197(36) e^2fm^4 [111], 172(25) e^2fm^4 [114], and 227^{+35}_{-26} e^2fm^4 [115].
[4] Weighted mean of 221(29) e^2fm^4 [114] and 279^{+38}_{-30} e^2fm^4 [115].
[5] Weighted mean of 325(44) e^2fm^4 [114], 321^{+60}_{-49} e^2fm^4 [114], and 371^{+43}_{-35} e^2fm^4 [115].
[6] Weighted mean of 420(7) keV [118], 430(2) keV [119], and 435(15) keV [120].

...continued from previous page

Nucleus	$\mathbf{E(2_1^+)\,(keV)}$	$\mathbf{B(E2; 2_1^+ \rightarrow 0_{gs}^+)\,(e^2fm^4)}$
$^{52}_{26}Fe_{26}$	849.45(10) [99]	164(20) [122]
$^{54}_{26}Fe_{28}$	1408.19(19) [100]	$134.5^{+3.6}_{-3.4}$ [100]
$^{56}_{26}Fe_{30}$	846.7778(19) [108]	$214.1^{+8.4}_{-7.8}$ [108]
$^{58}_{26}Fe_{32}$	810.7662(2) [113]	$246.9^{+7.4}_{-7.0}$ [113]
$^{60}_{26}Fe_{34}$	823.83(9) [116]	$188.9^{+21.3}_{-17.4}$ [59]
$^{62}_{26}Fe_{36}$	877.31(10) [117]	204(17) [7]
$^{64}_{26}Fe_{38}$	746.40(10) [124]	$347.0^{+32.6}_{-31.6}$ [8]
$^{66}_{26}Fe_{40}$	573.4(10) [125]	304(20) [9]
$^{68}_{26}Fe_{42}$	522(1) [126]	356(44) [120]
$^{70}_{26}Fe_{44}$	480(13) [95]	-
$^{72}_{26}Fe_{46}$	520(16) [95]	-
$^{52}_{28}Ni_{24}$	1397(6) [99]	-
$^{54}_{28}Ni_{26}$	1392.3(4) [100]	$121.5^{+28.7}_{-19.5}$ [100]
$^{56}_{28}Ni_{28}$	2700.6(7) [108]	75^{+34}_{-30} [108]
$^{58}_{28}Ni_{30}$	1454.21(9) [113]	$133.4^{+4.4}_{-4.2}$ [113]
$^{60}_{28}Ni_{32}$	1332.514(4) [116]	$104.0^{+18.9}_{-19.5}$ [116]
$^{62}_{28}Ni_{34}$	1172.98(10) [117]	$175.7^{+5.0}_{-4.7}$ [117]
$^{64}_{28}Ni_{36}$	1345.75(5) [124]	$117.8^{+3.9}_{-3.7}$ [124]
$^{66}_{28}Ni_{38}$	1424.8(10) [125]	120(40) [127]
$^{68}_{28}Ni_{40}$	2034.08(16) [128]	52(8) [128]
$^{70}_{28}Ni_{42}$	1259.55(5) [129]	172(28) [130]
$^{72}_{28}Ni_{44}$	1095.2(5) [131]	74(10) [132]
$^{74}_{28}Ni_{46}$	1024(1) [133]	$128.4^{+43.2}_{-45.2}$ [134]

Table C.1.: Experimental level energies $E(2_1^+)$ and transition probabilities $B(E2; 2_1^+ \rightarrow 0_{gs}^+)$ for even-even nuclei for $20 \leq Z \leq 28$ and $20 \leq N \leq 46$.

[7] Weighted mean of $214(26)\,e^2fm^4$ [59], $198(25)\,e^2fm^4$ [58], and $190(58)\,e^2fm^4$ [123].
[8] Weighted mean of $470^{+210}_{-110}\,e^2fm^4$ [59] and $198(25)\,e^2fm^4$ [58].
[9] Weighted mean of $332(34)\,e^2fm^4$ [58] and $290(24)\,e^2fm^4$ [120].

Bibliography

[1] K. Bethge. Kernphysik: Eine Einführung. Springer-Lehrbuch. Springer Berlin Heidelberg, 2013 (cit. on pp. 7, 9, 24).

[2] R. F. Casten and S. Moszkowski. "Nuclear Structure from a Simple Perspective." *Physics Today* 44.11 (Jan. 1991), p. 91 (cit. on pp. 7–10).

[3] R. V. Janssens. "Unexpected doubly magic nucleus." *Nature* 459.7250 (2009), pp. 1069–1070 (cit. on p. 8).

[4] A. Ozawa, T. Kobayashi, T. Suzuki, K. Yoshida and I. Tanihata. "New Magic Number, $N = 16$, near the Neutron Drip Line." *Phys. Rev. Lett.* 84 (24 June 2000), pp. 5493–5495 (cit. on p. 8).

[5] T. Otsuka. "Exotic nuclei and nuclear forces." *Physica Scripta* T152 (Jan. 2013), p. 014007 (cit. on p. 8).

[6] E. K. Warburton, J. A. Becker and B. A. Brown. "Mass systematics for $A = 29 - 44$ nuclei: The deformed $A \sim 32$ region." *Phys. Rev. C* 41 (3 Mar. 1990), pp. 1147–1166 (cit. on p. 8).

[7] O. Sorlin and M.-G. Porquet. "Nuclear magic numbers: New features far from stability." *Progress in Particle and Nuclear Physics* 61.2 (2008), pp. 602–673 (cit. on p. 8).

[8] K. Heyde and J. L. Wood. "Publisher's Note: Shape coexistence in atomic nuclei [Rev. Mod. Phys. 83, 1467 (2011)]." *Rev. Mod. Phys.* 83 (4 Dec. 2011), pp. 1655–1655 (cit. on p. 8).

[9] O. Haxel, J. H. D. Jensen and H. E. Suess. "Zur Interpretation der ausgezeichneten Nucleonenzahlen im Bau der Atomkerne." *Naturwissenschaften* 35.12 (1948), pp. 376–376 (cit. on p. 9).

[10] O. Haxel, J. H. D. Jensen and H. E. Suess. "On the "Magic Numbers" in Nuclear Structure." *Phys. Rev.* 75 (11 June 1949), pp. 1766–1766 (cit. on p. 9).

[11] O. Haxel, J. H. D. Jensen and H. E. Suess. "Modellmäßige Deutung der ausgezeichneten Nukleonenzahlen im Kernbau." *Zeitschrift für Physik* 128.2 (1950), pp. 295–311 (cit. on p. 9).

[12] H. E. Sueß, O. Haxel and J. H. D. Jensen. "Zur Interpretation der ausgezeichneten Nucleonenzahlen im Bau der Atomkerne." *Naturwissenschaften* 36.5 (1949), pp. 153–155 (cit. on p. 9).

[13] M. G. Mayer. "On Closed Shells in Nuclei. II." *Phys. Rev.* 75 (12 June 1949), pp. 1969–1970 (cit. on p. 9).

[14] M. G. Mayer. "Nuclear Configurations in the Spin-Orbit Coupling Model. I. Empirical Evidence." *Phys. Rev.* 78 (1 Apr. 1950), pp. 16–21 (cit. on p. 9).

[15] M. Hjorth-Jensen, T. T. Kuo and E. Osnes. "Realistic effective interactions for nuclear systems." *Physics Reports* 261.3 (1995), pp. 125–270 (cit. on p. 11).

[16] M. Honma, T. Otsuka, B. A. Brown and T. Mizusaki. "Shell-model description of neutron-rich pf-shell nuclei with a new effective interaction GXPF1." *The European*

Physical Journal A - Hadrons and Nuclei 25.1 (Sept. 1, 2005), pp. 499–502 (cit. on pp. 11, 32).

[17] M. Honma, T. Otsuka and T. Mizusaki. "Shell-model description of neutron-rich Ca isotopes." *RIKEN Accel. Prog. Rep.* 41 (Jan. 2008), p. 32 (cit. on pp. 11, 80).

[18] A. Poves, J. Sánchez-Solano, E. Caurier and F. Nowacki. "Shell model study of the isobaric chains $A = 50$, $A = 51$ and $A = 52$." *Nuclear Physics A* 694.1 (2001), pp. 157–198 (cit. on p. 11).

[19] W. Richter, M. V. D. Merwe, R. Julies and B. Brown. "New effective interactions for the 0f1p shell." *Nuclear Physics A* 523.2 (1991), pp. 325–353 (cit. on pp. 11–12).

[20] M. Honma, T. Otsuka, B. A. Brown and T. Mizusaki. "Effective interaction for pf-shell nuclei." *Phys. Rev. C* 65 (6 May 2002), p. 061301 (cit. on pp. 11, 84).

[21] M. Honma, T. Otsuka, B. A. Brown and T. Mizusaki. "New effective interaction for pf-shell nuclei and its implications for the stability of the $N = Z = 28$ closed core." *Phys. Rev. C* 69 (3 Mar. 2004), p. 034335 (cit. on pp. 11, 32).

[22] M. Horoi, S. Stoica and B. A. Brown. "Shell-model calculations of two-neutrino double-β decay rates of ^{48}Ca with the GXPF1A interaction." *Phys. Rev. C* 75 (3 Mar. 2007), p. 034303 (cit. on p. 11).

[23] Y. Utsuno, T. Otsuka, B. A. Brown, M. Honma, T. Mizusaki and N. Shimizu. "Shape transitions in exotic Si and S isotopes and tensor-force-driven Jahn-Teller effect." *Phys. Rev. C* 86 (5 Nov. 2012), p. 051301 (cit. on p. 11).

[24] A. Poves and A. Zuker. "Theoretical spectroscopy and the fp shell." *Physics Reports* 70.4 (1981), pp. 235–314 (cit. on p. 11).

[25] T. Kuo and G. Brown. "Reaction matrix elements for the $0f - 1p$ shell nuclei." *Nuclear Physics A* 114.2 (1968), pp. 241–279 (cit. on p. 11).

[26] T. Otsuka, M. Honma and T. Mizusaki. "Structure of the $N = Z = 28$ Closed Shell Studied by Monte Carlo Shell Model Calculation." *Phys. Rev. Lett.* 81 (8 Aug. 1998), pp. 1588–1591 (cit. on p. 12).

[27] K.-H. Speidel, R. Ernst, O. Kenn, J. Gerber, P. Maier-Komor, N. Benczer-Koller, G. Kumbartzki, L. Zamick, M. S. Fayache and Y. Y. Sharon. "Core polarization in the light of new experimental g factors of fp shell, $N = 28$, isotones." *Phys. Rev. C* 62 (3 July 2000), p. 031301 (cit. on pp. 13, 81, 83).

[28] K.-H. Speidel, J. Leske, S. Schielke, S. Bedi, O. Zell, P. Maier-Komor, S. Robinson, Y. Sharon and L. Zamick. "Low-level structure of ^{52}Ti based on g factor and lifetime measurements." *Physics Letters B* 633.2 (2006), pp. 219–224 (cit. on pp. 13, 83).

[29] B. A. Brown, D. B. Fossan, A. R. Poletti and E. K. Warburton. "Lifetimes of yrast states in ^{51}Ti, ^{52}Ti, and ^{52}V." *Phys. Rev. C* 14 (3 Sept. 1976), pp. 1016–1022 (cit. on p. 13).

[30] B. Brown and W. Rae. "The Shell-Model Code NuShellX@MSU." *Nuclear Data Sheets* 120 (2014), pp. 115–118 (cit. on p. 13).

[31] N. Shimizu. Nuclear shell-model code for massive parallel computation, "KSHELL". 2013 (cit. on p. 13).

[32] M. Dufour and A. P. Zuker. "Realistic collective nuclear Hamiltonian." *Phys. Rev. C* 54 (4 Oct. 1996), pp. 1641–1660 (cit. on p. 13).

[33] T. R. Rodríguez and J. L. Egido. "New Beyond-Mean-Field Theories: Examination of the Potential Shell Closures at $N = 32$ or 34." *Phys. Rev. Lett.* 99 (6 Aug. 2007), p. 062501 (cit. on pp. 13, 32).

[34] T. R. Rodríguez and J. L. Egido. "On the robustness of sub-shell closures: A high angular momentum analysis of the titanium isotopes." *Physics Letters B* 804 (2020), p. 135359 (cit. on p. 13).

[35] A. Dewald, O. Möller and P. Petkov. "Developing the Recoil Distance Doppler-Shift technique towards a versatile tool for lifetime measurements of excited nuclear states." *Progress in Particle and Nuclear Physics* 67.3 (2012), pp. 786–839 (cit. on pp. 13, 16–18).

[36] A. Dewald, S. Harissopulos and P. von Brentano. "The differential plunger and the differential decay curve method for the analysis of recoil distance Doppler-shift data." *Zeitschrift für Physik A Atomic Nuclei* 334.2 (1989), pp. 163–175 (cit. on pp. 14, 16).

[37] M. Vandebrouck, A. Lemasson, M. Rejmund, G. Fremont, J. Pancin, A. Navin, C. Michelagnoli, J. Goupil, C. Spitaels and B. Jacquot. "Dual Position Sensitive MWPC for tracking reaction products at VAMOS++." *Nuclear Instruments and Methods in Physics Research Section A: Accelerators, Spectrometers, Detectors and Associated Equipment* 812 (2016), pp. 112–117 (cit. on pp. 14, 20–21).

[38] S. Akkoyun, A. Algora, B. Alikhani, F. Ameil, G. de Angelis, L. Arnold, A. Astier, A. Ataç, Y. Aubert, C. Aufranc, A. Austin, S. Aydin, F. Azaiez, S. Badoer, D. Balabanski, D. Barrientos, G. Baulieu, R. Baumann, D. Bazzacco, F. Beck, T. Beck, P. Bednarczyk, M. Bellato, M. Bentley, G. Benzoni, R. Berthier, L. Berti, R. Beunard, G. L. Bianco, B. Birkenbach, P. Bizzeti, A. Bizzeti-Sona, F. L. Blanc, J. Blasco, N. Blasi, D. Bloor, C. Boiano, M. Borsato, D. Bortolato, A. Boston, H. Boston, P. Bourgault, P. Boutachkov, A. Bouty, A. Bracco, S. Brambilla, I. Brawn, A. Brondi, S. Broussard, B. Bruyneel, D. Bucurescu, I. Burrows, A. Bürger, S. Cabaret, B. Cahan, E. Calore, F. Camera, A. Capsoni, F. Carrió, G. Casati, M. Castoldi, B. Cederwall, J.-L. Cercus, V. Chambert, M. E. Chambit, R. Chapman, L. Charles, J. Chavas, E. Clément, P. Cocconi, S. Coelli, P. Coleman-Smith, A. Colombo, S. Colosimo, C. Commeaux, D. Conventi, R. Cooper, A. Corsi, A. Cortesi, L. Costa, F. Crespi, J. Cresswell, D. Cullen, D. Curien, A. Czermak, D. Delbourg, R. Depalo, T. Descombes, P. Désesquelles, P. Detistov, C. Diarra, F. Didierjean, M. Dimmock, Q. Doan, C. Domingo-Pardo, M. Doncel, F. Dorangeville, N. Dosme, Y. Drouen, G. Duchêne, B. Dulny, J. Eberth, P. Edelbruck, J. Egea, T. Engert, M. Erduran, S. Ertürk, C. Fanin, S. Fantinel, E. Farnea, T. Faul, M. Filliger, F. Filmer, C. Finck, G. de France, A. Gadea, W. Gast, A. Geraci, J. Gerl, R. Gernhäuser, A. Giannatiempo, A. Giaz, L. Gibelin, A. Givechev, N. Goel, V. González, A. Gottardo, X. Grave, J. Grębosz, R. Griffiths, A. Grint, P. Gros, L. Guevara, M. Gulmini, A. Görgen, H. Ha, T. Habermann, L. Harkness, H. Harroch, K. Hauschild, C. He, A. Hernández-Prieto, B. Hervieu, H. Hess, T. Hüyük, E. Ince, R. Isocrate, G. Jaworski, A. Johnson, J. Jolie, P. Jones, B. Jonson, P. Joshi, D. Judson, A. Jungclaus, M. Kaci, N. Karkour, M. Karolak, A. Kaşkaş, M. Kebbiri, R. Kempley, A. Khaplanov, S. Klupp, M. Kogimtzis, I. Kojouharov, A. Korichi, W. Korten, T. Kröll, R. Krücken, N. Kurz, B. Ky, M. Labiche, X. Lafay, L. Lavergne, I. Lazarus, S. Leboutelier, F. Lefebvre, E. Legay, L. Legeard, F. Lelli, S. Lenzi, S. Leoni, A. Lermitage, D. Lersch, J. Leske, S. Letts,

S. Lhenoret, R. Lieder, D. Linget, J. Ljungvall, A. Lopez-Martens, A. Lotodé, S. Lunardi, A. Maj, J. van der Marel, Y. Mariette, N. Marginean, R. Marginean, G. Maron, A. Mather, W. Męczyński, V. Mendéz, P. Medina, B. Melon, R. Menegazzo, D. Mengoni, E. Merchan, L. Mihailescu, C. Michelagnoli, J. Mierzejewski, L. Milechina, B. Million, K. Mitev, P. Molini, D. Montanari, S. Moon, F. Morbiducci, R. Moro, P. Morrall, O. Möller, A. Nannini, D. Napoli, L. Nelson, M. Nespolo, V. Ngo, M. Nicoletto, R. Nicolini, Y. L. Noa, P. Nolan, M. Norman, J. Nyberg, A. Obertelli, A. Olariu, R. Orlandi, D. Oxley, C. Özben, M. Ozille, C. Oziol, E. Pachoud, M. Palacz, J. Palin, J. Pancin, C. Parisel, P. Pariset, G. Pascovici, R. Peghin, L. Pellegri, A. Perego, S. Perrier, M. Petcu, P. Petkov, C. Petrache, E. Pierre, N. Pietralla, S. Pietri, M. Pignanelli, I. Piqueras, Z. Podolyak, P. L. Pouhalec, J. Pouthas, D. Pugnére, V. Pucknell, A. Pullia, B. Quintana, R. Raine, G. Rainovski, L. Ramina, G. Rampazzo, G. L. Rana, M. Rebeschini, F. Recchia, N. Redon, M. Reese, P. Reiter, P. Regan, S. Riboldi, M. Richer, M. Rigato, S. Rigby, G. Ripamonti, A. Robinson, J. Robin, J. Roccaz, J.-A. Ropert, B. Rossé, C. R. Alvarez, D. Rosso, B. Rubio, D. Rudolph, F. Saillant, E. Şahin, F. Salomon, M.-D. Salsac, J. Salt, G. Salvato, J. Sampson, E. Sanchis, C. Santos, H. Schaffner, M. Schlarb, D. Scraggs, D. Seddon, M. Şenyiğit, M.-H. Sigward, G. Simpson, J. Simpson, M. Slee, J. Smith, P. Sona, B. Sowicki, P. Spolaore, C. Stahl, T. Stanios, E. Stefanova, O. Stézowski, J. Strachan, G. Suliman, P.-A. Söderström, J. Tain, S. Tanguy, S. Tashenov, C. Theisen, J. Thornhill, F. Tomasi, N. Toniolo, R. Touzery, B. Travers, A. Triossi, M. Tripon, K. Tun-Lanoë, M. Turcato, C. Unsworth, C. Ur, J. Valiente-Dobon, V. Vandone, E. Vardaci, R. Venturelli, F. Veronese, C. Veyssiere, E. Viscione, R. Wadsworth, P. Walker, N. Warr, C. Weber, D. Weisshaar, D. Wells, O. Wieland, A. Wiens, G. Wittwer, H. Wollersheim, F. Zocca, N. Zamfir, M. Zięblíński and A. Zucchiatti. "AGATA—Advanced GAmma Tracking Array." *Nuclear Instruments and Methods in Physics Research Section A: Accelerators, Spectrometers, Detectors and Associated Equipment* 668 (2012), pp. 26–58 (cit. on pp. 14, 20, 22, 24).

[39] R. M. Pérez Vidal. "Collectivity along N=50: Nuclear Structure studies on the neutron-magic nuclei ^{92}Mo and ^{94}Ru with AGATA and VAMOS++." PhD thesis. U. Valencia (main), 2019 (cit. on pp. 15, 26).

[40] J. Blatt and V. Weisskopf. Theoretical Nuclear Physics. Springer New York, 2012 (cit. on p. 19).

[41] H. Morinaga and T. Yamazaki. In-beam Gamma-ray Spectroscopy. North-Holland Publishing Company, 1976 (cit. on p. 19).

[42] Aug. 15, 2020. URL: `https://www.ganil-spiral2.eu/scientists/ganil-spiral-2-facilities/available-beams/` (cit. on p. 20).

[43] A. Villari. "The accelerated ISOL technique and the SPIRAL project." *Nuclear Physics A* 693.1 (2001), pp. 465–476 (cit. on p. 20).

[44] H. Savajols. "VAMOS: A variable mode high acceptance spectrometer for identifying reaction products induced by SPIRAL beams." *Nuclear Instruments and Methods in Physics Research Section B: Beam Interactions with Materials and Atoms* 204 (2003), pp. 146–153 (cit. on p. 21).

[45] S. Pullanhiotan, A. Chatterjee, B. Jacquot, A. Navin and M. Rejmund. "Improvement in the reconstruction method for VAMOS spectrometer." *Nuclear Instruments and*

Methods in Physics Research Section B: Beam Interactions with Materials and Atoms 266.19 (2008), pp. 4148–4152 (cit. on p. 21).

[46] M. Rejmund, B. Lecornu, A. Navin, C. Schmitt, S. Damoy, O. Delaune, J. Enguerrand, G. Fremont, P. Gangnant, L. Gaudefroy, B. Jacquot, J. Pancin, S. Pullanhiotan and C. Spitaels. "Performance of the improved larger acceptance spectrometer: VAMOS++." *Nuclear Instruments and Methods in Physics Research Section A: Accelerators, Spectrometers, Detectors and Associated Equipment* 646.1 (2011), pp. 184–191 (cit. on p. 21).

[47] A. Wiens, H. Hess, B. Birkenbach, B. Bruyneel, J. Eberth, D. Lersch, G. Pascovici, P. Reiter and H.-G. Thomas. "The AGATA triple cluster detector." *Nuclear Instruments and Methods in Physics Research Section A: Accelerators, Spectrometers, Detectors and Associated Equipment* 618.1 (2010), pp. 223–233 (cit. on pp. 22–23).

[48] L. Corradi, G. Pollarolo and S. Szilner. "Multinucleon transfer processes in heavy-ion reactions." *Journal of Physics G: Nuclear and Particle Physics* 36.11 (Sept. 2009), p. 113101 (cit. on pp. 25–26).

[49] Aug. 19, 2020. URL: `http://personalpages.to.infn.it/~nanni/grazing/` (cit. on p. 26).

[50] A. Winther. "Grazing reactions in collisions between heavy nuclei." *Nuclear Physics A* 572.1 (1994), pp. 191–235 (cit. on p. 26).

[51] A. Winther. "Dissipation, polarization and fluctuation in grazing heavy-ion collisions and the boundary to the chaotic regime." *Nuclear Physics A* 594.2 (1995), pp. 203–245 (cit. on p. 26).

[52] S. Klaumünzer, C. Li and G. Schumacher. "Plastic flow of borosilicate glass under bombardment with heavy ions." *Applied physics letters* 51.2 (1987), pp. 97–99 (cit. on p. 27).

[53] R. L. Fleischer, P. B. Price, R. M. Walker and R. M. Walker. Nuclear tracks in solids: principles and applications. Univ of California Press, 1975 (cit. on p. 29).

[54] F. Seitz and J. Koehler. "Solid State Phys." *Adv. Res. Appl* 2 (1956), p. 305 (cit. on p. 29).

[55] Z. Wang, C. Dufour, E. Paumier and M. Toulemonde. "The Se sensitivity of metals under swift-heavy-ion irradiation: a transient thermal process." *Journal of Physics: Condensed Matter* 6.34 (1994), p. 6733 (cit. on p. 29).

[56] M. Toulemonde, C. Dufour and E. Paumier. "Transient thermal process after a high-energy heavy-ion irradiation of amorphous metals and semiconductors." *Physical review B* 46.22 (1992), p. 14362 (cit. on p. 29).

[57] C. Stodel, M. Toulemonde, C. Fransen, B. Jacquot, E. Clément, G. Frémont, M. Michel and C. Dufour. ""Thermal Spike" model applied to thin targets irradiated with swift heavy ion beams at few MeV/u." *EPJ Web of Conferences*. Vol. 229. EDP Sciences. 2020, p. 05001 (cit. on p. 29).

[58] W. Rother, A. Dewald, H. Iwasaki, S. M. Lenzi, K. Starosta, D. Bazin, T. Baugher, B. A. Brown, H. L. Crawford, C. Fransen, A. Gade, T. N. Ginter, T. Glasmacher, G. F. Grinyer, M. Hackstein, G. Ilie, J. Jolie, S. McDaniel, D. Miller, P. Petkov, T. Pissulla, A. Ratkiewicz, C. A. Ur, P. Voss, K. A. Walsh, D. Weisshaar and K.-O.

Zell. "Enhanced Quadrupole Collectivity at $N = 40$: The Case of Neutron-Rich Fe Isotopes." *Phys. Rev. Lett.* 106 (2 Jan. 2011), p. 022502 (cit. on pp. 30, 86, 94).

[59] J. Ljungvall, A. Görgen, A. Obertelli, W. Korten, E. Clément, G. de France, A. Bürger, J.-P. Delaroche, A. Dewald, A. Gadea, L. Gaudefroy, M. Girod, M. Hackstein, J. Libert, D. Mengoni, F. Nowacki, T. Pissulla, A. Poves, F. Recchia, M. Rejmund, W. Rother, E. Sahin, C. Schmitt, A. Shrivastava, K. Sieja, J. J. Valiente-Dobón, K. O. Zell and M. Zielińska. "Onset of collectivity in neutron-rich Fe isotopes: Toward a new island of inversion?" *Phys. Rev. C* 81 (6 June 2010), p. 061301 (cit. on pp. 30, 94).

[60] N. Hoteling, W. B. Walters, R. V. F. Janssens, R. Broda, M. P. Carpenter, B. Fornal, A. A. Hecht, M. Hjorth-Jensen, W. Królas, T. Lauritsen, T. Pawłat, D. Seweryniak, X. Wang, A. Wöhr, J. Wrzesiński and S. Zhu. "Yrast structure of ^{64}Fe." *Phys. Rev. C* 74 (6 Dec. 2006), p. 064313 (cit. on p. 30).

[61] R. Broda, B. Fornal, W. Królas, T. Pawłat, D. Bazzacco, S. Lunardi, C. Rossi-Alvarez, R. Menegazzo, G. de Angelis, P. Bednarczyk, J. Rico, D. De Acuña, P. J. Daly, R. H. Mayer, M. Sferrazza, H. Grawe, K. H. Maier and R. Schubart. "$N = 40$ Neutron Subshell Closure in the ^{68}Ni Nucleus." *Phys. Rev. Lett.* 74 (6 Feb. 1995), pp. 868–871 (cit. on p. 30).

[62] M. Klintefjord, J. Ljungvall, A. Görgen, S. M. Lenzi, F. L. Bello Garrote, A. Blazhev, E. Clément, G. de France, J.-P. Delaroche, P. Désesquelles, A. Dewald, D. T. Doherty, C. Fransen, A. Gengelbach, G. Georgiev, M. Girod, A. Goasduff, A. Gottardo, K. Hadyńska-Klek, B. Jacquot, T. Konstantinopoulos, A. Korichi, A. Lemasson, J. Libert, A. Lopez-Martens, C. Michelagnoli, A. Navin, J. Nyberg, R. M. Pérez-Vidal, S. Roccia, E. Sahin, I. Stefan, A. E. Stuchbery, M. Zielińska, D. Barrientos, B. Birkenbach, A. Boston, L. Charles, M. Ciemala, J. Dudouet, J. Eberth, A. Gadea, V. González, L. Harkness-Brennan, H. Hess, A. Jungclaus, W. Korten, R. Menegazzo, D. Mengoni, B. Million, A. Pullia, D. Ralet, F. Recchia, P. Reiter, M. D. Salsac, E. Sanchis, O. Stezowski, C. Theisen and J. J. Valiente Dobon. "Measurement of lifetimes in ^{62,64}Fe,^{61,63}Co, and ^{59}Mn." *Phys. Rev. C* 95 (2 Feb. 2017), p. 024312 (cit. on pp. 30, 86).

[63] S. M. Lenzi, F. Nowacki, A. Poves and K. Sieja. "Island of inversion around ^{64}Cr." *Phys. Rev. C* 82 (5 Nov. 2010), p. 054301 (cit. on p. 30).

[64] T. C. Braunroth. "Lifetime Measurements in Neutron-rich Isotopes close to $N = 40$ and Development of a Simulation Tool for RDDS Spectra." PhD thesis. Universität zu Köln, Dezember 2017 (cit. on pp. 30, 86).

[65] J. Kotila and S. M. Lenzi. "Collective features of Cr and Fe isotopes." *Phys. Rev. C* 89 (6 June 2014), p. 064304 (cit. on p. 30).

[66] Sept. 12, 2020. URL: `https://people.physics.anu.edu.au/~ecs103/chart/` (cit. on p. 30).

[67] S. N. Liddick, P. F. Mantica, R. Broda, B. A. Brown, M. P. Carpenter, A. D. Davies, B. Fornal, T. Glasmacher, D. E. Groh, M. Honma, M. Horoi, R. V. F. Janssens, T. Mizusaki, D. J. Morrissey, A. C. Morton, W. F. Mueller, T. Otsuka, J. Pavan, H. Schatz, A. Stolz, S. L. Tabor, B. E. Tomlin and M. Wiedeking. "Development of shell closures at $N = 32, 34$. I. β decay of neutron-rich Sc isotopes." *Phys. Rev. C* 70 (6 Dec. 2004), p. 064303 (cit. on p. 31).

[68] D.-C. Dinca, R. V. F. Janssens, A. Gade, D. Bazin, R. Broda, B. A. Brown, C. M. Campbell, M. P. Carpenter, P. Chowdhury, J. M. Cook, A. N. Deacon, B. Fornal, S. J. Freeman, T. Glasmacher, M. Honma, F. G. Kondev, J.-L. Lecouey, S. N. Liddick, P. F. Mantica, W. F. Mueller, H. Olliver, T. Otsuka, J. R. Terry, B. A. Tomlin and K. Yoneda. "Reduced transition probabilities to the first 2^+ state in ^{52,54,56}Ti and development of shell closures at $N = 32, 34$." *Phys. Rev. C* 71 (4 Apr. 2005), p. 041302 (cit. on pp. 31–32, 80, 83, 85, 93).

[69] S. Zhu, R. Janssens, B. Fornal, S. Freeman, M. Honma, R. Broda, M. Carpenter, A. Deacon, B. Kay, F. Kondev, W. Królas, J. Kozemczak, A. Larabee, T. Lauritsen, S. Liddick, C. Lister, P. Mantica, T. Otsuka, T. Pawłat, A. Robinson, D. Seweryniak, J. Smith, D. Steppenbeck, B. Tomlin, J. Wrzesiński and X. Wang. "One-particle excitations outside the ^{54}Ti semi-magic core: The ^{55}V and ^{55}Ti yrast structures." *Physics Letters B* 650.2 (2007), pp. 135–140 (cit. on p. 31).

[70] A. Gade, R. V. F. Janssens, D. Bazin, B. A. Brown, C. M. Campbell, M. P. Carpenter, J. M. Cook, A. N. Deacon, D.-C. Dinca, S. J. Freeman, T. Glasmacher, M. Horoi, B. P. Kay, P. F. Mantica, W. F. Mueller, J. R. Terry, J. A. Tostevin and S. Zhu. "One-neutron knockout in the vicinity of the $N = 32$ sub-shell closure: ^{9}Be(^{57}Cr,^{56}Cr+γ)X." *Phys. Rev. C* 74 (4 Oct. 2006), p. 047302 (cit. on p. 31).

[71] E. Leistenschneider, M. P. Reiter, S. Ayet San Andrés, B. Kootte, J. D. Holt, P. Navrátil, C. Babcock, C. Barbieri, B. R. Barquest, J. Bergmann, J. Bollig, T. Brunner, E. Dunling, A. Finlay, H. Geissel, L. Graham, F. Greiner, H. Hergert, C. Hornung, C. Jesch, R. Klawitter, Y. Lan, D. Lascar, K. G. Leach, W. Lippert, J. E. McKay, S. F. Paul, A. Schwenk, D. Short, J. Simonis, V. Somà, R. Steinbrügge, S. R. Stroberg, R. Thompson, M. E. Wieser, C. Will, M. Yavor, C. Andreoiu, T. Dickel, I. Dillmann, G. Gwinner, W. R. Plaß, C. Scheidenberger, A. A. Kwiatkowski and J. Dilling. "Dawning of the $N = 32$ Shell Closure Seen through Precision Mass Measurements of Neutron-Rich Titanium Isotopes." *Phys. Rev. Lett.* 120 (6 Feb. 2018), p. 062503 (cit. on pp. 32, 83).

[72] M. P. Reiter, S. Ayet San Andrés, E. Dunling, B. Kootte, E. Leistenschneider, C. Andreoiu, C. Babcock, B. R. Barquest, J. Bollig, T. Brunner, I. Dillmann, A. Finlay, G. Gwinner, L. Graham, J. D. Holt, C. Hornung, C. Jesch, R. Klawitter, Y. Lan, D. Lascar, J. E. McKay, S. F. Paul, R. Steinbrügge, R. Thompson, J. L. Tracy, M. E. Wieser, C. Will, T. Dickel, W. R. Plaß, C. Scheidenberger, A. A. Kwiatkowski and J. Dilling. "Quenching of the $N = 32$ neutron shell closure studied via precision mass measurements of neutron-rich vanadium isotopes." *Phys. Rev. C* 98 (2 Aug. 2018), p. 024310 (cit. on p. 32).

[73] T. Otsuka, T. Suzuki, R. Fujimoto, H. Grawe and Y. Akaishi. "Evolution of Nuclear Shells due to the Tensor Force." *Phys. Rev. Lett.* 95 (23 Nov. 2005), p. 232502 (cit. on p. 32).

[74] D. Steppenbeck, S. Takeuchi, N. Aoi, P. Doornenbal, M. Matsushita, H. Baba, N. Fukuda, S. Go, M. Honma, J. Lee, K. Matsui, S. Michimasa, T. Motobayashi, D. Nishimura, T. Otsuka, H. Sakurai, Y. Shiga, P.-A. Söderström and K.-I. Yoneda. "Evidence for a new nuclear 'magic number' from the level structure of ^{54}Ca." *Nature* 502 (Oct. 2013), pp. 207–210 (cit. on pp. 32, 83, 93).

[75] J. L. Egido. "State-of-the-art of beyond mean field theories with nuclear density functionals." *Physica Scripta* 91.7 (June 2016), p. 073003 (cit. on p. 32).

[76] J. L. Egido. private communication. 2019 (cit. on p. 33).

[77] B. Fornal, S. Zhu, R. V. F. Janssens, M. Honma, R. Broda, B. A. Brown, M. P. Carpenter, S. J. Freeman, N. Hammond, F. G. Kondev, W. Królas, T. Lauritsen, S. N. Liddick, C. J. Lister, S. Lunardi, P. F. Mantica, N. Marginean, T. Mizusaki, E. F. Moore, T. Otsuka, T. Pawłat, D. Seweryniak, B. E. Tomlin, C. A. Ur, I. Wiedenhöver and J. Wrzesiński. "Yrast structure of neutron-rich ^{53}Ti." *Phys. Rev. C* 72 (4 Oct. 2005), p. 044315 (cit. on pp. 33, 91).

[78] A. N. Deacon, D. Steppenbeck, S. Zhu, S. J. Freeman, R. V. F. Janssens, M. P. Carpenter, B. Fornal, M. Honma, B. P. Kay, F. G. Kondev, J. Kozemczak, A. Larabee, T. Lauritsen, C. J. Lister, A. P. Robinson, D. Seweryniak, J. F. Smith, Y. Sun, X. Wang, F. R. Xu and Y.-C. Yang. "Single-particle and collective structures in ^{55}Cr and ^{55}V." *Phys. Rev. C* 83 (6 June 2011), p. 064305 (cit. on p. 33).

[79] L. Coraggio, A. Covello, A. Gargano and N. Itaco. "Realistic shell-model calculations for isotopic chains "north-east" of ^{48}Ca in the (N,Z) plane." *Phys. Rev. C* 89 (2 Feb. 2014), p. 024319 (cit. on p. 34).

[80] A. Goldkuhle, C. Fransen, A. Dewald, K. Arnswald, M. Bast, M. Beckers, A. Blazhev, T. Braunroth, G. Hackenberg, G. Häfner, J. Litzinger, J. Jolie, C. Müller-Gatermann, F. von Spee, N. Warr, D. Werner and K. O. Zell. "Lifetime measurement of excited states in ^{46}Ti." *The European Physical Journal A* 55.4 (2019), p. 53 (cit. on pp. 35, 79).

[81] A. Goldkuhle, C. Fransen, A. Blazhev, M. Beckers, B. Birkenbach, T. Braunroth, E. Clément, A. Dewald, J. Dudouet, J. Eberth, H. Hess, B. Jacquot, J. Jolie, Y.-H. Kim, A. Lemasson, S. M. Lenzi, H. J. Li, J. Litzinger, C. Michelagnoli, C. Müller-Gatermann, B. S. Nara Singh, R. M. Pérez-Vidal, D. Ralet, P. Reiter, A. Vogt, N. Warr, K. O. Zell, A. Ata ç, D. Barrientos, C. Barthe-Dejean, G. Benzoni, A. J. Boston, H. C. Boston, P. Bourgault, I. Burrows, J. Cacitti, B. Cederwall, M. Ciemala, D. M. Cullen, G. De France, C. Domingo-Pardo, J.-L. Foucher, G. Fremont, A. Gadea, P. Gangnant, V. González, J. Goupil, C. Henrich, C. Houarner, M. Jean, D. S. Judson, A. Korichi, W. Korten, M. Labiche, A. Lefevre, L. Legeard, F. Legruel, S. Leoni, J. Ljungvall, A. Maj, C. Maugeais, L. Ménager, N. Ménard, R. Menegazzo, D. Mengoni, B. Million, H. Munoz, D. R. Napoli, A. Navin, J. Nyberg, M. Ozille, Z. Podolyak, A. Pullia, B. Raine, F. Recchia, J. Ropert, F. Saillant, M. D. Salsac, E. Sanchis, C. Schmitt, J. Simpson, C. Spitaels, O. Stezowski, C. Theisen, M. Toulemonde, M. Tripon, J.-J. Valiente Dobón, G. Voltolini and M. Zielińska. "Lifetime measurements in ^{52,54}Ti to study shell evolution toward $N = 32$." *Phys. Rev. C* 100 (5 Nov. 2019), p. 054317 (cit. on pp. 35, 79).

[82] Goldkuhle, Alina, Fransen, Christoph, Dewald, Alfred, Alahari, Navin, Beckers, Marcel, Birkenbach, Benedikt, Blazhev, Andrey, Braunroth, Thomas, Clément, Emmanuel, De France, Gilles, Dudouet, Jérémie, Eberth, Jürgen, Hess, Herbert, Jacquot, Bertrand, Kim, Yung-Hee, Lemasson, Antoine, Lenzi, Silvia Monica, Li, Hongjie, Ljungvall, Joa, Litzinger, Julia, Michelagnoli, Caterine, Müller-Gatermann, Claus, Napoli, Daniel Ricardo, Nara Singh, Bondili Sreenivasa, Perez-Vidal, Rosa Maria, Ralet, Damian, Reiter, Peter, Rejmund, Maurycy, Vogt, Andreas, Warr, Nigel, Zell, Karl Oskar and Zieli´nska, Magda. "Preliminary results of lifetime measurements in neutron-rich 53Ti." *EPJ Web Conf.* 223 (2019), p. 01022 (cit. on pp. 36, 80).

[83] A. Goldkuhle, A. Blazhev, C. Fransen, A. Dewald, M. Beckers, B. Birkenbach, T. Braunroth, E. Clément, J. Dudouet, J. Eberth, H. Hess, B. Jacquot, J. Jolie, Y.-H. Kim, A. Lemasson, S. M. Lenzi, H. J. Li, J. Litzinger, C. Michelagnoli, C. Müller-Gatermann, B. S. Nara Singh, R. M. Pérez-Vidal, D. Ralet, P. Reiter, A. Vogt, N. Warr and K. O. Zell. "Lifetime measurements of excited states in neutron-rich ^{53}Ti: Benchmarking effective shell-model interactions." *Phys. Rev. C* 102 (5 Nov. 2020), p. 054334 (cit. on pp. 36, 80).

[84] K.-H. Speidel, S. Schielke, O. Kenn, J. Leske, D. Hohn, H. Hodde, J. Gerber, P. Maier-Komor, O. Zell, Y. Y. Sharon and L. Zamick. "Nuclear structure of the stable even-A calcium isotopes based on new experiments and shell model calculations." *Phys. Rev. C* 68 (6 Dec. 2003), p. 061302 (cit. on p. 83).

[85] A. R. Poletti, B. A. Brown, D. B. Fossan, P. Gorodetzky, J. J. Kolata, J. W. Olness and E. K. Warburton. "Lifetimes of the $(f_{\frac{7}{2}})^3 \frac{15}{2}^-$ states in ^{51}V and ^{43}Ca and $(f_{\frac{7}{2}})^2 4^+$ states in ^{50}Ti and ^{42}Ca via heavy-ion recoil-distance-method measurements." *Phys. Rev. C* 10 (3 Sept. 1974), pp. 997–1000 (cit. on p. 83).

[86] T. Otsuka, R. Fujimoto, Y. Utsuno, B. A. Brown, M. Honma and T. Mizusaki. "Magic Numbers in Exotic Nuclei and Spin-Isospin Properties of the *NN* Interaction." *Phys. Rev. Lett.* 87 (8 Aug. 2001), p. 082502 (cit. on p. 83).

[87] T. Otsuka, T. Suzuki, R. Fujimoto, H. Grawe and Y. Akaishi. "Evolution of Nuclear Shells due to the Tensor Force." *Phys. Rev. Lett.* 95 (23 Nov. 2005), p. 232502 (cit. on p. 83).

[88] T. Otsuka, T. Suzuki, M. Honma, Y. Utsuno, N. Tsunoda, K. Tsukiyama and M. Hjorth-Jensen. "Novel Features of Nuclear Forces and Shell Evolution in Exotic Nuclei." *Phys. Rev. Lett.* 104 (1 Jan. 2010), p. 012501 (cit. on p. 83).

[89] B. Linard, D. Kennedy, I. Morrison, J. Heggie and H. Bolotin. "Level structure and lifetimes of excited states in ^{48}Ti." *Nuclear Physics A* 302.1 (1978), pp. 214–236 (cit. on p. 85).

[90] Z. I. Adymov, N. Burtebayev and S. B. Sakuta. "Lifetimes of ^{48}Ti, ^{52}Cr and ^{80}Se excited states." *Bulletin of the Russian Academy of Sciences: Physics* 75.7 (2011), p. 914 (cit. on p. 85).

[91] T. Burrows. "Nuclear Data Sheets for A = 48." *Nuclear Data Sheets* 107.7 (2006), pp. 1747–1922 (cit. on pp. 85, 93).

[92] A. Gade, R. V. F. Janssens, D. Weisshaar, B. A. Brown, E. Lunderberg, M. Albers, V. M. Bader, T. Baugher, D. Bazin, J. S. Berryman, C. M. Campbell, M. P. Carpenter, C. J. Chiara, H. L. Crawford, M. Cromaz, U. Garg, C. R. Hoffman, F. G. Kondev, C. Langer, T. Lauritsen, I. Y. Lee, S. M. Lenzi, J. T. Matta, F. Nowacki, F. Recchia, K. Sieja, S. R. Stroberg, J. A. Tostevin, S. J. Williams, K. Wimmer and S. Zhu. "Nuclear Structure Towards $N = 40$ ^{60}Ca: In-Beam γ-Ray Spectroscopy of ^{58,60}Ti." *Phys. Rev. Lett.* 112 (11 Mar. 2014), p. 112503 (cit. on pp. 85, 93).

[93] M. Cortés, W. Rodriguez, P. Doornenbal, A. Obertelli, J. Holt, S. Lenzi, J. Menéndez, F. Nowacki, K. Ogata, A. Poves, T. Rodríguez, A. Schwenk, J. Simonis, S. Stroberg, K. Yoshida, L. Achouri, H. Baba, F. Browne, D. Calvet, F. Château, S. Chen, N. Chiga, A. Corsi, A. Delbart, J.-M. Gheller, A. Giganon, A. Gillibert, C. Hilaire, T. Isobe, T. Kobayashi, Y. Kubota, V. Lapoux, H. Liu, T. Motobayashi, I. Murray, H. Otsu, V. Panin, N. Paul, H. Sakurai, M. Sasano, D. Steppenbeck, L. Stuhl, Y.

Sun, Y. Togano, T. Uesaka, K. Wimmer, K. Yoneda, O. Aktas, T. Aumann, L. Chung, F. Flavigny, S. Franchoo, I. Gašparić, R.-B. Gerst, J. Gibelin, K. Hahn, D. Kim, T. Koiwai, Y. Kondo, P. Koseoglou, J. Lee, C. Lehr, B. Linh, T. Lokotko, M. MacCormick, K. Moschner, T. Nakamura, S. Park, D. Rossi, E. Sahin, D. Sohler, P.-A. Söderström, S. Takeuchi, H. Toernqvist, V. Vaquero, V. Wagner, S. Wang, V. Werner, X. Xu, H. Yamada, D. Yan, Z. Yang, M. Yasuda and L. Zanetti. "Shell evolution of $N = 40$ isotones towards ^{60}Ca: First spectroscopy of ^{62}Ti." *Physics Letters B* 800 (2020), p. 135071 (cit. on p. 85).

[94] F. Nowacki, A. Poves, E. Caurier and B. Bounthong. "Shape Coexistence in ^{78}Ni as the Portal to the Fifth Island of Inversion." *Phys. Rev. Lett.* 117 (27 Dec. 2016), p. 272501 (cit. on p. 86).

[95] C. Santamaria, C. Louchart, A. Obertelli, V. Werner, P. Doornenbal, F. Nowacki, G. Authelet, H. Baba, D. Calvet, F. Château, A. Corsi, A. Delbart, J.-M. Gheller, A. Gillibert, T. Isobe, V. Lapoux, M. Matsushita, S. Momiyama, T. Motobayashi, M. Niikura, H. Otsu, C. Péron, A. Peyaud, E. C. Pollacco, J.-Y. Roussé, H. Sakurai, M. Sasano, Y. Shiga, S. Takeuchi, R. Taniuchi, T. Uesaka, H. Wang, K. Yoneda, F. Browne, L. X. Chung, Z. Dombradi, S. Franchoo, F. Giacoppo, A. Gottardo, K. Hadynska-Klek, Z. Korkulu, S. Koyama, Y. Kubota, J. Lee, M. Lettmann, R. Lozeva, K. Matsui, T. Miyazaki, S. Nishimura, L. Olivier, S. Ota, Z. Patel, N. Pietralla, E. Sahin, C. Shand, P.-A. Söderström, I. Stefan, D. Steppenbeck, T. Sumikama, D. Suzuki, Z. Vajta, J. Wu and Z. Xu. "Extension of the $N = 40$ Island of Inversion towards $N = 50$: Spectroscopy of ^{66}Cr, ^{70,72}Fe." *Phys. Rev. Lett.* 115 (19 Nov. 2015), p. 192501 (cit. on pp. 86, 93–94).

[96] H. H. Gutbrod. "International Facility for Antiproton and Ion Research (FAIR) at GSI, Darmstadt." *Nuclear Physics A* 752 (2005), pp. 457–469 (cit. on p. 86).

[97] H. Geissel, H. Weick, M. Winkler, G. Münzenberg, V. Chichkine, M. Yavor, T. Aumann, K.H. Behr, M. Böhmer, A. Brünle, K. Burkard, J. Benlliure, D. Cortina-Gil, L. Chulkov, A. Dael, J.-E. Ducret, H. Emling, B. Franczak, J. Friese, B. Gastineau, J. Gerl, R. Gernhäuser, M. Hellström, B. Jonson, J. Kojouharova, R. Kulessa, B. Kindler, N. Kurz, B. Lommel, W. Mittig, G. Moritz, C. Mühle, J.A. Nolen, G. Nyman, P. Roussell-Chomaz, C. Scheidenberger, K.-H. Schmidt, G. Schrieder, B.M. Sherrill, H. Simon, K. Sümmerer, N.A. Tahir, V. Vysotsky, H. Wollnik and A.F. Zeller. "The Super-FRS project at GSI." *Nuclear Instruments and Methods in Physics Research Section B: Beam Interactions with Materials and Atoms* 204 (2003), pp. 71–85 (cit. on p. 86).

[98] J. Chen and B. Singh. "Nuclear Data Sheets for A=50." *Nuclear Data Sheets* 157 (2019), pp. 1–259 (cit. on pp. 89, 93).

[99] Y. Dong and H. Junde. "Nuclear Data Sheets for A = 52." *Nuclear Data Sheets* 128 (2015), pp. 185–314 (cit. on pp. 89, 93–94).

[100] Y. Dong and H. Junde. "Nuclear Data Sheets for A = 54." *Nuclear Data Sheets* 121 (2014), pp. 1–142 (cit. on pp. 90, 93–94).

[101] H. Junde. "Nuclear Data Sheets for A = 53." *Nuclear Data Sheets* 110.11 (2009), pp. 2689–2814 (cit. on p. 91).

[102] J. A. Cameron and B. Singh. "Nuclear Data Sheets for $A = 40$." *Nuclear Data Sheets* 102.2 (2004), pp. 293–513 (cit. on p. 93).

[103] J. Chen and B. Singh. "Nuclear Data Sheets for A = 42." *Nuclear Data Sheets* 135 (2016), pp. 1–192 (cit. on p. 93).

[104] J. Chen, B. Singh and J. A. Cameron. "Nuclear Data Sheets for A = 44." *Nuclear Data Sheets* 112.9 (2011), pp. 2357–2495 (cit. on p. 93).

[105] S.-C. Wu. "Nuclear Data Sheets for A = 46." *Nuclear Data Sheets* 91.1 (2000), pp. 1–116 (cit. on p. 93).

[106] D. Mengoni, J. J. Valiente-Dobón, E. Farnea, A. Gadea, A. Dewald, A. Latina and the CLARA-PRISMA Collaboration. "Lifetime measurements of neutron-rich nuclei around ^{48}Ca with the CLARA-PRISMA setup." *The European Physical Journal A* 42.3 (2009), p. 387 (cit. on p. 93).

[107] D. Montanari, S. Leoni, D. Mengoni, J. J. Valiente-Dobon, G. Benzoni, N. Blasi, G. Bocchi, P. F. Bortignon, S. Bottoni, A. Bracco, F. Camera, P. Casati, G. Colò, A. Corsi, F. C. L. Crespi, B. Million, R. Nicolini, O. Wieland, D. Bazzacco, E. Farnea, G. Germogli, A. Gottardo, S. M. Lenzi, S. Lunardi, R. Menegazzo, G. Montagnoli, F. Recchia, F. Scarlassara, C. Ur, L. Corradi, G. de Angelis, E. Fioretto, D. R. Napoli, R. Orlandi, E. Sahin, A. M. Stefanini, R. P. Singh, A. Gadea, S. Szilner, M. Kmiecik, A. Maj, W. Meczynski, A. Dewald, T. Pissulla and G. Pollarolo. "γ spectroscopy of calcium nuclei around doubly magic ^{48}Ca using heavy-ion transfer reactions." *Phys. Rev. C* 85 (4 Apr. 2012), p. 044301 (cit. on p. 93).

[108] H. Junde, H. Su and Y. Dong. "Nuclear Data Sheets for A = 56." *Nuclear Data Sheets* 112.6 (2011), pp. 1513–1645 (cit. on pp. 93–94).

[109] P. E. Garrett, S. M. Lenzi, E. Algin, D. Appelbe, R. W. Bauer, J. A. Becker, L. A. Bernstein, J. A. Cameron, M. P. Carpenter, R. V. F. Janssens, C. J. Lister, D. Seweryniak and D. D. Warner. "Spectroscopy of the $N = Z - 2$ nucleus ^{46}Cr and mirror energy differences." *Phys. Rev. C* 75 (1 Jan. 2007), p. 014307 (cit. on p. 93).

[110] K. Yamada, T. Motobayashi, N. Aoi, H. Baba, K. Demichi, Z. Elekes, J. Gibelin, T. Gomi, H. Hasegawa, N. Imai, et al. "Reduced transition probabilities for the first 2^+ excited state in ^{46}Cr, ^{50}Fe, and ^{54}Ni." *The 4th International Conference on Exotic Nuclei and Atomic Masses*. Springer. 2005, pp. 409–413 (cit. on p. 93).

[111] A. Bürger, T. Saito, H. Grawe, H. Hübel, P. Reiter, J. Gerl, M. Górska, H. Wollersheim, A. Al-Khatib, A. Banu, T. Beck, F. Becker, P. Bednarczyk, G. Benzoni, A. Bracco, S. Brambilla, P. Bringel, F. Camera, E. Clément, P. Doornenbal, H. Geissel, A. Görgen, J. Grębosz, G. Hammond, M. Hellström, M. Honma, M. Kavatsyuk, O. Kavatsyuk, M. Kmiecik, I. Kojouharov, W. Korten, N. Kurz, R. Lozeva, A. Maj, S. Mandal, B. Million, S. Muralithar, A. Neußer, F. Nowacki, T. Otsuka, Z. Podolyák, N. Saito, A. Singh, H. Weick, C. Wheldon, O. Wieland and M. Winkler. "Relativistic Coulomb excitation of neutron-rich ^{54,56,58}Cr: On the pathway of magicity from $N = 40$ to $N = 32$." *Physics Letters B* 622.1 (2005), pp. 29–34 (cit. on p. 93).

[112] M. Seidlitz, P. Reiter, A. Dewald, O. Möller, B. Bruyneel, S. Christen, F. Finke, C. Fransen, M. Górska, H. Grawe, A. Holler, G. Ilie, T. Kotthaus, P. Kudejová, S. M. Lenzi, S. Mandal, B. Melon, D. Mücher, J.-M. Regis, B. Saha, P. von Brentano, A. Wiens and K. O. Zell. "Precision lifetime measurements of the first 2^+ and 4^+ states in ^{56}Cr at the $N = 32$ subshell closure." *Phys. Rev. C* 84 (3 Sept. 2011), p. 034318 (cit. on p. 93).

[113] C. D. Nesaraja, S. D. Geraedts and B. Singh. "Nuclear Data Sheets for A = 58." *Nuclear Data Sheets* 111.4 (2010), pp. 897–1092 (cit. on pp. 93–94).

[114] T. Baugher, A. Gade, R. V. F. Janssens, S. M. Lenzi, D. Bazin, B. A. Brown, M. P. Carpenter, A. N. Deacon, S. J. Freeman, T. Glasmacher, G. F. Grinyer, F. G. Kondev, S. McDaniel, A. Poves, A. Ratkiewicz, E. A. McCutchan, D. K. Sharp, I. Stefanescu, K. A. Walsh, D. Weisshaar and S. Zhu. "Intermediate-energy Coulomb excitation of ^{58,60,62}Cr: The onset of collectivity toward $N = 40$." *Phys. Rev. C* 86 (1 July 2012), p. 011305 (cit. on p. 93).

[115] T. Braunroth, A. Dewald, H. Iwasaki, S. M. Lenzi, M. Albers, V. M. Bader, T. Baugher, T. Baumann, D. Bazin, J. S. Berryman, C. Fransen, A. Gade, T. Ginter, A. Gottardo, M. Hackstein, J. Jolie, A. Lemasson, J. Litzinger, S. Lunardi, T. Marchi, V. Modamio, C. Morse, D. R. Napoli, A. Nichols, F. Recchia, S. R. Stroberg, R. Wadsworth, D. Weisshaar, K. Whitmore and K. Wimmer. "Reduced transition strengths of low-lying yrast states in chromium isotopes in the vicinity of $N = 40$." *Phys. Rev. C* 92 (3 Sept. 2015), p. 034306 (cit. on p. 93).

[116] E. Browne and J. Tuli. "Nuclear Data Sheets for A = 60." *Nuclear Data Sheets* 114.12 (2013), pp. 1849–2022 (cit. on pp. 93–94).

[117] A. L. Nichols, B. Singh and J. K. Tuli. "Nuclear Data Sheets for A = 62." *Nuclear Data Sheets* 113.4 (2012), pp. 973–1114 (cit. on pp. 93–94).

[118] A. Gade, R. V. F. Janssens, T. Baugher, D. Bazin, B. A. Brown, M. P. Carpenter, C. J. Chiara, A. N. Deacon, S. J. Freeman, G. F. Grinyer, C. R. Hoffman, B. P. Kay, F. G. Kondev, T. Lauritsen, S. McDaniel, K. Meierbachtol, A. Ratkiewicz, S. R. Stroberg, K. A. Walsh, D. Weisshaar, R. Winkler and S. Zhu. "Collectivity at $N = 40$ in neutron-rich ^{64}Cr." *Phys. Rev. C* 81 (5 May 2010), p. 051304 (cit. on p. 93).

[119] S. Suchyta, S. N. Liddick, C. J. Chiara, W. B. Walters, M. P. Carpenter, H. L. Crawford, G. F. Grinyer, G. Gürdal, A. Klose, E. A. McCutchan, J. Pereira and S. Zhu. "β and isomeric decay of ^{64}V." *Phys. Rev. C* 89 (6 June 2014), p. 067303 (cit. on p. 93).

[120] H. L. Crawford, R. M. Clark, P. Fallon, A. O. Macchiavelli, T. Baugher, D. Bazin, C. W. Beausang, J. S. Berryman, D. L. Bleuel, C. M. Campbell, M. Cromaz, G. de Angelis, A. Gade, R. O. Hughes, I. Y. Lee, S. M. Lenzi, F. Nowacki, S. Paschalis, M. Petri, A. Poves, A. Ratkiewicz, T. J. Ross, E. Sahin, D. Weisshaar, K. Wimmer and R. Winkler. "Quadrupole Collectivity in Neutron-Rich Fe and Cr Isotopes." *Phys. Rev. Lett.* 110 (24 June 2013), p. 242701 (cit. on pp. 93–94).

[121] C. Dossat, N. Adimi, F. Aksouh, F. Becker, A. Bey, B. Blank, C. Borcea, R. Borcea, A. Boston, M. Caamano, G. Canchel, M. Chartier, D. Cortina, S. Czajkowski, G. de France, F. de Oliveira Santos, A. Fleury, G. Georgiev, J. Giovinazzo, S. Grévy, R. Grzywacz, M. Hellström, M. Honma, Z. Janas, D. Karamanis, J. Kurcewicz, M. Lewitowicz, M. López Jiménez, C. Mazzocchi, I. Matea, V. Maslov, P. Mayet, C. Moore, M. Pfützner, M. Pravikoff, M. Stanoiu, I. Stefan and J. Thomas. "The decay of proton-rich nuclei in the mass $A = 36 - 56$ region." *Nuclear Physics A* 792.1 (2007), pp. 18–86 (cit. on p. 93).

[122] K. L. Yurkewicz, D. Bazin, B. A. Brown, C. M. Campbell, J. A. Church, D.-C. Dinca, A. Gade, T. Glasmacher, M. Honma, T. Mizusaki, W. F. Mueller, H. Olliver, T.

Otsuka, L. A. Riley and J. R. Terry. "Intermediate-energy Coulomb excitation of ^{52}Fe." *Phys. Rev. C* 70 (3 Sept. 2004), p. 034301 (cit. on p. 94).

[123] L. P. Gaffney, J. Van de Walle, B. Bastin, V. Bildstein, A. Blazhev, N. Bree, J. Cederkäll, I. Darby, H. De Witte, D. DiJulio, J. Diriken, V. N. Fedosseev, C. Fransen, R. Gernhäuser, A. Gustafsson, H. Hess, M. Huyse, N. Kesteloot, T. Kröll, R. Lutter, B. A. Marsh, P. Reiter, M. Seidlitz, P. Van Duppen, D. Voulot, N. Warr, F. Wenander, K. Wimmer and K. Wrzosek-Lipska. "Low-energy Coulomb excitation of ^{62}Fe and ^{62}Mn following in-beam decay of ^{62}Mn." *The European Physical Journal A* 51.10 (2015), p. 136 (cit. on p. 94).

[124] B. Singh. "Nuclear Data Sheets for A = 64." *Nuclear Data Sheets* 108.2 (2007), pp. 197–364 (cit. on p. 94).

[125] E. Browne and J. Tuli. "Nuclear Data Sheets for A = 66." *Nuclear Data Sheets* 111.4 (2010), pp. 1093–1209 (cit. on p. 94).

[126] J. M. Daugas, I. Matea, J.-P. Delaroche, M. Pfützner, M. Sawicka, F. Becker, G. Bélier, C. R. Bingham, R. Borcea, E. Bouchez, A. Buta, E. Dragulescu, G. Georgiev, J. Giovinazzo, M. Girod, H. Grawe, R. Grzywacz, F. Hammache, F. Ibrahim, M. Lewitowicz, J. Libert, P. Mayet, V. Méot, F. Negoita, F. de Oliveira Santos, O. Perru, O. Roig, K. Rykaczewski, M. G. Saint-Laurent, J. E. Sauvestre, O. Sorlin, M. Stanoiu, I. Stefan, C. Stodel, C. Theisen, D. Verney and J. Żylicz. "β-decay measurements for $N > 40$ Mn nuclei and inference of collectivity for neutron-rich Fe isotopes." *Phys. Rev. C* 83 (5 May 2011), p. 054312 (cit. on p. 94).

[127] O. Sorlin, S. Leenhardt, C. Donzaud, J. Duprat, F. Azaiez, F. Nowacki, H. Grawe, Z. Dombrádi, F. Amorini, A. Astier, D. Baiborodin, M. Belleguic, C. Borcea, C. Bourgeois, D. M. Cullen, Z. Dlouhy, E. Dragulescu, M. Górska, S. Grévy, D. Guillemaud-Mueller, G. Hagemann, B. Herskind, J. Kiener, R. Lemmon, M. Lewitowicz, S. M. Lukyanov, P. Mayet, F. de Oliveira Santos, D. Pantalica, Y.-E. Penionzhkevich, F. Pougheon, A. Poves, N. Redon, M. G. Saint-Laurent, J. A. Scarpaci, G. Sletten, M. Stanoiu, O. Tarasov and C. Theisen. "$^{68}_{28}\mathrm{Ni}_{40}$: Magicity versus Superfluidity." *Phys. Rev. Lett.* 88 (9 Feb. 2002), p. 092501 (cit. on p. 94).

[128] E. McCutchan. "Nuclear Data Sheets for A = 68." *Nuclear Data Sheets* 113.6 (2012), pp. 1735–1870 (cit. on p. 94).

[129] G. Gürdal and E. McCutchan. "Nuclear Data Sheets for A = 70." *Nuclear Data Sheets* 136 (2016), pp. 1–162 (cit. on p. 94).

[130] O. Perru, O. Sorlin, S. Franchoo, F. Azaiez, E. Bouchez, C. Bourgeois, A. Chatillon, J. M. Daugas, Z. Dlouhy, Z. Dombrádi, C. Donzaud, L. Gaudefroy, H. Grawe, S. Grévy, D. Guillemaud-Mueller, F. Hammache, F. Ibrahim, Y. Le Coz, S. M. Lukyanov, I. Matea, J. Mrazek, F. Nowacki, Y.-E. Penionzhkevich, F. de Oliveira Santos, F. Pougheon, M. G. Saint-Laurent, G. Sletten, M. Stanoiu, C. Stodel, C. Theisen and D. Verney. "Enhanced Core Polarization in ^{70}Ni and ^{74}Zn." *Phys. Rev. Lett.* 96 (23 June 2006), p. 232501 (cit. on p. 94).

[131] C. J. Chiara, W. B. Walters, I. Stefanescu, M. Alcorta, M. P. Carpenter, B. Fornal, G. Gürdal, C. R. Hoffman, R. V. F. Janssens, B. P. Kay, F. G. Kondev, W. Królas, T. Lauritsen, C. J. Lister, E. A. McCutchan, T. Pawłat, A. M. Rogers, D. Seweryniak, N. Sharp, J. Wrzesiński and S. Zhu. "Seniority, collectivity, and $B(E2)$ enhancement in ^{72}Ni." *Phys. Rev. C* 84 (3 Sept. 2011), p. 037304 (cit. on p. 94).

[132] K. Kolos, D. Miller, R. Grzywacz, H. Iwasaki, M. Al-Shudifat, D. Bazin, C. R. Bingham, T. Braunroth, G. Cerizza, A. Gade, A. Lemasson, S. N. Liddick, M. Madurga, C. Morse, M. Portillo, M. M. Rajabali, F. Recchia, L. L. Riedinger, P. Voss, W. B. Walters, D. Weisshaar, K. Whitmore, K. Wimmer and J. A. Tostevin. "Direct Lifetime Measurements of the Excited States in ^{72}Ni." *Phys. Rev. Lett.* 116 (12 Mar. 2016), p. 122502 (cit. on p. 94).

[133] C. Mazzocchi, R. Grzywacz, J. Batchelder, C. Bingham, D. Fong, J. Hamilton, J. Hwang, M. Karny, W. Krolas, S. Liddick, A. Lisetskiy, A. Morton, P. Mantica, W. Mueller, K. Rykaczewski, M. Steiner, A. Stolz and J. Winger. "Low energy structure of even–even Ni isotopes close to ^{78}Ni." *Physics Letters B* 622.1 (2005), pp. 45–54 (cit. on p. 94).

[134] T. Marchi, G. de Angelis, J. J. Valiente-Dobón, V. M. Bader, T. Baugher, D. Bazin, J. Berryman, A. Bonaccorso, R. Clark, L. Coraggio, H. L. Crawford, M. Doncel, E. Farnea, A. Gade, A. Gadea, A. Gargano, T. Glasmacher, A. Gottardo, F. Gramegna, N. Itaco, P. R. John, R. Kumar, S. M. Lenzi, S. Lunardi, S. McDaniel, C. Michelagnoli, D. Mengoni, V. Modamio, D. R. Napoli, B. Quintana, A. Ratkiewicz, F. Recchia, E. Sahin, R. Stroberg, D. Weisshaar, K. Wimmer and R. Winkler. "Quadrupole Transition Strength in the ^{74}Ni Nucleus and Core Polarization Effects in the Neutron-Rich Ni Isotopes." *Phys. Rev. Lett.* 113 (18 Oct. 2014), p. 182501 (cit. on p. 94).

List of Figures

List of Tables

List of publications

Publications in refereed journals

[1] D. Kocheva, G. Rainovski, J. Jolie, N. Pietralla, A. Blazhev, R. Altenkirch, S. Ansari, A. Astier, M. Bast, M. Beckers, T. Braunroth, M. Cappellazzo, A. Dewald, F. Diel, M. Djongolov, C. Fransen, K. Gladnishki, A. Goldkuhle, A. Hennig, V. Karayonchev, J. M. Keatings, E. Kluge, T. Kröll, J. Litzinger, K. Moschner, C. Müller-Gatermann, P. Petkov, M. Scheck, P. Scholz, T. Schmidt, P. Spagnoletti, C. Stahl, R. Stegmann, A. Stolz, A. Vogt, N. Warr, V. Werner, D. Wölk, J. C. Zamora, K. O. Zell, V. Y. Ponomarev and P. Van Isacker.
Low collectivity of the 2_1^+ state of ^{212}Po.
Phys. Rev. C 96.4 (2017), p. 044305.

[2] A. Goldkuhle, C. Fransen, A. Dewald, K. Arnswald, M. Bast, M. Beckers, A. Blazhev, T. Braunroth, G. Hackenberg, G. Häfner, J. Litzinger, J. Jolie, C. Müller-Gatermann, F. von Spee, N. Warr, D. Werner and K. O. Zell.
Lifetime measurement of excited states in ^{46}Ti.
The European Physical Journal A 55.4 (2019), p. 53.

[3] M. Ciemala, S. Zilani, F. Crespi, S. Leoni, B. Fornal, A. Maj, P. Bednarczyk, G. Benzoni, A. Bracco, C. Boiano, S. Bottoni, S. Brambilla, M. Bast, M. Beckers, T. Braunroth, F. Camera, N. Cieplicka-Oryńczak, E. Clément, O. Dorvaux, S. Ertürk, G. De France, A. Goldkuhle, J. Grębosz, M. N. Harakeh, L. W. Iskra, B. Jacquot, A. Karpov, M. Kicińska-Habior, Y. Kim, M. Kmiecik, A. Lemasson, H. Li, I. Matea, K. Mazurek, C. Michelagnoli, B. Millio, C. Müller-Gatermann, P. Napiorkowski, V. Nanal, M. Matejska-Minda, M. Rejmund, B. Sowicki, C. Schmitt, M. Stanoiu, I. Stefan, B. Wasilewska, M. Zielińska and M. Zięblński.
Determination of lifetimes of excited states in neutron-rich ^{20}O isotope from experiment with the AGATA+PARIS+VAMOS setup.
Acta Physica Polonica B 50.3 (2019), pp. 615–624.

[4] S. Zilani, M. Ciemala, F. Crespi, S. Leoni, B. Fornal, A. Maj, P. Bednarczyk, G. Benzoni, A. Bracco, C. Boiano, S. Bottoni, S. Brambilla, M. Bast, M. Beckers, T. Braunroth, F. Camera, N. Cieplicka-Oryńczak, E. Clément, O. Dorvaux, S. Erturk, G. De France, A. Goldkuhle, J. Grębosz, M. N. Harakeh, L. W. Iskra, B. Jacquot, M. Kicińska-Habior, Y. Kim, M. Kmiecik, A. Lemasson, H. Li, I. Matea, K. Mazurek, C. Michelagnoli, B. Million, C. Müller-Gatermann, P. Napiorkowski, V. Nanal, M. Matejska-Minda, M. Rejmund, C. Schmitt, M. Stanoiu, I. Stefan, B. Wasilewska and M. Zięblński.
Spectroscopy of neutron-rich C, O, N and F isotopes with the AGATA+ PARIS+VAMOS setup at GANIL.
Acta Physica Polonica B 50.3 (2019), pp. 625–631.

[5] C. Müller-Gatermann, F. von Spee, A. Goasduff, D. Bazzacco, M. Beckers, T. Braunroth, A. Boso, P. Cocconi, G. de Angelis, A. Dewald, C. Fransen, A. Goldkuhle, A. Gottardo, A. Gozzelino, K. Hadyńska-Klek, G. Jawroski, P. John, J. Jolie, S. Lenzi, J. Litzinger, R. Menegazzo, D. Mengoni, D. Napoli, F. Recchia, M. Siciliano, D. Testov, S. Thiel, J. Valiente-Dobón and K. Zell.
A new dedicated plunger device for the GALILEO γ-ray detector array.

Nuclear Instruments and Methods in Physics Research Section A: Accelerators, Spectrometers, Detectors and Associated Equipment 920 (2019), pp. 95–99.

[6] M. M. Giles, B. S. Nara Singh, L. Barber, D. M. Cullen, M. J. Mallaburn, M. Beckers, A. Blazhev, T. Braunroth, A. Dewald, C. Fransen, A. Goldkuhle, J. Jolie, F. Mammes, C. Müller-Gatermann, D. Wölk, K. O. Zell, S. M. Lenzi and A. Poves.
Probing isospin symmetry in the (^{50}Fe, ^{50}Mn, ^{50}Cr) isobaric triplet via electromagnetic transition rates.
Phys. Rev. C 99.4 (2019), p. 044317.

[7] C. Müller-Gatermann, A. Dewald, C. Fransen, K. Auranen, H. Badran, M. Beckers, A. Blazhev, T. Braunroth, D. M. Cullen, G. Fruet, A. Goldkuhle, T. Grahn, P. T. Greenlees, A. Herzáň, U. Jakobsson, D. Jenkins, J. Jolie, R. Julin, S. Juutinen, J. Konki, M. Leino, J. Litzinger, K. Nomura, J. Pakarinen, P. Peura, M. G. Procter, P. Rahkila, P. Ruotsalainen, M. Sandzelius, J. Sarén, C. Scholey, J. Sorri, S. Stolze, M. J. Taylor, J. Uusitalo and K. O. Zell.
Shape coexistence in ^{178}Hg.
Phys. Rev. C 99.5 (2019), p. 054325.

[8] P. A. Butler, L. P. Gaffney, P. Spagnoletti, J. Konki, M. Scheck, J. F. Smith, K. Abrahams, M. Bowry, J. Cederkäll, T. Chupp, G. de Angelis, H. De Witte, P. E. Garrett, A. Goldkuhle, C. Henrich, A. Illana, K. Johnston, D. T. Joss, J. M. Keatings, N. A. Kelly, M. Komorowska, T. Kröll, M. Lozano, B. S. Nara Singh, D. O'Donnell, J. Ojala, R. D. Page, L. G. Pedersen, C. Raison, P. Reiter, J. A. Rodriguez, D. Rosiak, S. Rothe, T. M. Shneidman, B. Siebeck, M. Seidlitz, J. Sinclair, M. Stryjczyk, P. Van Duppen, S. Vinals, V. Virtanen, N. Warr, K. Wrzosek-Lipska and M. Zielińska.
The observation of vibrating pear-shapes in radon nuclei.
Nature Communications 10.1 (2019), p. 2473.

[9] A. Goldkuhle, C. Fransen, A. Blazhev, M. Beckers, B. Birkenbach, T. Braunroth, E. Clément, A. Dewald, J. Dudouet, J. Eberth, H. Hess, B. Jacquot, J. Jolie, Y.-H. Kim, A. Lemasson, S. M. Lenzi, H. J. Li, J. Litzinger, C. Michelagnoli, C. Müller-Gatermann, B. S. Nara Singh, R. M. Pérez-Vidal, D. Ralet, P. Reiter, A. Vogt, N. Warr, K. O. Zell, A. Ataç, D. Barrientos, C. Barthe-Dejean, G. Benzoni, A. J. Boston, H. C. Boston, P. Bourgault, I. Burrows, J. Cacitti, B. Cederwall, M. Ciemala, D. M. Cullen, G. De France, C. Domingo-Pardo, J.-L. Foucher, G. Fremont, A. Gadea, P. Gangnant, V. González, J. Goupil, C. Henrich, C. Houarner, M. Jean, D. S. Judson, A. Korichi, W. Korten, M. Labiche, A. Lefevre, L. Legeard, F. Legruel, S. Leoni, J. Ljungvall, A. Maj, C. Maugeais, L. Ménager, N. Ménard, R. Menegazzo, D. Mengoni, B. Million, H. Munoz, D. R. Napoli, A. Navin, J. Nyberg, M. Ozille, Z. Podolyak, A. Pullia, B. Raine, F. Recchia, J. Ropert, F. Saillant, M. D. Salsac, E. Sanchis, C. Schmitt, J. Simpson, C. Spitaels, O. Stezowski, C. Theisen, M. Toulemonde, M. Tripon, J.-J. Valiente Dobón, G. Voltolini and M. Zielińska.
Lifetime measurements in ^{52,54}Ti to study shell evolution toward N = 32.

Phys. Rev. C 100.5 (2019), p. 054317.

[10] P. A. Butler, L. P. Gaffney, P. Spagnoletti, K. Abrahams, M. Bowry, J. Cederkäll, G. de Angelis, H. De Witte, P. E. Garrett, A. Goldkuhle, C. Henrich, A. Illana, K. Johnston, D. T. Joss, J. M. Keatings, N. A. Kelly, M. Komorowska, J. Konki, T. Kröll, M. Lozano, B. S. Nara Singh, D. O'Donnell, J. Ojala, R. D. Page, L. G. Pedersen, C. Raison, P. Reiter, J. A. Rodriguez, D. Rosiak, S. Rothe, M. Scheck,

M. Seidlitz, T. M. Shneidman, B. Siebeck, J. Sinclair, J. F. Smith, M. Stryjczyk, P. Van Duppen, S. Vinals, V. Virtanen, N. Warr, K. Wrzosek-Lipska and M. Zielińska.
Evolution of Octupole Deformation in Radium Nuclei from Coulomb Excitation of Radioactive ^{222}Ra and ^{228}Ra Beams.
Phys. Rev. Lett. 124.4 (2020), p. 042503.

[11] S. Ziliani, M. Ciemała, F. Crespi, S. Leoni, B. Fornal, A. Maj, P. Bednarczyk, G. Benzoni, A. Bracco, C. Boiano, S. Bottoni, S. Brambilla, M. Bast, M. Beckers, T. Braunroth, F. Camera, N. Cieplicka-Oryńczak, E. Clément, S. Coelli, O. Dorvaux, S.Erturk, G. de France, C. Fransen, A. Goldkuhle, J. Grębosz, M. Harakeh, Ł. Iskra, B. Jacquot, A. Karpov, M. Kicińska-Habior, Y. Kim, M. Kmiecik, A. Lemasson, S. Lenzi, M. Lewitowicz, H. Li, I. Matea, K. Mazurek, C. Michelagnoli, M. Matejska-Minda, B. Million, C. Müller-Gatermann, V. Nanal, P. Napiorkowski, D. Napoli, R. Palit, M. Rejmund, C. Schmitt, M. Stanoiu, I. Stefan, E. Vardaci, B. Wasilewska, O. Wieland, M. Zięblński and M. Zielińska.
Spectroscopy of Neutron-rich Nitrogen Isotopes with AGATA+PARIS+VAMOS.
Acta Phys. Polon. B 51 (2020), p. 709.

[12] L. Barber, D. Cullen, M. Giles, B. N. Singh, M. Mallaburn, M. Beckers, A. Blazhev, T. Braunroth, A. Dewald, C. Fransen, A. Goldkuhle, J. Jolie, F. Mammes, C. Müller-Gatermann, D. Wölk and K. Zell.
Performing the differential decay curve method on γ-ray transitions with unresolved Doppler-shifted components.
Nuclear Instruments and Methods in Physics Research Section A: Accelerators, Spectrometers, Detectors and Associated Equipment 950 (2020), p. 162965.

[13] M. Ciemała, S. Ziliani, F. C. L. Crespi, S. Leoni, B. Fornal, A. Maj, P. Bednarczyk, G. Benzoni, A. Bracco, C. Boiano, S. Bottoni, S. Brambilla, M. Bast, M. Beckers, T. Braunroth, F. Camera, N. Cieplicka-Oryńczak, E. Clément, S. Coelli, O. Dorvaux, S. Erturk, G. de France, C. Fransen, A. Goldkuhle, J. Grębosz, M. N. Harakeh, Ł. W. Iskra, B. Jacquot, A. Karpov, M. Kicińska-Habior, Y. Kim, M. Kmiecik, A. Lemasson, S. M. Lenzi, M. Lewitowicz, H. Li, I. Matea, K. Mazurek, C. Michelagnoli, M. Matejska-Minda, B. Million, C. Müller-Gatermann, V. Nanal, P. Napiorkowski, D. R. Napoli, R. Palit, M. Rejmund, C. Schmitt, M. Stanoiu, I. Stefan, E. Vardaci, B. Wasilewska, O. Wieland, M. Zięblński, M. Zielińska, A. Ataç, D. Barrientos, B. Birkenbach, A. J. Boston, B. Cederwall, L. Charles, J. Collado, D. M. Cullen, P. Désesquelles, C. Domingo-Pardo, J. Dudouet, J. Eberth, V. González, J. Goupil, L. J. Harkness-Brennan, H. Hess, D. S. Judson, A. Jungclaus, W. Korten, M. Labiche, A. Lefevre, R. Menegazzo, D. Mengoni, J. Nyberg, R. M. Perez-Vidal, Z. Podolyak, A. Pullia, F. Recchia, P. Reiter, F. Saillant, M. D. Salsac, E. Sanchis, O. Stezowski, C. Theisen, J. J. Valiente-Dobón, J. D. Holt, J. Menéndez, A. Schwenk and J. Simonis.
Testing ab initio nuclear structure in neutron-rich nuclei: Lifetime measurements of second 2^+ state in ^{16}C and ^{20}O.
Phys. Rev. C 101.2 (2020), p. 021303.

[14] M. Siciliano, J. Valiente-Dobón, A. Goasduff, F. Nowacki, A. Zuker, D. Bazzacco, A. Lopez-Martens, E. Clément, G. Benzoni, T. Braunroth, F. Crespi, N. Cieplicka-Oryńczak, M. Doncel, S. Ertürk, G. de France, C. Fransen, A. Gadea, G. Georgiev, A. Goldkuhle, U. Jakobsson, G. Jaworski, P. John, I. Kuti, A. Lemasson, T. Marchi, D. Mengoni, C. Michelagnoli, T. Mijatović, C. Müller-Gatermann, D. Napoli, J. Nyberg, M. Palacz, R. Pérez-Vidal, B. Sayği, D. Sohler, S. Szilner, D. Testov, M. Zielińska,

D. Barrientos, B. Birkenbach, H. Boston, A. Boston, B. Cederwall, J. Collado, D. Cullen, P. Désesquelles, C. Domingo-Pardo, J. Dudouet, J. Eberth, F. Egea-Canet, V. González, L. Harkness-Brennan, H. Hess, D. Judson, A. Jungclaus, W. Korten, M. Labiche, A. Lefevre, S. Leoni, H. Li, A. Maj, R. Menegazzo, B. Million, A. Pullia, F. Recchia, P. Reiter, M. Salsac, E. Sanchis, O. Stezowski and C. Theisen.
Pairing-quadrupole interplay in the neutron-deficient tin nuclei: First lifetime measurements of low-lying states in ^{106,108}Sn.
Physics Letters B 806 (2020), p. 135474.

[15] M. Beckers, C. Müller-Gatermann, A. Blazhev, T. Braunroth, A. Dewald, C. Fransen, A. Goldkuhle, L. Kornwebel, J. Litzinger, F. von Spee and K.-O. Zell.
Lifetime measurement of excited states in ^{144}Ce: Enhanced E1 strengths in a candidate for octupole deformation.
Phys. Rev. C 102.1 (2020), p. 014324.

[16] P. A. Butler, L. P. Gaffney, P. Spagnoletti, J. Konki, M. Scheck, J. F. Smith, K. Abrahams, M. Bowry, J. Cederkäll, T. Chupp, G. de Angelis, H. De Witte, P. E. Garrett, A. Goldkuhle, C. Henrich, A. Illana, K. Johnston, D. T. Joss, J. M. Keatings, N. A. Kelly, M. Komorowska, T. Kröll, M. Lozano, B. S. N. Singh, D. O'Donnell, J. Ojala, R. D. Page, L. G. Pedersen, C. Raison, P. Reiter, J. A. Rodriguez, D. Rosiak, S. Rothe, T. M. Shneidman, B. Siebeck, M. Seidlitz, J. Sinclair, M. Stryjczyk, P. Van Duppen, S. Vinals, V. Virtanen, N. Warr, K. Wrzosek-Lipska and M. Zielińska.
Addendum: The observation of vibrating pear-shapes in radon nuclei.
Nature Communications 11.1 (2020), p. 3560.

[17] L. Knafla, G. Häfner, J. Jolie, J.-M. Régis, V. Karayonchev, A. Blazhev, A. Esmaylzadeh, C. Fransen, A. Goldkuhle, S. Herb, C. Müller-Gatermann, N. Warr and K. O. Zell.
Lifetime measurements of ^{162}Er: Evolution of collectivity in the rare-earth region.
Phys. Rev. C 102.4 (2020), p. 044310.

[18] K. Arnswald, P. Reiter, A. Blazhev, T. Braunroth, A. Dewald, M. Droste, C. Fransen, A. Goldkuhle, R. Hetzenegger, R. Hirsch, E. Hoemann, L. Kaya, L. Lewandowski, C. Müller-Gatermann, P. Petkov, D. Rosiak, M. Seidlitz, B. Siebeck, A. Vogt, D. Werner, K. Wolf and K.-O. Zell.
Lifetime measurements in ^{44}Ti.
Phys. Rev. C 102.5 (2020), p. 054302.

Publications in conference proceedings

[19] M. Siciliano, J. Valiente-Dobón, A. Goasduff, D. Bazzacco, N. Alahari, G. Benzoni, T. Braunroth, N. Cieplicka, F. Crespi, E. Clément, G. De France, M. Doncel, S. Erturk, C. Fransen, A. Gadea, G. Georgiev, A. Goldkuhle, U. Jakobsson, G. Jaworski, P. John, I. Kuti, A. Lemasson, A. Lopez-Martens, H. Li, S. Lunardi, T. Marchi, D. Mengoni, C. Michelagnoli, T. Mijatovic, C. Müller-Gatermann, D. Napoli, J. Nyberg, M. Palacz, R. Perez-Vidal, M. Rejmund, B. Saygi, D. Sohler, S. Szilner and D. Testov.
Study of Quadrupole Correlations in N = Z = 50 region via lifetime measurements.
Acta Physica Polonica B 48 (2017), pp. 331–336.

[20] D. Kocheva, G. Rainovski, J. Jolie, N. Pietralla, A. Blazhev, A. Astier, R. Altenkirch, M. Bast, M. Beckers, S. Ansari, T. Braunroth, M. Cappellazzo, M. Cortés, A. Dewald, F. Diel, M. Djongolov, C. Fransen, K. Gladnishki, A. Goldkuhle, A. Hennig, V. Karayonchev, J. Keatings, E. Kluge, T. Kröll, J. Litzinger, K. Moschner, C. Müller-Gatermann, P. Petkov, M. Rudigier, M. Scheck, P. Spagnoletti, P. Scholz, T. Schmidt, M. Spieker, C. Stahl, R. Stegmann, A. Stolz, A. Vogt, M. Stoyanova, P. Thöle, N. Warr, V. Werner, W. Witt, D. Wölk, J. Zamora, K. Zell, P. V. Isacker and V. Ponomarev.
Low collectivity of the first 2^+ states of ^{212,210}Po.
Journal of Physics: Conference Series 1023 (2018), p. 012019.

[21] P. Butler, L. Gaffney, P. Spagnoletti, J. Konki, M. Scheck, J. Smith, K. Abrahams, M. Bowry, J. Cederkäll, T. Chupp, G. de Angelis, H. De Witte, P. Garrett, A. Goldkuhle, C. Henrich, A. Illana, K. Johnston, D. Joss, J. Keatings, N. Kelly, M. Komorowska, T. Kröll, M. Lozano, B. Nara Singh, D. O'Donnell, J. Ojala, R. Page, L. Pedersen, C. Raison, P. Reiter, J. A. Rodriguez, D. Rosiak, S. Rothe, T. Shneidman, B. Siebeck, M. Seidlitz, J. Sinclair, M. Stryjczyk, P. Van Duppen, S. Vinals, V. Virtanen, N. Warr, K. Wrzosek-Lipska and M. Zielińska.
Coulomb excitation of pear-shaped nuclei.
EPJ Web Conf. 223 (2019), p. 01007.

[22] A. Goldkuhle, C. Fransen, A. Dewald, N. Alahari, M. Beckers, B. Birkenbach, A. Blazhev, T. Braunroth, E. Clément, G. De France, J. Dudouet, J. Eberth, H. Hess, B. Jacquot, Y. Kim, A. Lemasson, S. M. Lenzi, H. Li, J. Ljungvall, J. Litzinger, C. Michelagnoli, C. Müller-Gatermann, D. R. Napoli, B. S Nara Singh, R. M. Perez-Vidal, D. Ralet, P. Reiter, M. Rejmund, A. Vogt, N. Warr, K. O. Zell and M. Zielińska.
Preliminary results of lifetime measurements in neutron-rich ^{53}Ti.
EPJ Web Conf. 223 (2019), p. 01022.

[23] D. Kocheva, A. Yaneva, D. Kalaydjieva, G. Rainovski, J. Jolie, N. Pietralla, M. Beckers, A. Blazhev, L. Bussmann, M. Cappellazzo, A. Dewald, F. Diel, M. Djongolov, F. Dunkel, A. Esmaylzadeh, B. Falk, C. Fransen, J. Garbe, L. Gerhard, R.-B. Gerst, K. A. Gladnishki, A. Goldkuhle, G. Hackenberg, C. Henrich, I. Homm, K. Ide, V. Karayonchev, R. Kern, J. Kleeman, L. Knafla, L. Kornwebel, T. Kröll, M. Ley, C. Müller-Gatermann, M. Scheck, T. Schmidt, P. Spagnoletti, M. Stoyanova and V. Werner.
Lifetime measurements of the low-lying excited states of ^{208}Po.
Journal of Physics: Conference Series 1555 (2020), p. 012020.

[24] M. Ciemala, S. Ziliani, F. Crespi, S. Leoni, B. Fornal, A. Maj, P. Bednarczyk, G. Benzoni, A. Bracco, C. Boiano, S. Bottoni, S. Brambilla, M. Bast, M. Beckers, T. Braunroth, F. Camera, N. Cieplicka-Oryńczak, E. Clément, O. Dorvaux, S. Erturk, G. De France, C. Fransen, A. Goldkuhle, J. Grębosz, M. Harakeh, Ł. Iskra, B. Jacquot, A. Karpov, M. Kicińska-Habior, Y. Kim, M. Kmiecik, A. Lemasson, S. Lenzi, M. Lewitowicz, H. Li, I. Matea, K. Mazurek, C. Michelagnoli, M. Matejska-Minda, B. Million, C. Müller-Gatermann, V. Nanal, P. Napiorkowski, D. Napoli, R. Palit, M. Rejmund, C. Schmitt, M. Stanoiu, I. Stefan, E. Vardaci, B. Wasilewska, O. Wieland, M. Zielińska and M. Ziębliński.
Short-range Lifetime Measurements for Deep-inelastic Reaction Products: the ^{19}O Test Case.
Acta Phys. Polon. B 51 (2020), p. 699.

Publications in annual reports

[25] M. Siciliano, A. Goasduff, J. J. Valiente-Dobón, R. M. Pérez-Vidal, D. Bazzacco, N. Alahari, G. Benzoni, T. Braunroth, N. Cieplicka, F. C. L. Crespi, E. Clément, M. Doncel, S. Ertürk, C. Fransen, A. Gadea, G. Georgiev, A. Goldkuhle, U. Jakobsson, G. Jaworski, P. R. John, I. Kuti, A. Lemasson, H. Li, T. Marchi, D. Mengoni, C. Michelagnoli, T. Mijatovic, C. Müller-Gatermann, D. R. Napoli, J. Nyberg, M. Palacz, M. Rejmund, B. Saygi, D. Sohler, S. Szilner and D. Testov.
Study of Quadrupole Correlations in the ^{106,108}Sn Isotopes via Lifetime Measurements.
LNL Annual Report 2015 242 (2016), pp. 76–77.

[26] M. Siciliano, J. J. Valiente-Dobón, A. Goasduff, D. Bazzacco, A. Lopez-Martens, N. Alahari, G. Benzoni, T. Braunroth, N. Cieplicka, E. Clément, F. Crespi, M. Doncel, S. Ertürk, G. De France, C. Fransen, A. Gadea, G. Georgiev, A. Goldkuhle, U. Jakobsson, G. Jaworski, P. John, I. Kuti, A. Lemasson, H. Li, S. Lunardi, T. Marchi, D. Mengoni, C. Michelagnoli, T. Mijatovic, C. Müller-Gatermann, D. Napoli, J. Nyberg, M. Palacz, R. Pérez-Vidal, M. Rejmund, B. Saygi, D. Sohler, S. Szilner and D. Testov.
Lifetime measurement in Z = N = 50 region: Optimization of OFT parameters.
LNL Annual Report 2016 250 (2017), pp. 102–103.

[27] M. Siciliano, J. J. Valiente-Dobón, A. Goasduff, D. Bazzacco, N. Alahari, G. Benzoni, T. Braunroth, N. Cieplicka, F. Crespi, E. Clément, G. de France, M. Doncel, S. Ertürk, C. Fransen, A. Gadea, G. Georgiev, A. Goldkuhle, U. Jakobsson, G. Jaworski, P. R. John, I. Kuti, A. Lemasson, A. Lopez-Martens, H. Li, S. Lunardi, T. Marchi, D. Mengoni, C. Michelagnoli, T. Mijatovic, C. Müller-Gatermann, D. Napoli, J. Nyberg, M. Palacz, R. Pérez-Vidal, M. Rejmund, B. Saygi, D. Sohler, S. Szilner and D. Testov.
Neutron-deficient Sn isotopes populated via deep-inelastic collisions.
LNL Annual Report 2017 251 (2018), pp. 57–58.

Acknowledgements – *Danksagung*

The research leading to the results of this thesis has received from the German Bundesministerium für Bildung und Forschung (BMBF) under Contract Nos. 05P18PKFN9 and 05P19PKGNA, the European Union Seventh Framework through ENSAR under Contract No. 262010, partially supported by the Generalitat Valenciana, Spain, Conselleria d'Eduació, Investigació, Cultura i Esport under the grant PROMETEU/2019/005 and Ministerio de Ciencia, Innovación y Universidades Spain, under grants Nos. FPA2017-84756-C4 and SEV-2014-0398, by the EU FEDER funds, and by the U.S. Department of Energy, Office of Science, Office od Nuclear Physics, under Contract No. DE-AC02-06CH11357.

Nach der formalen Danksagung möchte ich noch ein paar persönliche Worte verlieren. An erster Stelle danke ich Dir, Alfred, als mein Doktorvater für die Vergabe des interessanten Forschungsthemas und für die Möglichkeit diese Arbeit in Deiner Arbeitsgruppe am Institut für Kernphysik durchgeführt haben zu können. Bereits im Rahmen meiner Staatsexamensarbeit konnte ich den Umgang mit Plunger-Auswertungen erlernen. Ich danke Dir für die Betreuung der gesamten Bearbeitungsphase meiner Dissertation und für den großzügig gewährten Forschungsfreiraum. Vielen Dank, dass Du mir die Möglichkeit gegeben hast, die Ergebnisse meiner Arbeit auf Konferenzen präsentieren und bei vielen weiteren Experimenten mitarbeiten zu können. Dafür gebührt Dir mein aufrichtiger Dank.

Weiterhin danke ich Dir, Andreas, für die Übernahme des Koreferats sowie Ihnen, Herrn Prof. Dr. Andreas Schadschneider für die Übernahme des Vorsitzes der Prüfungskommission. Trotz des ungewöhnlichen Formats, das der Corona Situation geschuldet war, haben/habt Sie/ihr für eine reibungsfreie und angenehme Prüfungssituation während meiner Disputation gesorgt.

Ein besonderer Dank geht an Dich, Christoph. Du hast Dich um meine Anliegen immer schnellstmöglich gekümmert und warst eine unersetzbare Person bei meinen Experimenten. Vielen Dank für die zahlreichen Anmerkungen in der Korrekturphase meiner Publikationen und meiner Arbeit sowie für die Hilfe bei kleinen und größeren Dingen. Dir ist es aufgrund Deines großen Einsatzes am GANIL zu verdanken, dass diese Daten für meine Doktorarbeit entstanden sind.

Ein weiterer Dank geht an Dich, Andrey, für die vielen Gespräche und aufschlussreichen Diskussionen. Großen Dank für die Unterstützung bei den Schalenmodellrechnungen sowie beim Verfassen meiner Publikationen. Durch Deine wertvollen Denkanstöße, die viel Licht ins Dunkle gebracht haben, konnte ich viele Zusammenhänge aus einem neuen Blickwinkel betrachten und viel dazu lernen.

Großer Dank geht an Dich, Thomas, insbesondere für die Bereitstellung Deiner Simulation, auf deren Anwendung ein großer Teil meiner Datenanalyse beruht. Ohne Dich und Deine Arbeit hätte ich mir wohl einen anderen Ansatz für meine Datenanalyse überlegen müssen.

Danke, dass Du mit viel Engagement, Fachwissen und Tatkraft auch nach Deiner Zeit im IKP jederzeit zur Seite standest und für meine vielen Fragen und Probleme stets erreichbar warst. Aber auch die vielen nicht-fachlichen Gespräche, Fußballabende, und vor allem die verschiedensten Geldinvestitionen haben für einen guten Ausgleich gesorgt. Für letzteres hast natürlich auch Du, Konni, (mal mehr, mal weniger) gesorgt.

Ein weiterer Dank geht an Dich, Claus, der Du zu jeder Tages- und Nachtzeit Fragen beantwortet und Probleme gelöst hast. Du warst eine tragende Säule bei jedem meiner Experimente. Danke für die vielen konstruktiven Hilfestellungen und das Korrekturlesen meiner Arbeit!

I would also like to thank you, Emmanuel and Antoine, from GANIL for your help with the VAMOS++ simulation code and with the analysis of the AGATA data. Thank you for the great collaboration.

I would like to thank all participants in the experiment at GANIL for the help in planning, performing and taking over beamtime shifts.

Liebe Arbeitsgruppe, vielen Dank für die zahlreichen fachlichen Gespräche, Ratschläge und Anmerkungen und für die freundliche und angenehme Arbeitsatmosphäre im und außerhalb des Büros.

Außerdem bedanke ich mich bei euch, Arwin, Julia, Konrad, Levent, Susan und Richard für die enge Zusammenarbeit und Unterstützung in vielen Projekten und Experimenten.

Weiterhin bedanke ich mich bei Euch Operateuren des Tandembeschleunigers: Albert, Frank, Otto und Victor. Ihr habt immer für einen reibungslosen Strahlbetrieb bei meinen Experimenten am IKP gesorgt, sodass genügend Zeit für das ein oder andere Gespräch blieb. So vergingen die Schichten wie im Flug! Haltet die Maschine(n) weiter so gut am laufen!

Außerdem bedanke ich mich ganz herzlich bei Dir, liebe Theresa! Die gemeinsamen sportlichen Stunden mehrmals in der Woche sorgten immer dafür, den Kopf frei zu bekommen.

Liebe Dani, auch dir gilt es zu danken: für all die Jahre, die wir uns nun kennen. Danke für eine tolle Studienzeit, für die aufbauenden Worte, die zahlreichen Gespräche und vor allem für die schönen langen Spaziergänge, die die Arbeit für eine kurze Zeit in den Hintergrund rücken ließ.

Zum Abschluss gilt mein Dank meinen geliebten Eltern und meiner Schwester: Liebe Mama, lieber Papa, liebe Maren, ihr habt mich nicht nur auf meinem Weg durch das Studium und durch die anschließende Promotion begleitet, sondern ihr standet auf meinem gesamten Lebensweg immer zur Seite und ward für mich da! Herzlichen Dank für die bedingungslose Unterstützung und Förderung vor allem auch abseits meiner Schul- und Studienzeit, dass ich viel Zeit der Musik widmen konnte und das alles ohne Druck! Nicht zuletzt gilt mein persönlicher Dank Dir, Felix, für die Geduld und Stärkung in anstrengenden Zeiten der Vielfachbelastungen. Danke, dass Du mir in dieser Zeit ausnahmslos zur Seite standest. Ich liebe dich!

Erklärung zur Dissertation

Hiermit versichere ich an Eides statt, dass ich die vorliegende Dissertation selbstständig und ohne die Benutzung anderer als der angegebenen Hilfsmittel und Literatur angefertigt habe. Alle Stellen, die wörtlich oder sinngemäß aus veröffentlichten und nicht veröffentlichten Werken dem Wortlaut oder dem Sinn nach entnommen wurden, sind als solche kenntlich gemacht. Ich versichere an Eides statt, dass diese Dissertation noch keiner anderen Fakultät oder Universität zur Prüfung vorgelegen hat; dass sie - abgesehen von unten angegebenen Teilpublikationen und eingebundenen Artikeln und Manuskripten - noch nicht veröffentlicht worden ist sowie, dass ich eine Veröffentlichung der Dissertation vor Abschluss der Promotion nicht ohne Genehmigung des Promotionsausschusses vornehmen werde. Die Bestimmungen dieser Ordnung sind mir bekannt. Darüber hinaus erkläre ich hiermit, dass ich die Ordnung zur Sicherung guter wissenschaftlicher Praxis und zum Umgang mit wissenschaftlichem Fehlverhalten der Universität zu Köln gelesen und sie bei der Durchführung der Dissertation zugrundeliegenden Arbeiten und der schriftlich verfassten Dissertation beachtet habe und verpflichte mich hiermit, die dort genannten Vorgaben bei allen wissenschaftlichen Tätigkeiten zu beachten und umzusetzen. Ich versichere, dass die eingereichte elektronische Fassung der eingereichten Druckfassung vollständig entspricht.

Köln, 14.01.2020 (Alina Goldkuhle)

Die Dissertation beinhaltet die Gewinnung von Primärdaten sowie die Analyse solcher Daten, die auf den Servern[10] des Instituts für Kernphysik der Universität zu Köln gesichert und zugänglich sind.

Teilpublikationen

- A. Goldkuhle *et al.* "Lifetime measurements of excited states in neutron-rich ^{53}Ti: benchmarking effective shell-model interactions". *Phys. Rev. C* 102, 054334 (2020).
- A. Goldkuhle *et al.* "Preliminary results of lifetime measurements in neutron-rich ^{53}Ti". *The European Physical Journal Web Conferences* 223 01022 (2019).
- A. Goldkuhle *et al.* "Lifetime measurements in ^{52,54}Ti to study shell evolution toward $N = 32$". *Phys. Rev. C*, 100, 054317 (2019).
- A. Goldkuhle *et al.* "Lifetime measurement of excited states in ^{46}Ti". *The European Physical Journal A* 55(4) 53 (2019).

[10] unter: /data/agoldkuhle/54Ti
/data/agoldkuhle/46Ti
/data/agoldkuhle/50Ti_2